DISSERTATION / DOCTORAL THESIS

Titel der Dissertation /Title of the Doctoral Thesis

„Orion Belt Population"

verfasst von / submitted by

Mag. Karolina Kubiak

angestrebter akademischer Grad / in partial fulfilment of the requirements for the degree of

Doktorin der Naturwissenschaften (Dr. rer. nat.)

Wien, 2019 / Vienna 2019

ii

To my inspiration,
my mentor
and I'm proud to say
my friend

Acknowledgements

Personal

I owe my deepest gratitude and appreciation to all those whose support and expertise made this fantastic journey possible for me. I would never have been able to aspire to a PhD, much less to complete one, without the lifelong support and encouragement of them. Writing, for the most part, is a solitary act, but it certainly wouldn't be possible for me without the loving support of my family and friends. My parents introduced me to science when I was a young child. And since then they have never stopped to endorse my interest in the Universe. When I was a teenager my father brought me a telescope so I could pursue my growing interest in astronomy. My mother has supported me in many more ways that I can say. My studies have kept me away from home for many years, I thank my sister, Monika, for taking care of things at home.

I thank my sister and my parents who continue to support me despite my long absences.

Thanks also must go to Rainer. I couldn't have gotten through this without your steady reassurance, your barrage of questions, your constant challenges, the occasional swift kick in the pants and, oh yes, your unwavering enthusiasm, love and support.

Thank you all.

Institutional

I am very grateful for the overwhelmingly positive interactions that I have had with members of the Astronomical Institute in Vienna.

First and foremost, I would like to thank my supervisor Prof. Joao Alves for being my advocate and a devil's advocate when needed and being there time after time no matter how small the question or how difficult the problem. Joao has been extremely generous and patient with me, especially during the times when my progress was slow. He showed me how to carry out a research project. Joao has also tried to teach me how to communicate my ideas clearly.

Your contribution, your dedication and your expertise constantly challenge me and always improve my work. I hope that I will eventually learn to put my thoughts into writing as clearly and effectively as you do.

Abstract

One of the governing questions driving my current research is to understand how stellar clusters and OB associations are formed and how they evolve. The Orion star-forming region (SFR) is an ideal laboratory to investigate the connection between clusters and OB association – i.e., how their star formation histories (SFH) and dynamical evolution compare. The proximity of the region, also known as the Orion OB 1 association, makes it one of the most significant stars formation laboratories in astronomy since it harbors a half dozen subgroups containing well-known OB stars and giant molecular clouds and has generated about 10^4 low- and high-mass stars for at least the last $\sim$12 Myr. To explain the complexity of the Orion region, Blaauw proposed a sequential star formation scenario, where a previous generation of stars is responsible for the formation of a new one via positive feedback.

The goal of this dissertation is to characterize the poorly studied population of stars in the vicinity of the supergiant ϵ Orionis (Orion Belt sub-region, Blaauw's OB 1b population) and put them in the context of the Orion star-forming region. The ϵ Orionis region was first mentioned in 1931 by the Per Collinder in his catalog of open clusters, which is today known as the Collinder catalog. He distinguished the Orion Belt asterism (Alnitak, Alnilam, Mintaka) as Collinder 70. Notation commonly used for this particular region was introduced by Blaauw. He sliced Orion into the divisions according to the differences in age and content of gas and dust.

My goal was to disentangle the different populations and construct a consistent catalog of positions and photometry measurements for objects in the region. I identified members of the population and specified the most important observables and the contextual relation with the whole Orion star-forming region.

My work has identified a rich and well-defined stellar population north of NGC 1981, the Orion Belt Population – OBP. The newly discovered population is likely the low-mass counterpart to the Ori OB 1b subgroup. I present the results of *Gaia* DR2 data application in the attempt to resolve the 3D structure of the Orion Belt Population. To obtain more quantitative results I extended my research by complementing previously obtained data with other bands and by modeling the spectral energy distributions (SED) of the infrared counterparts of young stellar objects (YSO). The colors and spectral index analysis revealed the general nature of the point sources. By constructing and analyzing a wide

SED, it is possible to quantify several physical parameters and also constrain the evolutionary stage of the YSOs.

Such an analysis, however, requires not only a good coverage of the wavelength range but also high spatial resolution data to ensure that the fluxes we are studying arise mainly from the star-disk system and are not contaminated by their surroundings. For this purpose, using infrared surveys such as 2MASS, All-WISE, IRAS and several optical surveys from the literature, I assembled the best data available for a sample of bonafide IR counterparts of OBP candidates and constructed their SED to the best possible extent.

In parallel to that analysis I investigated the variability of members in OBP. The primary motivation was to inspect YSO variability amongst OBP members with a statistical approach. I highlight my analysis and attempt to guide other researchers in their use of AllWISE multi-epoch photometry for thermal infrared variability studies. Multi-epoch photometry from AllWISE makes a useful resource in cases where mid-infrared variability is expected to be present with large amplitudes, or for YSOs where it can be connected to the presence of disks. I identified variables using the Stetson index, which quantifies the correlation of variability in two (or more) bands.

Many of the stars display unique variability characteristics that can only be appreciated from inspection of light curves. I also investigate the influence of mid-IR variability on the spectral index, which is a classical metric to identify YSO.

Zusammenfassung

Eine der vorherrschenden Fragen, die ich aktuell untersuche, ist es, die Entstehung und Entwicklung von Sternhaufen und OB-Assoziationen zu verstehen. Das Sternentstehungsgebiet im Orion ist ein ideales Studienobjekt, um die Zusammenhänge zwischen Sternhaufen und OB-Assoziationen zu untersuchen, d.h. wie vergleichbar die zeitliche Entwicklung der Sternentstehung und ihre dynamische Entwicklung sind. Die Nähe des Gebiets, das auch Orion-OB1-Assoziation genannt wird, macht es zu einem der wichtigsten Sternentstehungsgebiete für die astronomische Forschung, da es ein halbes Dutzend Untergruppen mit bekannten OB-Sternen und Riesenmolekülwolken enthält und im Laufe der vergangenen ~ 12 Millionen Jahre ungefähr 10^4 massearme und -reiche Sterne hervorgebracht hat. Zur Erklärung der Unübersichtlichkeit im Orion-Sternentstehungsgebiet schlug Blaauw die "sequential star formation" vor, bei der die vorhergehende Sterngeneration durch positives Feedback für die Entstehung der nächsten Generation verantwortlich ist.

Das Ziel dieser Dissertation ist es, die bisher kaum untersuchte Sternpopulation in der Umgebung des Superriesen ϵ Orionis zu charakterisieren (das Gebiet um Orions Gürtel, Blaauws OB 1b Population), und ihren Zusammenhang mit dem Orion Sternentstehungsgebiet zu verstehen. Das Gebiet um ϵ Orionis wurde zum ersten Mal im Jahr 1931 von Per Collinder in seinem Katalog von offenen Sternhaufen erwähnt, der heute als Collinder-Katalog bekannt ist. Er bezeichnete die Sterngruppe in Orions Gürtel (Alnitak, Alminam, Mintaka) als Collinder 70. Die allgemein verwendeten Bezeichnungen in diesem Gebiet wurde von Blaauw eingeführt. Er unterteilte Orion anhand der Unterschiede in Alter und Häufigkeit von Staub und Gas in vier Bereiche.

Mein Ziel war es, die verschiedenen Sternpopulationen zu trennen und einen konsistenten Katalog von Positionen und photometrischen Messungen für Objekte in diesem Gebiet zu erstellen. Ich identifizierte die Mitglieder der Sternpopulation und gebe die wichtigsten Beobachtungsgrößen sowie die Zusammenhänge mit dem gesamten Sternentstehungsgebiet im Orion an.

Meine Arbeit fand eine reichhaltige und wohldefinierte Sternpopulation nördlich von NGC 1981, die Orion Belt Population – OBP. Die neuentdeckte Population ist wahrscheinlich das massearme Gegenstück zur Untergruppe Ori OB 1b. Um genauere Ergebnisse zu erhalten, erweiterte ich meine Untersuchungen, indem ich die vorhandenen Daten mit anderen Spektralbereichen ergänzte und die spektralen Energieverteilungen (Spectral Energy Distribution – SED) der den jungen stellaren Objekten (YSO) entsprechenden Infrarotquellen modellierte. Die Analyse der Farben und Spektralindices ergab die allgemeine Beschaffenheit der Punktquellen. Durch die Erstellung und Analyse einer breiten SED ist es möglich, mehrere physikalische Parameter zu bestimmen und die Entwicklungsstufe der YSO einzugrenzen.

Eine solche Analyse erfordert nicht nur eine gute Abdeckung in Wellenlänge, sondern auch hohe räumliche Auflösung, um sicherzustellen, dass die untersuchten Flüsse überwiegend von dem System aus Stern und Scheibe stammen und nicht durch das Umfeld kontaminiert werden. Zu diesem Zweck habe ich unter Verwendung von Infrarot-Durchmusterungen wie 2MASS, All-WISE und IRAS sowie mehreren optischen Durchmusterungen aus der Literatur die besten verfügbaren Daten für eine Stichprobe der wahrscheinlichen Infrarot-Gegenstücke zu OBP Kandidaten zusammengetragen, und ihre SEDs mit der bestmöglichen Ausdehnung und Qualität erstellt.

Parallel zu dieser Analyse habe ich die Variabilität von Mitgliedern der OBP erforscht. Der Hauptgrund war, die Variabilität von YSO anhand der OBP Mitglieder auf statistische Weise zu untersuchen. Ich beleuchte meine Auswertung und versuche, andere Forscher dabei anzuleiten, wie sie AllWISE multi-epoch Photometrie für Studien der Variabilität im thermischen Infrarot verwenden können. Multi-epoch Photometrie von AllWISE ist ein wertvolles Hilfsmittel in Fällen, in denen Variabilität im mittleren Infrarot mit großer Amplitude zu erwarten ist, oder bei YSO, bei denen sie mit der Anwesenheit von Scheiben zusammenhängt. Ich entdeckte veränderliche Sterne unter Verwendung des Stetson-Index, der die Korrelation der Variabilität in zwei (oder mehr) Spektralbändern misst.

Viele der Sterne zeigen charakteristische Helligkeitsänderungen, die nur durch die Betrachtung der Lichtkurven verstanden werden können. Ich habe auch die Auswirkung der Helligkeitsänderungen im mittleren Infraroten auf den Spektralindex untersucht, der eine der klassischen Größen darstellt, anhand derer YSO entdeckt werden können.

Fasten with a stellar belt (composed of the stars Alnitak, Alnilam, and Mintaka) at which the sword hangs, with a bow in his hand extended to the west and with his other hand raised north after shooting. Orion is considered the most beautiful constellation of the sky. This annotated image of the Orion constellation shows the clouds of nebulous, glowing dust that sit in the field.

Credit: Image courtesy of Rogelio Bernal Andreo.
Labels by Richard Talcott. Published: November 1, 2018.

SH2-261

Lambda
Orionis
(SH2 264)

Meissa

Betelgeuse

Bellatrix

Witch Head Nebula

NGC 1788

LBN 917

Mintaka

Alnilam

Alnitak

vdb62/63

M78

Flame Nebula

Horsehead Nebula

Orion Nebula

LBN 915

Barnard's Loop

Rigel

NGC 2170

Saiph

Rogelio Bernal Andreo
DeepSkyColors.com

Orion is one of 88 constellations officially recognized by the International Astronomical Union in 1922; The modern constellation boundaries were set by Eugéne Delporte in 1930. Orion ranks as twenty-sixth constellations in size, covering 594 square degrees.

The map of the Orion constellation where the brightest stars and Messier Catalog objects are marked. The basic properties of stars are summarized in the Table 1. The Bayer designation, the star proper name, Henry Draper Catalogue (HD) and Hipparcos Catalogue (HIP) designation numbers are presented in first four columns, followed by the V band brightness in magnitude, right ascension and declination positions and the spectral type for each star. In the case of multiple systems only the brightness components are listed. The origin and meaning of the proper names are presented in Table 1.1.
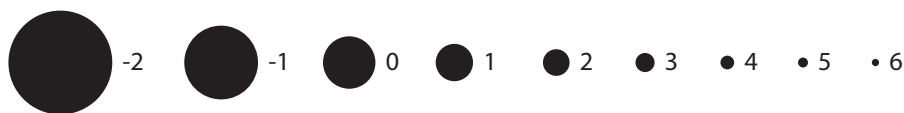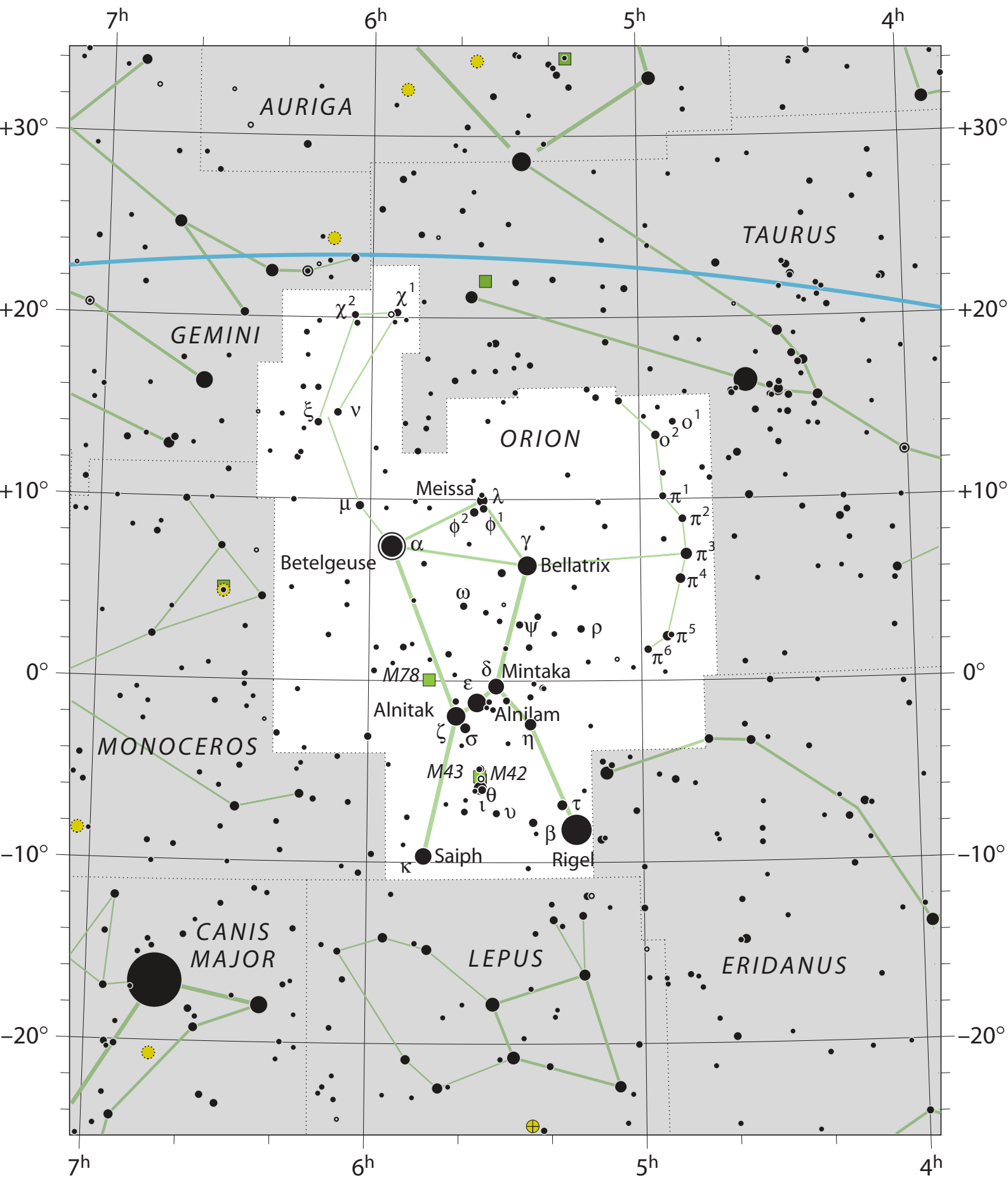
Credit: IAU and Sky & Telescope

Table 1: Properties of Orion stars

Bayer	Name	HD	HIP	V	RA	Dec	Sp. class
α Ori	Betelgeuse	HD39801	HIP27989	0.42	05^{h}55^{m}10.29^s	+07° 24' 25.3"	M2Ib
β Ori	Rigel	HD34085	HIP24436	0.13	05^{h}14^{m}32.27^s	−08° 12' 05.9"	B8Ia
γ Ori	Bellatrix	HD35468	HIP25336	1.64	05^{h}25^{m}07.87^s	+06° 20' 59.0"	B2V
δ Ori	Mintaka	HD36486	HIP25930	2.41	05^{h}32^{m}00.40^s	−00° 17' 56.7"	O9V
ϵ Ori	Alnilam	HD37128	HIP26311	1.69	05^{h}36^{m}12.81^s	−01° 12' 06.9"	B0Ia
ζ Ori	Alnitak	HD37742	HIP26727	1.79	05^{h}40^{m}45.52^s	−01° 56' 33.3"	O9.7Ib
η Ori		HD35411	HIP25281	3.35	05^{h}24^{m}28.62^s	−02° 23' 49.7"	B1V
θ Ori		HD37020	HIP26220	6.73	05^{h}35^{m}15.82^s	−05° 23'14.3"	B0.5V
ι Ori		HD37043	HIP26241	2.77	05^{h}35^{m}25.98^s	−05° 54' 35.6"	O9III
κ Ori	Saiph	HD38771	HIP27366	2.06	05^{h}47^{m}45.39^s	−09° 40' 10.6"	B0.5Ia
λ Ori	Meissa	HD36861	HIP26207	3.66	05^{h}35^{m}08.28^s	+09° 56'03.0"	O8III
μ Ori		HD40932	HIP28614	4.13	06^{h}02^{m}22.99^s	+09° 38' 50.5"	A1V
ν Ori		HD41753	HIP29038	4.40	06^{h}07^{m}34.32^s	+14° 46' 06.7"	B3V
ξ Ori		HD42560	HIP29426	4.48	06^{h}11^{m}56.40^s	+14° 12'31.7"	B3IV
o^1 Ori		HD30959	HIP22667	4.72	04^{h}52^{m}31.96^s	+14° 15' 02.8"	M3III
o^2 Ori		HD31421	HIP22957	4.06	04^{h}56^{m}22.32^s	+13° 30' 52.5"	K2III
π^1 Ori		HD31295	HIP22845	4.65	04^{h}54^{m}53.70^s	+10° 09' 04.1"	A0V
π^2 Ori		HD30739	HIP22509	4.35	04^{h}50^{m}36.72^s	+08° 54' 00.9"	A1V
π^3 Ori		HD30652	HIP22449	3.19	04^{h}49^{m}50.14^s	+06° 57'40.5"	F6V
π^4 Ori		HD30836	HIP22549	3.68	04^{h}51^{m}12.37^s	+05° 36' 18.4"	B2III
π^5 Ori		HD31237	HIP22797	3.73	04^{h}54^{m}15.10^s	+02° 26' 26.4"	B2III
π^6 Ori		HD31767	HIP23123	4.46	04^{h}58^{m}32.90^s	+01° 42' 50.5"	K2II
ρ Ori		HD33856	HIP24331	4.44	05^{h}13^{m}17.48^s	+02° 51' 40.5"	K1III.
σ Ori		HD37468	HIP26549	3.79	05^{h}38^{m}44.77^s	−02° 36' 00.2"	O9.5V
τ Ori		HD34503	HIP24674	3.59	05^{h}17^{m}36.40^s	−06° 50' 39.8"	B5III
υ Ori		HD36512	HIP25923	4.63	05^{h}31^{m}55.86^s	−07° 18' 05.5"	O9.7V
ϕ^1 Ori		HD36822	HIP26176	4.41	05^{h}34^{m}49.24^s	+09° 29' 22.5"	B0III
ϕ^2 Ori		HD37160	HIP26366	4.09	05^{h}36^{m}54.33^s	+09° 17' 29.1"	G9.5III
χ^1 Ori		HD39587	HIP27913	4.40	05^{h}54^{m}23.08^s	+20° 16' 35.1"	G0V
χ^2 Ori		HD41117	HIP28716	4.63	06^{h}03^{m}55.18^s	+20° 08' 18.5"	B2Ia
ψ^1 Ori		HD35439	HIP25302	4.96	05^{h}24^{m}44.83^s	+01° 50' 47.2"	B1V
ψ^2 Ori		HD35715	HIP25473	4.61	05^{h}26^{m}50.23^s	+03° 05' 44.4"	B2IV
ω Ori		HD37490	HIP26594	4.59	05^{h}39^{m}11.15^s	+04° 07' 17.3"	B3V

Contents

List of Figures

List of Tables

Poets say science takes away from the beauty of the stars, mere globs of gas atoms. Nothing is 'mere'. I too can see the stars on a desert night, and feel them. But do I see less or more? The vastness of the heavens stretches my imagination stuck on this carousel my little eye can catch one-million-year-old light. A vast pattern of which I am a part... What is the pattern or the meaning or the why? It does not do harm to the mystery to know a little more about it.

— Richard Feynman

1

The unmistakable image of a man walking across the heavens

The beginnings of the astronomic interests of the man are lost in the depths of the ages, but we can assume that as soon as the man took upright posture, he raised his gaze to heaven and with amazement - and probably with fear - he stared at phenomena taking place somewhere, far away over his head, on a huge canopy covering the area of his residence - a flat circle of land.

The primitive man did not realize the size of the surrounding world and the scale of phenomena occurring in it, but when in the course of arduous evolution he learned to formulate his thoughts, express them and ask questions, then he began to inquire: who am I to the world? The answer to this question was not easy - looking for it, he coped how he could: he saw certain connections between different phenomena, but he could not get to the cause of these sometimes strange correlations ... Then he filled the gaps in the image of the world with supernatural beings. This is how, at the stage of civilization's beginnings, knowledge was inseparably connected with magical practices and religious beliefs, which allowed humanity to survive even in the most dramatic circumstances, establish a certain order of things and define at least to some degree its place in the Universe.

We do not know what the Neanderthal felt and thought, looking at the starry sky at night. In the almost forgotten novel of J.H. Rosny 'The giant cat'[1], the author gives such a literary vision of the beginnings of astronomical interests:

'A month passed half his way, he descended toward the west, and a few stars flickered over the wastes. Zur wondered what people were lighting them every night. However, it burned for so long, it means that their flame is constantly being stoked, Zur tried to see those who healed wood and could not understand why they were invisible ... Sometimes he wondered about the heat of the sun, stronger when it is at the top of the sky than in the evening when it becomes enormous ... These thoughts quickly discouraged and bore Zur, he abandoned them and even forgot them completely ... '

Moreover, it is enough to raise your head at night and turn your eyes to the shimmering lights of distant worlds, to understand how much still remains to discover and explore.

The prevailing conviction that astronomy is one of the oldest sciences, at least several thousand years old, has in recent years been confirmed not only in written sources, but also thanks to archaeological discoveries and reinterpretations of legends, myths, and beliefs of ancient people. The issue of the interpretation of written and unwritten astronomical sources is dealt with by archeoastronomy, which appeared several decades ago as a scientific discipline at the interface between archeology and astronomy. The main task of this science is, on the one hand, the support of archeology and ancient history when researching historical accounts of all kinds of phenomena taking place on the celestial sphere, orientation and construction of ancient buildings, usually connected with a cosmic religious ritual, as well as an iconography containing motifs or astronomical themes. Moreover, on the other hand, determining, at least approximately, when a person began to be interested in phenomena on the celestial sphere in a practical and cognitive sense.

Many ancient cultures shared the belief that the humankind came from the stars. Perhaps this is why so much time, effort, and energy has been put into the study of the celestial bodies from ancient times right up through today.

---

[1]Sometimes known as 'Quest of the Dawn Man'.

Several constellations and stars have played an especially important role in ancient mythology surrounding the celestial origins of our species. In the places where these legends emerge, we find structures that correlate with the position of these stars and constellations in the sky.

The configurations of the constellation Orion roughly formed about 1.5 million years ago. Because of relatively slow movements of stars within the constellation from Earth's perspective (especially the belt of Orion), the constellation will remain visible in the night sky for the next 1 to 2 million years in almost unchanged shape. This makes the constellation of Orion one of the longest observable constellations parallel to the rise of human civilization. Its location on the celestial equator entirely south of the ecliptic allows it to be visible from almost every part of the globe[2]. Being so prominent and distinctive, the pattern of stars that form Orion was recognized as a coherent constellation by many ancient civilizations, though with different representations and mythologies. It was of central importance to many ancient cultures.

Manilius, (1st century AD) an ancient Roman poet and author of *Astronomica* called it 'the mightiest of constellations','golden Orion'. He exaggerated its brilliance by saying that, when Orion rises, 'night feigns the brightness of day and folds its dusky wings'. Manilius described Orion as 'stretching his arms over a vast expanse of sky and rising to the stars with no less huge a stride' (see Figure 1.1). In fact, ranked as 26th in size according to the modern constellation boundaries, Orion is not an exceptionally large constellation. It is, for instance, smaller than Perseus. It is the brilliance of its stars that gives Orion the illusion of being much larger. His right shoulder and left foot are marked by the brilliant stars Betelgeuse and Rigel, with a distinctive line of three stars forming his belt.

The Giant, The Hunter, generally has been represented with back turned toward us and faced in profile, armed with club, or sword, and protected by his shield, or,

---

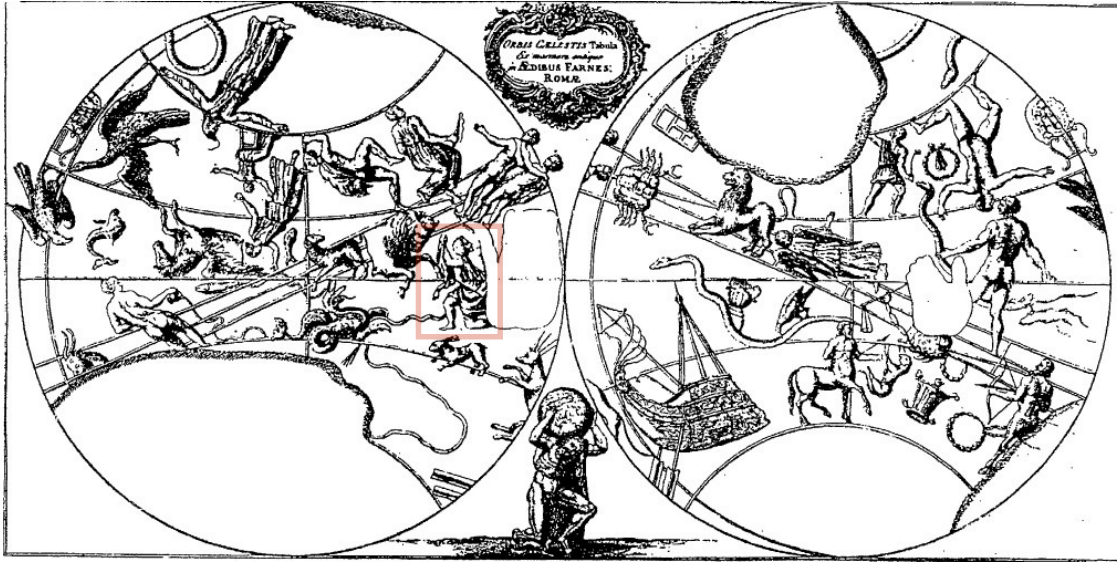[2]Orion constellation can be seen from latitude between +85° to -75°.

Figure 1.1: The map of the sky from in Manilius' Astronomicaon (1739). It is an illustration of celestial glob carried by the Farnes Atlas. The globe is part of an exhibition of the National Museum in Naples. The Farnes Atlas is the only known surviving celestial map or globe from Greek antiquity it is dated to the second century AD. The shapes of the constellation have been copied from it in almost exactly the same way for next millennium. Since the Farnes Atlas carries the globe the figures are presented back-to-front, as the celestial sphere is being viewed outside.

as illustrated in *Uranographia*, the largest star atlas that has ever been published (see Figure 1.2) and H.W. Longfellow[3] wrote in 'The occultation of Orion':

> '(...) on his arm the lion's hide
>
> Scatters across the midnight air
>
> The golden radiance of its hair.'

Now let us examine the origin of Orion constellation. Having a trip through centuries of human histories all over the globe.

Mesopotamia In the distant times date back to the beginnings of the astronomy of Mesopotamia, where the Sumerians had already been observing before five millennia. First of all, the changes of the Moon's phases and the movement of the Sun on the celestial sphere were observed, mainly for the needs of counting time and for religious reasons. The earliest messages about systematic observations of

---

[3]Henry Wadsworth Longfellow (1807 - 1882) an American poet and educator. He was the first American to translate Dante Alighieri's Divine Comedy.

Figure 1.2: Orion raises his club against the charging Taurus. XII in the Uranographia of Johann Bode (1801). Orion's right shoulder is marked by the bright star Betelgeuse, and his left foot by Rigel. A line of three stars forms his belt. From *Uranographia Sive Astrorum.*

other phenomena come from the period of the rule of Ammizaduga (1646-1626 BC). They contain information about the observations of the rises and sets of Ishtar, or the planet Venus – the third object of the sky (after the Sun and the Moon).

The Sumerian Orion constellation has its origins in the epic of Gilgamesh. Records point to Gilgamesh being a historical king who ruled over the Sumerian city of Uruk in southern Mesopotamia sometime between 2700 and 2500 BC. In the Sumerian mythology, Gilgamesh was a demigod possessing superhuman strength whose great accomplishments assured his divine status amongst his subjects. He is associated with the story of the hero fighting 'The Bull of Heaven', Gugalanna (see Figure 1.3) who had been unleashed by the supreme god Anu to kill Gilgamesh, as an act of revenge for spurning his daughter's (Ishtar) affection.

Around 1000 BC, Babylonian astronomers compiled the MUL.APIM, a comprehensive star and constellation catalog in which the constellation of Orion was called

Figure 1.3: Mesopotamian clay tablet illustrating the myth of Gilgamesh. Exhibit of Berlin Museum.

MULSIPA.ZI.AN.NA[4], meaning the 'The Heavenly Shepherd' or 'True Shepherd of Anu'. This refers to the messenger to Anu, attendant deity walking bird of Ninshubur or Papshukal (Rogers 1998). Rochberg (2010) connects the myth of ruler with the shepherd translating the latest and the analogy between the king and the shepherd as the protector of his people[5].

In some of the ancient text (e.g., List VI, Astrolobe B, Reiner & Pingree (1999)), from the region of Mesopotamia, the constellations in the path of the Moon are listed as the Stars (Pleiades), the Jaw of the Bull (Hyades and α Taurii) and the True Shepherd of Anu (Figure 1.4).

Orion was also known as Sitaddalu (in Mul.Alpin) meaning 'he who was smitten by a weapon'. This name refers to the constellation covering our Canis Major, which were a Bow and Arrow, aimed at Orion. It shows great similarities to the Hindu myth and to one of the Greek legends of the death of Orion had him being shot by an arrow from the goddess Artemis while he was swimming far out at sea.

Egypt   Astronomy played an important role in the life of ancient Egypt, where special attention was paid to the phenomena taking place on the celestial sphere. Changes of the Moon's phases and the rises of Sirius were followed. Priests have been

---

[4]AN.NA means 'of heaven'

[5]Kings, like gods, are called shepherd of their people, for example hammurapu, 'The shepherd called Enlil(to rule),' (Codex Hammurabi I 51)
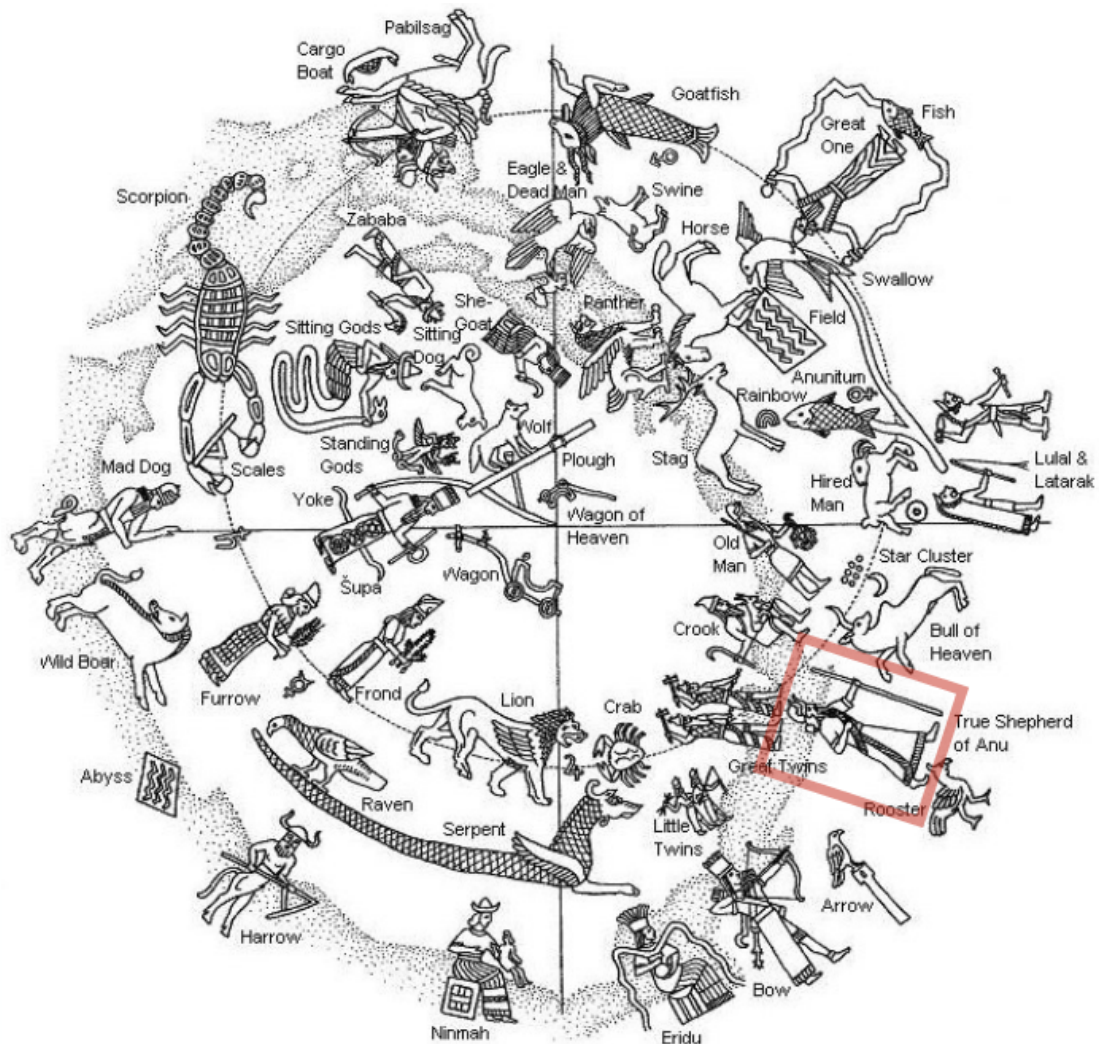
Figure 1.4: The Babylonian star map. The constellation, associated with Orion, depicted Ninshubu as a shepherd with his left foot forward, and a staff in his extended left hand.

plotting the movement of the stars, studying the heavens, constructing calendars, and erecting monuments to track the procession of the constellations and heavenly bodies across the night sky and used to trace periodicity of seasonal weather changes. What can be explained by the great care of Egyptian astronomers in observing the celestial sphere; Orion was, to the ancient Egyptians, the most distinctive of all the constellations in the night sky, and it rose directly before the nearby star Sirius. The knowledge of the Egyptian priests, however, was hermetic, not accessible to outsiders, so the information about ancient Egyptian astronomy is very fragmentary, although there is no doubt that its level was very high for those

times, which indirect evidence, for example, is the precise orientation according to the world of Pharaoh Khufu's pyramid (Cheops) from the 4th Dynasty.

The myths of Osiris and the description of Orion in the sky   'The Scorpion rises as Orion starts to sink into the other side of the sky, and this was seen as Orion running away from the attacker, and still in fear of him. Thus, Scorpius rule the northern hemisphere's summer while Orion rules the winter skies.'[6]

The Ancient Egyptians were one of the first to write about Orion, and place him into their mythologies. They associate the stars of Orion with Sah and Sopdet were later syncretized with the deities Osiris (the God of Light) and Isis. While the appearance of Sirius (Isis) rising with the Sun (heliacal rising) around the time of the summer solstice start of the agricultural year, the appearance of the three 'king-stars' of Osiris (Orion) at night after a similarly absent period, before pointing to Isis, signified the flooding's end around the time of the winter solstice.

Osiris was the sun-god of rebirth and afterlife, one of the most important gods of the ancient Egyptians[7]. Orion was considered the home of Osiris following his resurrection. Isis lived on Sirius. In Egyptian mythology, Osiris was murdered and dismembered by his jealous brother, Seth. Osiris and Seth were in a never-ending battle for supremacy. Seth tricked Osiris, closed and suffocated him in a box, which he constructed to fit Osiris exactly. Seth chopped the body of his brother into fourteen pieces and scattered them in all directions. Isis found only thirteen pieces of Osiris body. She constructed the final missing part of her husband body out of the wood. She breathes into them, and Osiris rose into the sky.

The Pyramid Texts speaks of the Nile in connection with Osiris: '... The two mountains are split apart. The God comes into being, the God has power in his body. The month is born, the fields live.'

---

[6]http://www.constellationsofwords.com/Constellations/Orion.html

[7]The Oxford Guide: Essential Guide to Egyptian Mythology, Edited by Donald B. Redford, p302-307, 2003. Berkley.
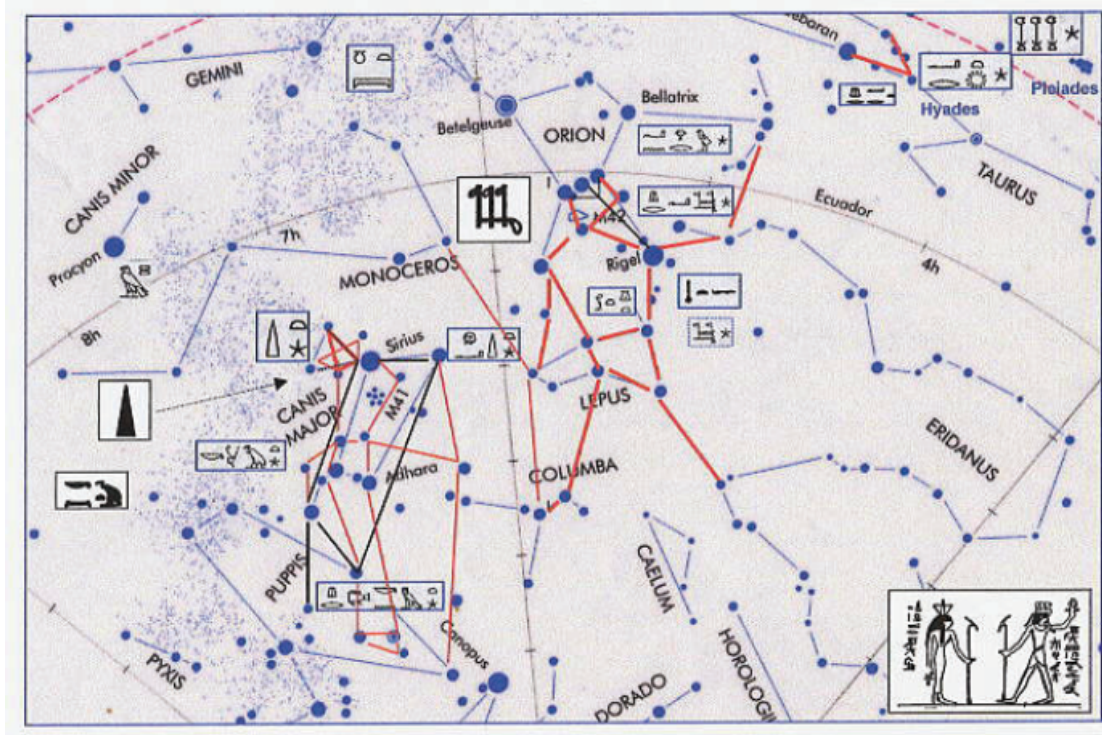
Figure 1.5: The sky map of the region from the Pleiades to Canopus. The most important ancient Egyptian constellations and asterisms have been identified. Adopted from Belmonte (2002). Sah would be the belt and sword of Orion. Sah and Sopdet are represented on the lower right corner with their hieroglyphic crowns over their head.

Moreover, 'O Osiris! The inundation is coming; abundance surges in. The flood-season is coming, arising from the torrent issuing from Osiris, O King may Heaven give birth to thee as Orion!'

Also, in a hymn to Osiris, Rameses IV says 'You are the Nile, Gods and men live from your outflow.'

In Egyptian astronomy, Sah has an anthropomorphic representation of a large constellation that mostly corresponds to today's Orion and Lepus including some stars from modern Eridanus, Monoceros, and Columba constellations (see Figure 1.5). Sah with Orion's Belt imagined as a crown upon his head, while the star Sirius was his wife Sopdet (Sothis), a woman wearing a tall crown adorned with a five-pointed star. The ancient Egyptians believed that the gods descended from the three stars of Orion's Belt.

In ancient Egypt, Orion was prominent and of great importance. It could not be missed on the great relief of the square Zodiac of Dendera. Described by

John H. Rogers as 'the only complete map that we have of an ancient sky' (see Figure 1.6); The Dendera Zodiac shows the Mesopotamian zodiac surrounded by the Egyptian constellation for the rest of the sky (Rogers 1998); and nearly three thousand years earlier had been sculptured on the walls of the temple of Sakkara, and in the great Ramesseum of Thebes as Sahu (Sadek 1991) or as presented on the ceiling of the Tomb of Senenmunt (see Figure 1.7).

This twice appears in the Book of the Dead:

'The shoulders of the constellation Sahu;'

and:

'I see the motion of the holy constellation Sahu.'

Orion's Belt and the Giza Plateau   Explorers like to find many connections between the Orion constellation and the way ancient cultures built the *pyramids.* As an example, Orion Belt matches the arrangement of the three Pyramids in Giza, a feature also seen in China and South America. This idea first entered the public imagination in the 1970s by J.J. Hurtak[8], and was later revived by Graham Hancock[9].

Robert Bauval, a Belgian mining engineer, wrote a fascinating book, 'The Orion Mystery'. He describes that the stars in Orion Belt are precisely not aligned and he noticed, that the Pyramids of Giza were not, either.

Graeco-Roman tradition   Greek astronomy was born in slightly different conditions than in Egypt and Mesopotamia, because in everyday life of the Hellenic nation, apart from agriculture and pastoralism, it also played a major role in naval navigation. The milestone of the development of astronomy was the great breakup of Alexander's empire and the birth of the Hellenistic world, which made the exchange of civilizational gains of individual nations: the Babylonians, Egyptians, Greeks, and Persians - much easier.

The earliest known written description was by Eudoxus (around 370 BC) in his book of constellations, the 'Phenomena'. He learned much of his astronomy

---

[8]The Book of Knowledge: The Keys of Enoch
[9]Orion correlation theory
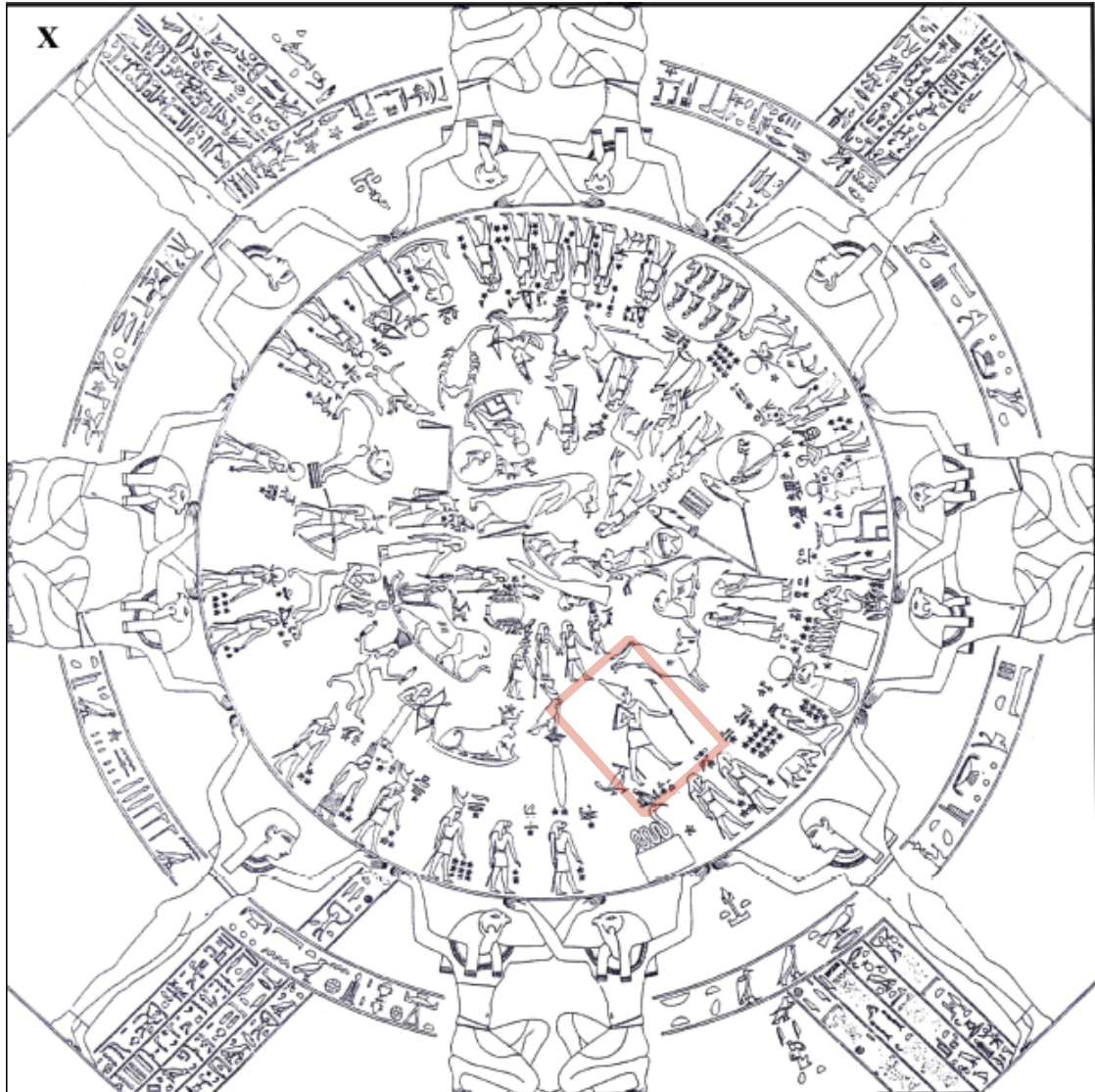
Figure 1.6: The Zodiak of Dendara. The description has been translated as: *(This is) the sky of gold, the sky os gold, (it is) Isis the Great, mother of the god (Horus), Lady of the Primordial Hill at Iunut (Dendara), (this is) the sky of Gold. His great divinities are the stars: Horus-son-of-Isis, his god of the morning: Sokar, his god of light; Ihy, his visible star; Osiris the Moon, Sah is his god; Sopdet is his goddess. They enter and exit (…?) of the Lower Valley.*

Figure 1.7: The imprint from the ceiling in the tomb of Senenmut, the favorite of Queen Hatshepsut. It presents the ancient Egyptian view of Sopdet (on the left) and Sah (Orion, on the right). Adapted from Belmonte (2002).

during a visit to Egypt and Cnidus. We know the contents of 'Phaenomena', for Eudoxus' prose text was the basis for a poem of the same name by Aratus of Soli (an illus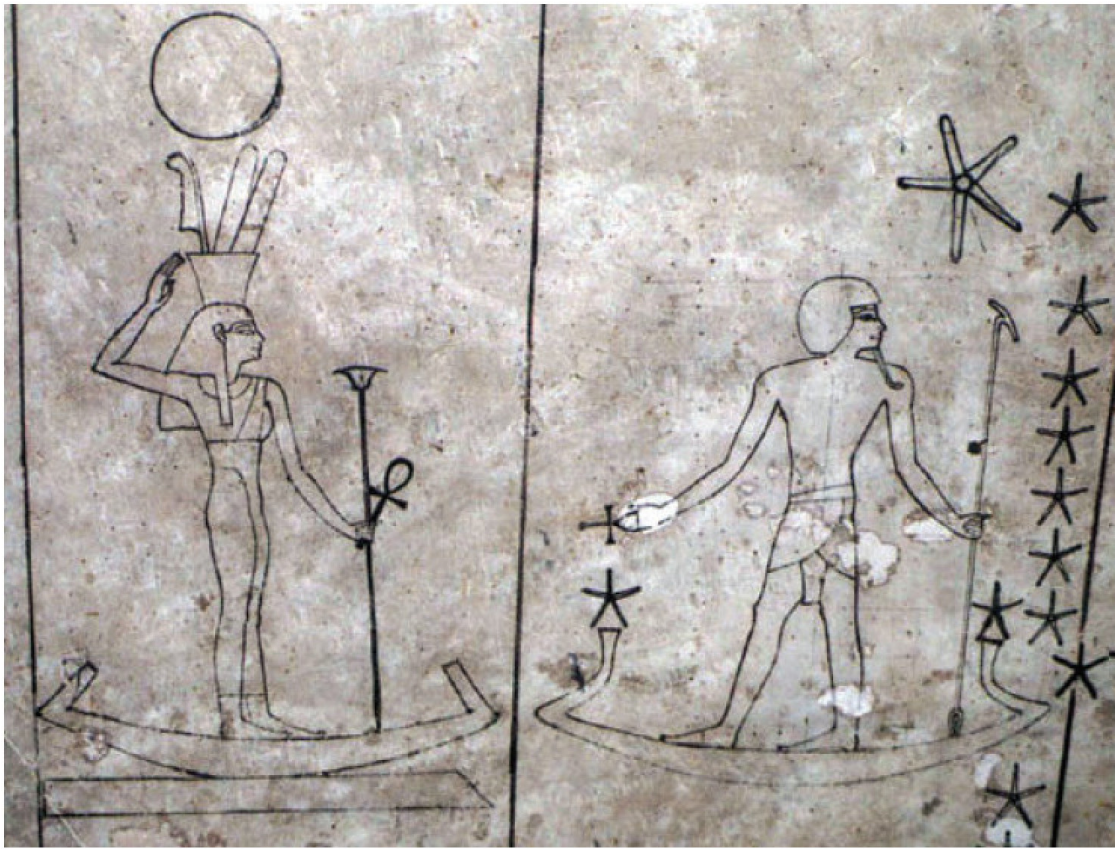tration of Orion from a later edition of 'Phaenomena' is presented in Figure 1.8). Hipparchus refer to the text of Eudoxus in his comments on Aratus. The purpose of the 'Phenomena' was to give an introduction to the constellations (shapes and the positions of stars). It gave the relative times of their rising and settings, referred only briefly to myths about them but explaining extensively their use for weather-forecasting for seamen. The positions of the constellation, north of the ecliptic, are described by reference to the main groups surrounding the north pole (Ursa Major, Ursa Minor, Draco, and Cepheus), while Orion serves as a point of departure for those to the south. Orion is known as the 'Mighty Hunter' and is one of the most recognizable and splendid constellations in the sky. The three stars in the Belt of
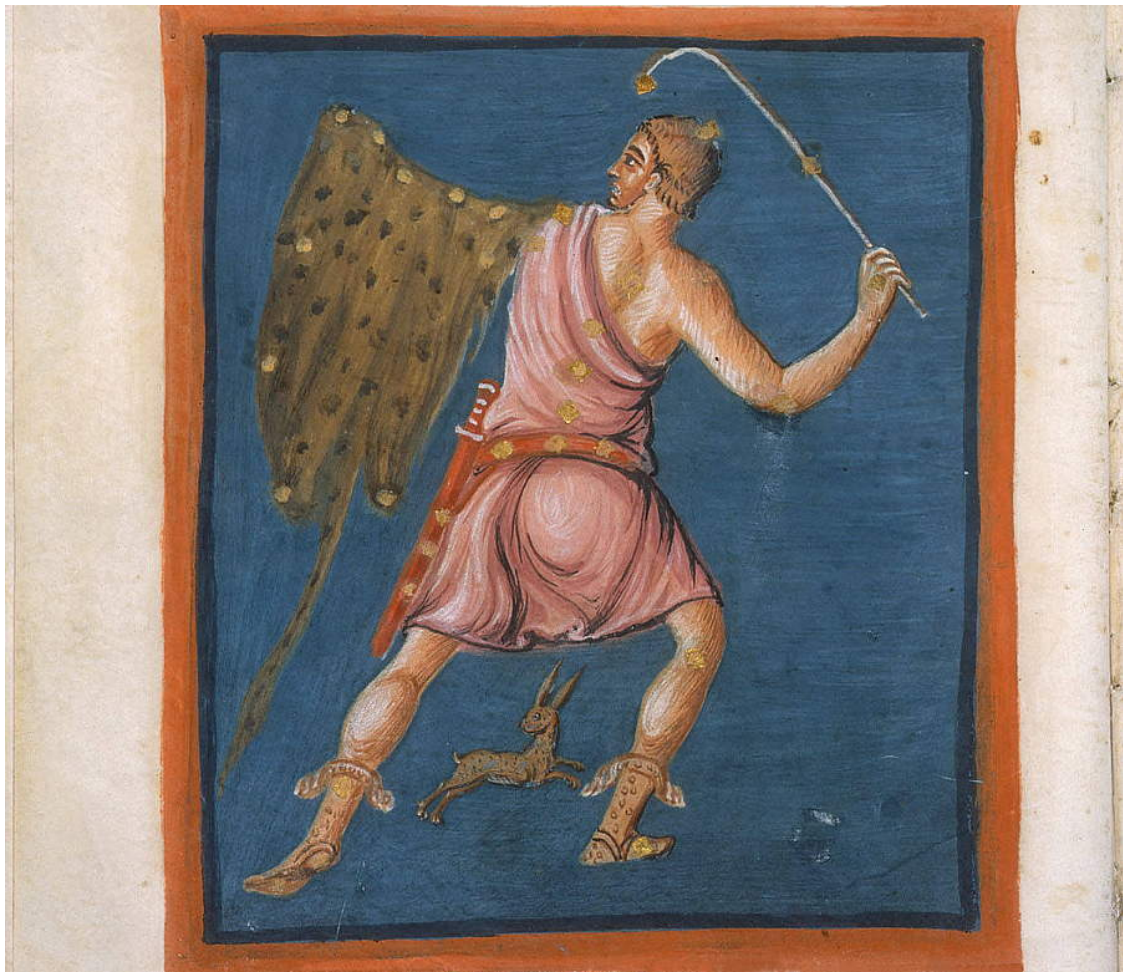
Figure 1.8: This unusual visualization of Orion and Lepus the hare at his feet comes from the Leiden Aratea (816 AD) (Leiden University). The Leiden Aratea is a copy of Germanicus Caesar's Latin translation of the Phaenomena of Aratus.

Orion show up clearly in the northern winter sky and align with the celestial equator.

Ancient Greek sources tell several different stories about Orion. According to the myth described by Hesiod in his Astronomy Fragment 4, Orion was the son of Poseidon and Euryale, daughter of King Minos of Crete. The sea god, Poseidon, gave his son the power to walk on water. He was a giant of a man, feared no creature.

There is a strange and persistent story (preserved at pseudo-Eratosthenes Catasterismi Farg 22, trans. Evelyn-White) about the birth of Orion. According to this story, an old farmer from Thebes, named Hyrieus offered his hospitality to three passing strangers. Who happened to be the gods Zeus, Poseidon, and Hermes. In repay for the hospitality the visitors asked Hyrieus about his wishes.

Hyrieus said that he would have liked a son. The three gods promised to fulfill this wish. The gods urinated on the bull's hide they had just eaten and told Hyrieus to bury it. A boy was born from the underground hidden hide. Hyrieus named his soon Urion after the mode of his conception.

Orion fell in love with Merope on the island of Chios[10] and won her hand by ridding the island of wild animals. Merope's father refused to grant her to Orion, for he hated the idea of having such a man as his daughter's husband. The Hunter got drunk and assaulted his beloved. In punishment, Oenopion, Merope's father, put out Orion's eyes and banished him from the island. Orion, who could walk on water, found his way to the god of fire and metalworking, Hephaestus. The god felt pity on Orion and offered one of his assistants to act as his eyes. Putting his new assistant on his shoulders, Orion moved east towards the sunrise, gain his sight back.

There are several other stories about the Orion in Greek mythology, including one that involves the Pleiades star cluster in Taurus. The story says that Orion fell in love with the Pleiades and pursued them with sexual intent. However, according to Hyginus[11], it was actually their mother Pleione he was after. Zeus gathered the group up and placed them among the stars, where Orion still pursues them across the sky each night.

There were various accounts of Orion's death. One version of it says that Artemis was in love with Orion. Her brother Apollo did not approve her choice. Apollo tricked Artemis into killing Orion. In grief, Artemis placed Orion and the scorpion on opposite sides of the sky. The different version of his death says that when he threatened to kill every beast on Earth Gaia (Mother Earth), the angry goddess tried to kill Orion with a scorpion. This is the reason why the constellations of Scorpius and Orion never appear in the sky at the same time.

---

[10]according to Pindar (lyric poet 5th century BC)

[11]Gaius Julius Hyginus (64 BC-AD 17) was a Latin author of 'De Astronomica' or 'Poeticon Astronomicon' :
'When Pleione once was traveling through Boeotia with her daughters [the Pleiades], Orion, who was accompanying her, tried to attack her. She escaped, but Orion sought her for seven years and couldn't find her. Jove [Zeus], pitying the girls, appointed a way to the stars, and later, by some astronomers, they were called the Bull's tail. Moreover, so up to this time, Orion seems to be following them as they flee towards the west.'

In the 'Astronomica' of Hyginus, we find the following explanation for the origin of the constellations Scorpio and Orion:

'But the whole of the constellation (Scorpio) was put in the sky, it is said, for the following reason: Orion since he used to hunt, and felt confident that he was most skilled of all in that pursuit, said even to Diana and Latona that he was able to kill anything they produced. Earth, angered at this, sent the scorpion which is said to have killed him. Jove, however, admiring the courage of both, put the scorpion among the stars, as a lesson to men not to be too self-confident. Diana, then, because of her affection for Orion, asked Jove to show to her request the same favor he had given of his own accord to Earth. Moreover, so the constellation was established in such a way that when Scorpion rises, Orion sets.' Figure 1.9 presents the XV-th century visualization of Orion, printed by E. Randolt in his edition of 'Poeticon Astronomicon' from 1482. The Orion has been presented here as a model medieval knight in full *shiny* armor with a sword on his side carrying his shield and rising mace.

In Greek mythology Orion was never recorded as fighting a bull, but in the sky, he confronts the Taurus.

The constellation is mentioned in many poems written by antics masters and philosophers like Horace, Virgil, Hesiod, Callimachus, Strabo, Diodorus Siculus, Antoninus Liberalis, Servius, Seneca or Valerius Flaccus.

Globes were the main form of celestial maps in classical times. Although polar projection maps were not common, they did exist, presenting both figures and/or stars. Direct copies that have survived to our times are:

- European manuscripts of Aratus from the early 9th century AD (see Figure 1.8 and Whitfield (1995))

- an Islamic palace ceiling from the early 8th century AD (see Figure 1.10)

- a Byzantine manuscript of Ptolemy from the 9th century AD (see Figure 1.15)

Rion:hunc a zona τ reliquo corpore equinoctialis circulus diuidit cū tauro decertantē collocatū: de/ xtra manu clauā tenentē τ incinctū ense: spectantē ad occasum: τ occidentē exorta scorpionis posterio re parte τ sagictario exoriēte: cū cancro autem toto corpore pariter exurgentē .Hic habet in capite stellas tres claras . Jn vtrisqꝛ humeris singulas. Jn cubito dextro obscurā vnam. Jn manu similem vnam. Jn zona tres. Jn eo quo gladius eius defor matur tres obscuras. Jn vtrisqꝛ gēnibus singulas claras . Jn pedi bus singulas obscuras. Omnino sunt decē τ septē.

Orion

f

Figure 1.9: A page from the E. Ratdolt edition of the 'De Astronomica' showing of the constellation of Orion. Courtesy of the US Naval Observatory Library.
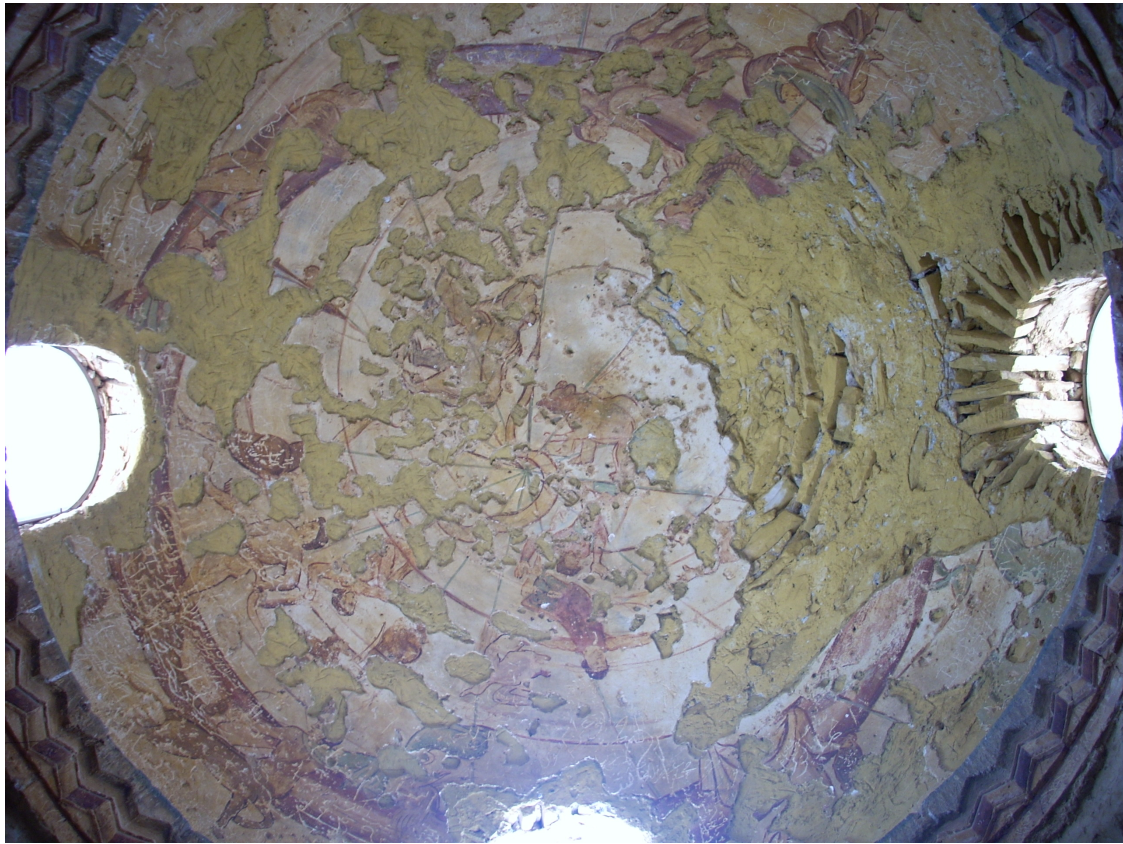
Figure 1.10: The remains of the vault of the heaven. The design is what which would be seen looking down the globe. Hemispheric dome has a representation of the heavens with 35 separate identifiable constellations.

Through the centuries from antique almost to the end of the middle ages, the classical sky-pictures were transmitted through somewhat schematic plain illustrations, but also through accurate Islamic star-globes, and mostly through the written specification of the figures in the Ptolemy's 'Almagest'. The Austrian National Library in its collection of manuscripts dating from the late antiquity and the medieval period posses an astonishing set of planispheres. Two of them presented in Figure 1.12 and 1.13 are undoubtedly one of the richest in information and details and became the model for subsequent renaissance maps of the sky. The origin of these two handwritten papers, dating around 1440, is still unknown. The exactness and precision of the position of the stars lead to the conclusion that the author not only uses the written specification of the figures in Ptolemy's 'Almagest' but that somehow he used real observations, produced by himself or

Figure 1.11: Planispheric map of the sky from a fifteenth-century byzantine manuscript. Biblioteca Apostolica Vaticana, Rome.

another astronomer of that period.

If this hypothesis is valid, the Vienna manuscript would be almost a photograph of the sky at that time. It would be after many centuries the first artifact made on fresh and recent observations.

Ptolemy and Almagest   Ptolemy was the Greek astronomer who lived and worked in Alexandria (Egypt) in 2nd century AD. He collected ancient Greek descriptions of 1,022 stars in his famous work 'Syntaxis Mathematica' or 'Almagestum' in Latin (the modern English name 'Almagest' comes from the Arabic 'al-majisti'). Ptolemy's catalog of stars is arranged into 48 constellations. Orion has

Figure 1.12: Vienna manuscript, Northern celestial planisphere about 1440. Courtesy of Österreichie Nationalbibliothek Wien

been listed as 35th (Figure 1.15). Ptolemy estimates the brightnesses of stars, based largely on the observations of the earlier Greek astronomers, such as Hipparchus. Ptolemy's book has been translated into Arabic in the 9th century by Al Sufi and became famous. Many of the Arabic-language star descriptions in the Almagest came to be used widely as names for stars.

Arabic   The medieval Muslim astronomy known Orion as al-jabbar, 'the giant'. Orion's sixth brightest star, Saiph, is named from the Arabic, saif al-jabbar, meaning 'sword of the giant'. Algebra, another Arabic title for Orion, has the same spelling

Figure 1.13: Vienna manuscript, Northern celestial planisphere about 1440. Courtesy of Öesterreich Nationalbibliothek Wien

as that branch of mathematics.

Abd-al-Rahman Al Sufi[12], was one of the most outstanding practical astronomers of the Middle Ages. He contributed several corrections to Ptolemy's star list, in particular he did own brightness estimates that deviated from those in Ptolemy's work. Al Sufi published his famous Kitab al-Kawatib al-Thabit al-Musawwar ('Book of Fixed Stars') in 964. This masterpiece of stellar astronomy describes much of his work, both in textual descriptions and pictures. He related the Greek and Arabic constellations, which was difficult as these constellations were completely unrelated and overlapped in a complicated way (see Figures 1.15 and 1.16). It is considered important even now for the study of proper motions and long period variables.

---

[12]or Abr-ar Rahman As Sufi, Abd al Rahman Abu al Husain, sometimes referred to as Azophi; December 7, 903 - May 25, 986 A.D. Persia.
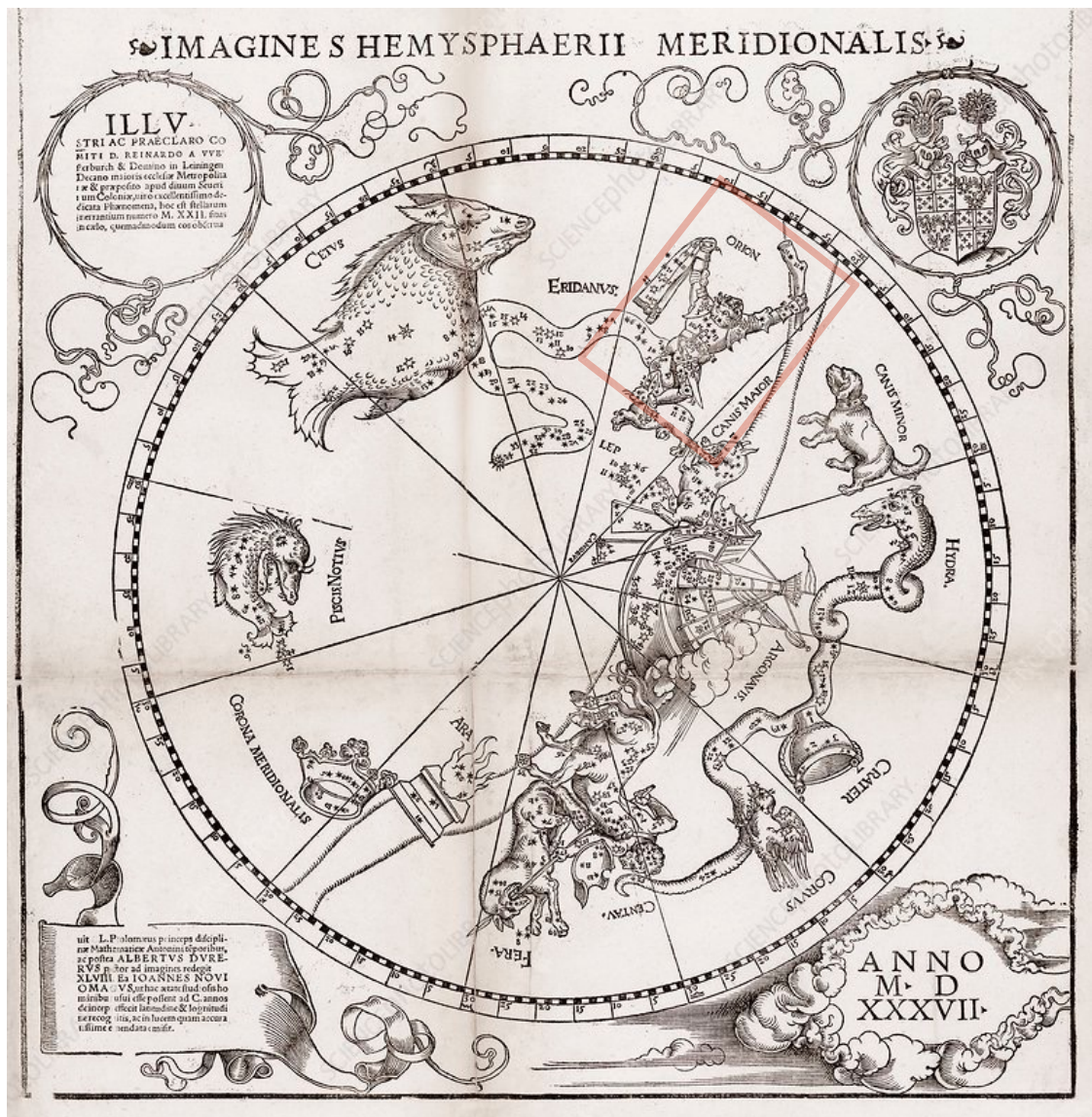
Figure 1.14: The illustrations of the southern hemisphere constellations, based on Albrecht Durer's star charts of 1515. From Stellarum MXXII (Books 7-8 of an edition of Ptolemy's Almagest), printed in Cologne in 1537.

When the Arabic texts were translated into Latin, the Arabic tradition of star names has been adopted by the Latin world.

This happened often in a highly contaminated form that either changed the meaning, or in extreme cases gave birth to words with no meaning at all. Other names were mistakenly transferred from one star to another, so that a name might even refer to a different constellation (Greek or Arabic) rather than to the one of the star's actual residence.
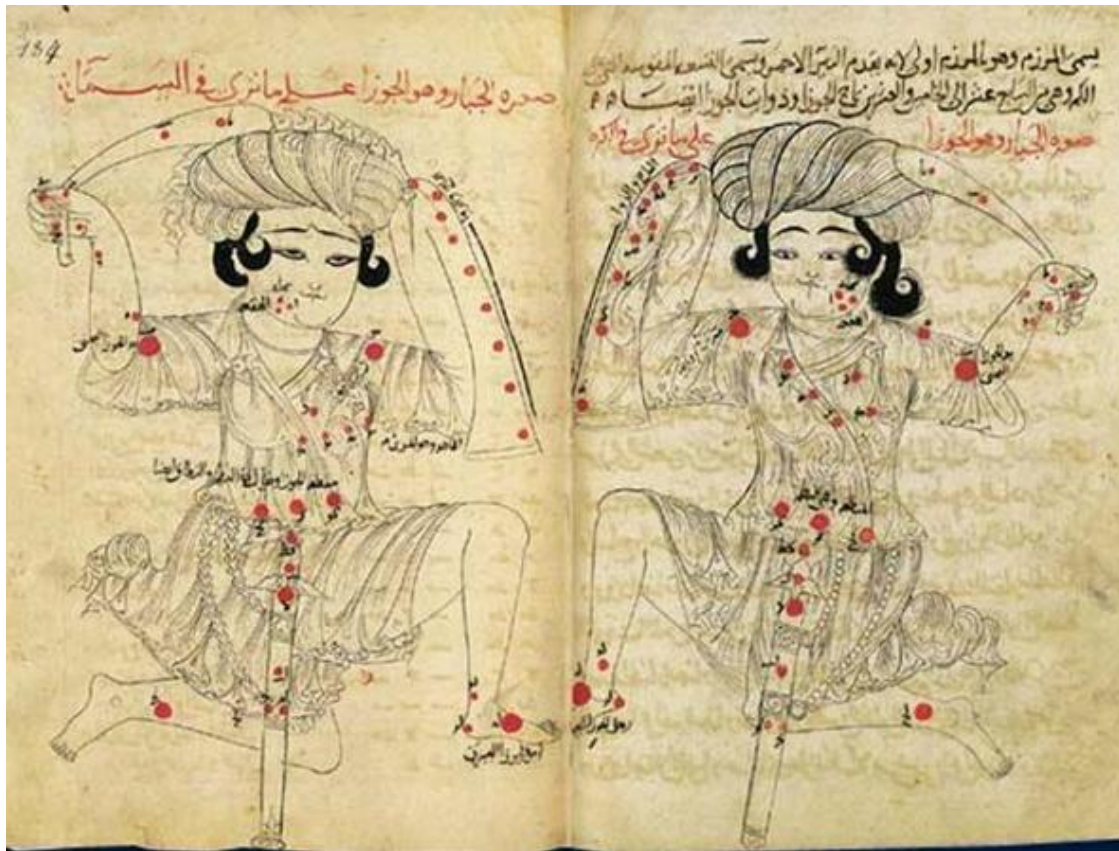
Figure 1.15: The depiction of Orion, as seen from Earth (left) and a mirror-image, from a 13th-century copy of al-Sufi's 'Book of the Fixed Stars'. Here, Orion's shield has become a long sleeve, typical of Islamic dress. Each constellation description was augmented by a mirrored pair of star maps, as viewed in the sky and as viewed on a celestial globe. Credits: Museum of Islamic Art, Doha.

The majority of star names are Arabic in origin.

Europe In Hungarian mythology, Orion is known as (magic) Archer or Reaper, named Nimrod, 'a mighty hunter before the Lord'[13], a famous hunter and father of Hunor and Magor, the twins known as Hun and Hungarian. In some of the Hungarian traditions, Orion belt is known as 'Judge's stick'. The Hungarians preserve the name of Orion as Nimrod, a mighty hunter before the Lord (Gen 10) who is at best an ambivalent figure.

Nimrod (sometimes Nimrud, Meroth or Menmarot) the great king of ancient Mesopotamia. The ruler of the world, the mighty hunter before the Lord. One

---

[13]Gen 10:9 ('He was a mighty hunter before the Lord: wherefore it is said, Even as Nimrod the mighty hunter before the Lord.')
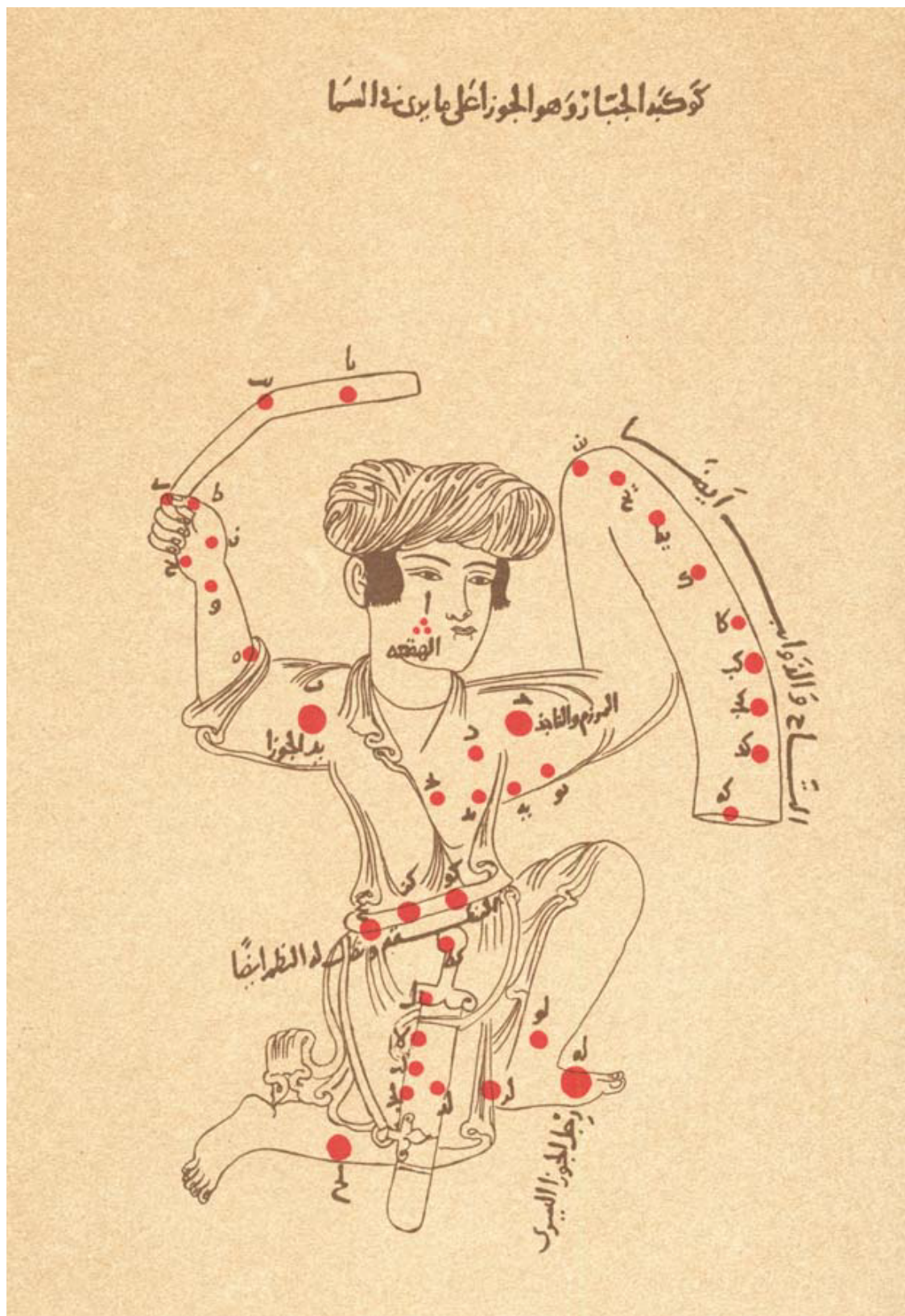
Figure 1.16: Orion in the Bodleian manuscript, which is the oldest copy of al-Sufi's 'Book of Fixed Stars'.

Table 1.1: Star names of arabic origin in Orion

Star name	Bayer designation	Arabic origin	Meaning
Algebar	β Ori	Al-Jabbar	The giant
Alnilam	ϵ Ori	An-Nidham	The string of pearls
Alnitak	ζ Ori	An-Nitaq	The belt
Betelgeuse	α Ori	Yad al-Jauza'	Hand of Orion
Heka	λ Ori	Al-Haq'ah	The white spot
Meissa	λ Ori	Al-Maisan	The shining one
Mintaka	δ Ori	Al-Mintaqah	The belt
Rigel	β Ori	Ar-Rijl	The foot
Saiph	κ Ori	As-Saif	The sword
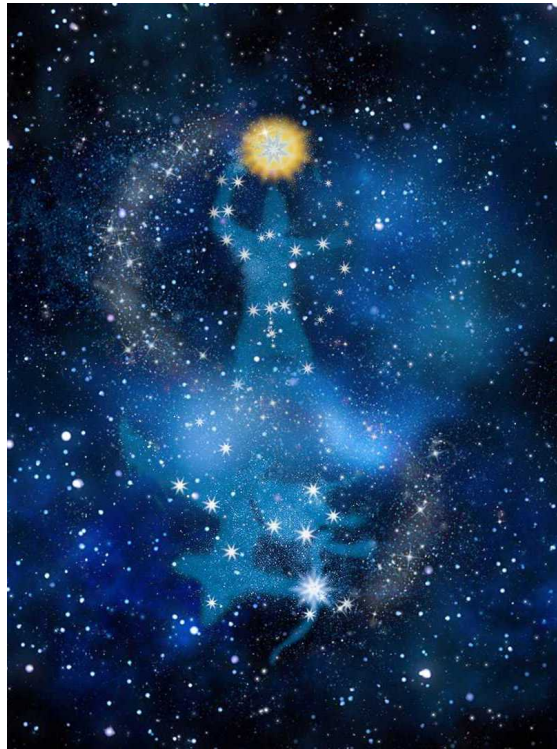
Figure 1.17: The artistic visualisation of the myth about Nimrod.

day, his sons, Hunor and Magor went hunting. They saw a great white stag. The stag escapes from them and led them to a beautiful land, Scythia. Hunor and Magor settled there with their people.

Although Orion is a hunter from the Greeks mythology, in ancient Scandinavia its stars had a more local identity. There are several views of what this constellation was to Norse and Teutonic ancestors. The Danes, Norwegians, and Swedes stitched the Belt of Orion to the celestial textile industry. In pre-Christian Scandinavia, the
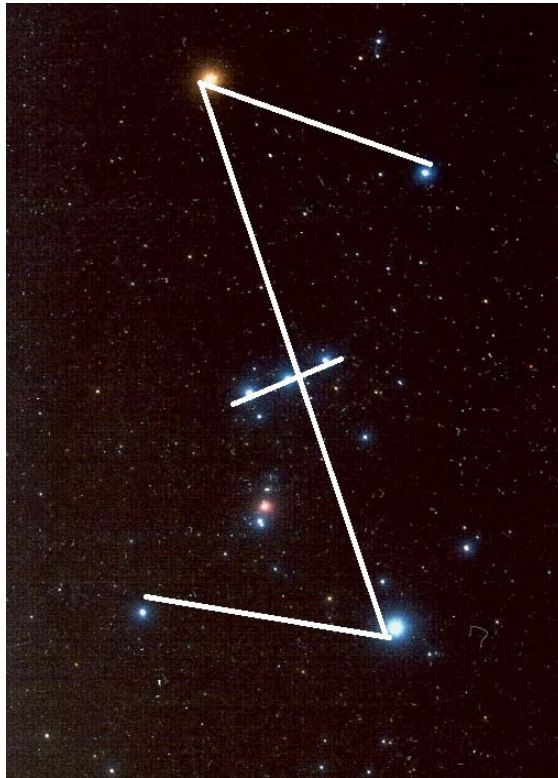
Figure 1.18: By joining the seven brightest stars of Orion we see how the constellation becomes the Skuld's Net.

Orion belt portion of the constellation was known as Frigg's Distaff (Friggerock) or Freyja's distaff also Rejerock or Frójas Rock. The three stars of Orion Sword were the spindle. Assuming the Orion constellation was also viewed as a figure in the sky, in this case, the goddess Frigg, the belt of Orion is still a belt, but the sword has a vertical orientation as does the spindle as it would have been known in a society where women were the spinners. In areas where it was known as such, the entire constellation may have been seen to be a representation of Freya (Frigg), the wife of Odin.

In this scope, it might also be seen as the symbol known as Skuld's Net (see Figure 1.18), which overlay with the constellation nicely. The web of fate guided one to other stars, and therefore either to disaster or home, depending on one's ability to navigate, it is quite appropriate. Orion was also known as Freyja's Dress, and the belt and sword as Freyja's Girdle.

According to, a medieval collection of Norse myths, the Prose Edda, Frigg 'will
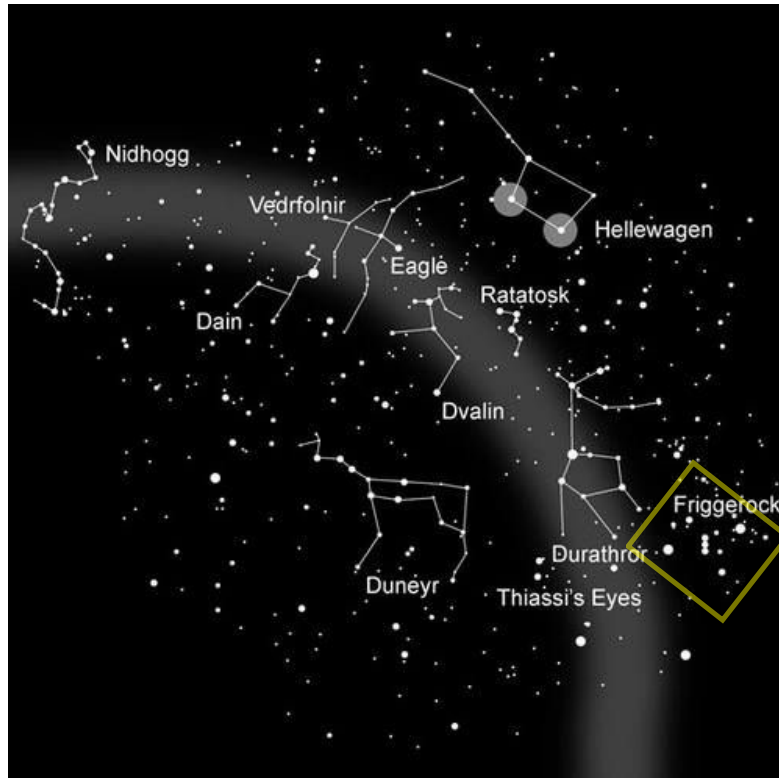
Figure 1.19: The presentation of constellations that appear to have the old norse names. Credits: Jonas Persson

tell no fortunes, yet well she knows the fates of men.' Moreover, even though she knew the fate of things to come, she did not influence the events. In Eddic tradition the Norns, the three goddesses of destiny: Urd (Past), Verdandi (Present), and Skuld (Future) had the power to control the fate

In order to ask the same questions of the northern sky, one must ask to what degree the medieval Norsemen saw roughly the same shapes in the constellations as those handed down by classical antiquity. First, as heirs to an Indo-European cultural system, they divided the zodiac into 12 sectors (as suggested by the Vafpbruðnismál), they associated Venus with a goddess of love (i.e., as the Friggjarstjarna) and they interpreted the constellation Orion as a male human figure, rather than, for example, as a turtle, as did the Maya. Secondly, as this audience knows best, the Norsemen had access to European culture through travel, trade, and tribal ties.

In Finnish mythology, the constellation of Orion is called the scythe of Váinámóisen viikate (Váinámóinen's scythe). The term most likely comes from the fact it can

be seen in the sky in early autumn in the Northern Hemisphere, the time of haymaking. Another name for the asterism of Alnilam, Alnitak and Mintaka are Váinámóisen vyó (Váinámóinen's Belt) and the stars 'hanging' from the belt as Kalevanmiekka (Kaleva's sword).

The Hittites (a Bronze Age people of Anatolia) associated the constellation with Aqhat, a famous mythical hunter. The war goddess Anat fell in love with him, but after he refused to lend her his bow, she tried to steal it. However, the man she sent to get the bow messed up the assignment pretty badly, killing Aqhat and dropping the bow into the sea. This is why, according to the myth, the constellation drops below the horizon for two months in the spring.

The Bible   The Armenians identified Orion with their legendary patriarch and founder Hayk. The name Hayk survived to nowadays in Armenian translation of the Old Testament. The Bible mentions Orion at least three times[14]:

Job 9:9 ('He is the maker of the Bear and Orion'),

Job 38:31 ('Can you loosen Orion's belt?'),

Amos 5:8 ('He who made the Pleiades and Orion').

In ancient Aram, the constellation was known as Nephila, Orion's descendants were known as Nephilim - a race of giants. The Nephilim could then be identified with the Orionids meteor shower.

China   The reason why not much attention has been paid to Chinese otherwise splendid astronomy is that the contacts between Chinese and Oriental and Hellenic civilizations were sporadic and limited, due to the hermetic nature of the Middle Kingdom. The consequence of this was the lack of mutual influence, which is why the astronomical achievements of the peoples of the Middle East and the Mediterranean world have reached the general treasury of knowledge. It was in the nineteenth century that Europe discovered the achievements of astronomy in China. It turned out, for example, that the first catalog of 800 stars, entitled Sing-Czing, was already arranged around 355 BC, by astronomers Szih-Szenia and Han-Hung.

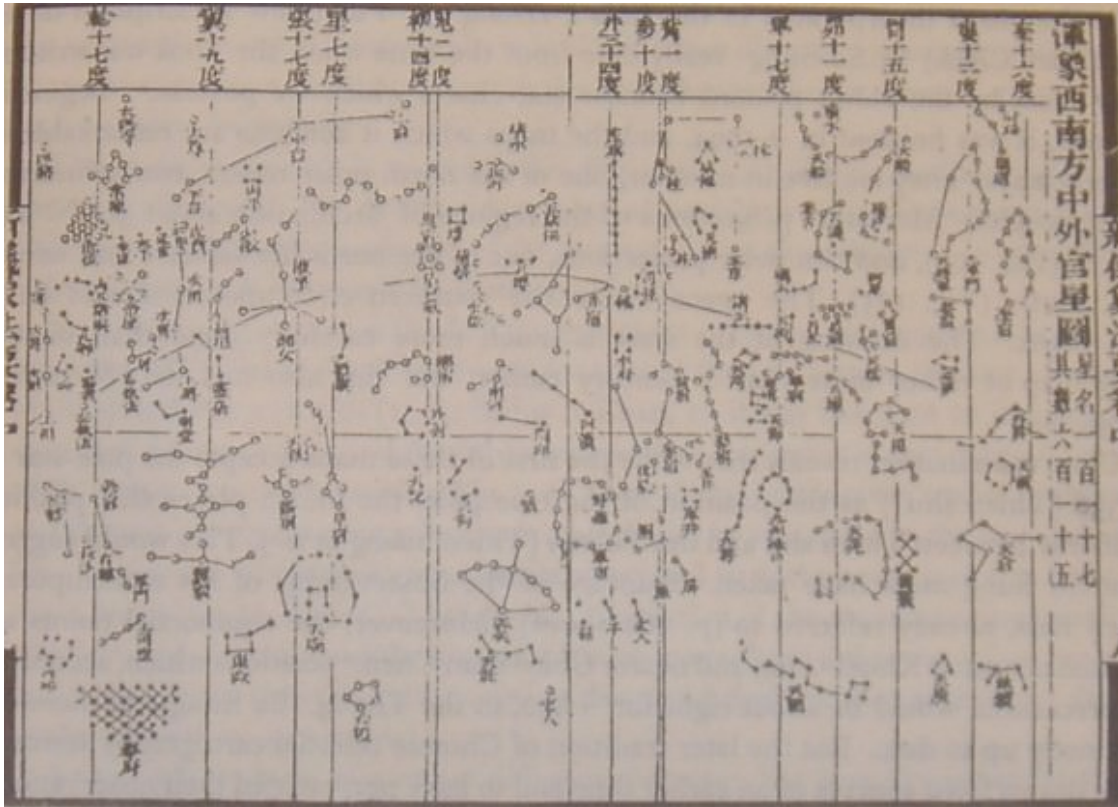[14]four if we count the Gen 10, mentioned before

Figure 1.20: Star map showing the celestial globe of Su Song (1020-1101, China). Credits: Needham (1959).

Orion is one of the rare cases in which a constellation was visualized almost precisely the same way in China as in Europe.

Chinese astronomers knew Orion as a great hunter or warrior. Shen literally means 'three', associated with the stars of Orion's Belt. Shen was in the center of a great celestial hunting scene, as it was the part of the sky during the hunting season, November and December. The ten major stars were also imagined as his various army generals. The stars that we see today as Orion's shield was interpreted in China as a banner, Shenqi, or sometimes a longbow. The triangle of stars that forms Orion's head (λ, ϕ^1, and ϕ^2) was known as Zi, 'turtle beak', or it might also be the beak of a falcon used for hunting.

India There is another story, this one from the old Hindu texts.Where Orion's belt is actually an arrow aimed at the supreme god, Prajapati. He was attracted to his daughter, Rohit. In order to consummate this abusive affair, he changed himself
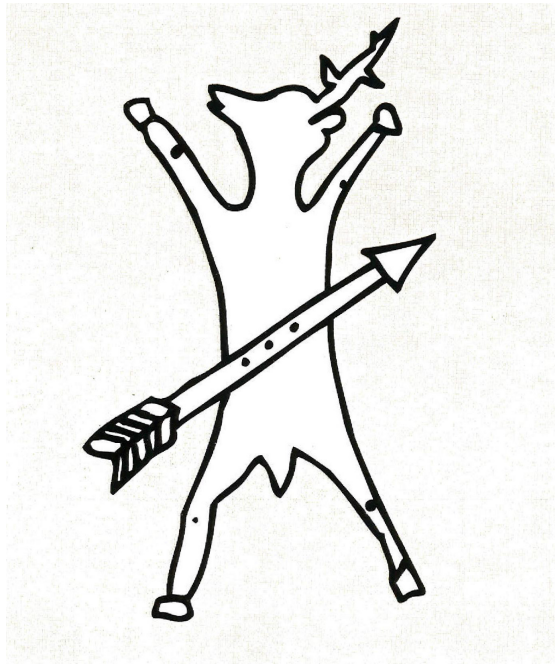
Figure 1.21: Prajapati represents Orion, and the three stars that form belt of Orion, are the arrow that pierced him[15]. Figure taken from http://www.sapienzamisterica.it/parte-xv—sirio.html.

into a deer, a buck, and his daughter changed herself into a celestial doe. This was observed by the other gods who were offended by this ungodly behavior and had an arrow shot at Prajapati, killing him. According to the Hindus, the celestial doe is the star Aldebaran, and the hunter is actually Sirius (Figure 1.21).

In the Rig Veda, Orion Constellation is named 'Mriga (The Deer).' According to them, the two bright stars in the front (Saiph, Rigel), and the two bright stars in the back (Betelgeuse, Bellatrix) are the four dogs hunting The Deer, the three, aligned stars in the middle (Alnitak, Alnilam, and Mintaka) are the deer. The three little aligned but less bright stars are The Baby Deer (NGC 1981, the Orion nebula, and Iota Orionis) are the baby deer.

Australia   Orion is also important in Australian Aboriginal astronomy. The Yolngu people of Arnhem Land (Northern Australia) see that the constellation of Orion, which they call Julpan, as a canoe (see Figure 1.22)

They tell the story of two brothers who went fishing, and caught and ate a fish which they had been commanded not to do. Seeing this, the Sun sent a
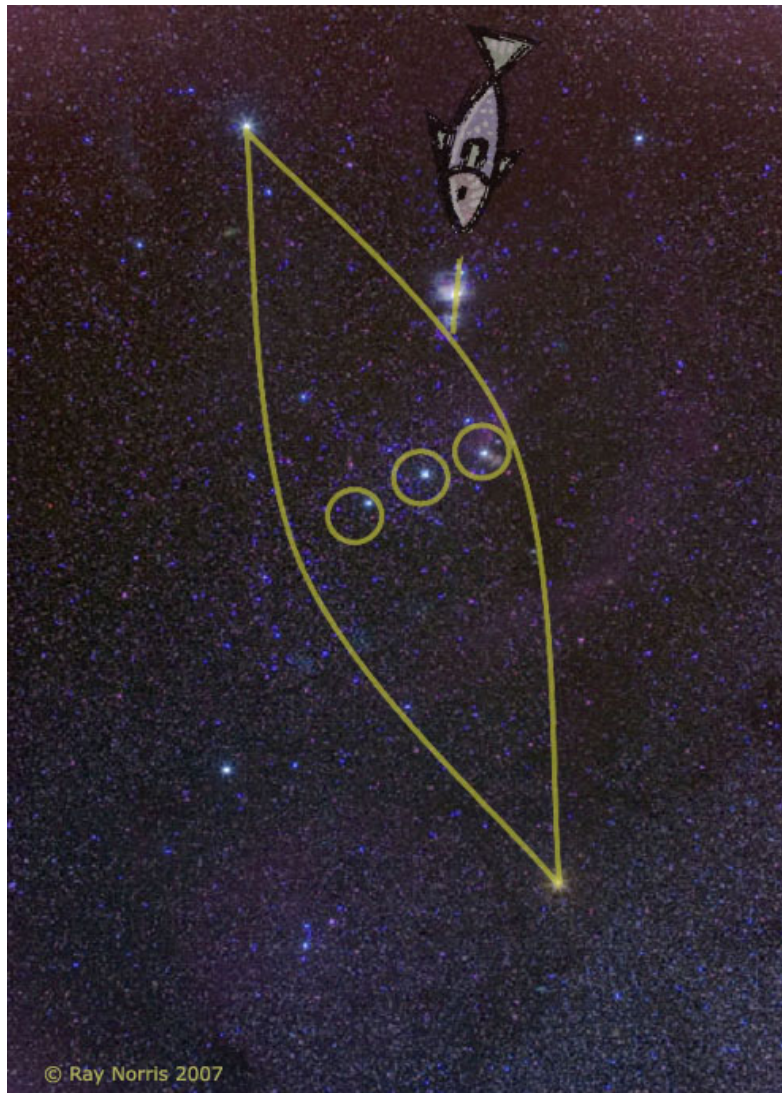
Figure 1.22: A Yolngu visualisation of Orion. Credits: Ray Norris

waterspout that carried the two brothers along with their canoe up into the sky. When Yolngu people die, they are taken by a mystical canoe, Larrpan, to the spirit-land (Baralku) in the sky. We can see our ancestors campfires along the edge of the great river of the Milky Way.

The myth concerning Orion and the Pleiades belongs to a tribe living near Wandunya (Central Australia). Mythical Ming-arri were all women who never wished to mate with men. They lived by themselves and kept a pack of dingo dogs to keep all men away. Nyiruna was a great hunter. He wanted Ming-arri very badly for his wives. He left food as a bite to attract them and tried to catch them, but

the dingoes ate the food and chased Nyiruna away. When Ming-arri (the sisters of Pleiades, Yugarilya, a 'lot of women') went into the sky, Nyiruna (Orion) followed them. And there he is, still chasing them round and round, while the dingoes keep him away. The story has been first documented by Daisy Bates in her work from 1921 called 'The Orion Story' and then revisited by Leaman & Hamacher (2014).

Nyeeruna is forever prevented from reaching Yugarilya by Kambugudha, their eldest sister, represented by the Hyades, who guards her younger sisters. Kambugudha places a line of dingo puppies between her and Nyeeruna, represented by an arc of stars between Orion and the Hyades.

Of the various Aboriginal traditions across Australia regarding the stars in Orion and the Pleiades, nearly 90% associate the stars of Orion with a man or group of men and the stars of the Pleiades with a woman or group of women. Although there are similarities between the Greek myth of Orion and Bates' (Leaman & Hamacher 2014) record of the Orion Story presented above, there is no evidence of postcolonial Western cultural influence.

In Australia, the stars forming Orion's Belt and sword are sometimes, rather less commonly called the Pot or the Saucepan (Figure 1.24). The Sword forms the Saucepan's handle, while the stars of the Belt form its base (the Saucepan is upside-down, with its base pointing northwards). The shape is completed by η Orionis, a star not belonging to either the Belt or the Sword, which completes an approximate square that represents the Saucepan's bowl.
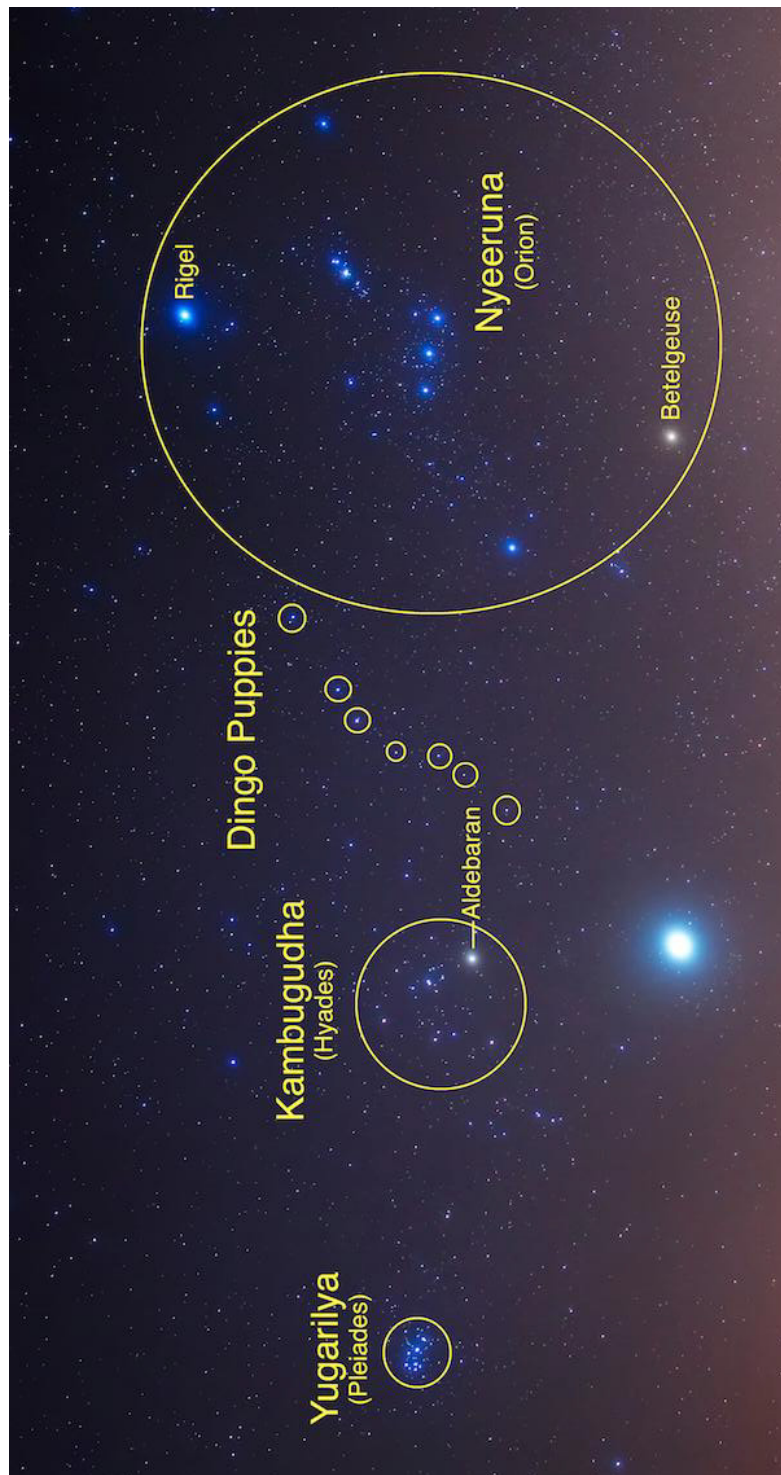
Figure 1.23: An illustration of 'The Orion Story', including: the Pleiades - Yugarilya, the seven Mingari Sisters, the Hyades - Kambugudha's legs, the 'horns of the bull' - Babba the father dingo, Orion's 'shield' - the Dingo puppies, Orion - Nyeeruna. The bright object below the Hyades is the planet Jupiter (image credit: free stock image from www.favewalls.com). After Leaman & Hamacher (2014).

Figure 1.24: The shape of Saucepan is sometimes ascribed to Orion.

Orion with his golden bow is on watch during the night.

— Aesop Fables

2
Introduction

2.1 Overview of low-mass star formation

Stars less massive than $3M_\odot$ fit into the definition of low-mass stars. Low-mass stars are born in thick, dusty cocoons. The envelopes keep them hidden from sight and are the reservoirs from which the protostars will feed (Wilking 1989).

A general outline of the formation of an isolated low-mass star starts with a hydrostatic core surrounded by a dense envelope which begins to collapse. This prestellar core collapses from the inside out to form a dense core (Shu 1977). The envelope is a reservoir from which the protostar will feed. The central object contains a very small fraction of the total stellar mass with which the star will enter the Main Sequence (MS). As long as the mass of the envelope is more than half of the total mass of the system, the central object will be a Class[1] 0 source or a protostar. Observationally, a Class 0 source is defined to have $L_{bol}/L_{1.3mm} < 2 \times 10^4$ (Andre et al. 1993) and with the SED peaking at millimeter wavelengths. This Class 0 protostellar phase is characterized by mass-loss via energetic bipolar jets

---

[1]The spectral index α has been defined in Lada & Wilking (1984) and Lada (1987) as:

$$\alpha = \frac{d\log(\lambda F)}{d\log(\lambda)}.$$

Lada & Wilking (1984) used the spectral index calculated between near- and mid-infrared bands to classify YSOs into three distinct classes (Class I–III).

and molecular outflows, likely powered by protostellar disk accretion. The star is still obscured by a thick envelope, which reprocesses most of the star's energy. Once the central object has accreted most of the mass of the envelope, the system will consist of a young star with most of its final mass and a disk of large angular momentum material which continues to accrete. The envelope mass is decreasing substantially, when $M_{env} \ll M_\star$, the mass of the protostar is greater than the envelope mass, it would correspond observationally to a class I source (Lada 1987; Adams et al. 1987). Depending on the orientation of the system, the protostar may be visible in optical and NIR wavelengths (e.g., near face-on or along the outflow direction), and the envelope cavity carved out by the outflow may be seen in scattered light (Padgett et al. 1999). Class I sources are characterized by a spectral energy distribution (SED) which rises into the far infrared (see Figure 2.1). The end of this phase marks the end of the protostellar phases and the beginning of the pre-main-sequence (PMS) phases. Acquired almost all of its final mass, the source is reaching its peak luminosity (Myers et al. 1998); further evolution (contraction) along the Hayashi track towards the MS in the Hertzsprung-Russell (H-R) diagram (Hertzsprung 1905; Russell 1914) is characterized by decreasing luminosity. The location of the transitional point in the H-R diagram for low mass sources is known as the birthline, first defined by Stahler (1983).

As accretion continues, the envelope is dissipated and becomes transparent, and the star becomes an optically visible Class II source. PMS low-mass stars are called T Tauri stars (Ambartsumian 1947a).

Class II sources have large infrared excess. These sources begin to become optically revealed, as the protostellar outflow cleared away the remnant parental molecular cloud. The combined emission of the accretion disk and the remnants of the star's envelope dominates in the IR wavelengths. Eventually, the final remains of the envelope and the accretion disk are accreted or driven off, and the detected light is all from the star's photosphere.

The T Tauri stars are divided further into Classical T Tauri Stars (CTTS) and Weak-lined T Tauri Stars (WTTS), which belong to the Class II and Class III

evolutionary phases, respectively. Henceforth I will use the terms Class II source and CTTS (or Class III source and WTTS) interchangeably.

Classical T Tauri Stars   T Tauri stars are young, pre-main sequence (PMS) stars. Joy (1945) defined T Tauri stars as a class of variable star with: rapid, irregular, large amplitude variations; spectral types ranging from mid F to mid G; low luminosity; and an association with interstellar matter. Nowadays CTTS are defined by having broad H_α emission lines, typically with equivalent widths $\geq$10Å. The spectra of CTTS also show strong emission lines from Ca II (3933Å and 3968Å).

Weak-Lined or Naked T Tauri Stars   Class III are post-accretion but still PMS sources. Walter (1986) surmised that these PMS stars were physically the same as the classical T Tauri stars, but did not have actively accreting disks.

This final evolutionary phase is observationally characterized by an SED dominated by a naked stellar photosphere: the protoplanetary disk has been almost completely dispersed ($W_{disk} \sim M_{Jupiter}$). This would make them Naked T Tauri stars (NTTs). What remains is a PMS star still contracting onto the MS, possibly harboring a forming or already assembled planetary system. Herbig & Bell (1988) expanded this category to include T Tauri stars that have some spectroscopic indicators of low-level accretion and called them all weak-line T Tauri stars (WTTs). WTTS have narrow and weak H_α emission lines, showing no indication of active accretion occurring.

Bary et al. (2002) reported the detection of 2.12μm emission from the H_2 gas orbiting a weak-lined T Tauri star, DoAr 21. This star shows no evidence of excess near-infrared thermal emission, a small mid-infrared excess, and the non-detection of 1.3 mm continuum emission from dust. They suggest that the dust has been incorporated into larger bodies (such as proto-comets). They postulate that the theory that disks are largely absent around WTTS stars should be reconsidered and that the widespread presence of such disks would indicate that planetesimals can form quickly and giant planet formation can proceed to completion before the gas in circumstellar disks disperses.
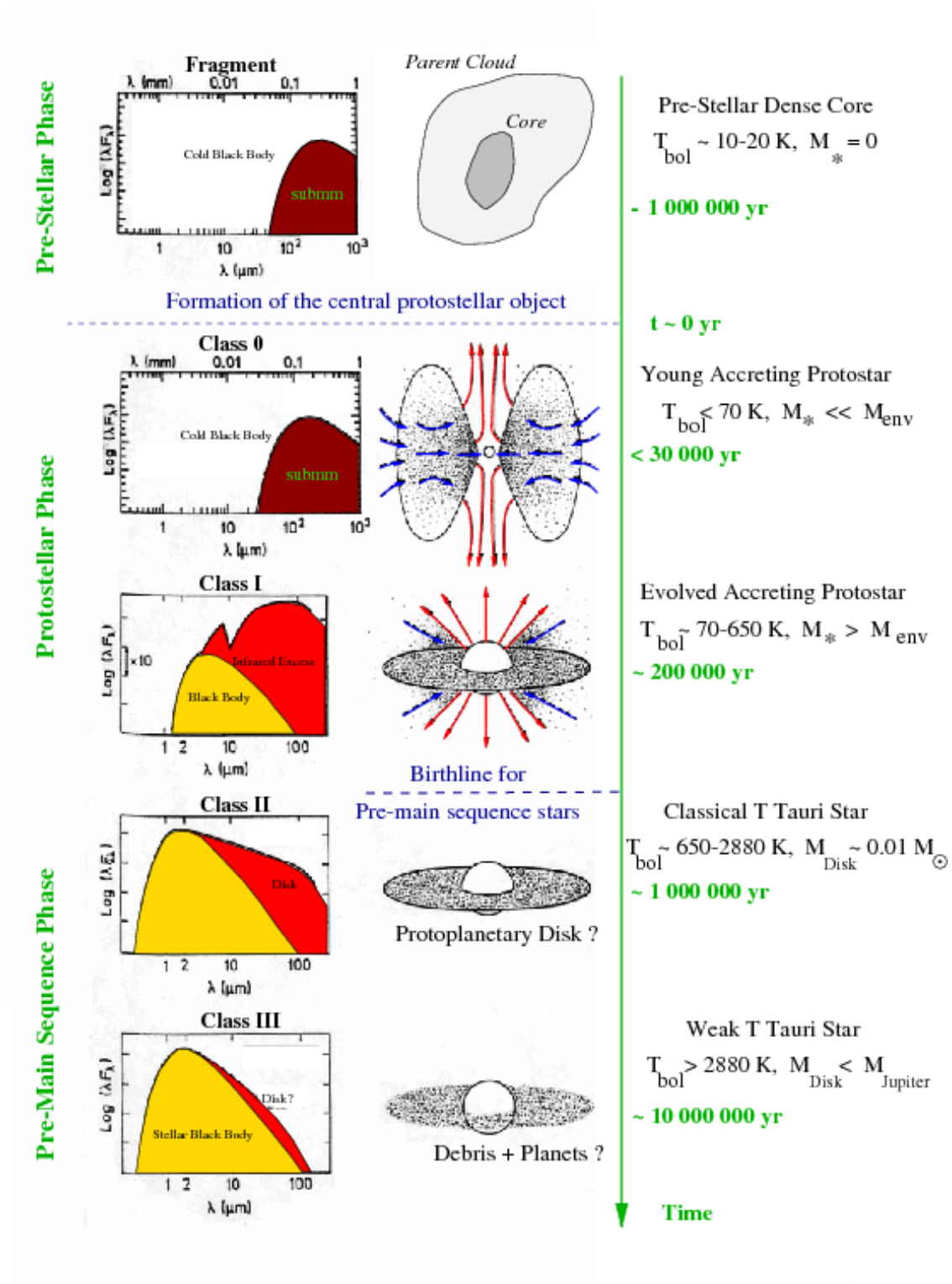
Figure 2.1: Schematic illustration of observational evolutionary phases of YSOs, from the pre-stellar cores to classical T-Tau stars (CTTS). Credits: André (2002).

Victor Ambartsumian noted that T Tauri stars are often found in loose groups, T associations, often in the vicinity of OB associations. He suggested that T Tauri stars were recently formed low-mass stars and that T associations were the low-mass counterparts to the OB associations (Ambartsumian 1947b).

2.2 The Initial Mass Function

Mass is the most important parameter which determines the structure and the whole evolutionary path of every star. At the same time, stellar mass is one of the hardest to determine. The question how to determine the mass of a star is one central to the development of a theory of star formation. Stellar mass distributions decide about the evolution, surface brightness, chemical enrichment, and baryonic content of galaxies. There is currently no universal theory of star formation that explains in a consistent way the mechanism of formation of a star nor the observed mass distribution.

The stellar initial mass function (IMF) as the distribution of stellar masses in a given volume of space is one of the most fundamental distributions in astrophysics. The determination of this relation is a cornerstone in astrophysics. Its origin is one of the most critical but least understood aspects of the star-forming process and is perhaps the most fundamental unsolved problem of star formation (e.g., Corbelli et al. 2005; Bonnell et al. 2007; Krumholz 2014). Introduced by Edwin Salpeter in 1955 (Salpeter 1955) it informs us about the distribution of mass of stars at birth. Salpeter described the IMF as a power-law of an index -1.35 in logarithmic units of density and mass. It was recognized later, with more sensitive observations, that the IMF is probably not a single power law over all stellar masses. Three-segment power-low IMF has been proposed by Scalo (1986), and Kroupa (2001) obtained the following function:

$$\Gamma = \frac{d\log N}{d\log M} = \begin{cases} -1.35 & 0.5 \leq M/M_\odot, \\ -0.3 & 0.08 \leq M/M_\odot \leq 0.5, \\ +0.7 & 0.01 \leq M/M_\odot \leq 0.08, \end{cases}$$

where N is the number of stars and M is the mass. Γ, the slope of the IMF, is

often represented by $\alpha = 1 - \Gamma$, depending on how the function is defined.

Elegant in its simplicity, the IMF becomes nowadays crucial in its significance. Many modern observations can be solved by *invoking either the IMF to be invariant or variable.* Any variations in the IMF could provide deep insights into the star formation process because the theory of star formation must explain both its shape, as well as how it might vary with initial conditions. If we can confidently observe variations in the IMF, we can hope to study those variations to understand the scales or conditions under which stars of a certain mass form. Nevertheless combining IMF estimates for different populations in which the stars can be observed individually, unveils an extraordinary uniformity of the IMF. This general insight appears to hold for populations including present-day star formation in small molecular clouds, to rich and dense massive star clusters forming in giant clouds, to ancient and metal-poor exotic stellar populations that may be dominated by dark matter. This apparent universality of the IMF is a challenge for star formation theory because elementary considerations suggest that the IMF ought to systematically vary with star-forming conditions. But as is too rarely stressed, there is no direct observational determination of the IMF. Stellar masses cannot be weighted directly in most instances, so the mass has to be deduced indirectly from observations.

The only way to determine the masses of stars directly from observations is through Kepler's third law, which describes the motions of orbiting bodies. This method requires resolving all orbital parameters of the system, which make it extremely inefficient and hard to use. Nevertheless, this determination serves as the definition for the fundamental stellar mass scale. The standard way of mass determination is to use the mass-luminosity relation. The empirical relation between the mass of a star and its luminosity was first shown around 1920 by A.S. Eddington (1924). This relation concerns only stars of the same type (the same interior structure), so mainly to the zero-age main sequence stars. From the position of a star on the main sequence, its mass can be determined in a relatively easy manner, but the same is not true for stars that have left the main sequence because we

cannot reconstruct their evolutionary history. Which is extremely important when we want to examine the complex evolution history of short-lived massive stars.

For example Massey et al. (1989) and Massey et al. (1995) have shown convincingly that the *luminosity function* (LF) is inadequate for estimating the IMF of massive stars. First, because the bolometric correction is a strong function of effective temperature for massive stars, and because of their significant evolution to cooler temperatures, stars in a given absolute visual magnitude range will represent a mixture of masses; there is no one-to-one correspondence between M_V and mass. Second, because optical and even near-UV cannot sample the high-frequency region of high temperature stars, and so colors are insensitive to effective temperature. This means that even a comparison of an observed color-magnitude diagram with theoretical evolutionary tracks is incapable of yielding a reliable IMF. They showed that an 85 $M_\odot$ star cannot be distinguished from a 40 $M_\odot$ star on the basis of M_V alone. Obtaining masses based on M_V for a mixed-age population does not work if optical, or even UV bands are used. Instead, spectral classification and broadband photometry for estimation of the reddening of the star light through interstellar dust has to be performed on a star-by-star basis to measure the effective temperature, T_{eff}, and the bolometric magnitude, M_{bol}, from which mass is obtained. To minimize some difficulties, it is preferable to study associations/clusters of massive stars.

The young stellar clusters have been long recognized as important natural laboratories for astrophysical research. Because stars in such groups share the common heritage of being formed more or less simultaneously from the same progenitor molecular cloud, observations of the cluster's color-magnitude diagrams (CMDs) can be, and indeed, have been used to provide classical tests of the stellar evolution theory. Moreover, clusters offer the smallest physical scale over which a meaningful determination of the stellar initial mass function (IMF) can be made.

The Orion star-forming region is the nearest to Earth and the best studied region of star formation in the sky. Its young stars and gas provide important clues about the physics of star formation, as well as the formation, evolution and destruction of star-forming clouds, the dynamics and energetic of the interstellar medium (ISM)

and the role that OB associations and high mass stars play in the cycling of gas between the various phases of the ISM. Although the Orion Star Forming Region has been studied very widely for many years, there are still many questions to answer.

2.3 OB Associations

After spectral types were available, the concentration of O and B stars on the sky into loose groups has been noticed. The term *association* was first used by Ambartsumian in the 1940s to groups of O and B stars (Ambartsumian 1947b). He calculated that the space density of these groups was less than $0.1\mathrm{M_\odot pc^{-3}}$. Groups of stars with space densities that low would be destroyed by galactic tidal forces (Bok 1934). 'It is not entirely trivial to accurately define what is meant by the term OB association', said Brown et al. (1999) and adopted a working definition that *OB associations are young (<50 Myr) groups of stars with densities that are so low that they are likely to be unbound.* Bound groups of stars are classified as clusters.

For a long time, it was thought that star formation was bimodal: low-mass stars formed in T associations; high-mass stars formed in OB associations. Observational biases created the impression that there were few, if any, low-mass stars in OB associations. Finally, the X-ray observations indicated that there were many low-mass stars in OB associations (Walter 1994).

Observations of T associations and the theory of the formation of an isolated star (see Section 2.1) are the foundation for our understanding of low-mass star formation. Nevertheless, they do not present a complete picture of low-mass star formation because most low-mass stars form in OB associations (Walter et al. 2000). Understanding how low-mass stars form in such an energetic and violent environment allows us to place low-mass star formation in context.

The size of OB associations is a few to ∼100 pc (Brown et al. 1999), which is in the magnitude range of the size of giant molecular clouds. In the solar vicinity, OB associations are located near star-forming regions (Bally 2008). The canonical methods to identify the members of OB associations rely on the assumption that stars belonging to the same OB association share the same kinematics. OB associations

consist of several subgroups or sub-associations. These sub-associations may differ from each other in their properties ages, spatial extent, and the amount of interstellar matter (Blaauw 1964). The boundaries of individual sub-associations are vaguely defined, if at all (Brown et al. 1999; Kounkel et al. 2018). Each sub-association is a snapshot of stellar evolution over a wide range of masses.

The observations that OB associations consist of spatially separated and distinct subgroups which lie in a sequence of monotonically changing age led Blaauw to infer that the star formation did, in fact, occur in sequential bursts (Blaauw 1964). The formation of next-generation stars in a molecular cloud has been triggered by the feedback from the previous generation of stars. Elmegreen & Lada (1977) proposed the first quantitative model of this mechanism (see Figure 2.2). They showed that the powerful high energetic ultraviolet photons from the massive stars create an ionization front that moves forward in the molecular cloud and is preceded by a shock front. The neutral gas between these two fronts gets compressed and become gravitationally unstable what leads to its collapse and formation of a new generation of massive stars. They estimated the time scale of collapse of a few millions years. If, in fact, the stars which eventually form in the shocked layer are OB stars, then a new system of ionization-shock fronts will propagate into the remaining cloud after this second generation reaches the main sequence, and another cycle of OB star formation will be initiated. This avalanche of births of groups of massive stars produces a chain of OB associations with an age gradient. Recurrence of triggered star formation results in sequential star formation.

Elmegreen & Lada (1977) estimated the propagation velocity of few km s^{-1}. For a region larger than 100 pc, this would imply an age difference of the order of ∼20 million years between the extremities.

Recently, Bouy & Alves (2015) investigated the Hipparcos distances towards the massive blue stars closer than 500 pc from the Sun. The blue streams architecture of this analysis reveals two types of star formation events. The primary and dominant one that created the elongated large galactic structures with the indication of the existence of an age gradient. Causing the secondary event of star formation in
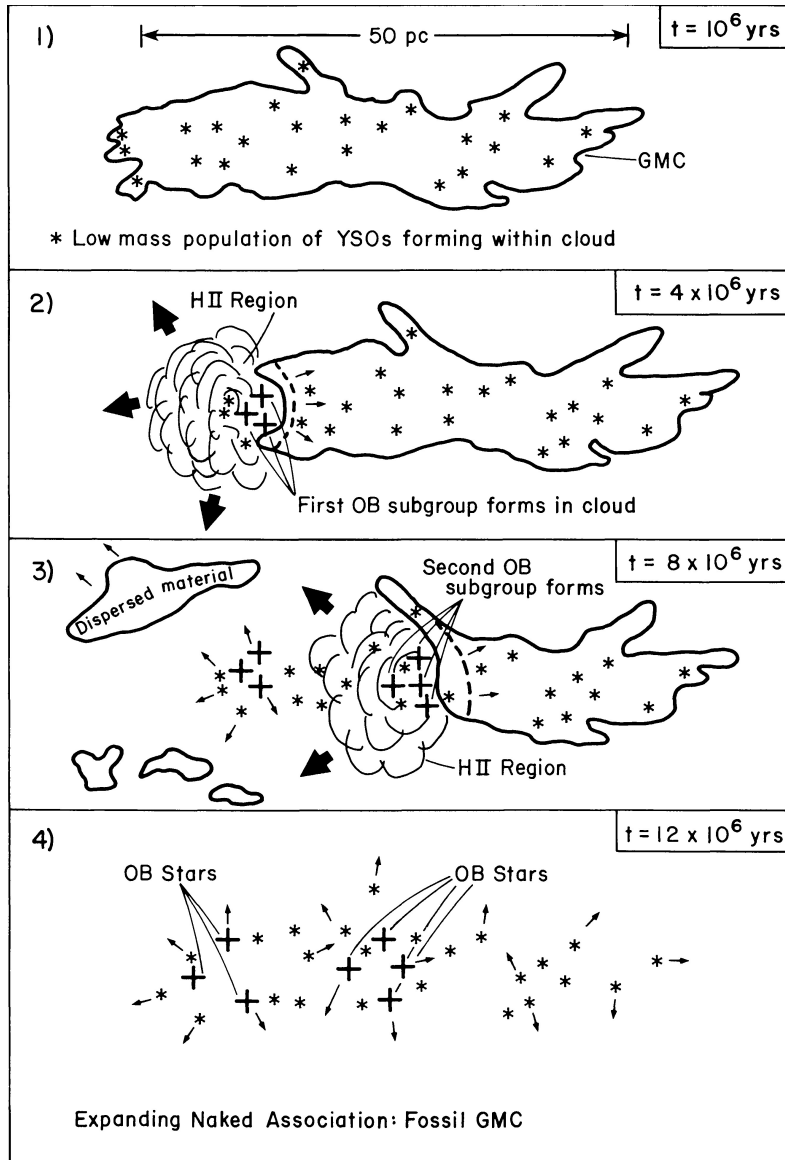
Figure 2.2: Theoretical model for triggering mechanisms in OB association has been presented by Elmegreen & Lada (1977) and Lada (1987). The spatial distribution and age sequence are good evidence for propagation of star formation. Radiation from massive stars drives an ionization front into the surrounding molecular gas leading to the birth of the new generation of massive stars and the dissipation of the cloud. It is widely believed that newly born stars compress nearby clouds and trigger formation of next-generation stars. Credits: Lada (1987).

low-mass clouds as a result of the feedback from the stream's massive stars. Given this new view on the organisation of the local neighborhood, in particular, the realization that the Orion OB association may be part of the Orion stream, there is a clear need to bring more information on the region, on scales larger than previously done, and for the regions further away from the molecular clouds.

2.4 The Orion OB1 Association

The Orion star-forming complex is the nearest active star-forming region (SFR) to Earth producing massive stars and by far the richest of all star-forming regions in the nearest 1kpc. It has long been recognized as a benchmark laboratory for star and planet formation studies as well as the formation and dispersal of OB associations. The entire Orion star formation complex spreads across 200 pc and has spawned about 10000 stars in the last 12 Myr (e.g., Bally 2008; Muench et al. 2008; Briceno 2008).

The Orion Star Forming Region is often used as the best example of sequential star formation. As first discussed by Blaauw (1964), it appears that at least four sub-populations of young stars within the complex, are forming an age sequence. Starting from the older and dust free Orion OB 1a group to the North (age 10 Myr), then OB 1b containing the group of stars located around the Belt, then OB 1c in which the stars around the Sword are included, finally to the youngest Orion OB 1d containing the Orion Nebula (including the Trapezium Cluster, age 1 Myr), to the South (see Figure 2.3). Although initially each sub-population was assumed to be a distinct object belonging to a single star formation event, it was early realized that the groups Orion OB 1c and 1d overlapped, at least in part along the line of sight (e.g., Warren & Hesser 1978; Gomez & Lada 1998).

It has long been suspected that the Orion complex has a more sophisticated three-dimensional structure, requiring star formation to have started independently and in a more stochastic manner than Blaauw's original idea. The existence of a rich and close foreground seen in projection against the embedded population, as found in Alves & Bouy (2012), Bouy et al. (2014), Kubiak et al. (2017), Kounkel
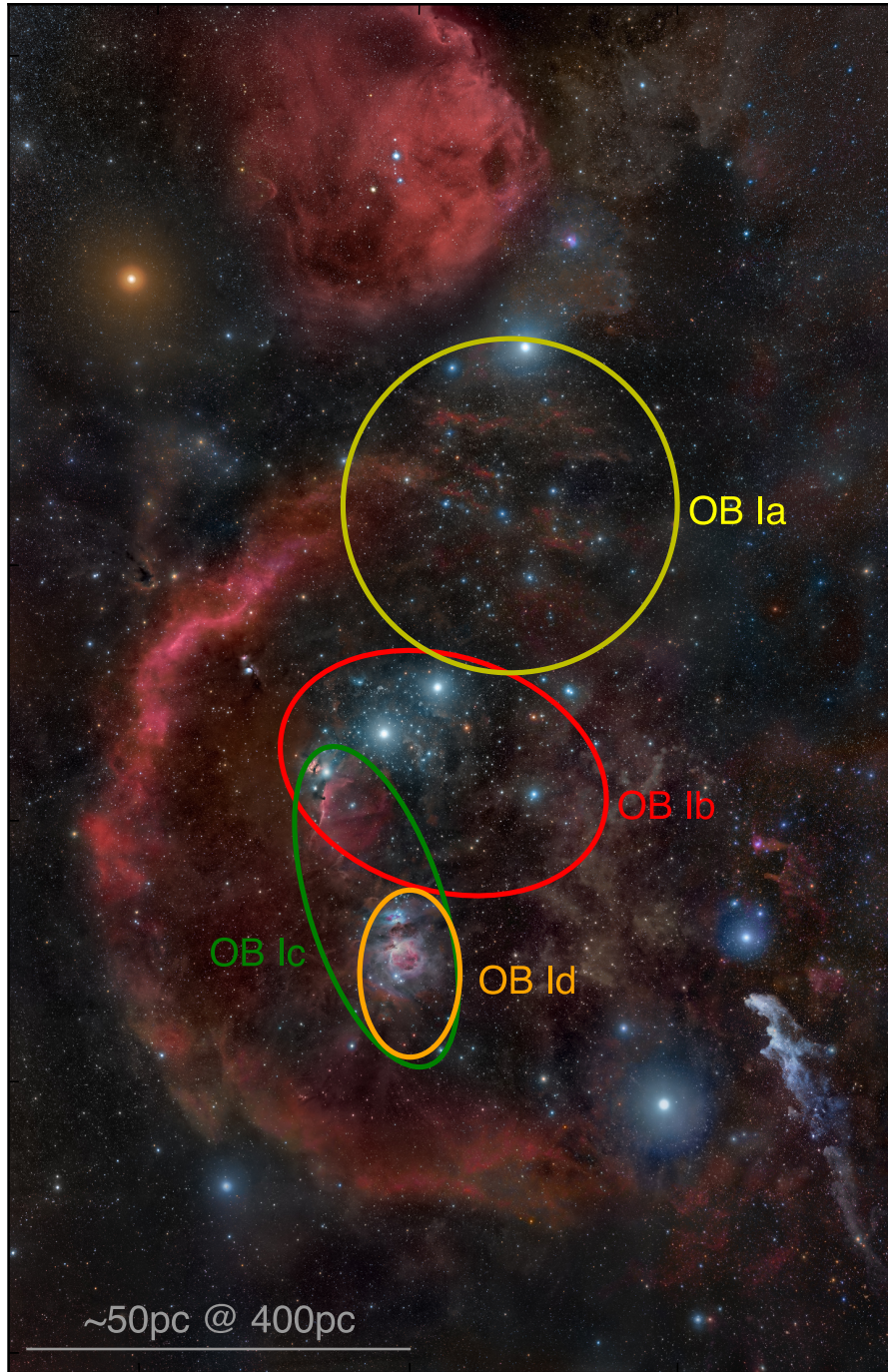
Figure 2.3: The image of the Orion OB1 association shows many of the interesting features of the region. East is left, north is up. The red arc of Barnard's loop is visible to the left (east) of the Orion Belt. The three belt stars are from left to right: ζOri, ϵOri, and δOri. The circular large H$_\alpha$ emission (red) in the upper part of the image is the λOri association. The blue reflection nebula in the lower left part of the figure is The Witch Head Nebula illuminated by Rigel. The ellipses denote the approximate boundaries of the Orion OB1 a, b, c, and d sub-associations (Brown et al. 1994). Photo credits: R. Bernal Andreo, www.deepskycolors.com.

Figure 2.4: The astonishing optical image of the Orion Belt region. The region is rich in blue massive young stars. Four of the most massive supergiants are diagonally from the top δ, ϵ, ζ Orionis and σ Orionis below the famous asterisk. North is up, East is left. Photo credits: Davide De Martin.

et al. (2018), Briceno et al. (2018) suggests that massive star-forming regions indeed have complex star formation histories. One immediate consequence of this result is that the basic observables (ages, age spreads, masses, etc.) on the nearest massive star-forming region, the Orion Nebula Cluster, are contaminated.

2.5 Historical notes on the exploration of the Orion Belt region

Still, and in spite of being recognizable to the naked eye, the Orion Belt region is paradoxically poorly studied (Figure 2.4).

The Orion association, Orion OB 1, is defined by Blaauw (1964) to lie between $199° < l < 210°$. In the center of this area lies the Orion Belt, first recognized by

Ptolemy in his 'Almagest' who described these objects with numbers 759-761, and studied with the telescope by Galilei (1610) who counted about a dozen stars therein. The overdensity of blue massive stars in the Orion Belt region was first pointed out in Galileo's 'Sidereus Nuncius' in 1609 as an example of how the telescope could resolve stars that are not visible by the human eye (Figure 2.5). It subsequently appeared in the catalog of Collinder (1931).

The ϵ Orionis association was first mentioned in 1931 by the Swedish astronomer Per Collinder[2] in his catalog of open clusters, which is today known as the Collinder catalog, published as part of his doctoral dissertation (Figure 2.6). He distinguished the Orion Belt asterism (Alnitak, Alminam, Mintaka or ζ, ϵ, δ Ori, respectively) as Collinder 70. In the Winter 2005 issue of Amateur Astronomy magazine Nancy Thomas published an article 'Per Collinder and His Catalog' where she revisit the catalog[3] and its application for the amateur astronomers.

Collinder (1931) described the region as the group of about a hundred stars stating that 'this is a very fine cl.[uster]'. The diameter of the cluster was estimated to 240×140 arcmin (Figure 2.6). The actual size of Collinder 70 has not been ascertained, which may be the reason why the name is also not common in the astronomical society. Some authors (e.g., Gieseking 1983; Dias et al. 2001) have identified the Collinder 70 cluster, sometimes called the 'ϵ Orionis cluster', as the whole Ori OB 1b association. Markarian (1951) (and, therefore, Lynga 1987 and Dias et al. 2002) tabulated an angular diameter of $\sim$140 arcmin, which would mean the cluster comprise the stellar populations surrounding σ Ori and δ Ori. Subramaniam et al. (1995) proposed that both Collinder 70 and NGC 1981 (to the north of the Orion Nebula Cluster) form a 'probable binary open star cluster in the Galaxy'.

The Orion OB 1 association was first split into four divisions due to differences in age and in content of gas and dust. This historical division is now commonly in use although many authors in later publications have not confirmed the veracity of this approach. The original sketch of the Orion OB association by Blaauw

---

[2]22 May 1890 - 6 December 1974

[3]She used a copy of Collinder's catalog reproduced by the US Naval Observatory directly from his dissertation.

Figure 2.5: The printer version of the drawings Galileo made of Orion. He saw Orion up side down through his self made telescope. Photo credits: Regina v. Berlepsch, AIP Librarian; 2nd edition of 'Sidereus Nuncius'.

Catalogue of Open Clusters.   B3

N r.	NGC	α l	δ b	Dim.	m_t	C_N	C_M	N	Class	E	I_A	X x	Y y	Z z	π Distance
70	Or. Belt	5 30	− 1 10	240×140	0.6 (3)	0.15	1.0	90	Neb. cl.	125°	0.45 (120°)	− 1000	−- 410	− 320	0.00288
		172.5	− 16.4	250×120	0.6 (4)	0.2	0.1	125	Neb. cl.	140°	0.4 (140°)	− 886	− 367	−- 282	1130

Figure 2.6: Basic parameters of the Collinder 70 open cluster as presented by Collinder (1931). There are differences between the values presented in the catalog and the follow-up publications about the catalog. Table from: 'On Structural Properties of Open Galactic Clusters and their Spatial Distribution. Catalog of Open Galactic Clusters.' Collinder, Per Annals of the Observatory of Lund, vol. 2, pp.B1-B46.

Figure 2.7: Approximate boundary of the Collinder 70 cluster. The Great Orion Nebula is at the bottom of the image. Background image fragment of: 'Orion: Head to Toe', Credit & Copyright: Rogelio Bernal Andreo.

(1964) superimpose on the wide field image of the Orion by Bernard Andreo is presented in the Figure 2.8. Blaauw (1964) divided Orion OB 1 into four subgroups marked with different symbols:

- Orion OB 1a – which contains the stars to the northwest of the Belt stars; the older and dust free – the largest sub-association, marked with the crosses in Figure 2.8;

- Orion OB 1b – containing the group of stars located around the Belt (including the Belt stars themselves); and the σ Ori cluster – marked with open circles;

- Orion OB 1c – in which the stars around the Sword are included; – the most south sub-association marked as the filled circles;

- Orion OB 1d – which contains the stars in and close to the Orion Nebula (including the Trapezium Nebula) – mantled by the OB1 c, the youngest actively forming stars part of Orion 1b association.
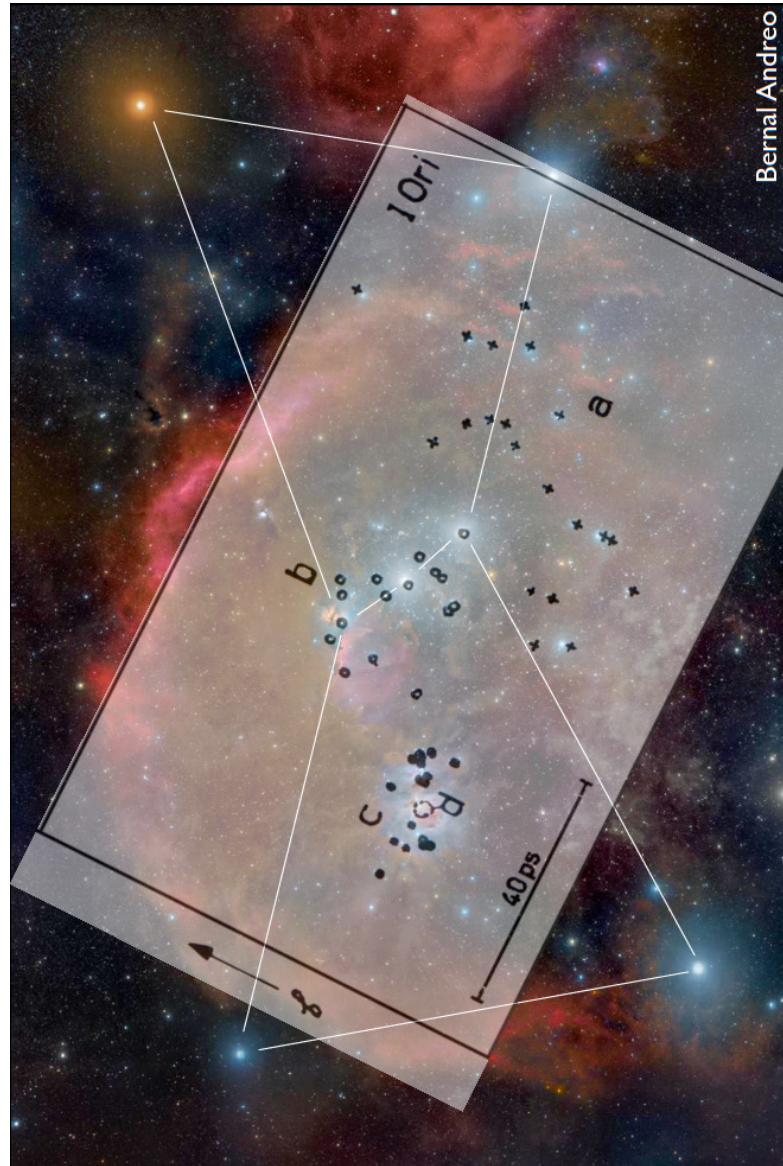

Figure 2.8: Blaauw's division of the Orion OB association. Different symbols indicate the different subgroups. The white lines mark the schematic shape of the Orion constellation. North is up, East is left.

It was early realized that the groups Orion OB 1c and 1d overlapped, at least in

part, along the line of sight (e.g., Warren & Hesser 1978; Gomez & Lada 1998).

Since the seminal work of Blaauw, it has been suggested that the age, distance, and radial velocity of the stellar components of subgroup OB 1b may not be consistent with a simple sequential star formation scenario (e.g., Hardie et al. 1964; Warren & Hesser 1978; Guetter 1981; Gieseking 1983).

In the same year Hardie et al. (1964) presented results of four years of UBV photometric observations of almost a hundred B stars close to the Belt region. They investigated the distance moduli in the Orion Belt region and pointed out that some evolutionary and/or age differences could explain the observed, systematic progression of residuals in distance modulus relative to the mean value. Figure 2.9 presents their results. Different symbols are assigned to the different sign and value of residuals: open circles represent the 'small residuals' (in a range ± 0.3 mag, with the mean distance modulus 8.2 mag), plus and minus signs indicate the negative and positive residuals, respectively. The dashed lines divide the Belt region into having predominantly positive and negative or small residuals, in the East, West and in the center, respectively.
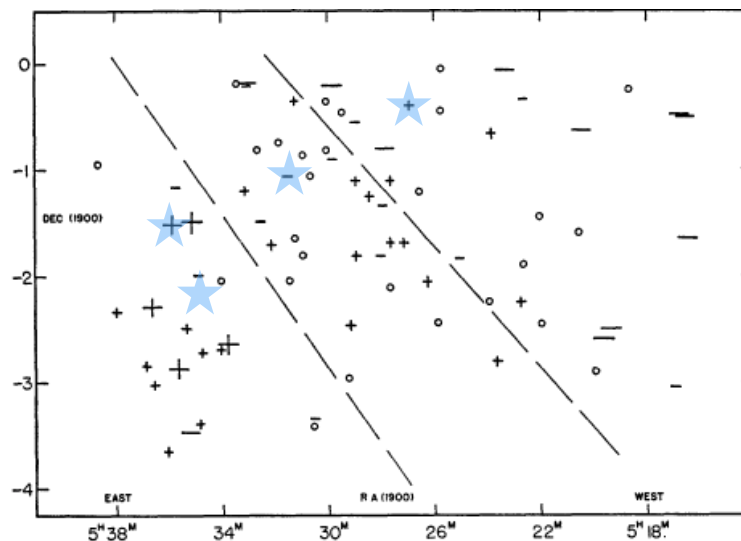

Figure 2.9: The distribution of the residuals between distance moduli for individual stars and the mean value for the region on a sky projection as presented by Hardie et al. (1964). The blue asterisks show to the positions of the Orion Belt supergiants and σ Ori.

Crawford & Barnes (1966) followed the Blaauw (1964) notation and concentrated on a region investigated by Hardie et al. (1964). Based on additional observation of H_β they found that all target stars are nearly the same age and propose that Hardie's results should be explained as real distance differences. They confirm that the distance to the Orion 1b stars increases from west to east.

The kinematics of this complex region was first investigated in 1977 by Warren & Hesser (1977), where some evidence was already presented towards a more complex star formation history of one of the sub-regions. They determined membership of program stars based on proper motions and radial velocities derived from different sources and on distance moduli obtained from *uvby′* photometry. Based on these criteria they were able to distinguish three subsets in the Orion OB1 b region and were the first to formally assign boundaries between Orion OB1 sub-associations.

A kinematic study of the Orion Belt sub-region by Gieseking (1983) and another by Jeffries et al. (2006) present clear evidence for the existence of two kinematic components in the vicinity of σ Ori (see Figure 2.10), unaccounted for in Blaauw's sequential star formation picture. Gieseking (1983) defined the region of his study as stars close to the Orion Belt region with an angular diameter of 3 degrees centered at ϵ Orionis. Jeffries et al. (2006) measured the radial velocities for a large number of low-mass stars in four fields in the proximity of σ Ori. Both studies showed that the overall kinematics of the region does not seem to be cluster-, field-, nor association-like. They postulate that the observed radial velocity distribution can be explained by two distinct star populations with different space motions.

Brown et al. (1994) used the three subdivisions of Orion 1b to determine memberships but they found no significant differences in their mean distances, and no trend within right ascension for the Ib stars as claimed by previous authors (Hardie et al. 1964; Crawford & Barnes 1966; Warren & Hesser 1977).

Towards another Orion sub-region, Alves & Bouy (2012) found an increase in the velocity dispersion for sources located in the vicinity of the Orion Nebula (NGC1980 or ι Ori cluster), suggesting a mixing of different populations (NGC 1980 was found to lie in the foreground of the Orion Nebula, about 20 pc from

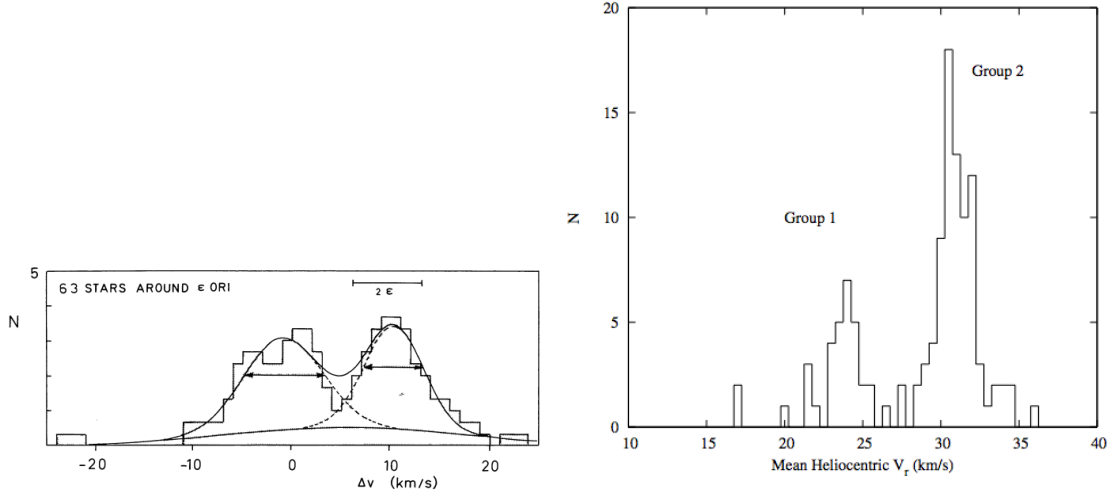**Figure 2.10:** The bimodal distribution of radial velocities for the stars in the vicinity of ϵ Ori as reporterd by Gieseking (1983) (left panel) and Jeffries et al. (2006) (right panel).

it). Disentangling these populations of young stars is critical to understand how massive star formation proceeds in Nature, and in particular quantifying the role of feedback (the engine in the sequential star formation model).

In particular, the eastern part of the Orion OB 1b subgroup, which includes Alnitak, the Horsehead Nebula, the Flame Nebula (associated with NGC 2024 in the Orion B cloud), and the H II region IC 434, would be the farthest and youngest one. The fourth brightest star in Orion's Belt region is σ Ori (48 Ori, HD 37468, O 9.5 V), the brightest source of the very well-studied σ Orionis Cluster (Walter et al. 1997), which has been assigned to OB 1b based on its spatial proximity. Still, two solid cases can be made against σ Ori belonging to OB 1b. First, the age of the σ-Ori cluster (3 Myr; Caballero (2008)) is younger than most of the stars in the Belt region and, second, the radial velocity of stars toward the cluster shows that the young σOri cluster consists of two spatially superimposed components that are kinematically separated by 7 km/s in radial velocity (Jeffries et al. 2006). In the review of Bally (2008) the σ-Ori cluster appears as a member of OB 1c, as in Figure 5 therein.

Surveys to probe the stellar and substellar populations in the Orion belt region have been Sherry et al. (2000), Sherry (2003), Briceño et al. (2005), Béjar et al. (2001), Pérez-Garrido et al. (2005) and Scholz & Eislöffel (2005). Within the

uncertainties and the incompleteness and extreme inhomogeneity of those surveys, the distribution of young stars and candidates surrounding Alnilam clearly departs from a radially concentrated distribution, as found in σ Orionis (most of those surveys were limited to a few tenths of arcmin). This result fits with the classical view of Collinder 70 as a sparse, very wide clustering that might extend to, and overlap with, neighbouring regions (e.g. δ Ori or the 'halo' of the σ Orionis cluster, Caballero 2008), pointing out that a broader study of the radial distribution of young stars, covering the whole Orion Belt, is needed to ascertain the real nature of the Collinder 70 cluster.

Caballero & Solano (2008) observed two circular areas of 45 arcmin radius each, centered on Alnilam and Mintaka and found 136 low-mass stars displaying features of extreme youth, and a total of 289 young stars in the surveyed area. They concluded that the two regions could be analogs to the σ Ori cluster, but more massive, extended, and slightly older.

Recent work on the low-mass stars of the Orion OB1 association includes the very large scale optical CIDA-QUEST survey Briceno et al. (2018). This survey uses variability to identify likely low-mass PMS stars. Briceno et al. (2018) finds that there is significant overlap between the low-mass stars of the Orion OB 1a and Orion OB 1b sub-associations.

The short overview of the literature presented above is far from complete. Nevertheless, it shows that the stellar content of the Orion OB 1b is not well defined. The role and place of this sub-population in the star formation history of the Orion star-forming region is still far from being known.

*No other constellation more accurately represents the
figure of a man.*

— Germanicus Caesar (15 BC-19 AD)

3

Orion Belt Population

3.1   Overview

In the first publication presented in this thesis, I introduce the Orion Belt Population,
OBP. In this manuscript, I present the Orion Star Forming Region as the nearest
massive star-forming region. It is also one of the most well-studied regions for
research into fundamental questions regarding star formation. The main subject
of this paper is the identification of OBP. It has been defined based on the
multi-dimensional analysis of color-magnitude diagrams (Sarro et al. 2014). The
introduction puts the OBP into the context of star formation history and describes
its place in the sequential star formation scenario by Blaauw (1964). The main
body of the paper contains detailed descriptions of the archival data and the
methods that have been used here.

The main goal of this paper is to extend the work of Alves & Bouy (2012) and
Bouy et al. (2014) to the North and (i) further investigate the extent of the young
foreground population presented, (ii) investigate the relation between OB Ic and Ib
populations, and (iii) contribute towards the reconstruction of the star formation
history of the Orion complex. I focus my study on Blaauw's subgroup OB Ib by
studying almost 30 square degrees of sky centered on Orion's Belt. Within the

limitations of the data, I compare the recently proposed Orion blue stream scenario (Bouy & Alves 2015) with that of Blaauw's classical sequential star formation.

3.2 Publication details

Title: Orion revisited. III. The Orion Belt population

Authors: Kubiak, K.; Alves, J.; Bouy, H.; Sarro, L. M.; Ascenso, J.; Burkert, A.; Forbrich, J.; Grossschedl, J.; Hacar, A.; Hasenberger, B.; Lombardi, M.; Meingast, S.; Köhler, R.; Teixeira, P. S.

Status: Published in Astronomy & Astrophysics, Volume 598, id.A124, 13 pp

Bibliographic reference: 2017A&A...598A.124K

Own contributions: Literature research, auxiliary data collection, data analysis, and final membership selection, preparation of figures and plots, paper writing.

Reprint Permission

Material:
Article by Kubiak et al. 2017, A&A, 598, A124

To be used in:
PhD thesis, University of Vienna

Permission granted to:
Karolina Kubiak
karolina.kubiak@gmail.com

I hold copyright on the material referred to above, and hereby grant permission for its use as requested herewith.

The article should be reproduced in the same format as that published in A&A (for example, in an appendix). In particular, the present permission rules do not allow copy-and-pasting parts of the article into the main text of the thesis.

Credit should be given as follows:
Credit: Author, A&A, vol, page, year, reproduced with permission © ESO.

Thierry Forveille
A&A Editor-in-Chief

Orion revisited

III. The Orion Belt population[*]

K. Kubiak[1], J. Alves[1], H. Bouy[2], L. M. Sarro[6], J. Ascenso[4,5], A. Burkert[8,9], J. Forbrich[1], J. Großschedl[1], A. Hacar[1],
B. Hasenberger[1], M. Lombardi[3], S. Meingast[1], R. Köhler[7,1], and P. S. Teixeira[1]

[1] Department of Astrophysics, University of Vienna, Türkenschanzstrasse 17, 1180 Vienna, Austria
    e-mail: karolina.kubiak@gmail.com
[2] Center for Astrobiology (INTA-CSIC), Camino Bajo del Castillo S/N, 28692 Villanueva de la Cañada, Madrid, Spain
[3] University of Milan, Department of Physics, via Celoria 16, 20133 Milan, Italy
[4] CENTRA, Instituto Superior Tecnico, Universidade de Lisboa, Av. Rovisco Pais 1, 1049-001 Lisbon, Portugal
[5] Universidade do Porto, Departamento de Engenharia Fisica da Faculdade de Engenharia, rua Dr. Roberto Frias, s/n,
    4200-465 Porto, Portugal
[6] Dpto. de Inteligencia Artificial, ETSI Informatica, UNED, Juan del Rosal, 16, 28040 Madrid, Spain
[7] Institut für Astro- und Teilchenphysik, Universität Innsbruck, Technikerstr. 25/8, 6020 Innsbruck, Austria
[8] Universitäts-Sternwarte Ludwig-Maximilians-Universität (USM), Scheinerstr. 1, 81679 München, Germany
[9] Max-Planck-Institut für extraterrestrische Physik (MPE), Giessenbachstr.1, 85748 Garching, Germany

ABSTRACT

Aims. This paper continues our study of the foreground population to the Orion molecular clouds. The goal is to characterize the foreground population north of NGC 1981 and to investigate the star formation history in the large Orion star-forming region. We focus on a region covering about 25 square degrees, centered on the ϵ Orionis supergiant (HD 37128, B0 Ia) and covering the Orion Belt asterism.

Methods. We used a combination of optical (SDSS) and near-infrared (2MASS) data, informed by X-ray (*XMM-Newton*) and mid-infrared (WISE) data, to construct a suite of color–color and color–magnitude diagrams for all available sources. We then applied a new statistical multiband technique to isolate a previously unknown stellar population in this region.

Results. We identify a rich and well-defined stellar population in the surveyed region that has about 2000 objects that are mostly M stars. We infer the age for this new population to be at least 5 Myr and likely ~10 Myr and estimate a total of about 2500 members, assuming a normal IMF. This new population, which we call the Orion Belt population, is essentially extinction-free, disk-free, and its spatial distribution is roughly centered near ϵ Ori, although substructure is clearly present.

Conclusions. The Orion Belt population is likely the low-mass counterpart to the Ori OB Ib subgroup. Although our results do not rule out Blaauw's sequential star formation scenario for Orion, we argue that the recently proposed blue streams scenario provides a better framework on which one can explain the Orion star formation region as a whole. We speculate that the Orion Belt population could represent the evolved counterpart of an Orion nebula-like cluster.

Key words. stars: formation – stars: late-type – stars: pre-main sequence – ISM: clouds – globular clusters: general

1. Introduction

The Orion star formation complex is the closest massive star-forming region to the Sun and has generated about 10^4 low- and high-mass stars for at least the last ~12 Myr (e.g., Blaauw 1964; Brown et al. 1994; Bally 2008; Muench et al. 2008; Briceno 2008). The entire region, also known as the Orion OB I association, covers an area of approximately $10° \times 20°$ on the sky and harbors a half dozen subgroups containing well-known OB stars and giant molecular clouds (see Fig. 1). The proximity of the region (~400 pc; Hirota et al. 2007; Menten et al. 2007; Sandstrom et al. 2007; Bally 2008) makes it one of the most significant star formation laboratories in astronomy. Indeed, much has been learned in Orion about star formation,

for example, clues to the evolution and destruction of clouds, the physics and dynamics of the interstellar medium (ISM), and the role that OB associations and high-mass stars play in the cycling of gas between various phases of the ISM. It is very remarkable, although understandable given its size, that for a region of such fundamental importance most attention has been devoted to the embedded and dusty stellar populations (age ≤3 Myr) emerging from the molecular clouds complexes Orion A and Orion B (e.g., Lada et al. 1991; Allen & Davis 2008; Megeath et al. 2012; Gutermuth et al. 2009; Da Rio et al. 2010; Spezzi et al. 2015), whilst only a few studies have tackled the Orion star-forming region as a whole.

The Orion OB I association (Blaauw 1964) is composed of several stellar subgroups of different ages, gas, and dust amount. Blaauw divided Orion's association into four groups. Figure 1 presents a widefield image of the Orion Constellation super-imposed with ellipses denoting the approximate boundaries of
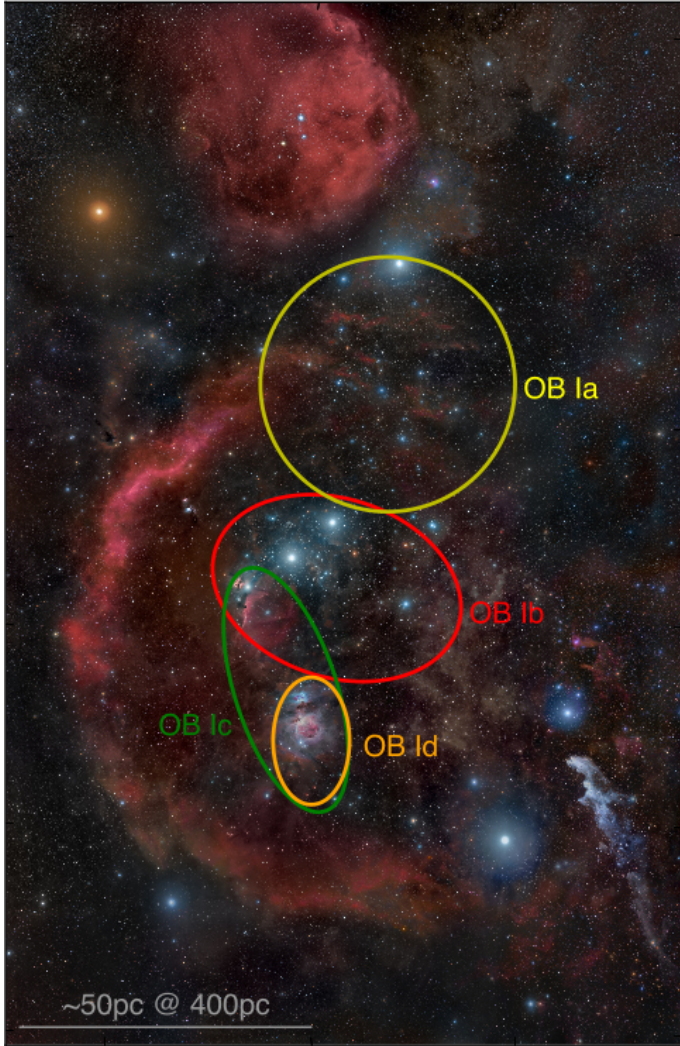

Fig. 1. Widefield image of the Orion OB I stellar associations as described by A. Blaauw (1964) and revised in Bally (2008). North is up, and east is left. Background image: R. Bernal Andreo, www.deepskycolors.com

these four OB I subgroups. These groups appear to show a spatial-temporal relation that is suggestive of a sequence of star formation events, from dust free Ia subgroup to still dust embedded Id. This led Blaauw (1964) to propose a sequential star formation scenario, where a previous generation of stars is responsible for the formation of a new one via positive feedback; this idea was later quantified by Elmegreen & Lada (1977) and has remained very popular in the literature.

Although there are differences in the estimated ages or exact sizes of the various groups, most of the published works in the region agree that the Orion OB Ia group toward the north is the oldest with an age of ~8−10 Myr (Bally 2008, with a distance ~350 pc) or even 12 Myr as originally proposed by Blaauw (1964). This group is also dust free. The OB Ib subgroup, containing the stars around the Orion Belt asterism, is located at a distance of ~400 pc (Bally 2008). This subgroup has an estimated age of ~3−6 Myr (Bally 2008) or ~1.7 Myr (Brown et al. 1994), although the lower estimate is inconsistent with the age of the three supergiants (ζ Ori, ϵ Ori, and δ Ori) that form the naked-eye Belt. According to their spectral types, these three stars must be at least 5 Myr old. The 3−6 Myr old OB I c subgroup consists of stars around the Sword (about 4° below the

Belt asterism). The older stars in the OB Ic are superimposed on the much younger and still embedded subgroup OB Id, which is associated with the Orion nebula and including the Trapezium stars, M43, NGC 1977, and the OMC1, 2, and 3 regions in the integral shaped filament along with the northern part of the Orion A molecular cloud (age <2 Myr, $d \sim 420$ pc, Bally 2008). Although initially each subpopulation was assumed to be a distinct episode in a large star formation event, it was early realized that the subgroups are partially superimposed along our line of sight and several authors have described the boundaries between subgroups, their characteristics, and some discrepancies with the sequential star formation scenario (e.g., Warren & Hesser 1978; de Geus et al. 1990; Brown et al. 1994; Gomez & Lada 1998). Unfortunately, the three-dimensional arrangement of star-forming regions, in particular massive ones, is far from simple and is essentially unknown for any massive star-forming region given the current distance accuracies.

Recently, Alves & Bouy (2012) and Bouy et al. (2014) presented evidence for a young and massive foreground population (~5 Myr) that is detached from the Orion A cloud but seen in projection toward it. They argue that this foreground population was formed about 4−5 Myr ago in a different, but perhaps related, event in the larger Orion star formation complex and not in the existing Orion A molecular cloud like, for example, the Orion nebula cluster. This foreground population includes in part Blaauw's OB Ic population, but does not include the younger σ-Ori cluster, as suggested in Bally (2008). An intriguing result of their study was that the Orion A foreground population seemed to extend to the north, toward OB Ib, beyond the limits of their survey. This was later confirmed in Meingast et al. (2016) in their ESO-VISTA near-infrared (NIR) imaging of the entire Orion A cloud, who found a southern boundary to the foreground population, but not an obvious boundary toward the north. This raises the question of how well Ori OB Ic and Ib are separated spatially, if at all, and how they fit in a sequential star formation scenario.

In a related study, Bouy & Alves (2015) revisited the HIPPARCOS catalog and studied the spatial distribution in 3D of OB stars that are closer than 500 pc from the Sun. Their analysis reveals that massive OB stars form large-scale structures that are well defined and elongated, which they refer to as "blue streams". The spatial coherence of these blue streams, and the monotonic age sequence over hundreds of parsecs, suggest that they are made of young stars. The two main blue streams are the Sco-CMa stream, including the Sco-Cen association, and the surprising Orion stream, originating in the Orion clouds and extending to regions as close to Earth as ~200 pc, but likely even closer. In this scenario, the foreground population presented in Alves & Bouy (2012) and Bouy et al. (2014) could be part of the Orion blue stream. Given this new scenario for the distribution of young stars in the local neighborhood, and in particular the realization that the Orion OB I association may be part of the Orion stream, there is a clear need to gather more information about the region on larger scales than collected previously and for regions further away from the molecular clouds.

The main goal of this paper is to extend the work of Alves & Bouy (2012) and Bouy et al. (2014) to the north and, (i) further investigate the extent of the young foreground population presented; (ii) investigate the relation between OB Ic and Ib populations; and (iii) contribute to the reconstruction of the star formation history of the Orion complex. We focus our study on Blaauw's subgroup OB Ib by studying almost 30 square degrees of sky centered on Orion's Belt. Within the limitations of our

data, we compare the recently proposed Orion blue stream scenario with that of Blaauw's classical sequential star formation.

The overdensity of blue massive stars in the Orion Belt region was first pointed out in Galileo's Sidereus Nuncius in 1609 as an example of how the telescope could resolve stars that are not visible by the human eye. The stellar overdensity was also recognized in 1931 by Swedish astronomer Per Collinder in his catalog of open clusters (Collinder 1930). He distinguished the Orion's Belt asterism, comprised of the three famously aligned bright stars: Alnitak (ζ Ori, HD 37742J, O9.7 Ib+B0 III), Alnilam (ϵ Ori, HD 37128, B0 Ia), and Mintaka (δ Ori, HD 36486, B0 III +O9 V) as Collinder 70 (Col 70). Still, and even though it is immediately recognizable to the naked eye, the Orion Belt stellar population is paradoxically poorly known. Caballero & Solano (2008) observed two circular areas of 45 arcmin radius each, centered on Alnilam and Mintaka and found 136 low-mass stars displaying features of extreme youth, and a total of 289 young stars in the surveyed area. They concluded that the two regions could be analogs to the σ Ori cluster, but more massive, extended, and slightly older.

Since the seminal work of Blaauw, it has been suggested that the age, distance, and radial velocity of the stellar components of subgroup OB Ib may not be consistent with a simple sequential star formation scenario (e.g., Hardie et al. 1964; Warren & Hesser 1978; Guetter 1981; Gieseking 1983). In particular, the eastern part of the subgroup, which includes Alnitak, the Horsehead Nebula, the Flame Nebula (associated with NGC 2024 in the Orion B cloud), and the H II region IC 434, would be the farthest and youngest subgroup. The fourth brightest star in Orion's Belt is σ Ori (48 Ori, HD 37468, O 9.5 V), the brightest source in the well-studied σ Orionis Cluster (Walter et al. 1997), which has been assigned to OB Ib based on its spatial proximity. Still, two solid cases can be made against σ Ori belonging to OB Ib. These two cases, which are discussed later in this paper, are, first, the age of the σ-Ori cluster (3 Myr; Caballero 2008) is younger than most of the stars in the Belt region and, second, the radial velocity of stars toward the cluster shows that the young σ-Ori cluster consists of two spatially superimposed components that are kinematically separated by 7 km s^{-1} in radial velocity (Jeffries et al. 2006). In the review of Bally (2008) the σ-Ori cluster appears as member of OB Ic, as in Fig. 1.

This paper is organized as follows. The next section briefly describes the data used in this study. Sections 3 and 4 present our results, centering on the discovery of a large population of young stars around ϵ Ori. In Sect. 5 we discuss our results and we summarize them in Sect. 6.

2. Data

2.1. Survey field

We first retrieved and cross-matched all the sources from the Two Micron All-Sky Survey (Skrutskie et al. 2006) and Sloan Digital Sky Survey DR12 (Ahn et al. 2014) catalogs located within a radius of 3 degrees centered around ϵ Ori at $(l, b) = (205.21, -17.24)°$. The size and location of our field were chosen to achieve the best coverage of Ori Ib in both catalogs. The 2MASS catalog homogeneously covers the entire area of interest, while the SDSS DR12 catalog is missing a significant fraction in the southern half. Figure 2 shows the coverage of the different surveys used in this study over a photograph of the region. It includes, by design, most of the σ-Ori, and a significant fraction of the NGC 1980/NGC 1981 area surveyed

Table 1. Catalogs and observations used in this study.

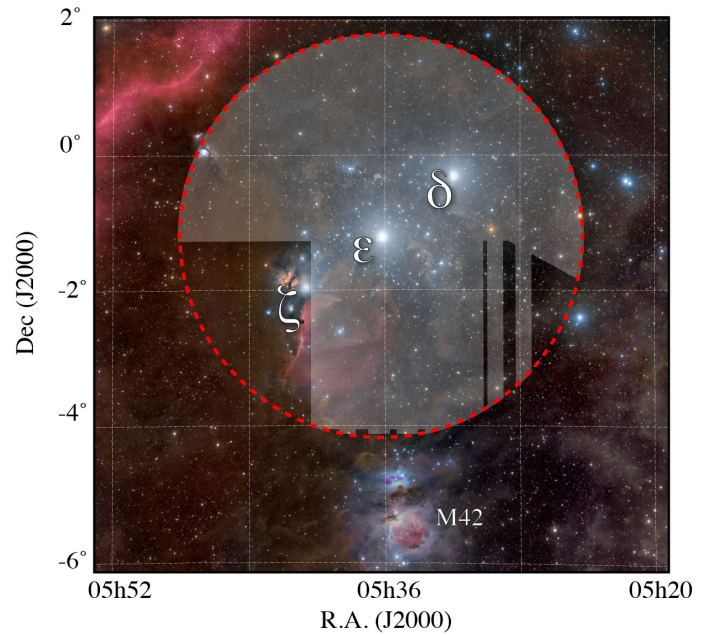| Survey	Band/channel
SDSS	g, r, i, z
2MASS	J, H, K_s
WISE	$W1, W2, W3, W4$
XMM-Newton	0.2–12 keV
KISO	Hα
Planck	857 GHz

Fig. 2. Coverage of the study. The selected SDSS survey coverage is represented by the gray area. The 2MASS survey, an all-sky survey, is available for the entire region of study (red dotted circle). Background image: R. Bernal Andreo, www.deepskycolors.com

in Bouy et al. (2014). All in all, about 21% of the $\sim$28 deg^2 surveyed area is incomplete. A total of 200 497 2MASS and 909 619 SDSS sources were found in the corresponding area. Of these, 189 620 sources appear in both surveys.

In an effort to compile the most complete data set in terms of spatial and wavelength coverage, we then collected complementary photometry from the ALLWISE catalog obtained with the Wide-field Infrared Survey Explorer (Cutri et al. 2013), the Hα emission-line KISO survey (Wiramihardja et al. 1994), and the *XMM-Newton* serendipitous sources catalog (Watson et al. 2009). We also investigated the dust distribution in this region based on the *Planck* 857 GHz Survey image (Planck Collaboration I 2014; Tauber et al. 2010).

2.2. Control field

Control fields provide an efficient and simple method to estimate excess stellar population statistics and luminosity functions. We selected the control field (CF) using the following criteria:

– Same size as the survey field;
– Centered on the same Galactic latitude as the area of interest described above ($b = -17.24°$) to minimize any enhancements in stellar surface density caused by the Milky Way structure;

- Located in a region with low extinction, as reported in Lombardi et al. (2011) extinction map, to obtain the best characterization of the background population (Fig. B.1);
- Covered by the SDSS DR12 catalog.

The selected CF is located almost 30° away from the scientific field toward lower galactic longitudes and centered on $(l, b) = (187.0, -17.24)°$. Owing to the peculiar specific coverage of the Sloan's survey away from the Galactic cap, this is the closest satisfactory field. Unfortunately, despite our best efforts, the control field is not extinction free and suffers from about 1 mag of visual extinction. Because we estimate the population size in the NIR, this is not critical because one magnitude of visual extinction is on the order of the extinction noise measurement in the NIR. Figure B.1 shows the location of the science and control fields as blue and red circles, respectively, superimposed on NICER extinction map by Lombardi et al. (2011). The green *strips* correspond to the coverage of SDSS catalog, illustrating the incomplete coverage of optical data. The CF contains 167 105 2MASS sources and 376 846 SDSS sources, of which only 59 546 sources have photometry available from both surveys.

3. A new rich and large stellar group around ϵ Ori

3.1. Stellar surface density

The surface density of sources provides a simple first step to search for stellar groups. Figure 3 shows the kernel density estimate (KDE) of the positions of sources in the 2MASS J band within a magnitude cut of 15.3 mag (0.2 mag above the completeness limit to avoid the different level of photometric noise level for different 2MASS strips) and was obtained using a Gaussian kernel with a bandwidth of 10′.

We investigated the KDE maps for all eight available bands with bandwidths ranging from 0.01° to 1°. The *ugriz* density maps showed low-density areas around the bright OB stars of the Orion Belt and we interpret these as artifacts related to the presence of the bright stars, in particular the super-giants in Orion's Belt asterism. The near-IR 2MASS survey covers a broader dynamic range and is less affected by the presence of bright stars. Furthermore, the NIR is better suited to study the stellar spatial distribution thanks to its lower sensitivity to extinction and better sensitivity to low-mass stars that dominate the initial mass function (IMF).

A clear overdensity is seen around σ Ori in the JHK_s surface density maps, and ζ Ori (Alnitak) in the H and K_s maps. These two density enhancements are associated with the well-known σ Orionis and NGC 2024 stellar clusters (e.g., Meyer et al. 2008). Another density enhancement is clearly visible around ϵ Ori (Alnilam) in the J and H maps. We measured the significance of overdensities by estimating a rms noise level from ten measurements around the main enhancement in Fig. 3. The main overdensity toward the center of this figure, the main object of study throughout this work, is defined by a threshold of 7σ.

While the overdensity around σ Orionis and NGC 2024 region are uniform and compact at the spatial scale probed by our analysis (10′), the density enhancement around ϵ Ori is much more extended and shows some internal structure. We also note the lack of any obvious density enhancement around δ Ori (Mintaka), in contrast with the result by Caballero & Solano (2008), who investigated the population of young stars and brown dwarfs in a comparatively smaller region around Mintaka and Alnilam. It is still possible, however, that a potential
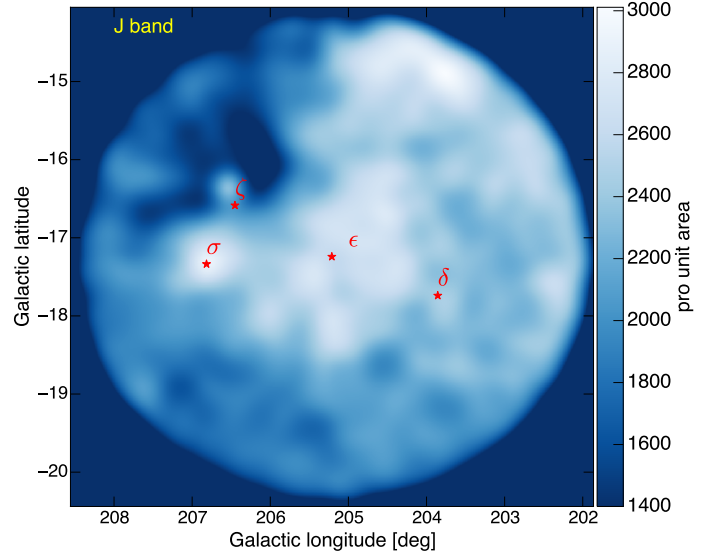
Fig. 3. Surface densities calculated based on J-band 2MASS. Asterisks denote the positions of the three Orion Belt stars and σ Orionis. Similar results are obtained for the H and K bands.

Table 2. Properties of the main overdensity in Fig. 3

Properties		Value
Significance		$>7\sigma$
Size	Ellipse $1.7° \times 2.2°$	2.94 °²
Number of stars		2345
Total mass		~1200 $M_\odot$
Surface density		800 stars/ °²
	for $d = 380$ pc	18 stars/pc²
	for $d = 250$ pc	41 stars/pc²
Volume density	for $d = 380$ pc	8 stars/pc³
	for $d = 250$ pc	17 stars/pc³
Position of peaks	σ-Ori	14σ
A	$205.5°, -17.5°$	11σ
B	$204.5°, -16.8°$	10σ
C	$204.5°, -17.5°$	9σ
D	$205.2°, -18.2°$	8.5σ

enhancement around δ Ori is less significant than our 5σ significance threshold. Finally, the KDE maps also show a surface density enhancement at almost all wavelengths in the northern part of the field, closer to the Galactic plane, which we tentatively interpret as the increasing stellar density produced by the Galactic structure and do not discuss further here. Finally, the Orion B molecular clouds are clearly visible north of ζ and σ Ori and appear as a region of lower density. Some of the properties of this enhancement are presented in Table 2.

To estimate the size of the population included in the density enhancement around ϵ Ori, we estimate the number of sources falling into a $1.7° \times 2.2°$ ellipse (7σ threshold in overdensity in the J-band KDE map) encompassing it (9466 sources), and the number of sources included in an equal area located in the control field (7121 sources). The latter gives an estimate of the number of foreground and background sources that one can expect to find in that region of the galaxy. Subtraction of both values gives 2345 sources, which we use as an estimate for the size of the population producing the density enhancement. Repeating the
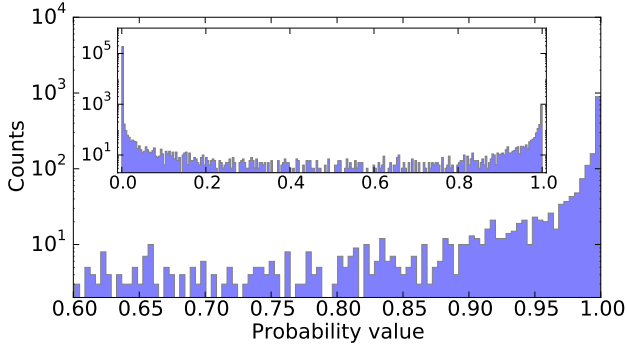
Fig. 4. Distribution of membership probabilities obtained for all sources (*inner plot*) and for sources with probability greater than 60%.

count in 9 equal-area random positions within the CF leads to a dispersion of ~215 sources.

3.2. Color–magnitude and color–color diagrams of the survey

Figure B.2 shows a $(i, i − K_s)$ color–magnitude diagram for the sample of sources in our survey (left panel) and CF (right panel). A rather dense sequence is clearly visible in the science field but not in the CF, suggesting the existence of a nearby young and rich population (indicated approximately by the green ellipse). The dispersion in color along the sequence, which is less than 1 mag, is lower than the typical dispersion observed for very young clusters (≤5 Myr, Mayne et al. 2008).

The sequence is also clearly visible in other optical and NIR color–magnitude diagrams for the science field, but is not present in the corresponding color–magnitude diagrams for the control field; this confirms that the population separates well photometrically from the field population across a broad range of wavelengths. A closer qualitative examination of the photometric properties of stars in the survey field can be carried out by comparing various color–color diagrams.

3.3. Selection method

We took advantage of the clear separation of the sequence in various color–magnitude diagrams and the apparent absence of significant extinction to select the members of this new population. As in Bouy et al. (2014), we applied the novel maximum-likelihood approach described in detail in Sarro et al. (2014) to infer the membership of all the sources in our sample. This multidimensional probabilistic analysis offers the advantage of using multiple color–magnitude diagrams simultaneously and includes a statistically sound treatment of errors and censored data. The u band was excluded from the analysis because the observations are significantly shallower and extremely sensitive to interstellar extinction, excess emission related to accretion, and stellar activity. Table A.1 gives the list of all sources in our final catalog and includes the identification number, J2000 coordinates, *griz* SDSS, and *JHK*$_{\rm S}$ 2MASS magnitudes, as well as the membership probability computed as described above.

The choice of a membership probability threshold is not trivial. Figure 4 shows the distribution of membership probabilities for all the sources. It presents the typical bimodal distribution distribution comprised of a huge maximum around 0 and a smaller maximum around 1. Table 3 shows the number of members for various threshold values.

Table 3. Number of members at different membership probability thresholds.

Prob. threshold	0% initial sample	68%	80%	95%	99.73%
Sample size	189 620	1956	1850	1494	783

In an effort to be conservative, we select as members all the sources above a membership probability of 99.73%, leading to a sample of 783 highly probable objects.

Figure B.3 illustrates the efficiency of the multidimensional selection method used to compute membership probabilities. This figure shows a mosaic of color–color-diagrams constructed using the optical *griz* and near-infrared *JHK* colors of our input catalog. The high probability Orion Belt population (from hereafter, OBP) candidate members are overplotted with blue dots, and clearly separate from the field sources in most diagrams. The comparison of this positions of candidates with the intrinsic colors of luminosity V and III stars in the $J − H$ versus $H − K$s diagram from Straižys & Lazauskaitė (2009), shows, as expected, that the sample of OBP high probability members is made mostly of M stars.

This list of highly probable members is far from complete and suffers from several limitations. For example, there is no data close to the bright stars, contamination must still be present, and the different depths of the various optical and near-infrared data and the nonuniform spatial coverage of the data (in particular the SDSS data) biases the sample in some areas, and there are over specific luminosity ranges. This sample is nevertheless extremely useful to characterize the general properties of this new group and, in particular, its distance and age.

4. Properties of the selected sample

4.1. Spatial distribution

Figure 5 shows the 2D KDE of the spatial distribution of the 783 OBP candidate members computed using the same bandwidth as in Fig. 3. The stellar density appears clearly lower in the close vicinity of the Belt supergiants (δ, ϵ, ζ Orionis) as a result of the incompleteness of the SDSS catalog near these bright stars, as illustrated by the yellow contours in Fig. 5. A density enhancement is also visible around σ Ori and suggests that our selection includes a few σ Ori cluster members. As we see in Sect. 4.3, the σ Ori sequence is indeed very similar to that of the new population, but several pieces of evidence indicate that the two groups must be distinct. The corresponding contamination is nevertheless relatively low and concentrated around σ Ori itself. With these limitations in mind, we note that the most probable members seem to be located in an 0.5° wide ring that is roughly centered on ϵ Ori. The density in this ring is clearly not homogeneous, and a strong overdensity located south of ϵ Ori seems to dominate. The current data do not allow us to draw any further conclusions on the details of the spatial distribution of OBP members. More importantly, however, we retrieved a roughly similar structure to the *J*-band stellar density map (Fig. 3) in a completely independent manner. This gives us confidence in the main result of this paper and the presence of a rich and fairly coeval stellar population toward the Orion Belt.

To our knowledge, this coeval group does not correspond to any association previously identified in the literature. It is in particular more compact than what was defined as the Collinder 70
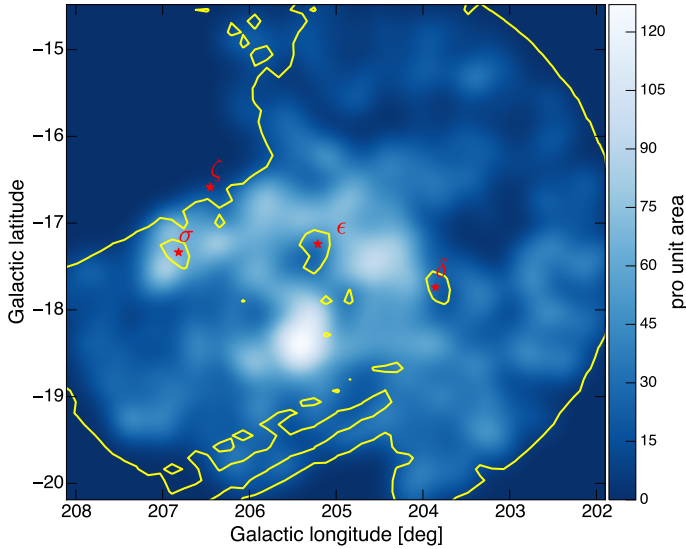
Fig. 5. Surface density map of the 783 OBP candidate members. Yellow contours represent source density from SDSS catalog. The map is affected by completeness near the supergiants and σ Orionis (indicated in red).
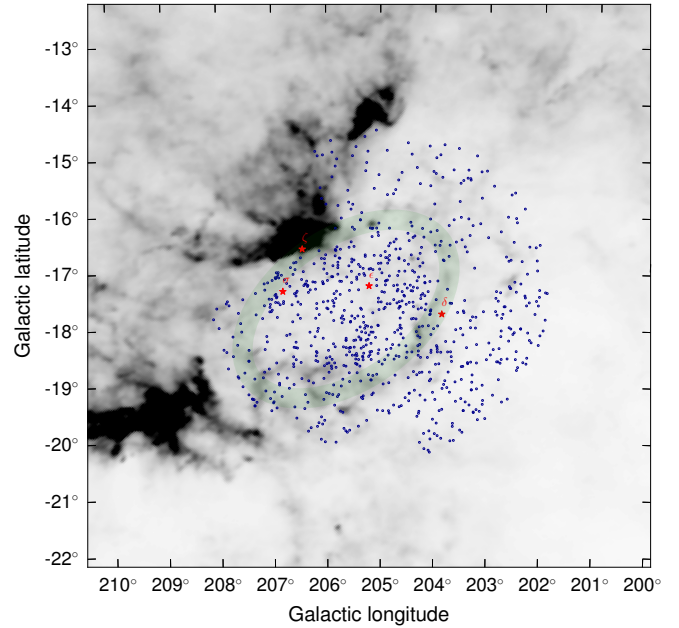

Fig. 6. IC 434 region and surroundings as seen by *Planck* 857 GHz. The emission map shows a dust/gas shell (Ochsendorf & Tielens 2015) (indicated in light green) superimposed with the OPB (blue dots). We found no evidence for reddening in the OBP, implying that this stellar population must lie between Earth and the dust shell.

cluster (Collinder 1930) and we propose that it is a distinct and new population of young stars.

4.2. Age and distance estimates

4.2.1. Disk and accretor frequencies as an age diagnostic

We use the WISE and KISO Hα surveys to study the disk and accretor frequencies among the sample of 783 high probability OBP members. The presence of a protoplanetary disk, which is probed by mid-infrared excesses in WISE, and intense accretion, which is probed by strong Hα emission, provide clues on the age of a population. Protoplanetary disks that are responsible for the 3–12 μm excess emission revealed by WISE typically disperse over timescales of $5 \sim 10$ Myr (Ribas et al. 2015). Accretion of the circumstellar material onto the star stops being strong enough to produce sufficiently intense Balmer lines after a similar or shorter timescale. We find that only two stars within our sample have a counterpart in the KISO catalog (KISO A-0904 21 and KISO A-0903 163) and only 27 stars display mid-infrared excess in one or more WISE bands[1]. The KISO and WISE surveys sensitivities should encompass most of the luminosity range of our sample. These two small numbers suggest that the OBP members have cleared most of their protoplanetary disks and allow us to place a lower limit on the age around ~5 Myr.

4.2.2. Relation with the ISM and distance to the OBP

In the 857 GHz *Planck* map, shown in Fig. 6, the Orion Belt population coincides, in part, with the IC 434 dust shell (Ochsendorf & Tielens 2015). This gives us the opportunity to figure out which of the dust and the new population lies closer to Earth, as stars located behind dust clouds should appear reddened in color–color diagrams.

Figure B.3 includes a $(g-r, r-i)$ color–color diagram for the 783 sources selected as the members of the Orion Belt population. These optical bands are particularly sensitive to extinction

and a small amount of dust in the line of sight should be easily noticeable. The red line represents the intrinsic colors for main-sequence stars from Covey et al. (2007) and an extinction vector is indicated. As we can see, the members of the Orion Belt population create a narrow and compact sequence that is mostly unaffected by extinction and lies slightly left of the main sequence in the red. The amount of interstellar dust in the line of sight between Earth and the OBP must therefore be negligible, and the OBP stars must be in front of the IC 434 shell, which is itself located at a distance of ~380 pc.

In an effort to obtain the minimum distance to the selected stars, we carry out a thought experiment. Knowing that our sample consists almost solely of M dwarfs, we estimate the distribution of brightness of M dwarfs for the different distances (from 100 to 400 pc) and extinction values ($A_{\rm v}$ in range $0 \dots 1$ mag). Although this is not a simple exercise because we do not know the age of the population, and the luminosity of young M dwarfs drops rapidly after 10 Myr, we can make an educated guess that our sample cannot be closer than ~250 pc to the Sun.

4.3. Comparison with other groups and clusters: σ-Ori and NGC 1980

The comparison with empirical pre-main sequences of well-known young clusters in color–magnitude diagrams can provide clues to the age and distance of a young population. In Fig. B.4 we compare the sequence formed by the high probability OBP candidate members with those of σ Orionis (3 Myr, 385 pc, and members list from Caballero 2007) and NGC 1980 (5–10 Myr, 400 pc, and members list from Bouy et al. 2014).

The figure shows that the OBP sequence is very similar to those of σ Orionis and NGC 1980. In fact, a cross-match between the three lists shows that 19 sources selected as OBP members were identified as σ Orionis members by Caballero (2007), 52 sources selected as OBP members were identified as

---

[1] A detailed description of the mid-infrared excess analysis will be given in Kubiak et al. (in prep.).

NGC 1980 members in Bouy et al. (2014), and this illustrates the complexity of isolating stellar groups in the Orion OBI region.

The low disk and accretor frequencies among OBP members suggest that the OBP must be significantly older than the 3 Myr σ Orionis, where as many as 35% of T Tauri stars display mid-infrared excess related to the presence of a disk (Hernández et al. 2007). For the two sequences to match, the OBP must therefore be closer to the Sun than σ Orionis, in agreement with our conclusion based on the extinction toward the OBP members.

Figure B.4 also shows that the OBP sequence is similar to that of NGC1980, but is slightly fainter by half a magnitude. If this difference is real, it could be the result of either a larger distance or an older age. In Bouy et al. (2014) of this series, we estimated an age of 5–10 Myr and distance of 380 pc for NGC 1980. Since the comparison with σ Orionis and the analysis of the extinction toward the OBP sources consistently imply a distance closer than 380 pc, we can rule out a significantly larger distance and conclude that the OBP must be older than NGC 1980.

For the mass determination, we assumed an age of 5–10 Myr for the OPB since that was the best fit to the produced HR diagram. At this point, we should recall the assumptions and caveats in these estimates. The uncertainty in the determination of the population distance, together with the uncertainty in the age ($\sim$5–10 Myr), are the largest contributors to the final error in the mass of each source; we assumed an uncertainty in the determination of the population distance of $\sim$380 pc, whilst we believe it is an upper limit for distance determination in this case. Based on this distance, the least massive candidate members have masses of 0.05 $M_\odot$. By assuming a normal IMF (using both Chabrier 2003; and Kroupa 2001) we estimate the total number of members as $\approx$2500. This value should not be considered as the definitive size of the population, but an educated guess given the assumptions. Still, it is similar to the statistical estimate of source counts from the control field (2345 ± 215), suggesting, although with strong caveats, that the population might have a normal IMF.

5. Discussion

We have found a population of about 2500 M stars (with 789 candidates with high probability) that are roughly coeval and extinction free and are distributed across $\sim$3 square degrees toward the Orion Belt asterism with an age of about 10 Myr. Photometry alone poorly constrains the distance to this population or its line-of-sight extent. This newly identified population can be as far as $\sim$380 pc (but in front of the Orion B cloud) or as close as 250 pc. In the closer case the OBP could be the low-mass counterpart to the well-known Orion supergiants at distances around 250 pc.

The new population, the OBP, is likely the low-mass counterpart of Blaauw's Ori OB Ib subgroup. Relevant to this discussion, Jeffries et al. (2006) performed radial velocity observations of low-mass stars toward a relatively large field toward σ Ori and found two spatially superimposed components that are kinematically separated by 7 km s^{-1} in radial velocity and with different mean ages. These authors suggest an age of about 10 Myr for the older component (their "group 1"), which has a mean radial velocity of 23.8 km s^{-1}. Jeffries et al. (2006) suggested that the older "group 1" was made by stars from the OB Ia subgroup, but the results in this paper suggest that this second component is most likely comprised of the stars in the Orion Belt population, or the OB Ib subgroup. Figure 2 of their paper further supports this statement as one can see how the field closer to the OBP (the NW field) is mostly dominated by stars belonging to the 23.8 km s^{-1} group. We cross-checked our list of targets against

the sources in Jeffries et al. (2006) and although their study is centered on σ Ori, we found that most of the matches with the OBP belong to the older group 1; albeit this finding also matches group 2, which probably suggests that our selection method is not accurate enough to clearly separate the two different populations. Overall, our results reinforce the idea that overlapping populations at different evolutionary states and distances coexist along lines of sight toward the Orion clouds, as suggested in Alves & Bouy (2012) and Bouy et al. (2014).

5.1. Is the Orion sequential star formation scenario in trouble?

Blaauw's original idea of sequential star formation calls for a star formation event being directly responsible for the genesis of the next event. In Orion, it was proposed that the spatial-temporal sequence of events proceeded as follows (e.g., Bally 2008):

Ia ($\sim$12 Myr) → Ib ($\sim$10 Myr) → Ic ($\sim$5–7 Myr) → Id ($\sim$1–3 Myr).
In recent decades, evidence has been accumulating suggesting that this attractive scenario suffers from several shortcomings. Brown et al. (1994) found that subgroup Ib is younger than Ic and, to address the problem of an obvious break in the spatial-temporal sequence, these authors argued that the sequential star formation scenario is still plausible if the Ic population had moved from its putative birthplace closer to the Ia population; this move has yet to be quantified. Nevertheless, if the OBP is indeed the low-mass counterpart of Ib, then the results in this paper are in tension with Brown et al. (1994) as we find that the age of the OBP is similar to the canonical age of Ib (around 10 Myr), apparently solving the break in the spatial-temporal sequence.

Another problem for the sequential star formation scenario is the superposition of populations with different ages, as they do not easily fit a star formation sequence that covers about 100 pc from west to east. Evidence for such overlapping stellar populations has been accumulating in the literature (e.g., Gomez & Lada 1998; Warren & Hesser 1977; Jeffries et al. 2006; Alves & Bouy 2012; Bouy et al. 2014). For example, what event triggered the formation of the 1–3 Myr old σ Ori cluster, seen along the same line of sight as the $\sim$10 Myr old OBP? Given that the Id subgroup is still forming stars and that Ia is too removed/old to be the trigger, one faces two options in a sequential star formation scenario: the trigger was either a) Ib or b) Ic, a subgroup closer to σ Ori in age but not in projection. If a) then one needs to explain the roughly 7–8 Myr delay in the formation of σ Ori. If b) one needs to explain the apparent break in spatial sequence (Ic is about 20 pc away from σ Ori in projection, so probably in reality more). Option a) seems unlikely as Ib would have to trigger the formation of Ic to the southeast 5–7 Myr ago and the σ Ori cluster 2–3 Myr ago toward its background, as seen from Earth. Regarding option b), a possible solution to the break of the spatial-temporal sequence is to evoke that σ Ori was formed elsewhere. This was recently suggested, in a different context by Ochsendorf & Tielens (2015). In the Ochsendorf-Tielens scenario σ Ori was formed to the south (in galactic coordinates, see their Fig. 1) of the Ic population and moved north toward the GS206-17+13 shell. It is hard to imagine how the feedback from Ic to the south would trigger the formation of the σ Ori cluster and cause it to move north. In summary, neither option seems satisfactory.

5.2. The Orion blue stream scenario

Recently, Bouy & Alves (2015) suggested a new scenario for the interpretation of the distribution of OB stars in the local

neighborhood. In a reanalysis of the Hipparcos catalog, these authors found that the distribution of OB stars followed large-scale structures that are well-defined and elongated, which they refer to as blue streams. The roughly constant width of the streams, together with a monotonic age sequence over hundreds of parsecs, suggests that they are the outcome of a large star formation event. They describe the existence of three streams in the local 500 pc neighborhood, one of these is the Orion stream, originating at the position of the Orion clouds and extending to regions as close to Earth as ~200 pc, but likely even closer. This scenario imposes a well-defined age sequence as it assumes that young stars stream away from their place of birth, currently the Orion A and B molecular clouds. The further a population is from its birth place, the older it should be. Given the current position of the Sun in the Galaxy, the Orion stream appears projected along its length for an observer on Earth, which implies that stellar populations at different ages and distances should appear superposed. Because of the particular projection effect the Orion stream, this new scenario does not require a spatial sequence, unlike Blaauw's sequential scenario for Orion.

The new blue streams scenario appears to accommodate well the available observational data of the Orion star-forming region as a whole. As discussed above, there is plenty of evidence in the literature for superposition of populations with different ages along the direction to the Orion clouds. For example, the OBP fits well this new view of Orion as a stream projected along its length; a roughly 10 Myr old population is seen in projection toward a significantly younger σ Ori, and an even younger NGC 2024 cluster, still embedded in the Orion B cloud. The OBP, we argue, is closer to Earth than σ Ori and the cloud interacting with it via the HII region. We also argue that there is some evidence that the OBP (Ib subgroup) is closer and older than NGC 1980/NGC 1981 (Ic subgroup), which is closer and older than the σ Ori cluster. This age and distance relation is in good agreement with the blue streams scenario presented in Bouy & Alves (2015). Finally, the Ia subgroup and the 25 Ori cluster (e.g., Briceno 2008; Downes et al. 2014, 2015), which are not addressed in this work, would also be part of the Orion stream. If older than the OBP, they should correspond to the nearest components of the Orion stream. But this remains to be confirmed, as the OBP could be older, hence nearer, and could be the low-mass counterpart to the well-known Orion supergiants at about 250 pc from Earth.

The streams scenario provides another advantage: it does not require that populations move substantially from each other, as proposed in Brown et al. (1994), to solve the apparent break in the spatial-temporal sequence in Blaauw's scenario. In the streams scenario, the OB subgroups should have a space motion toward the same general direction, so a prediction of the streams scenario is that the proper motions between subgroups should be relatively small. In the streams scenario, Blaauw's OB subgroups could represent different components of the same stream with different ages and distances; these are all formed at about 400 pc by clouds long gone with the exception of subgroup Id, the ONC, embedded in Orion A cloud, and NGC 2024 embedded in the Orion B cloud.

5.3. Is the OBP the future of the ONC?

Can the OBP be the evolved counterpart of an ONC-like cluster that was formed about 10 Myr ago or is it an altogether different type of object? A striking property of the OBP population is that it is distributed over a large area of the sky and its low stellar density is very different from other well-known stellar clusters

in Orion, such as the ONC, σ, λ, or ι Ori clusters. For example, the average stellar surface density in the Orion nebula cluster (~200 stars/pc^2; Hillenbrand & Hartmann 1998) is about an order of magnitude higher than that of the OBP. The volume density of stars in the core of the ONC ($2-3 \times 10^4$ stars/pc^3, Hillenbrand & Hartmann 1998) is about three orders of magnitude higher than that of the OBP.

Remarkably, both the ONC and the OBP have a similar number of stars. Assuming that the OBP is not a gravitationally bound population, and that it is expanding freely since it got rid of its parental molecular cloud early in its formation, it would have taken about 5 Myr for the OBP to expand from 2 pc to 7 pc radius at about 1 km s^{-1} expansion velocity, or 10 Myr for 0.5 km s^{-1} velocity. These rough estimates are not implausible according to models of an ONC-type cluster expanding after gas removal (e.g., Kroupa et al. 2001), and so the possibility that the OBP might represent an evolved ONC cannot be discarded with current data. High-resolution spectroscopic observations or accurate proper-motions measurements are needed for a more quantitative answer to this question; such measurements and observations do not exist at the moment.

6. Summary

In order to find the spatial extension of the foreground stellar population to the Orion A cloud found in Alves & Bouy (2012) and Bouy et al. (2014), and to investigate the relation between Blaauw's OB Ic and Ib subgroups, we analyzed a circular area with a radius of 3° centered on ϵ Orionis (HD 37128, B0Ib), covering the Orion Belt region. The main results of this investigation are as follows:

- We found two large stellar overdensities in the Orion Belt region: one centered on the well-known σ-Ori cluster, and a new, richer but more extended overdensity close to ϵ Ori. We compared the stellar density in the surveyed region with a control field and estimated an upper limit for the size of the new overdensity of about 2345 ± 215 sources.
- Optical and near-IR color–magnitude diagrams reveal a well-defined sequence above the Galactic field, which is suggestive of a large young stellar population that is approximately coeval and not affected by interstellar extinction. We used a new statistical multiband technique to select objects associated with the sequence detected in the color–magnitude diagram, and compiled a catalog of 783 probable members. Essentially, all of these objects have the colors of M stars. The selected sources are close, in projection, to ϵ Ori, but distributed in a roughly elliptical region (1° × 3°) showing spatial substructure.
- This new population, that we call the Orion Belt population, is likely the low-mass counter part to the Ori OB Ib subgroup. We found a negligible amount of bona fide young stellar objects in the Orion Belt population (less than 2% for all available youth tracers (*XMM-Newton*, KISO, and WISE surveys). This allows us to infer the minimum age of the cluster to be ~5 Myr. We estimate an age of about ~10 Myr for the OBP.
- We do not find evidence for an interaction between the selected members and the clouds, which together with the overall absence of extinction suggests that the new population lies in the foreground of Orion B. We estimate the distance to this newly identified population to be between ~250 and ~380 pc.

- Although our results do not rule out Blaauw's sequential star formation scenario for Orion, we argue that the current available evidence is shifting against it. We find, instead, that the blue stream scenario proposed in Bouy & Alves (2015) provides a better framework on which one can explain the Orion star formation region as a whole.
- We speculate that the Orion Belt population could represent the evolved counterpart of a Orion nebula-like cluster. At least high-resolution spectroscopic data would be needed to make a more solid statement about the origin of this newly identified population.

Finally, although we argue that the OBP fits the blue stream scenario best, we caution that independent work is needed to confirm the existence of the blue streams. Nevertheless, giving the tantalizing proximity and youth of the new stellar population presented in this work, there is a need for a dedicated spectral and dynamic characterization of the OBP. This population could become a benchmark region for future searches of brown dwarfs and planetary mass objects and the low-mass end of the IMF, as well circumstellar disk evolution and planet formation. The final ESA *Gaia* catalog, to be released around 2023, will include much if not all of the OBP candidates presented in this work, and will be able to shed much light on the origin of the OBP, the existence and role of the Orion blue dtream, and star formation in Orion.

References

Ahn, C. P., Alexandroff, R., Allende Prieto, C., et al. 2014, ApJS, 211, 17
Allen, L. E., & Davis, C. J. 2008, in Low Mass Star Formation in the Lynds 1641 Molecular Cloud, ed. B. Reipurth, 621
Alves, J., & Bouy, H. 2012, A&A, 547, A14
Astropy Collaboration, Robitaille, T. P., Tollerud, E. J., et al. 2013, A&A, 558, A33
Bally, J. 2008, Handbook of Star Forming Regions, Volume I: The Northern Sky, 4, 459
Blaauw, A. 1964, ARA&A, 2, 213
Boch, T., & Fernique, P. 2014, Astronomical Data Analysis Software and Systems XXIII, eds. N. Manset, & P. Forshay, ASP Conf. Ser., 485, 277
Bonnarel, F., Fernique, P., Bienayme, O., et al. 2005, A&AS, 143, 33
Bouy, H., & Alves, J. 2015, A&A, 584, A26
Bouy, H., Alves, J., Bertin, E., Sarro, L. M., & Barrado, D. 2014, A&A, 564, A12
Briceno, C. 2008, Handbook of Star Forming Regions, Volume I: The Northern Sky, 4, 838
Brown, A. G. A., de Geus, E. J., & de Zeeuw, P. T. 1994, A&A, 289, 101
Caballero, J. A. 2007, Astron. Nachr., 328, 917
Caballero, J. A. 2008, MNRAS, 383, 750
Caballero, J. A., & Solano, E. 2008, A&A, 485, 931
Cardelli, J. A., Clayton, G. C., & Mathis, J. S. 1989, ApJ, 345, 245
Chabrier, G. 2003, PASP, 115, 763
Collinder, P. 1930, Annals of the Observatory of Lund, 2, B1
Covey, K. R., Ivezić, Ž., Schlegel, D., et al. 2007, AJ, 134, 2398
Cutri, R. M., Wright, E. L., Conrow, T., et al. 2013, VizieR Online Data Catalog: II/328
Da Rio, N., Robberto, M., Soderblom, D. R., et al. 2010, ApJ, 722, 1092
de Geus, E. J., Lub, J., & van de Grift, E. 1990, A&AS, 85, 915
Downes, J. J., Briceño, C., Mateu, C., et al. 2014, MNRAS, 444, 1793
Downes, J. J., Román-Zúñiga, C., Ballesteros-Paredes, J., et al. 2015, MNRAS, 450, 3490
Elmegreen, B. G., & Lada, C. J. 1977, ApJ, 214, 725
Gieseking, F. 1983, A&A, 118, 102
Gomez, M., & Lada, C. J. 1998, AJ, 115, 1524
Guetter, H. H. 1981, AJ, 86, 1057
Gutermuth, R. A., Megeath, S. T., Myers, P. C., et al. 2009, ApJS, 184, 18
Hardie, R. H., Heiser, A. M., & Tolbert, C. R. 1964, ApJ, 140, 1472
Hernández, J., Hartmann, L., Megeath, T., et al. 2007, ApJ, 662, 1067
Hillenbrand, L. A., & Hartmann, L. W. 1998, ApJ, 492, 540
Hirota, T., Bushimata, T., Choi, Y. K., et al. 2007, PASJ, 59, 897
Jeffries, R. D., Maxted, P. F. L., Oliveira, J. M., & Naylor, T. 2006, MNRAS, 371, L6
Kroupa, P. 2001, MNRAS, 322, 231
Kroupa, P., Aarseth, S., & Hurley, J. 2001, MNRAS, 321, 699
Lada, E. A., Depoy, D. L., Evans, II, N. J., & Gatley, I. 1991, ApJ, 371, 171
Lombardi, M., Alves, J., & Lada, C. J. 2011, A&A, 535, A16
Mayne, N. J., Naylor, T., Littlefair, S. P., Saunders, E. S., & Jeffries, R. D. 2008, MNRAS, 375, 1220
Megeath, S. T., Gutermuth, R., Muzerolle, J., et al. 2012, AJ, 144, 192
Meingast, S., Alves, J., Mardones, D., et al. 2016, A&A, 587, A153
Menten, K. M., Reid, M. J., Forbrich, J., & Brunthaler, A. 2007, A&A, 474, 515
Meyer, M. R., Flaherty, K., Levine, J. L., et al. 2008, Handbook of Star Forming Regions, Volume I: The Northern Sky, 4, 662
Muench, A., Getman, K., Hillenbrand, L., & Preibisch, T. 2008, Handbook of Star Forming Regions, Volume I: The Northern Sky, 4, 483
Ochsenbein, F., Bauer, P., & Marcout, J. 2000, A&AS, 143, 23
Ochsendorf, B. B., & Tielens, A. G. G. M. 2015, A&A, 576, A2
Planck Collaboration I. 2014, A&A, 571, A1
Ribas, Á., Bouy, H., & Merín, B. 2015, A&A, 576, A52
Sandstrom, K. M., Peek, J. E. G., Bower, G. C., Bolatto, A. D., & Plambeck, R. L. 2007, ApJ, 667, 1161
Sarro, L. M., Bouy, H., Berihuete, A., et al. 2014, A&A, 563, A45
Skrutskie, M. F., Cutri, R. M., Stiening, R., et al. 2006, AJ, 131, 1163
Spezzi, L., Petr-Gotzens, M. G., Alcalá, J. M., et al. 2015, A&A, 581, A140
Straižys, V., & Lazauskaitė, R. 2009, Balt. Astron., 18, 19
Tauber, J. A., Mandolesi, N., Puget, J.-L., et al. 2010, A&A, 520, A1
Taylor, M. B. 2005, in Astronomical Data Analysis Software and Systems XIV, eds. P. Shopbell, M. Britton, & R. Ebert, ASP Conf. Ser., 347, 29
Walter, F. M., Wolk, S. J., Freyberg, M., & Schmitt, J. H. M. M. 1997, Mem. Soc. Astron. Ital., 68, 1081
Warren, Jr., W. H., & Hesser, J. E. 1977, ApJS, 34, 115
Warren, Jr., W. H., & Hesser, J. E. 1978, ApJS, 36, 497
Watson, M. G., Schröder, A. C., Fyfe, D., et al. 2009, A&A, 493, 339
Wiramihardja, S. D., Kogure, T., Yoshida, S., Ogura, K., & Nakano, M. 1994, VizieR Online Data Catalog: III/177

Appendix A: Final catalog

Table A.1 provides the photometric data for the candidate members of the Orion Belt population; it contains the name of each star, right ascension and declination, *girz* and *JHK*$_s$ band magnitudes from the SDSS and 2MASS catalogs with their associated uncertainties. This table is available in its entirety at the CDS. A portion is shown here for guidance regarding its form and content.

Table A.1. Final catalog.

| ID	RA (J2000)	Dec (J2000)	g (mag)	i (mag)	r (mag)	z (mag)	J (mag)	H (mag)	K_S (mag)	Prob. (%)
1	83.928031	−4.0978	20.132 ± 0.019	16.709 ± 0.0060	18.624 ± 0.01	15.673 ± 0.0070	13.979 ± 0.035	13.359 ± 0.043	13.072 ± 0.03	99.9
2	83.949248	1.887384	18.378 ± 0.0070	15.415 ± 0.0050	16.873 ± 0.0060	14.628 ± 0.0050	13.205 ± 0.027	12.595 ± 0.026	12.323 ± 0.023	99.9
3	82.444109	1.523527	16.621 ± 0.0040	14.383 ± 0.0040	15.225 ± 0.0030	13.859 ± 0.0040	12.481 ± 0.024	11.827 ± 0.024	11.611 ± 0.021	99.8
4	83.125498	−3.991311	17.657 ± 0.0060	14.701 ± 0.0050	16.195 ± 0.0050	13.857 ± 0.0050	12.405 ± 0.033	11.835 ± 0.03	11.548 ± 0.024	99.9
5	83.126417	−3.990177	20.353 ± 0.023	16.903 ± 0.0060	18.806 ± 0.011	15.816 ± 0.0070	14.207 ± 0.044	13.577 ± 0.046	13.29 ± 0.051	99.9
...	...	...	...	...	...	...	...	...	...	...
779	83.738131	−0.802611	16.332 ± 0.0040	14.062 ± 0.0040	14.919 ± 0.0040	13.534 ± 0.0040	12.207 ± 0.022	11.478 ± 0.03	11.3 ± 0.023	99.95
780	84.089487	−1.031828	19.386 ± 0.013	16.321 ± 0.0050	17.952 ± 0.0070	15.358 ± 0.0050	13.823 ± 0.024	13.253 ± 0.037	12.996 ± 0.03	100.0
781	83.70118	−1.146224	18.743 ± 0.0090	15.836 ± 0.0040	17.316 ± 0.0050	15.049 ± 0.0050	13.57 ± 0.039	12.979 ± 0.044	12.684 ± 0.039	99.8
782	83.826168	−1.014437	18.465 ± 0.0080	15.595 ± 0.0040	16.992 ± 0.0050	14.811 ± 0.0050	13.35 ± 0.026	12.623 ± 0.032	12.41 ± 0.026	100.0
783	83.856769	−1.048855	18.014 ± 0.0070	14.921 ± 0.0040	16.602 ± 0.0050	14.01 ± 0.0040	12.45 ± 0.024	11.839 ± 0.033	11.526 ± 0.019	99.9

Appendix B: Additional figures
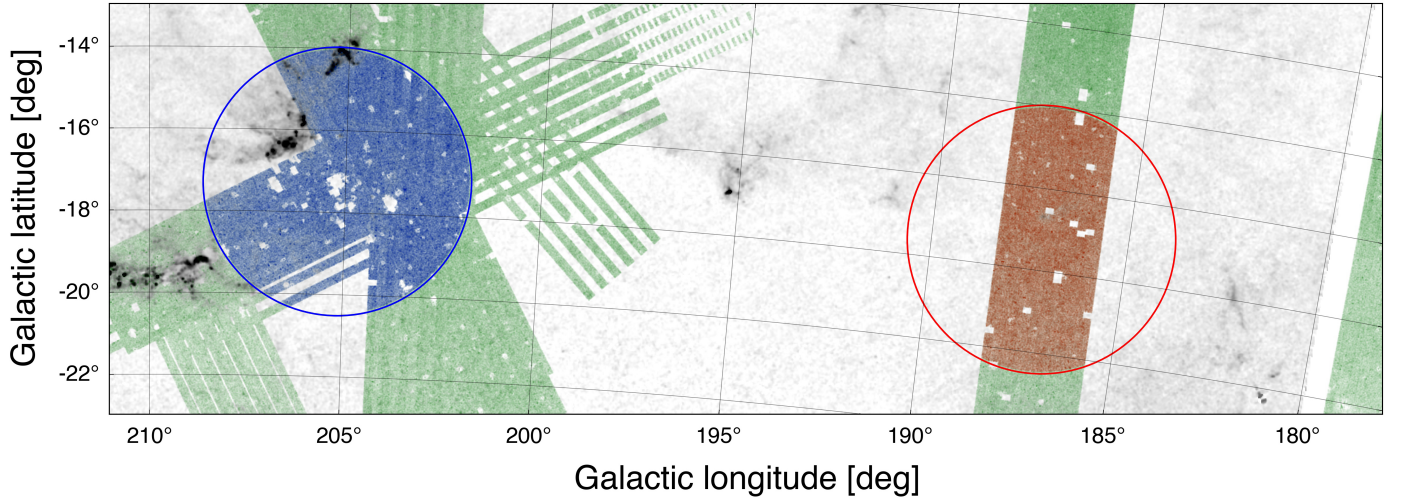
Fig. B.1. Science (blue) and control (red) fields plotted over the NICER dust extinction map by Lombardi et al. (2011). Green represents the coverage of SDSS catalog. We note the areas without data, in particular around the Orion Belt bright stars.
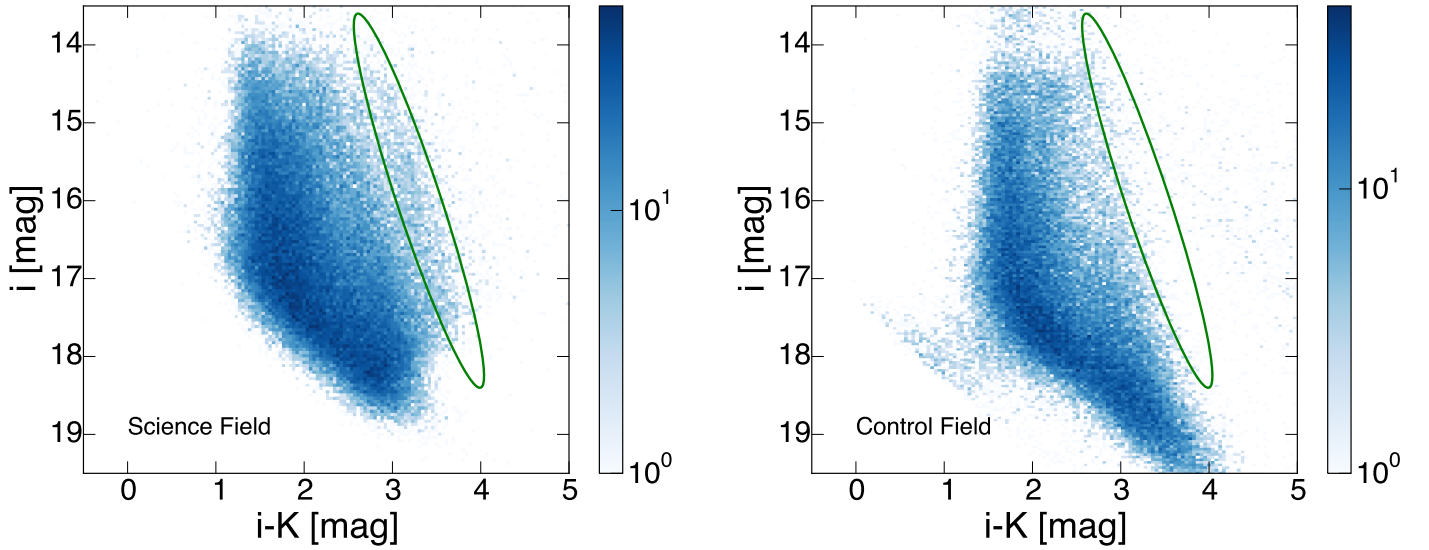

Fig. B.2. $(i, i - K_s)$ color–magnitude diagrams for all objects with 2MASS K_s and SDSS i-band photometry. *Left*: sources in a 3° radius region centered on the B0 Ib star, ϵ Orionis (the central star of Orion's Belt). *Right*: sources in the CF. The green ellipse plotted in each panel indicates the approximate position of the sequence in the science field.
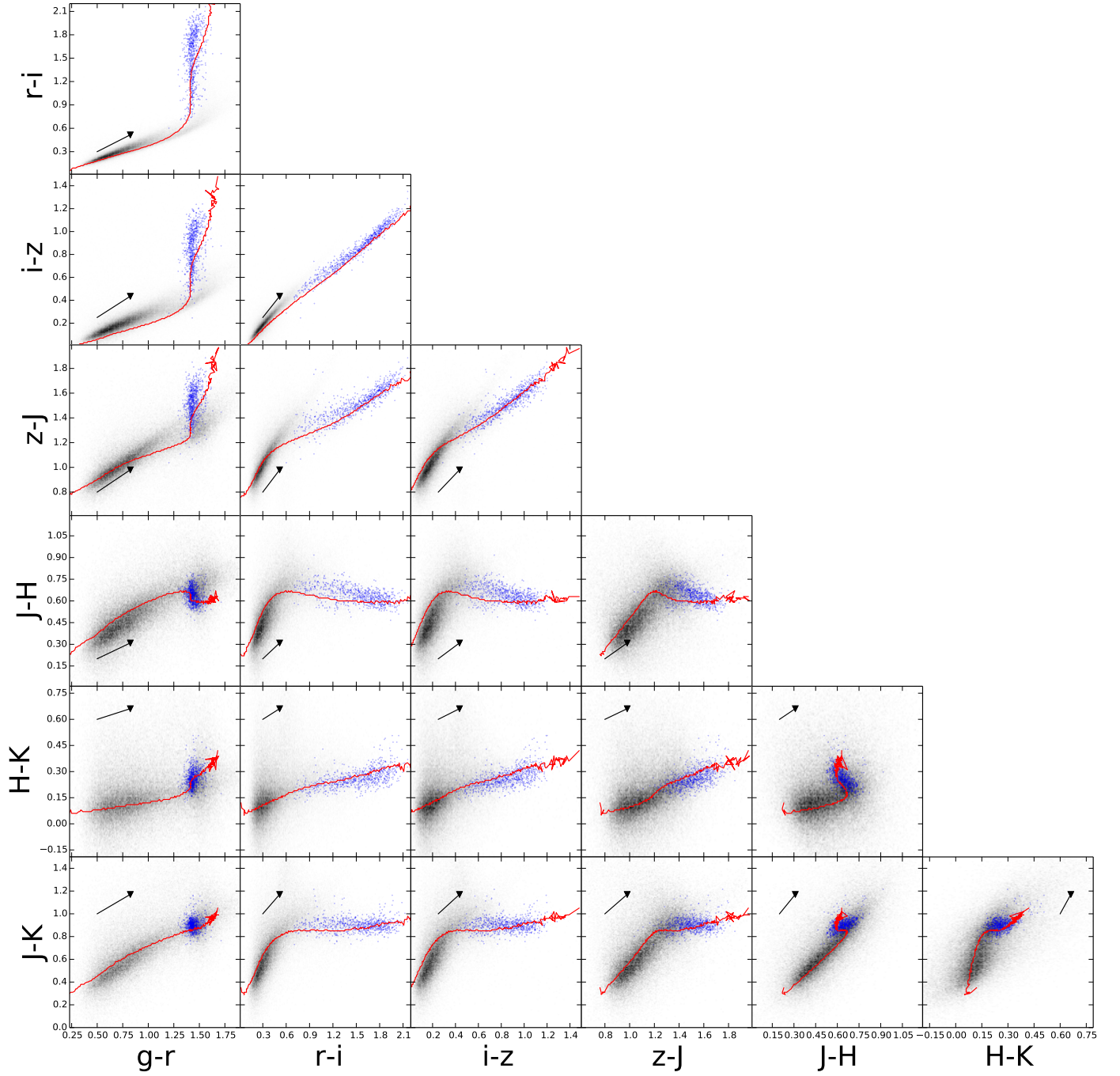
Fig. B.3. SDSS/2MASS color–color summarizing the photometric properties of the selected candidates (blue dots) compared to field sources (black dots). The color–color space of the selected sample coincides with that of unreddened M dwarfs. Also shown for each color–color space are the reddening vector for $A_V = 1$ mag (black solid line) (Cardelli et al. 1989) and the main sequence (red dashed line) from Covey et al. (2007).
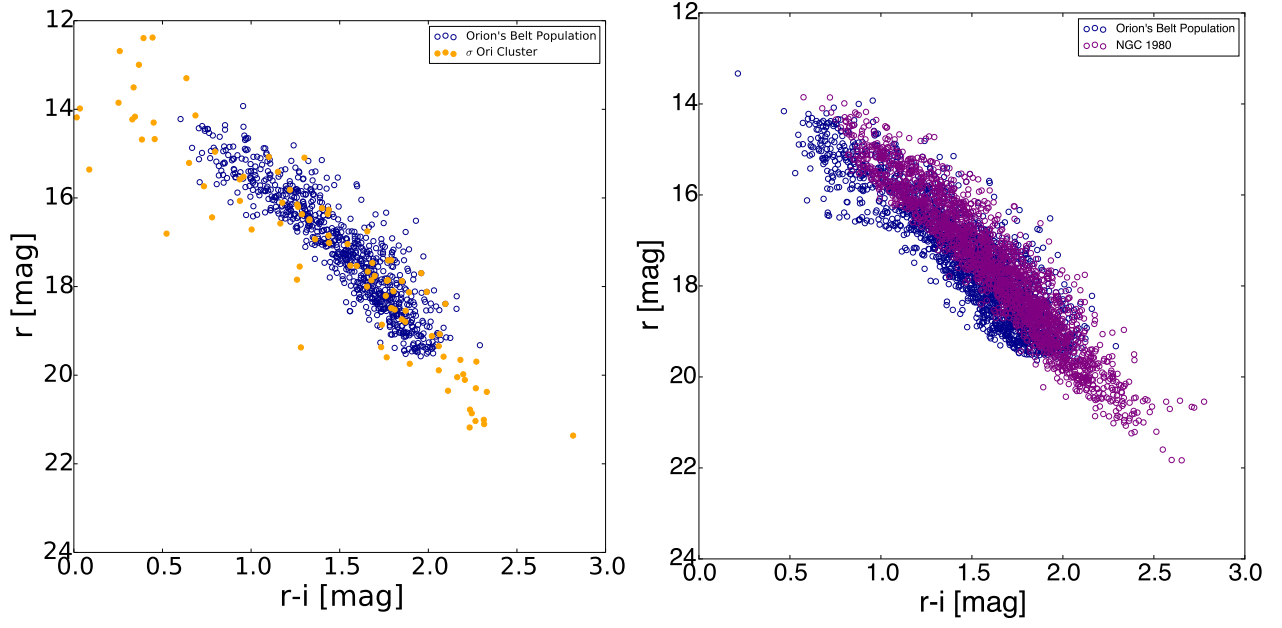
Fig. B.4. *r* vs. *r* − *i* color magnitude diagram for the OPB (blue circles) and σ Orionis (orange circles) or NGC 1980 members (violet circles).

<div align="right">

4

</div>

Distance, structure, and SED modeling of Orion Belt Population

4.1 Overview

In this manuscript, I present the revisited census and analysis of the spectral energy distributions (SED) of all candidate sources from the OBP. I present the results of *Gaia* DR2 data application in the attempt to resolve the 3D structure of the Orion Belt Population. The manuscript presents the analysis of distances, proper motions, and photometry followed by the discussion of results. *Gaia* DR 2 data has been used to remove remaining contamination from the initially selected members, to estimate the distance and physical size of the population but also confirmed sub-structuring reported in the first publication.

To analyze the nature of the sources, the SEDs has been constructed for all members in the selected field using available archival data over a broad spectral range. The main body of the paper focuses on describing the application of new models by Robitaille (2017) and the results obtained. These models can be used to determine specific parameters for a given young star, such as the properties of the central source, the inner and outer radius of the disk, the amount of flaring or dust settling, and more generally any parameter which may affect the SED.

The full set of SED is presented here after the main body of the article and will be available online after publishing the paper.

Building the SED for each source allows to compare the evolutionary status of each source and the properties of their circumstellar disks by directly comparing their SEDs, evaluate disk evolution and morphology, infer about the role played by this region in the complex three-dimensional structure of the Orion Complex, to understand whether star formation has occurred in a sequential way originally proposed by Blaauw, or in a more stochastic manner, where star formation started independently in each subregion.

4.2 Publication details

Title: The Orion Belt Population in Gaia DR2

Subtitle: Distance, structure, and SED modeling

Authors: K. Kubiak, P. S. Teixeira, R. Köhler, J. Alves, O. Czoske, T. Robitaille

Status: The manuscript has been submitted to A&A, in the refereeing process.

Own contributions: Literature research, auxiliary data gathering, data analysis, preparation of data and application of SED fitter, analysis of the results, preparation of figures and plots, paper writing.

The Orion Belt Population in Gaia DR2

Distance, structure, and SED modeling

K. Kubiak[1], P. S. Teixeira[2], R. Köhler[3, 1], J. Alves[1], O. Czoske[1], and T. Robitaille

[1] Department of Astrophysics, University of Vienna, Türkenschanzstrasse 17, A-1180 Vienna
e-mail: `karolina.kubiak@gmail.com`
[2] Scottish Universities Physics Alliance (SUPA), School of Physics and Astronomy, University of St. Andrews, North Haugh, St. Andrews, Fife KY16 9SS, UK
[3] Sterrewacht Leiden, P.O. Box 9513, NL-2300 RA Leiden, The Netherlands

December 14, 2018

ABSTRACT

Context. In a previous work, Kubiak et al. (2017) studied a field around the supergiant ϵ Ori using the SDSS and 2MASS point source catalogs. A colour-magnitude analysis of the point sources resulted in the identification of a sample of 797 Orion Belt Population (OBP) candidates. *Gaia* DR2 data allows us to remove the remaining contamination from unrelated sources and estimate a distance to this population.
Aims. We aimed to estimate and analyze the distance, structure, and physical properties of the infrared counterparts of these sources by comparing their spectral energy distributions (SED) with those predicted by radiative transfer accretion models of YSOs.
Methods. The *Gaia* DR2 data has been used to obtain distances and investigate the structure of the OBP. The atlas of SEDs of 664 OBP sources is constructed, from the optical to far-infrared wavelengths. A Python-based SED fitting tool that uses 3D radiative transfer code models of YSOs is employed to fit the observed SED and derive various physical parameters. We adopted a Monte Carlo method to estimate the influence of photometric errors on the fitting results.
Results. The Gaia DR2 data revealed different distances for the previously identified peaks in the stellar density maps. We find that the OBP extends for about 60 pc along the line-of-sight, comparable to its width, and is not homogeneously distributed in space. The SED fitting procedure to the observed data favours pre-main-sequence stars of low effective temperatures and disks. We find that 95% of the OBP population studied here (mostly M-stars) can be fitted with models of low-mass passive disks.

Key words. stars: formation, stars: evolution, infrared: stars

1. Introduction

The Orion Belt population (OBP, Kubiak et al. 2017) is a newly described young, rich, and massive population of stars in the vicinity of the supergiant ϵ Ori at $(l, b) = (205°21, -17°24)$. It has been defined based on the multi-dimensional analysis of color-magnitude diagrams. The new population, the OBP, is likely the low-mass counterpart of Blaauw's Ori OB Ib subgroup (Blaauw 1964). Photometry alone constrains poorly the distance to this population or its line-of-sight extent, and with photometry only, the population was estimated to be as far as $\sim$380 pc (but in front of the Orion B cloud) or as close as 250 pc. In the closer case, the OBP could be the low-mass counterpart to the well-known Orion supergiants at distances around 250 pc. A recent study (Zari et al. 2017) based on the *Gaia* TGAS data release gives the median parallax values for this region to be $\varpi = 2.76^{+0.33}_{-0.35}$ mas ($d \sim 362$ pc). The *Gaia* Data Release 2 (DR2) was made public on 25 April 2018, provides precise parallax measurements to 715 stars from OBP (see Sec. 2.1 for details of our analysis of new data). The overlapping region has been studied spectroscopically by Kounkel et al. (2018) and by Briceno et al. (2018). Unfortunately their target tables are not yet available in either SIMBAD, Vizier or the CDS data services, so we could not cross match their list with our sample.

In this paper, we extend the analysis from Kubiak et al. (2017) to obtain more quantitative results by complementing previously obtained data with other bands and by modelling the spectral energy distributions (SED) of the infrared counterparts of young stellar objects (YSO). The colors and spectral index analysis presented the general nature of the point sources. By constructing and analyzing a wide SED, it is possible to quantify several physical parameters and also constrain their evolutionary stage (Allard et al. 2012). Such an analysis, however, requires not only a good coverage of the wavelength range but also high spatial resolution data to ensure that the fluxes we are studying arise mainly from the star-disk system and are not contaminated by their surroundings. For this purpose, using the infrared surveys such as 2MASS, All-WISE, IRAS and several optical surveys from the literature, we assembled the best data available for a sample of bonafide IR counterparts of OBP candidates and construct their SED to the best possible extent. With this analysis, we expect to be sensitive to the presence of disks in the OBP sample and make a first rough estimate of their masses.

Recently, there has been significant improvement in radiative transfer modelling of the SEDs of YSOs, based on the physics of star formation that we have learned in the past few decades. An SED fitting tool has been successfully developed and tested on the SED of low mass young stellar objects by Robitaille et al. (2007). This tool uses a grid of 2D radiative transfer models of YSOs (Robitaille et al. 2006) that was developed by Whitney et al. (2003). These models successfully estimate the physical parameters and consistently explain the SED of low mass YSOs.

To the best of our knowledge these are the only publicly available models that include disks. In this work, we made use of recently published new sets of precomputed grids of models (Robitaille 2017). These models include significant improvements on the previous generation of published models: in particular, the new models cover a much wider and more uniform region of parameter space, do not include highly model-dependent parameters and include a number of improvements that make them more suited to modelling far-infrared and sub-mm observations of forming stars. In this paper, this fitting tool are applied to the SED of our bona fide OBP candidates and the resulting parameters are analyzed in an attempt to understand the nature of the OBP and also to assess the reliability of the assumed physics.

This paper is organized as follows. In Sect. 2 we describe the data used to build the SED of the OBP candidates, and discuss the aspects of the SED fitting tool pertinent to this analysis. In Sect. 3 the modelling procedure is described. In Sect. 4 and 5 the results are presented and in Sect. 6 we discuss the caveats of the data and the methods to identify unbiased results and we summarize.

2. Data selection

As described in Kubiak et al. (2017), we used two catalogs to identify probable candidates of the OBP. We retrieved and cross-matched all the sources located within a radius of 3° around ϵ Ori at (l, b) = (205°21, -17°24) from the Two Micron All-Sky Survey (2MASS, Skrutskie et al. 2006) and the Sloan Digital Sky Survey (SDSS, Ahn et al. 2014) DR12 catalogs.

2.1. Gaia DR2

Our previous study did not allow us to discuss the distance to OBP in detail. Based on negligible extinction to the population we were able to infer that is has to lie in front of molecular clouds (~380 pc, Ochsendorf & Tielens (2015)). None of the members of OBP was part of the TGAS catalog, therefore we had to wait for *Gaia* DR2 to study the distance of the population in detail. We crossmatched all the sources from *Gaia* DR2 within our field of interest with the known members of OBP. *Gaia* DR2 contains parallax measurements with errors for 715 sources. The probability density function of parallax is presented in Fig. 1. The peak of the distribution corresponds to ϖ = 2.86 mas.

The small peak at $100 - 150$ pc in the lower panel of Fig. 1 is caused by foreground contamination. These foreground stars are also easily identified in the colour-magnitude diagram based on *Gaia* photometry (Fig. 2). In this Figure, stars with distances less than 300 pc are marked by red dots, those between 300 and 390 pc by blue dots, and stars with distances larger than 390 pc by green dots. The subsample of foreground stars contains 133 objects. We do not detect any spatial correlation for these foreground objects, and we assume here that they are unrelated to the OBP, and as such, have been removed from our OBP catalog.

The "bimodal" shape of the main peak of the distance histogram (lower panel of Fig. 1) and the small bump on the left side of the parallax distribution (upper panel) suggests that the OBP is a mixture of two stellar populations located at different distances. Still, there is not a clear separation of these populations in the colour-magnitude diagram (green and blue dots in Fig. 2). In Fig. 4 we present the spatial distribution of these two OBP, near and far, subsamples. The overdensity of green dots (farther sources, d > 390 pc) centered at 205°2, -18°2 corresponds to the position of peak D from Table 2 and Fig. 3 in Kubiak et al.
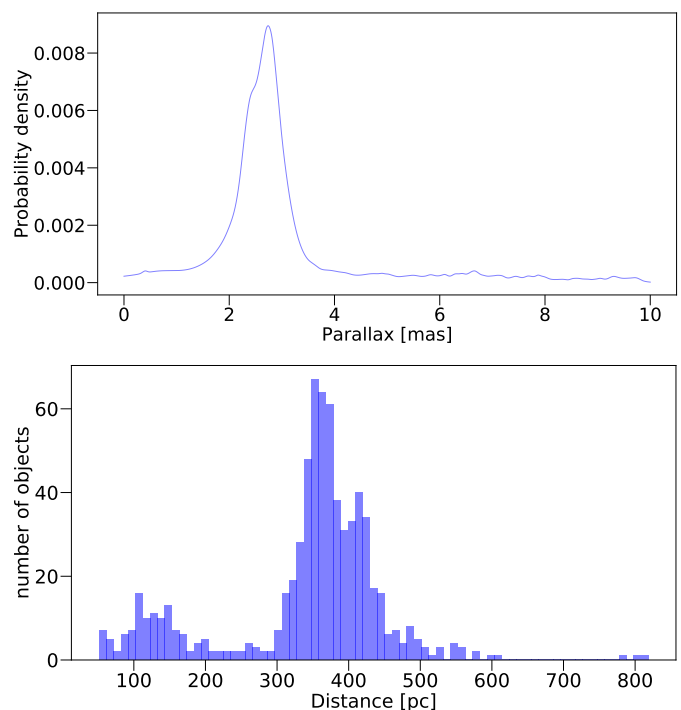

Fig. 1: *Upper panel:* Probability density function of *Gaia* DR2 parallaxes for the Orion Belt population members selected in Kubiak et al. (2017). *Lower panel:* Corresponding histogram of distances. The first peak on the left is due to contamination from foreground stars.
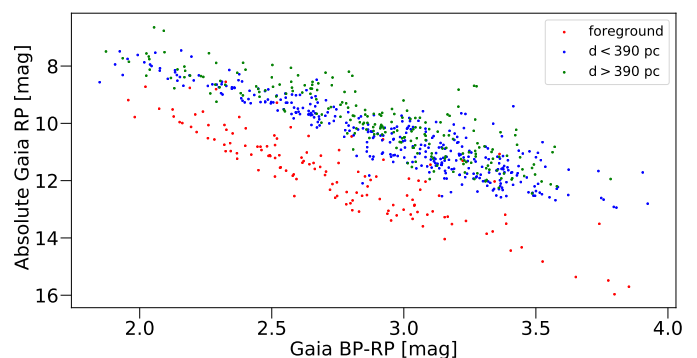

Fig. 2: Colour magnitude diagram of the OBP sources cross matched with *Gaia* DR2. Blue and red dots indicate sources with distances smaller and greater than 300 pc, respectively.

(2017). This has been also recently reported in Briceno et al. (2018). Both groups seems to have different spatial motions. The proper motions measured by *Gaia* for the OBP members are presented in Fig. 3 (crosses indicate the measurement errors). It appears as if the near sample is moving together towards the projected direction of the Orion clouds, whereas the proper motions of the far sample are distributed around zero, although a proper modeling of the space motion of these two populations, beyond the scope of this paper, is needed to rule out that we are not simply seeing a projection effect.

We do not find a clear case for two distinct OBP populations from the absolute color-magnitude diagrams (Fig. 2), as there is
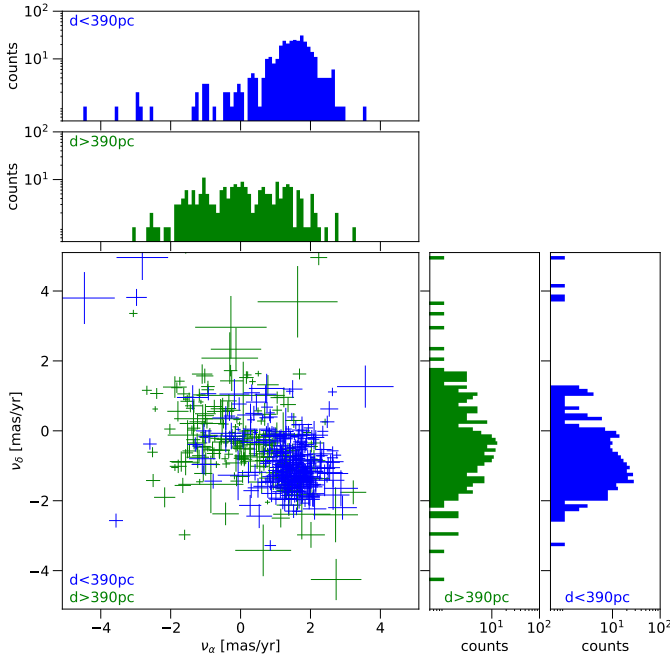
Fig. 3: The distribution of proper motions measured by *Gaia* . The color coding is the same as on Fig. 2

no clear separation between the green and blue dots. There a hint that the far sample (green) lies slightly above the near sample (blue). We investigated this by fitting regression lines to both samples with the following result:

$$G_{RP} = (2.73 \pm 0.11) \cdot (G_{BP} - G_{BP}) + (2.06 \pm 0.32)$$

for the far sources, and

$$G_{RP} = (2.74 \pm 0.11) \cdot (G_{BP} - G_{BP}) + (2.45 \pm 0.22)$$

for the near sources. The magnitude difference between the fits is 0.39 ± 0.39, which, while suggesting that the far populations is younger than the near sample, it is not a statistically significant result. A two-dimensional KS test on two samples run on color-magnitude distributions for nearer and far subsample also suggests no significant difference between the two samples. This is not surprising, since the initial selection of OBP members was based on their proximity on various color-magnitude and color-color diagrams (see Kubiak et al. 2017). Somewhat confusingly, the t-test shows that the average (expected) value of absolute magnitudes differs significantly for both samples.

Still, the far population, on average, seems to be slightly brighter than the near population, 9.76 and 10.50 mag, respectively. For the populations to differ in brightness and the distance as observed, a difference in age is required, in the sense tht the far sample is younger than the near sample. Making use of evolutionary tracks by Siess et al. (2000), assuming the M2 as a representative spectral type for our sample, we measured the age distance needed to reproduce the change in the brightness in V band at the level of 0.39 mag. Based on this exercise we estimate an age difference of 4 Myrs between both samples.

Alternatively, the existence of the second brighter sequence on the color-magnitude can be explained as an intrinsic spread in size of the sequence itself. A few physical effects can contribute to that, namely, 1) binarity, 2) variability, and 3) the intrinsic spread in age and distance of the sample itself.

Regarding 1), the OBP members are low mass M stars and the canonical binarity fraction for M stars is 33.5% (Duchêne & Kraus 2013). Since the census of OBP members contains 664 stars after removing the foreground population (d<300pc),

$$664 \times 0.33 \pm 0.05 = 219 \pm 33$$

The far population contains 221 stars. Simulations of the σ Ori populations done by Sherry (2003) suggest that binaries shift the center of the sequence to a position only slightly brighter ($\Delta V = 0.36$ mag) and redder than the center of the sequence for single stars. We tried to address the possibility of unresolved binarity influencing the Gaia DR2 results (distances and parallaxes) by analyzing the *astrometricExcessNoise* and *astrometricExcessNoiseSig* distributions in both far and near populations. We also investigate the behaviour of the *unit weight error* (Lindegren et al. 2018) and we find sources in both far and near population deviate from the standard five parameters astrometric model in a similar manner.

Concerning 2), the weak T Tauri stars vary with typical amplitudes of 0.05 to 0.6 mag in the V band (Herbst et al. 1994). By an age of a few Myr, most low-mass stars are WTTSs. We inspected the variability of sources in our sample, and we present the results in a forthcoming paper (Kubiak et al. 2019 in prep., Variability of the OBP)

Refering to 3), it has been investigated in an extend manner by Reggiani et al. (2011), Da Rio et al. (2010) where they analyse the distribution of stellar ages in the Orion nebula cluster (ONC). They point out that reliability of age measurements and the ability to detect possible age spreads in the young stellar population are fundamentally limited by several factors. Simulations presented by Preibisch (2012) shows that the observational uncertainties produce an almost uniform distribution of simulated stars, which mimics a large apparent age spread in this actual co-eval population. This shows that any age estimates for low-mass YSOs derived from a CMD suffer from substantial uncertainties. Age spreads can only be detected in a CMD if they are several times larger than the true age. The population of stars with identical ages of a few Myr may be wrongly interpreted to have an age spread of up to 10 Myr if the isochronal ages are assumed to be identical to the true ages.

For the understanding of the star formation process it would be very important to distinguish between a scenario of a slow continuous star formation process (that would produce a large age spread in a single stellar population) and the alternative scenario of a temporal sequence of individual short star formation episodes (where the individual populations can have age differences of several Myr but small internal age spreads).

Finally, a strong argument in favour of the two population scenario is the previously described *clustering* of the far sample at $(l, b) = (205°21, -17°24)$. Such a clustering of binary or variable stars is hard to explain if we drop the two population scenario.

In summary, we cannot clearly say that the two samples correspond to two sequences in the color-magnitude diagram with different ages, nor can we say unequivocally that what we are observing is an intrinsic spread of the pre-main sequence locus. We leave the question whether the second sequence exists and represents a younger population as an open one, hopefully, to be answered by the future releases of Gaia data. In the rest of the paper we do not split the OBP into two sub-populations but keep the OBP as one sample. The distance information to every source will be nevertheless used as an input parameter for SED modeling (see Sec.3). The OBP sample median distance is 357 pc, while the mean is 345 pc, so we adopt a distance of
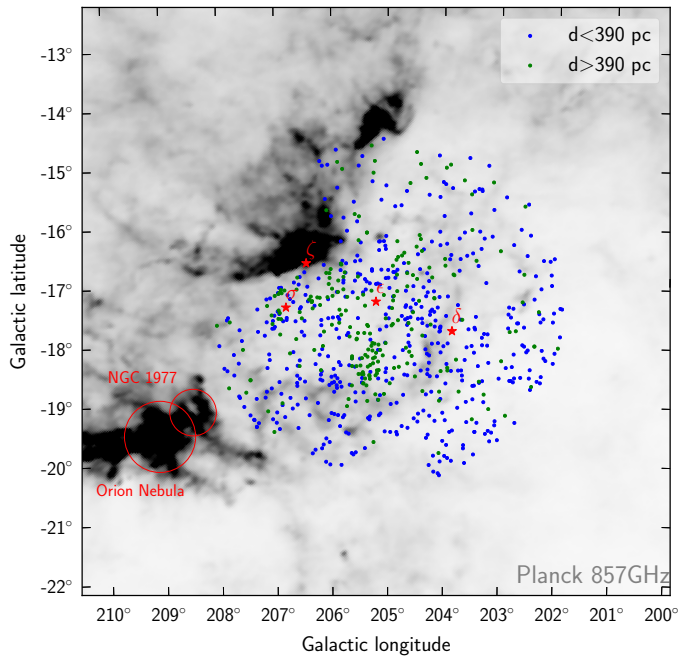
Fig. 4: The Orion Belt region as seen by Planck 857 GHz. The Orion Belt population members with distances smaller than 390 pc (blue dots) and larger (green dots). Asterisks denote the positions of the three Orion's Belt Stars and σ Orionis.

350 pc for all stars where no measurement is available (also if parallax values are negative in DR2 catalog).

2.2. Auxiliary photometry

The first step to produce the SED catalog is to extend the set of photometric measurements. For the whole region, we collected from archives available data covering a wide spectral range from sub/millimeter to X-ray surveys. In an effort to compile a complete dataset in terms of spatial and wavelength coverage, we then collected complementary photometry from other surveys. To achieve this we went through all available surveys that cover even partially the science field of Kubiak et al. (2017). Cross-matching between source lists was done via TopCat with 1.0 arc-sec positional uncertainty to keep the input catalog from Kubiak et al. (2017) as primary and to keep all sources from it. The full list of data obtained is presented in Table 1, where we provide an overview of the photometry used for this investigation. The first four columns give the name, wavelength band names, time frame and references for each survey. Column 5 gives short notes about the coverage. Column 6 presents the number of sources in the science field whilst column 7 gives the number of sources common with the OBP in each catalog.

2.2.1. Data points and upper limits

The SED fitting tool developed by Robitaille et al. (2007) was used to fit the data with a grid of YSO models presented by Robitaille (2017). This tool requires at least three wavelength points to fit the SED and any number of fluxes that can represent upper limits. The constraint on a data point is that the photometry extracted within a defined aperture must by all criteria represent a single source, with measured fluxes and associated errors.

2.2.2. Conversion from magnitudes to flux densities.

Since we obtained most measurements in magnitudes we need to convert them into flux densities corresponding to the multiwavelength photometry, according to the following equation:

$$F_\lambda = 10^{-0.4m} \cdot F_{\lambda,0}, \qquad (1)$$

where $F_{\lambda,0}$ is the flux density zeropoint for the wavelength λ, and m is the corresponding apparent magnitude. The flux density zeropoint values used are summarized in Table 2. The error of the flux density, σ_F, is given by

$$\sigma_{F_\lambda} = \sqrt{F_\lambda^2 \ln^2(10^{0.4\sigma_m}) + 10^{-0.8m}\sigma_{F_{\lambda,0}}^2}, \qquad (2)$$

where σ_m is the error associated with the magnitude and $\sigma_{F_{\lambda,0}}$ is the zero point uncertainty.

Before converting SDSS brightness into flux measurement we first follow the description of the conversion from the SDSS webpage manual, where the offset between SDSS and AB photometry systems has been discussed in detail and where corrections for u and z bands have been estimated. We followed the formulas presented there, namely: $u_{AB} = u_{SDSS} - 0.04$ mag and $z_{AB} = Z_{SDSS} + 0.02$mag. We did not find any information about the inconsistency between photometry systems in any other of the investigated surveys.

Table 2 gives filter names, effective wavelength, and flux density zero points in the appropriate photometric system. Flux densities are given in Jy. All values are taken from the SVO Filter Profile Service (Rodrigo et al. 2012) to keep consistency, appropriate references can be found therein. Unfortunately, no information about the Zero Point accuracy is provided by SVO. We were not able to obtain zero-point accuracy values for many of the used filters, despite intense work done during the literature research. In cases where we were not able to find the zero-point accuracy in the literature, it was calculated as 2% of the flux density zero points if not stated differently in the footnote. We decided on the value 2% after careful studies of zero-point accuracy for the other available bands. In Fig. 5 with red dots we present the distribution of zero-point uncertainties for each band where we were able to find this piece of information in the literature. As one can easily see, the largest uncertainty is for H-band, reaching almost 2%. We decided to use this value as an uncertainty for zero point values for rest of the photometric bands in our survey (blue dots in Fig. 5).
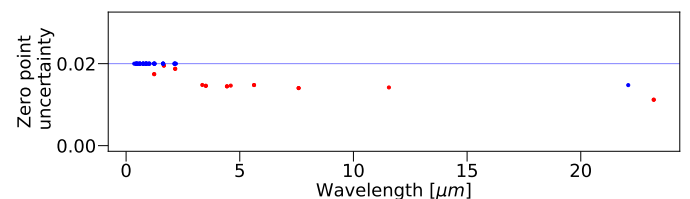

Fig. 5: Fractional error of the zero point values for each band used in this work. Red dots indicate the values from literature (see Table 2), the blue ones have been assumed at level of 2%.

3. SED fitting analysis

3.1. Models selection

For the purpose of this work we used newly published sets of models (Robitaille 2017). The new models were not computed

Table 1: Catalogs and observations used in this study.

Catalogue Mission Survey	Wavelengths covered (bands)	Date(s) of observations	Reference paper(s)	Notes on coverage area	Field common	OBP common
SDSS	u,g,r,i,z	2000–2017	Ahn et al. (2014)	not uniform	189620	797
2MASS	J,H,Ks	1997–2001	Skrutskie et al. (2006)	full	107423	790
AllWISE	W1,W2,W3,W4	2010–2011	Cutri et al. (2013)	full	1167778	771
DENIS	I,J,K	1996–2001	DENIS Consortium (2005)	Strips - missing	110409	652
UKIDSS	H,J,K,Y,Z	2005–2012	Lawrence (2013)	Dec< −2 deg	37318	220
APASS	Johnson B,V Sloan g',r',u',z' and Y	2010–2015	Henden et al. (2016)	full not for all stars	15649	132
Pan-STARRS	g,r,w,i,y	2001–2014	Magnier et al. (2016)	full	186755	784
VISTA	J,H,K,Z,Y	2009	Peña Ramírez et al. (2012)	single sources	44	21
	J,H,K	2009	Spezzi et al. (2015)	cluster	13	1
	J,H,K	2012–2013	Meingast et al. (2016)	Orion A	7287	32
SPITZER	IRAC3.6,IRAC4.5,IRAC5.8 IRAC5.8, IRAC8.0, MIPS24	2004–2009	Megeath et al. (2012)	Orion A	20	1
AKARI	IRC, FIS	2006–2011	Murakami et al. (2007)		2	
XMM-Newton	0.2-12 keV	2000–2007	Watson et al. (2009)	selected fields	572	42
KISO	H_α INT	1993	Wiramihardja et al. (1994)		19	1

Table 2: Photometry filters details.

Survey	Band name	Effective wavelength [Å]	Adopted apertures[1] [arcsec]	Data format flag[1]	Photometric system	Zero Point [Jy]	Zero Point accuracy [Jy]
SDSS	u	3595	10	3	AB	3631	72.6
	g	4640	10	1	AB	3631	72.6
	r	6122	10	1	AB	3631	72.6
	i	7440	10	1	AB	3631	72.6
	z	8897	10	1	AB	3631	72.6
2MASS	J	12350	3	1	Vega	1594	27.8[2]
	H	16620	3	1	Vega	1024	20.0[2]
	K	21590	3	1	Vega	666.8	12.5[2]
UKIDSS	Z	8815	2	1	Vega	2261.4	45.2
	Y	10289	2	1	Vega	2057.2	41.1
	J	12444	2	1	Vega	1556.8	31.1
	H	16221	2	1	Vega	1038.3	20.8
	K	21900	2	1	Vega	644.1	12.9
AllWISE	W1	33526	8.25	1	Vega	309.5	4.6
	W2	46028	8.25	1	Vega	171.8	2.5
	W3	115608	8.25	1	Vega	31.7	0.5
	W4	220883	16.5	1	Vega	8.4	0.1
DENIS	I	7862	7	1	Vega	2442.2	48.8
	J	12211	7	1	Vega	1588.3	31.8
	K	21465	7	1	Vega	667.4	13.3
APASS	V	5394	10	1	Vega	3998.3	80.0
	B	4297	10	1	Vega	3624.1	72.5
	g	4640	10	1	AB	10	0.2
	r	6122	10	1	AB	10	0.2
	i	7440	10	1	AB	10	0.2
Pan-STARRS	g	4776	6.5	1	AB	3631	72.6
	r	6130	6.5	1	AB	3631	72.6
	i	7485	6.5	1	AB	3631	72.6
	z	8658	6.5	1	AB	3631	72.6
	y	9603	6.5	1	AB	3631	72.6
VISTA	J	12464	5	1	Vega	1554	31.1
	H	16310	5	1	Vega	1030.4	20.6
	K	21337	5	1	Vega	674.8	13.5
	Z	8762	5	1	Vega	2263.8	45.3
	Y	10184	5	1	Vega	2087.3	41.7
SPITZER	IRAC1	35075	3	1	Vega	280.9	4.1[3]
	IRAC2	44366	3	1	Vega	179.7	2.6[3]
	IRAC3	56281	3	1	Vega	115	1.7[3]
	IRAC4	75892	3	1	Vega	64.1	0.9[3]
	MIPS24	232096	20	1	Vega	7.1	0.1[4]

[1] The flag and aperture size for each flux is a required parameter for the SED fitter; a detailed description can be found in the documentation.
[2] The values were taken from Cohen et al. (2003b).
[3] The values were taken from the Spitzer IRAC Data Handbook V.3.0 (http://ssc.spitzer.caltech.edu/irac/dh/).
[4] The values weretaken from the MIPS Data Handbook V.3.2.1 (http://ssc.spitzer.caltech.edu/mips/dh/).

in a single monolithic set, but rather as several sets of models with increasing complexity. For instance, one of the sets consists of models with only a star with a surrounding disk, another set includes a disk and an envelope, but no bipolar cavities, and yet another set includes a disk, envelope, and bipolar cavities. This modularity allows users to ask which model is the best represen-

tation of the data, before even looking at the actual values of the parameters. The full package consists of 18 sets and is fully described in Robitaille (2017). To save computing time, it is useful to lower the number of used sets to only those that seem to be the most appropriate. In order to do that it is useful to get a first impression about the nature of the observed sources. This can reasonably easily be done by calculating the so-called spectral index for each source and adopt the widely used YSO classification scheme based on it. The spectral index (α) has been defined in Lada & Wilking (1984) and Lada (1987) as:

$$\alpha = \frac{d \log(\lambda F_\lambda)}{d \log(\lambda)} \tag{3}$$

Lada & Wilking (1984) used the spectral index calculated between near- and mid-infrared bands to classify YSOs into three distinct classes (Class I – III). The original classification scheme has been widely used in the community and many times modified (in terms of used bandwidth, borders between, and/or number of distinctive classes). Although this empirical classification scheme is discrete, the evolutionary change between the different stages is continuous. Therefore, it is not straightforward to observationally classify sources that are transiting from one stage to another.

We calculated the slopes using wavelengths longer than K_S-band. For each source, we calculated the slopes including W4 (slope Ks-W4). In Fig. 6 we present an example of the spectral energy distribution between optical and mid-infrared (using the source nomenclature from Kubiak et al. 2017). We calculated the slopes based on flux measurements from Ks, W1, W2, W3, and W4. We used the python polyfit routine from the numpy package, taking photometric errors into account. Visual inspection of the plots with slopes did not reveal any issues or inconsistencies. Unfortunately, not all sources from OBP selected candidates have full sets of the data that has been used for slope calculation (only 771 sources have measurements in all 5 bands, which is due to missing AllWISE photometry). For our purpose we used the classification scheme from Teixeira et al. (2012), presented here in Table 3.
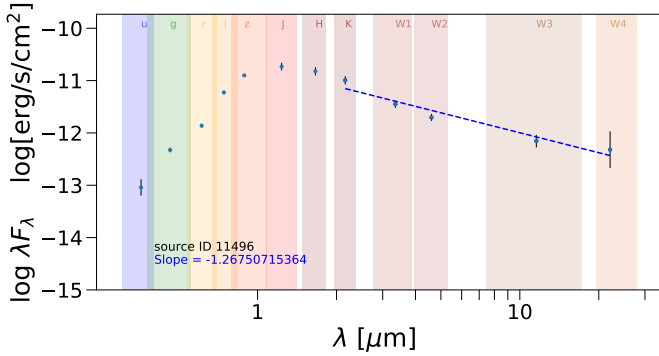
Fig. 6: An example of SED for the source No. 11496.

In Fig. 7 we present the distribution of SED slopes among the sources selected as highly probable members of the Orion Belt Population for which we have photometry in Ks (2MASS), W1–4 (AllWISE) bands. We present the slopes calculated from Ks to W4 bands.

It is clearly visible that the vast majority of sources exhibit the SED slopes of anemic and thick disk sources. In Table 3 we present the amount of sources in each Class. Based on this rough

Table 3: Source classification scheme using $\alpha_{K_S-\text{WISE}}$ adopted from Teixeira et al. (2012)

Source classification	α_{K_S-W4} value	Amount
Class I (C I) sources	$\alpha_{K_S-W4} \geq 0.5$	0
Flat spectrum (FS) sources	$0.5 > \alpha_{K_S\,W4} \geq -0.5$	16
Sources with thick disks (TD)	$-0.5 > \alpha_{K_S\,W4} \geq -1.8$	484
Sources with anaemic disks (AD)	$-1.8 > \alpha_{K_S\,W4} \geq -2.56$	147
Sources with naked photospheres (NP)	$\alpha_{K_S\,W4} \leq -2.56$	17

classification as SED slope we can immediately notice that OBP does not possess many sources with infrared excess caused by embedded or sources with envelopes, but despite this, there are some sources with IR excess. These sources need to be examined in a more precise way. Based on the distribution presented here we do not expect any sources with envelopes.
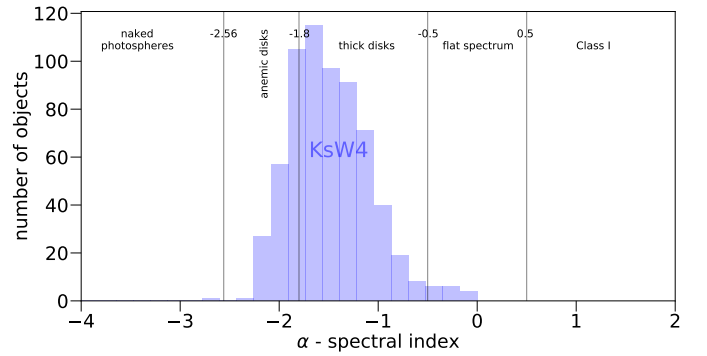
Fig. 7: Distribution of α_{KsW4} for sources in OBP after removing the foreground contamination. The areas correspond to the regions in the histograms occupied by Class I (C I) sources, flat spectrum (FS) sources, sources with thick disks (TD), sources with anaemic disks (AD), and sources with naked photospheres (NP).

The histogram shows no evidence for sources with envelopes. Based on Robitaille (2017) we use only the first six model sets to restrict ourselves to models without any envelope. We focus only on sets with a spherical central source with and without disks. Each set contained a grid of 10000 precomputed models (see Robitaille (2017) Table 2 and Paragraph 3.3 therein). In Table 4 we present the selected sets of models from Robitaille (2017) with the original names. The iconic symbol and the general description of each set are in the second and third column, respectively.

The Python-based SED fitting tool was fed with the data selected according to the criteria discussed above with appropriate treatment as points or upper limits. For each run of fitting, the tool retrieved a best fit model (with the smallest χ^2 value) and all the models for which the difference between their χ^2 value per data point and the best χ^2 per data point was smaller than 9, which provided a separation between good and bad fits. The number of such models for each target we refer as the fitting "degeneracy". This is similar to the approach used by Robitaille (2017). This approach is taken because the sampling of the model grid is too sparse to effectively determine the minima of the χ^2 surface and consequently obtain the confidence intervals. A total of 664 sources were fitted. Table 4 presents in a short way how often each model set was chosen as the most

Table 4: Selected models.

model set	icon	general description	number of variable parameters in set	Number of sources selected in the set
s–s-i		Central source, defined by stellar radius and temperature	2	18
s–smi		Central source, defined by stellar radius and temperature, embedded in a constant density interstellar medium (ambient)	2	14
sp-s-i		Central source, defined by stellar radius and temperature and a passive disk with the inner radius equal to the sublimation radius.	7	19
sp-smi		Central source, defined by stellar radius and temperature and a passive disk with the inner radius equal to the sublimation radius; embedded in a constant density interstellar medium	7	7
sp-h-i		Central source, defined by stellar radius and temperature and a passive disk with a variable inner radius (disk with a hole).	8	345
sp-hmi		Central source, defined by stellar radius and temperature and a passive disk with a variable inner radius; embedded in a constant density interstellar medium	8	261

likely representation of the source. One can easily see that for the majority of the sources the most likely models are those with central source with inner hole (345 and 261 sources for the case with and without ambient density, respectively). Only 32 sources were "fitted as" diskless sources, almost half of them with ambient density. The remaining 26 sources are described as sources with passive, dust disk without inner hole. Since a distance is used as an input in the fitting tool, we assumed the distance range from $1000/(\varpi + \sigma_\varpi)$ to $1000/(\varpi - \sigma_\varpi)$ parsec, where ϖ and σ_ϖ are the parallax and appropriate error values from the *Gaia* DR2 catalog.

Figure 8 shows the results of the SED fitting procedure. A sample is shown in the printed version and all the figures are presented online. Circles correspond to the photometric data points with respective error bars. In most of the cases, the error bars are so small that they are hidden behind the circles. The triangles are data points used as upper limits. The black curve in each figure shows the stellar photosphere model used in the best fit model within each model set. The panels in the figure are ordered roughly in order of increasing complexity from left to right, then from top to bottom, so that the top left panel shows models that include only a star, and the bottom right panel shows models that include a star, disk with an inner hole and an ambient medium. At first glance, a substantial fraction of the model sets provides a good fit to the data, with the exception of the models with only a spherical central source and no disk. All model sets with a disk provide a good fit.

Although the χ^2-criterion is a good representation of the goodness of fit and associated errors, it is interesting to note that in a few cases, the model with the lowest χ^2 may not actually represent the data very well. It thus initially appears that one cannot place strong constraints on the nature of the object. The assumption for the χ^2 analysis is that the reduced χ^2 is close to 1. If χ^2 is far from 1 then it can point into three problems:

- photometry do not fit together – measurements of different bands were not taken simultaneously, it can be a problem with variability of the source;
- errors of the input data are underestimated – by a single or all surveys;
- model is widely wrong – too simple – in the case of observed SEDs, there are a number of systematic sources of errors to consider, such as the fact that the models are only simplistic representations of a more complex 3D reality.

χ^2 can indicate which model fits best but the absolute value of χ^2 is meaningless and should not be used for the analysis.

Therefor, we follow the description in Robitaille (2017) and use not only χ^2 of the best fit, but also the fraction of models that provide a good fit (see below). With this criterion, it is possible to determine which model is most likely (even though many of the models remain possible). In other words, we simply look at which model set has the highest fraction of good models. In this way, even if a specific model set contains the best fit by χ^2 value, if only one model provides a good fit in that set, it means that the parameters need to be fine-tuned to reproduce the data, while a model set where a larger fraction of models can reproduce the data is more likely because it requires less fine-tuning. Following the methodology from Robitaille (2017) for each model set we calculate the model likelihood ($P(D|M)$), defined as:

$$P(D|M) \propto \frac{N^{\text{good}}}{N}, \qquad (4)$$

where N is the total number of models in each set and N^{good} is the number of models from each set fulfilling $\chi^2 - \chi^2_{\text{min,all}} \leq 9 \cdot n_{\text{data}}$. Here $\chi^2_{\text{min,all}}$ is the global minimum χ^2 from all model sets for the source, not the one from the corresponding model set. See Robitaille (2017) for a detailed description. Table 5 lists (for one example source 11496) for each model set the fraction of models providing a good fit, the best-fit χ^2 value, and the relative score, which is given by the ratio of $P(D|M)$ to the mean of the $P(D|M)$ values for all model sets. A higher relative score means a more likely model. Using this, we can see that the most likely model is that of a simple disk with an additional inner hole and ambient medium (sp-hmi), although the model set without ambient medium has a smaller χ^2_{min}.

3.2. Estimating the physical parameters

Having identified a most likely model set, we can take a look at some of the parameters from the models that fit well. However, since other model sets provided reasonable fits, we examine the parameters only under the assumption that this most likely model set is correct. We will focus our analysis only on parameters that are relevant for this study, namely: extinction, star radius, effective temperature, mass of a disk, inner and outer radius of a disk.

The SED fitter gives the inner disk radius (as an output from model sets sp-s-i and sp-smi) in units of dust sublimation radius.
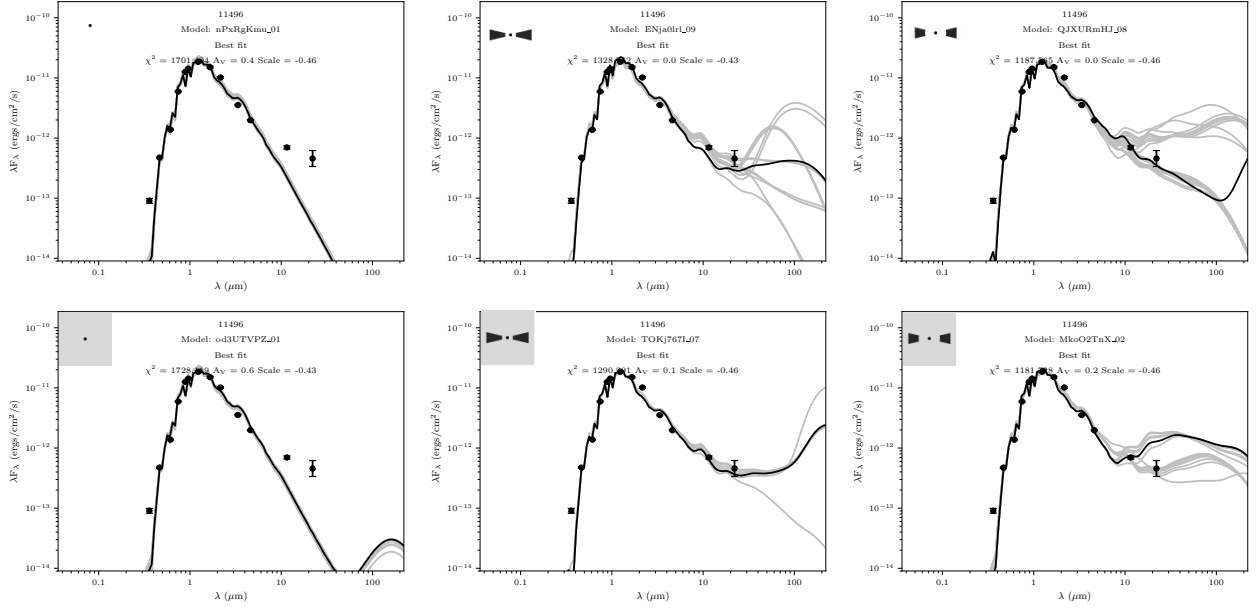
Fig. 8: Model fit to observations of source 11496 in OBP (using the source nomenclature from (Kubiak et al. 2017). Each panel shows all the fits for $\chi^2 - \chi^2_{\min} < 9 \cdot n_{\text{data}}$ for the specific model set ($\chi^2_{\min}$ is determined for each model set individually). Only the fits for preselected model sets are presented and used for far analysis.

Table 5: Relative likelihoods of the model sets for the source 11496.

Model set	icon	$P(D\|M)$	$\chi^2_{\min}$	Score
s—s-i		0.0017%	1701	1.2
s—smi		0.0009	1728	0.635
sp–h-i		0.0016	1182	1.129
sp–hmi		0.0021	1188	1.48
sp–s-i		0.0013	1329	0.918
sp–smi		0.0009	1290	0.625

We convert them to AU using the formula from Whitney et al. (2004):

$$\frac{R_{\text{sub}}}{R_\star} = \left(\frac{T_{\text{sub}}}{T_\star}\right)^{-2.086}, \tag{5}$$

where the dust sublimation temperature (T_{sub}) is chosen to be 1600 K.

As an example, the full parameter set for source 11496 is presented in Table 6.

To estimate the uncertainties, we adopted a Monte Carlo method to explore how the uncertainties of the flux measurements propagate to the uncertainties of the fit parameters. For each source, we created 1000 random variations of the fluxes according to the measurement errors, and ran the SED fitter on them. The standard deviation of the resulting fit parameters is

taken as estimate of the parameter unceratinty. The details of the method are described in Section

Table 6: Parameter set for source 11496.

Parameter	Value
Extinction A_V	0.0
Stellar Radius	$1.39 R_\odot$
Stellar Temperature	2671 K
Disk Mass [Dust]	$6.48 \cdot 10^{-2} M_\odot$
Disk outer Radius	5.774AU
Disk inner Radius	0.02AU
Disk flaring power	1.064
Disk surface density power	-1.973
Disk scaleheight	4.093 AU
Scattering	1
Inclination	7 deg

We adopted a Monte Carlo method to explore how the uncertainties of the flux measurements propagate to the results of the fitting procedure. For each of our candidate members of OBP we created a collection of distinct entities satisfying specified conditions: within the observation errors we varied the flux values by assuming gaussian distributions and we performed the SED fitting process. For each single source we repeat the process 1000 times.

Since the list of parameters obtained for each source depends on the set of models chosen based on the score value (see Section 3 and Robitaille 2017) the only "best-fits" that should be part of the analysis should come from the same model set as obtained during the analysis of the orginal data. Before analysing the distribution of best fit results for each parameter we first need to address the stability of the model set selection. For all sources

we counted the number of simulations that yield the correct set (identical with original data) and the number of incorrect sets.
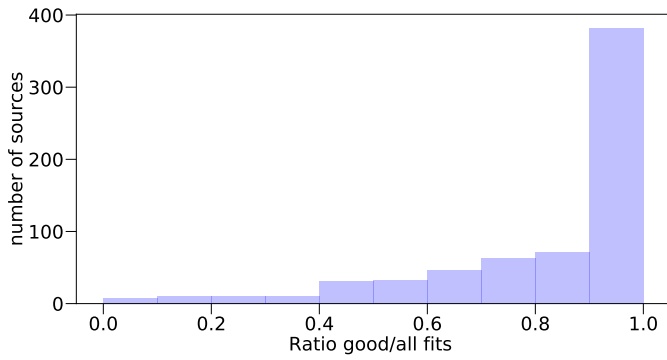
Fig. 9: The distribution of the fraction of simulated model sets that are identical with the model set selected based on the fit of the original data. This can be interpreted as a metric of how robust the selected model set is and how trustworthy is the described physics of the object.

As presented in Fig. 9, the fraction of simulations resulting in the correct set is not always equal to 1. Particularly in our case for the sources 327782, 252528, 251381 we get less than 5% of simulation resulting with the same model set as obtained for the original data sets. For 229 sources we got an agreement of more than 99%, whereas we got at least 50% consistency counts for 594 sources.

4. Results

In Table 7, we list the parameters from the best fit models for the sources in OBP (the full Table is available in the electronic version). The table contains only the columns relevant for this analysis. Given the models used and the large parameter space explored with only a few data points, the derived values of the various parameters should be treated as indicative. The error in each parameter is calculated as a standard deviation from the Monte Carlo simulations performed for each source individually. Empty fields are present if a parameter is not a part of the most probable model set.

The various columns in the table are as follows:

– Column 1: Source name (using the source nomenclature from Kubiak et al. 2017);
– Column 2: Model Set name (see Table 4);
– Column 3: Ratio – the percentage value measuring how robust the selection of model set is based on Monte Carlo simulations (see Appendix);
– Column 4: $\chi^2_{\min}$ per data point ;
– Column 5: Fitted "interstellar" extinction with errors [mag]
– Column 6: Radius of the central source with errors [$R_\odot$]
– Column 7: Temperature of the central source with errors [K]
– Column 8: Disk mass with errors [$M_\odot$]
– Column 9: Disk outer radius with errors [AU]
– Column 10: Disk inner radius with errors [AU]
– Column 11: Final Remarks: "*SET?*" means that based on the Monte Carlo simulations the agreement between the model set selection of simulated and original data is less than 50 % (see Sect.).
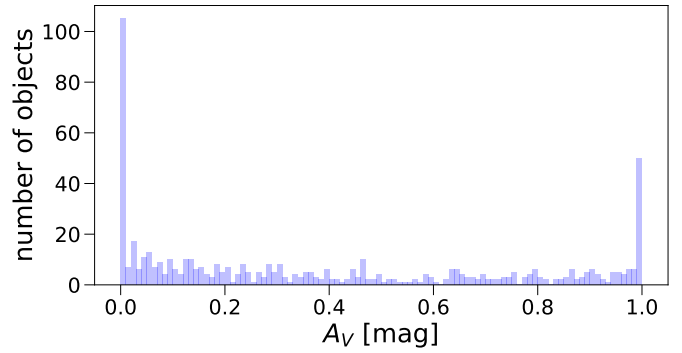
Fig. 10: The distribution of estimated line of sight interstellar extinction values (A_V).

The model provides estimates of the interstellar extinction, the disk properties, and the temperature and radius of the source. The interstellar extinction A_V is estimated to span a range between 0 – 1 mag, and the histogram shows a bimodal distribution with peaks at 0 and 1 mag and a flat distribution in between. Although those values can not be used as the single star extinction measurements the distribution is in good agreement with an extinction estimated based on Planck-Herschel data. The peaks at 0 and 1 are artifical, because the input A_V range was restricted to [0,1].

Photospheres The photospheres are the driving engines of pre-main sequence stars which is also the end product of the star formation process that we seek to understand. Using the values of the parameters for the photosphere from the SED fitting procedure, we can investigate the general properties of sources from OBP.

Figure 11 shows the overall statistics based on the estimated representative values for the stellar temperature and radii for all the fitted sources. The radii of the photospheres selected by the observed data are typically small, below 2 $R_\odot$. The stellar temperature is found typically to be between 2400 K to 4000 K but there is a considerable number of models spanning a range below 2800 K. In the models used for the SED fit, the radius and temperature are uniformly sampled on a log scale within the grid limits. Nevertheless, the model grid covers a range of stellar radii from a 0.1 $R_\odot$ to a hundred solar radii and temperatures from 2000 K to 30 000 K. It is interesting to note that the observed SEDs can select models with large stellar radii (50 $R_\odot$) and relatively low temperatures (2976 K), which is an obviously unphysical model of a star. These results describe most of the sources as pre-main sequence stars with a mean stellar temperature of 3000 K. The mean radius of all sources is 1.8 $R_\odot$.

Disks and envelopes Figures 12 and 13 compares the basic properties of the disks around the central sources. The data points from the fitting results occupy a region representing lower disk masses compared to the mean value of the grid (the grid extends from 10^{-8} to 0.1 $M_\odot$). But the results seem to be consistent with those obtained by Andrews & Williams (2007) for ρ Oph. In Fig. 12 both distributions are presented in blue (results for OBP) and red (results for ρ Oph).

Thus, the modeled sources are best represented with small disks. Most of the modeled sources show the presence of disks with or without inner hole. The disk inner and outer radius range

Table 7: Parameters obtained for 10 sources within our sample.

source	Set	ratio	$\chi^2_{\min}$	A_V [mag]	$R_\star$ [$R_\odot$]	$T_\star$ [K]	L [$L_\odot$]	M_{disk} [$\cdot 10^{-6} M_\odot$] [$M_\odot$]	$R_{\mathrm{disk}}^{\max}$ [AU]	$R_{\mathrm{disk}}^{\min}$ [AU]	Comment
96212	s—s-i	0.984	988.037	1.00	1.635	3495	0.358				
117677	s—s-i	0.279	850.265	0.03	0.723	2757	0.027				SET?
175164	s—smi	0.906	529.113	0.91	4.527	3089	1.674				
418287	s—smi	0.09	1078.595	1.00	1.228	3506	0.204				SET?
407172	sp–h-i	1	394.382	0.00	1.184	2890	0.088	1876	130	7	
19676	sp–h-i	0.226	654.291	0.00	0.870	2709	0.037	55600	2486	2	SET?
597549	sp–hmi	1	82.366	0.00	1.422	3573	0.296	22.72	102	31	
103938	sp–hmi	0.216	1691.812	1.00	0.841	3217	0.068	501.6	786	5	SET?
228216	sp–s-i	1	839.817	1.00	0.990	3880	0.199	0.031	56		
334243	sp–s-i	0.438	351.537	0.14	23.54	2724	27	874.8	2669		SET?
386774	sp–smi	0.994	627.478	0.90	2.001	3588	0.596	516.2	183		
381570	sp–smi	0.181	1233.251	0.90	1.187	2962	0.097	74090	157		SET?
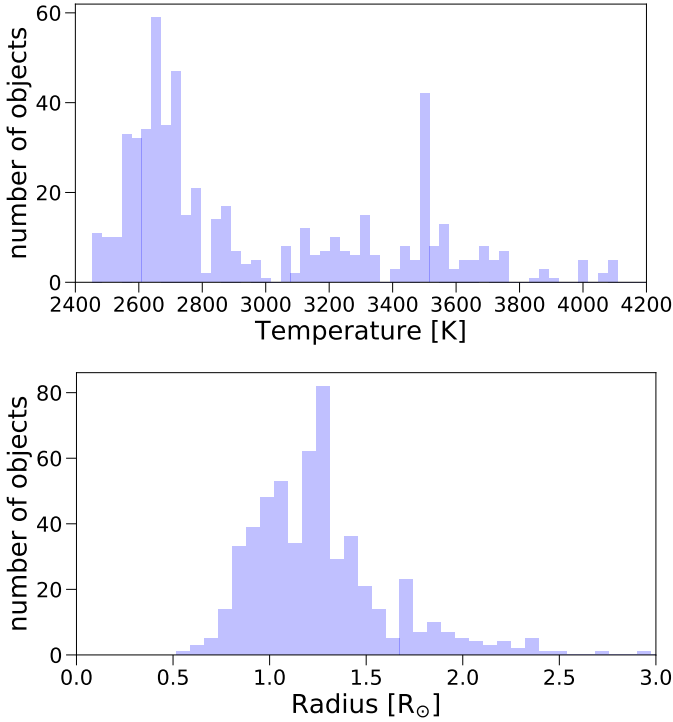
Fig. 11: Histograms of stellar temperature (top) and radius (bottom) for the fitted OBP candidates (after excluding unphysical outliers).
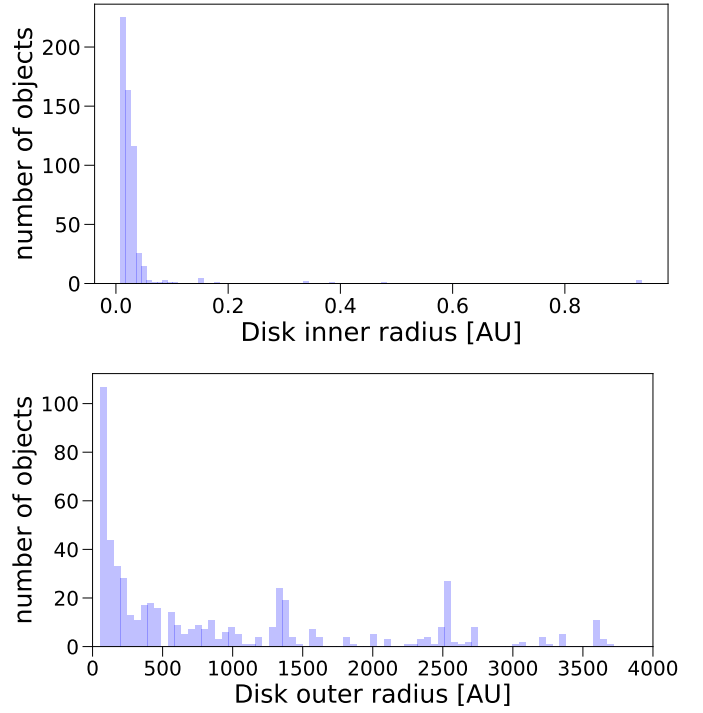
Fig. 13: Histograms of size parameters derived for disks. The inner and outer radii in AU are presented in the upper and lower figures.

5. Mass and age of OBP

The new models from Robitaille (2017) do not use highly model-dependent parameters, such as the stellar age and mass, which depend on stellar evolutionary tracks. Instead, the models are defined using parameters that have a direct impact on the radiative transfer. In order to obtain the mass and age we put our objects on a theoretical HR diagram and used the evolutionary tracks to estimate the parameters. Comparison of models in CMDs (or luminosity-T_{eff} diagrams) with observations in young stellar populations should always be taken with caution owing to the observed luminosity spread. This is likely a mixture of various effects, such as uncertainty in the determination of the effective temperature, contamination from non-members, some extinction effects, likely presence of disk, early accretion effects, surface inhomogeneity, rotation, molecular opacity, and many others. The match is in general relatively poor in any color-magnitude diagram made of near-infrared luminosities. As already known

Fig. 12: Histograms of masses in $M_\odot$ derived for disks.

from almost 0 to 1 AU and from 54 AU to ∼4000 AU, respectively.

(see, e.g., Bell et al. (2012); Baraffe et al. (1998), and references therein), the difference between observations and models is larger at the faint end and suggests that the current description of the atmospheres of late-K- and M-type stars and brown dwarfs presents a number of problems, all known to contribute to the differences between observations and model predictions.

We use the theoretical tracks from Baraffe et al. (2015). We decided to use these particular evolutionary tracks mainly for two reasons: First, to the best of our knowledge these are the tracks that reach the lowest temperatures and the authors claim overall improvement in near-infrared calibrations of evolutionary tracks compared to older models. Second, we made again use of the VOSA (VO Sed Analyzer, Bayo et al. (2008)) to compare all evolutionary tracks available there. After visual inspection we concluded that the tracks from Baraffe et al. (2015) provide the best fit (we are able to obtain masses and ages for the largest number of stars). In Fig. 14, we present our attempt to use both temperature-magnitude and colour-magnitude diagrams for OBP. On both panels the isochrones are red and cover the range from 0.5 – 15 Myr, evolutionary tracks are blue and spread from 0.05 to 1.4 $M_\odot$. Unfortunately the selection of photometric systems presented by Baraffe et al. (2015) is limited and to avoid conversion between photometric system we had to use 2MASS photometry. Instead of total luminosity of the stars we decided to use absolute H-band magnitudes for the sake of clarity. Total luminosity is a function of stellar radius and effective temperature with powers of two and four, respectively. Presenting it in Fig. 14 would make the plot unreadable due to the large error bars. The upper panel presents the effective temperatures and H-band absolute magnitudes for deredenned OBP members, both with appropriate errors. Unfortunately most of our sources do not fit within the ranges of evolutionary tracks. Only 195 out of 664 sources lie within the grid of Baraffe et al. (2015) models. The majority of the sample clusters in the regime of cool stars, with effective temperatures below 2700 K. This discrepancy between evolutionary tracks and effective temperatures derived from SED fitter is surprising for us. Despite our huge effort we are not able to point out what can cause it. We searched for correlation between position of the source on this diagram and its parameters (distance, position, selected model, disk mass and inclination, etc.), finding none. We then moved one step back, we decided to use the $J-H$ vs H colour-magnitude diagram and derive from it masses and ages for our sources. This way, we are independent of the effective temperature, and therefore we hope to avoid the additional ambiguity of two different ways of determining the effective temperature used in the two studies by Robitaille (2017) and Baraffe et al. (2015). The lower panel of Fig. 14 presents the color-magnitude diagram for OBP. Again our sample does not fit within the borders of the evolutionary track, but in this case the tracks cover 377 out of 664 stars. This is a large improvement on the number of sources. In general the evolutionary models and theoretical isochrones provide poor agreement with observations at young ages in near-infrared color-magnitude diagrams, as illustrated in many cases in the literature (see the discussion in, e.g., Baraffe et al. 2015; Bouy et al. 2015).

Using Fig. 14, we obtained ages and masses for 377 members of OBP. We performed a linear interpolation within the Baraffe et al. (2015) isochrones and evolutionary models. Those values should not be treated as exact individual results but can be used to investigate the overall distribution and trends in our sample. In Fig. 15 and 16 we present the distribution of stellar masses and ages. As expected the OBP is a relative young stellar population with a mean age of 4 ± 2.4 Myrs. The mass range from 0.04 – 1.15 $M_\odot$ reaches already into the brown dwarf domain.
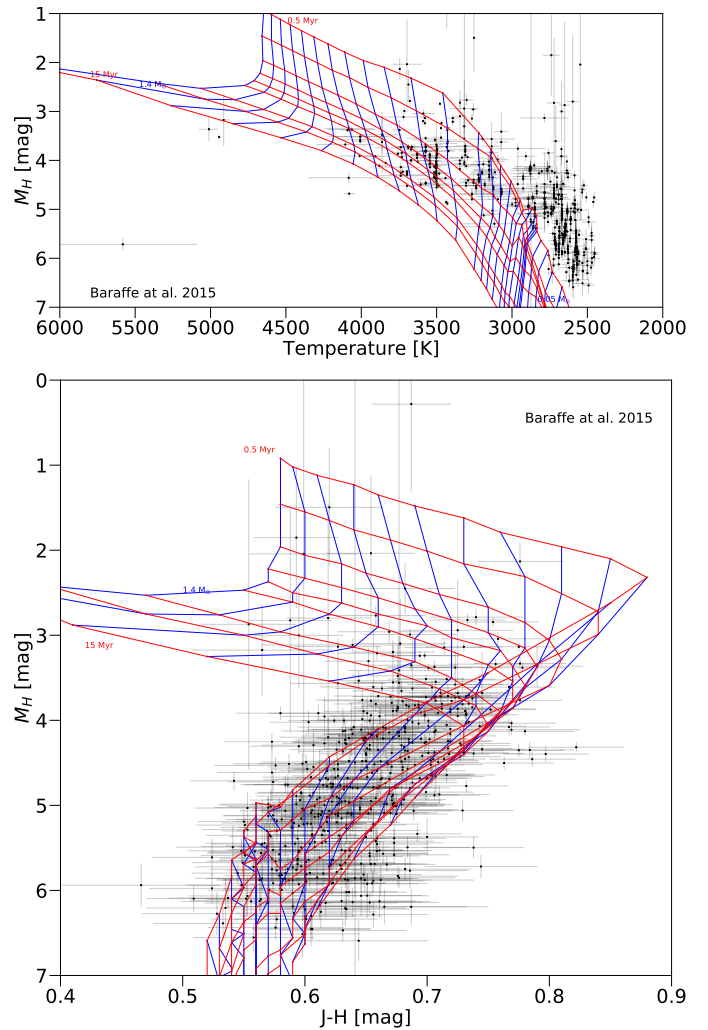
Fig. 14: *Upper panel:* Absolute M_H vs $T_{\rm eff}$ diagram for the OBP. The isochrones and evolutionary tracks are taken from Baraffe et al. (2015), the effective temperatures are derived via the SED fitter by Robitaille (2017). *Lower panel:* Absolute M_H vs $J-H$ diagram for the OBP with the same tracks.

The comparison with the σ Ori Cluster located near OBP (discussed in Kubiak et al. (2017)) allows us to believe that average mass and age obtained here should be treated as lower limits. Detailed spectroscopic observations are needed to confirm such a young age. If they are so young, OBP members should still present spectroscopic youth features such as H_α in emission and/or the Li 6707 Å line in absorption.

6. Caveats and Conclusions

In the previous section, the physical parameters of the star and disk were estimated by fitting the SEDs of the IR point sources. The resulting variables were compared to identify specific trends. In the following paragraphs we discuss some caveats pertinent to the observational data, fitting procedure, and selected sample.

Models   The basis of the SED fitting analysis is a radiative transfer model grid, computed assuming certain physics thought
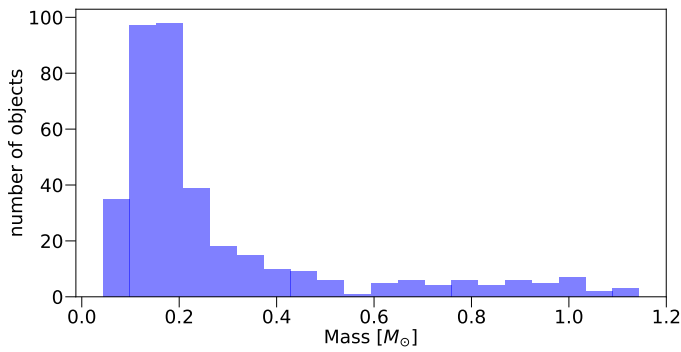
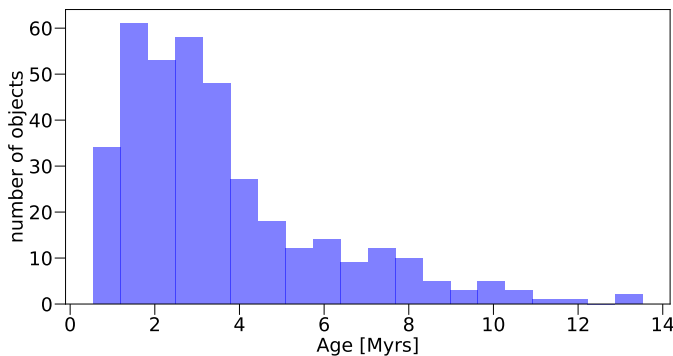Fig. 15: The distribution of masses for OBP.

Fig. 16: The distribution of ages for OBP.

to be valid for stars of a few solar masses (low mass stars). The model grid spans on a broad range of parameters up to $R = 100 R_\odot$ and in temperature range from $T = 2000\,\text{K}$ to $T = 30000\,\text{K}$. This may cause some of the combinations of parameters to be unphysical. It is, however, still possible to obtain useful information from the model grid by comparing the observed trends against the inherent trends in the grid. For this purpose and throughout this work, the parameter space from the full grid is compared to the derived values of the best fit models. By making such a comparison, it will be possible to visualize if the observed trend or a representative value is due to inherent biases in the model grid. We will see in the following discussion that the observed data indeed preferentially pick up certain narrow constraints on the physical properties of YSO components, even when the model grid provides a uniform or wide range of options.

Multiplicity   One of the important aspects of star formation is that stars are known to form in multiple systems or strongly clustered environments. Assuming a source in the simplest case of multiplicity – a binary system – there are two possible scenarios: a) two objects at the same evolutionary state and b) objects in different evolutionary states. In the first case, the SED modelling cannot detect possible multiplicity because the SED shapes will be similar for the two sources and may overlap. In the latter case, where sources are at different evolutionary stages, the SEDs are expected to flatten out because of the older component and the source is prone to be detected by its unfamiliar shape.

Variability   Variability for active, young K- and M-type stars is an important contaminant of any photometric survey in the optical and/or infrared. In extreme cases it can even cause the misclassification of the young source (if the classification is based on spectral index). Aware of those issues we inspected the variability of sources in our sample, and we present the results in a forthcoming paper (Kubiak et al. 2018 in prep., Variability of the OBP).

Given these caveats, the main results of this paper can be summarized as follows:

1. Gaia astrometry allowed us to prune the OBP catalog to about 664 M-stars at a mean distance of 345 pc. Surprisingly, the OBP population extends for ~ 60 pc along the line of sight, a size comparable to its width.
2. The OBP is sub-structured: there are two peaks in the distance distribution (360 and 410 pc) corresponding to measurable different proper motions of the stars at these two distances. Still, it is not clear if there are two populations or a single population with an age gradient along the line-of-sight. Future releases of Gaia data will be able to bring more light to this subject.
3. The SED fitting based on collected data favours selection of models with low-mass passive disks.
4. The derived mean disk masses ($\sim 0.007 M_\odot$) are consistent with disk masses derived by Andrews & Williams (2007) based on submillimeter studies of the ρ Ophiuchi star forming region. Still, and as a caveat, the OBP lacks far-IR/submm observations (only single measurements for a few sources). Because of that, the masses obtained from the SED fitting can only be taken as upper limits on the true disk masses.
5. We show that theoretical isochrones poorly match the empirical sequence in most color-magnitude diagrams made of near-infrared colors.
6. We use Monte Carlo simulations to investigate whether the photometric errors influence the selection of model set and hence the obtained results from the fit and conclude that the photometric errors are negligible

References

Ahn, C. P., Alexandroff, R., Allende Prieto, C., et al. 2014, ApJS, 211, 17
Allard, F., Homeier, D., & Freytag, B. 2012, Philosophical Transactions of the Royal Society of London Series A, 370, 2765
Andrews, S. M. & Williams, J. P. 2007, ApJ, 671, 1800
Baraffe, I., Chabrier, G., Allard, F., & Hauschildt, P. H. 1998, A&A, 337, 403
Baraffe, I., Homeier, D., Allard, F., & Chabrier, G. 2015, A&A, 577, A42
Bayo, A., Rodrigo, C., Barrado Y Navascues, D., et al. 2008, Astronomy & Astrophysics, 492, 277
Bell, C. P. M., Naylor, T., Mayne, N. J., Jeffries, R. D., & Littlefair, S. P. 2012, MNRAS, 424, 3178
Blaauw, A. 1964, ARA&A, 2, 213
Bouy, H., Bertin, E., Sarro, L. M., et al. 2015, A&A, 577, A148
Briceno, C., Calvet, N., Hernandez, J., et al. 2018, ArXiv e-prints [arXiv:1805.01008]
Cutri, R. M., Wright, E. L., Conrow, T., et al. 2013, VizieR Online Data Catalog, 2328, 0
Da Rio, N., Robberto, M., Soderblom, D. R., et al. 2010, ApJ, 722, 1092
DENIS Consortium. 2005, VizieR Online Data Catalog, 2263
Duchêne, G. & Kraus, A. 2013, ARA&A, 51, 269
Henden, A. A., Templeton, M., Terrell, D., et al. 2016, VizieR Online Data Catalog, 2336
Kounkel, M., Covey, K., Suárez, G., et al. 2018, AJ, 156, 84
Kubiak, K., Alves, J., Bouy, H., et al. 2017, A&A, 598, A124

Lada, C. J. 1987, in IAU Symposium, Vol. 115, Star Forming Regions, ed. M. Pe-
    imbert & J. Jugaku, 1–17
Lada, C. J. & Wilking, B. A. 1984, ApJ, 287, 610
Lawrence, A. 2013, in Astrophysics and Space Science Proceedings, Vol. 37,
    Thirty Years of Astronomical Discovery with UKIRT, ed. A. Adamson,
    J. Davies, & I. Robson, 271
Lindegren, L., Hernández, J., Bombrun, A., et al. 2018, A&A, 616, A2
Magnier, E. A., Schlafly, E. F., Finkbeiner, D. P., et al. 2016, ArXiv e-prints
    [arXiv:1612.05242]
Megeath, S. T., Gutermuth, R., Muzerolle, J., et al. 2012, AJ, 144, 192
Meingast, S., Alves, J., Mardones, D., et al. 2016, A&A, 587, A153
Murakami, H., Baba, H., Barthel, P., et al. 2007, PASJ, 59, S369
Ochsendorf, B. B. & Tielens, A. G. G. M. 2015, A&A, 576, A2
Peña Ramírez, K., Béjar, V. J. S., Zapatero Osorio, M. R., Petr-Gotzens, M. G.,
    & Martín, E. L. 2012, ApJ, 754, 30
Preibisch, T. 2012, Research in Astronomy and Astrophysics, 12, 1
Reggiani, M., Robberto, M., Da Rio, N., et al. 2011, A&A, 534, A83
Robitaille, T. P. 2017, A&A, 600, A11
Robitaille, T. P., Whitney, B. A., Indebetouw, R., & Wood, K. 2007, ApJS, 169,
    328
Robitaille, T. P., Whitney, B. A., Indebetouw, R., Wood, K., & Denzmore, P.
    2006, ApJS, 167, 256
Rodrigo, C., Solano, E., & Bayo, A. 2012
Sherry, W. H. 2003, PhD thesis, STATE UNIVERSITY OF NEW YORK AT
    STONY BROOK
Siess, L., Dufour, E., & Forestini, M. 2000, A&A, 358, 593
Skrutskie, M. F., Cutri, R. M., Stiening, R., et al. 2006, AJ, 131, 1163
Spezzi, L., Petr-Gotzens, M. G., Alcalá, J. M., et al. 2015, A&A, 581, A140
Teixeira, P. S., Lada, C. J., Marengo, M., & Lada, E. A. 2012, A&A, 540, A83
Watson, M. G., Schröder, A. C., Fyfe, D., et al. 2009, A&A, 493, 339
Whitney, B. A., Indebetouw, R., Bjorkman, J. E., & Wood, K. 2004, ApJ, 617,
    1177
Whitney, B. A., Wood, K., Bjorkman, J. E., & Wolff, M. J. 2003, ApJ, 591, 1049
Wiramihardja, S. D., Kogure, T., Yoshida, S., Ogura, K., & Nakano, M. 1994,
    VizieR Online Data Catalog, 3177, 0
Zari, E., Brown, A. G. A., de Bruijne, J., Manara, C. F., & de Zeeuw, P. T. 2017,
    A&A, 608, A148

5

Variability in the Orion Belt population

5.1 Overview

In the last publication included in this thesis, I present the analysis of the photometric variability among the members of the Orion Belt population. In this manuscript, I underline the importance of taking variability into account and consideration when analyzing the young stellar populations.

The main point of the paper is to present the analysis of variability among the OBP sources as well as to highlight the attempt to guide other researchers in their use of AllWISE multi-epoch photometry for thermal infrared variability studies. Findings present here show that there are a significant amount of passive circumstellar disks within the OBP and that more than $10\,\%$ of these sources show variability at a significant level in the optical and infrared.

5.2 Publication details

Title: Variability in the Orion Belt population

Authors: K. Kubiak, P. S. Teixeira, R. Köhler, J. Alves, O. Czoske, T. Robitaille

Status: Under internal review. To be submitted in December 2018 to A&A.

Own contributions: Literature research, data collection, Stetson index analysis,

variability criteria testing, variability analysis, light curves analysis, preparation of figures and plots, paper writing.

Variability in the Orion Belt population

K. Kubiak[1], P. S. Teixeira[2], R. Köhler[3, 1], J. Alves[1], O. Czoske[1], and T. Robitaille

[1] Department of Astrophysics, University of Vienna, Türkenschanzstrasse 17, A-1180 Vienna
e-mail: `karolina.kubiak@gmail.com`
[2] Scottish Universities Physics Alliance (SUPA), School of Physics and Astronomy, University of St. Andrews, North Haugh, St. Andrews, Fife KY16 9SS, UK
[3] Sterrewacht Leiden, P.O. Box 9513, NL-2300 RA Leiden, The Netherlands

December 18, 2018

ABSTRACT

Aims. By studying variability in young stellar objects (YSOs) in the optical, near- and mid-infrared we want to underline the importance of taking variability into account and consideration when analyzing young stellar populations. We can comment directly on the mid-infrared variability characteristics of young stars in different classes. Multi-epoch photometry from AllWISE provides the opportunity to investigate variability at 3.4 and 4.6 microns for most of the sources in Orion Belt Population. We study the light curves and color trajectories of the sources.
Methods. We investigate variability in optical and near-infrared based on a comparison of photometry from different surveys. We selected sources where the brightness of sources differ by more than a 3σ-related level of significance. We used the All-WISE Multiepoch Catalog to compute the Stetson index quantified variability as a function of the evolutionary stage of the YSO.
Results. We present a list of 475 sources with suspected variability. We present a subset of 83 sources for which the mid-infrared variability has been investigated based on multi-epoch All-WISE data. Different features on the light curves–color behavior in W2−W1 vs. W1 color-magnitude space contains information about the physical processes behind variability; almost all variable stars are getting bluer when getting fainter.

Key words. infrared: stars — stars: variables - stars:pre-main-sequence

1. Introduction

Young Stellar Objects (YSO) were first highlighted by their optical variability by Joy (1945). Nowadays the young star's variability is one of multiple signs of their early evolutionary status. Variability for active, young K and M-type stars is an important contaminant of any photometric survey in the optical and/or infrared. The photometric behavior of young stars in associations is best described as irregular, with an enormous range in amplitude, time scale and frequency of fluctuations. Naturally, the variability at optical wavelengths has been well studied and correspondingly the understanding of the physics is most developed. When moving from optical to infrared wavelengths the number of variability studies diminishes rapidly. Optical surveys have mainly focused on periodic variables, due to cool or hot spots on the stars (e.g., Stassun et al. 1999; Herbst et al. 2000, 2002). A few studies have also focused on the irregularly variable stars (e.g., Parihar et al. (2009)), and lately infrared studies, including those performed with Spitzer and Herschel, have produced a wealth of results (Carpenter et al. 2001; Morales-Calderón et al. 2011; Billot et al. 2012)). Unfortunately all of those surveys focused on the YSO populations related to the dark clouds, none of them extend to the off-cloud regions.

In a previous paper (Kubiak et al. 2018), we presented the modeling of the spectral energy distributions (SED) of the infrared counterparts of young stellar objects (YSO) in the Orion Belt Population (OBP, Kubiak et al. 2017).

We removed the contamination from foreground stars based on *Gaia* DR2 data. We determined the basic parameters for the central source and disk if present. In this paper, we extend upon that analysis to investigate the variability of members in OBP. We present our analysis of All-WISE multi-epoch photometry for thermal infrared variability studies. We also compare the brightness of sources measured by different surveys in an attempt to evaluate the variability in the optical and near-infrared.

The evolutionary class of these variables has been determined by Kubiak et al. (2018), allowing us to derive mid-infrared variability properties as a function of class. As established in NIR surveys of young stars (cf. Carpenter et al. 2001; Rice et al. 2012; Wolk et al. 2013), different variability mechanisms may impart different color signatures in JHK data: starspot-induced variability is nearly colorless, variable dust extinction makes stars redder as they get fainter, and accretion variability or other changes in inner disk geometry cause stars to get redder as they get brighter. Rice et al. (2012) identify different motions in H-K;K color-magnitude space and measure the fraction of stars showing either dust-reddening or disk/accretion variability, noting that the fraction of disk/accretion variables increases with longer monitoring campaigns.

This paper is organized as follows. The next section briefly describes the comparison to known variable sources. In Section 3 we use the AllWISE Multiepoch Photometry (MEP) Database (Cutri et al. 2013) to select variable stars, whereas in Section 4 we use data from different sur-

veys using similar filters. In particular, we discuss the possible source of contamination, i.e. sources that look but are not variable; the issue of apparent variability due to strong spectral features and the differences in spectral response. In Section 6 we present the analysis of the variability of the selected sources. We give an overview of the procedure used to select the sample of candidate variable stars. We show that variability mechanisms can be constrained via color-color and color-magnitude diagrams; we derive the fraction of stars that show blueing behavior (associated with accretion/disk activity) versus reddening behavior (associated with dust occultation).

In Table 6 we compile a final list of candidate variable stars. We summarize our results in Section 7.

2. Known variable sources

We searched for 664 sources from our list of members of the Orion Belt population in the Combined General Catalogue of Variable Stars (GCVS 5.1, Samus' et al. 2017), which has more than 52011 variable stars discovered and named by 2015. The GCVS lists stars with different variability types: eruptive, pulsating, binary cataclysmic, etc., identified mostly based on optical surveys. By crossmatching OBP members with GCVS using 1 arcsec crossmatch radius we found that 10 sources have been listed as known or suspected variable stars. This is expected as most of the members of OBP even though visible in optical wavelengths are considered as faint (*g* band brightness ∼15-21 mag). In Table 1 we present the names of the source in OBP and the GCVS in the first two columns. Column three and four give the assigned variability type and references. Column five, six and seven give the position in Ra and Dec and the Sloan g-band brightness, respectively. Column eight contains the *Gaia* DR2 (Gaia Collaboration et al. 2018) distance to the source. Column nine gives the Stetson index value (see Sec. 3.1) calculated based on *W1* and *W2* measurements. In the next columns, we present the name and symbol of the fitted model (see Kubiak et al. 2018). The last columns in the Table present the variability flags used in this work (see Section 5 for a detailed description). It is worth to notice that only for two sources the variability periods are given in GCVS, namely for 314963 (or V2713 Ori), 10.2 days and for 606073 (V2116 Ori), 1.25 days. In Figure 1 we present the spatial distribution of those stars inside the OBP field with the inverse-color DSS red-band image as background. All sources are distributed in the southern part of our field, this is due to the character of surveys conducted mainly to investigate the nature of the Orion Nebula Cluster (ONC).

3. AllWISE Multiepoch Photometry

Multi-epoch photometry from AllWISE provides the opportunity to investigate variability at $3.4\,\mu$m (*W1* band) and $4.6\,\mu$m (*W2* band) for the members of OBP. The wide-field Infrared Survey Explorer (WISE, Cutri et al. 2013) observed the same patch of sky repeatedly. Within a day's time, roughly 12 observations were obtained on a given patch of sky; then, another 12 were obtained roughly six months later when that patch of sky was again in view. For most of the sky, AllWISE contains two separate epochs of about a dozen observations each, although 30% of the sky
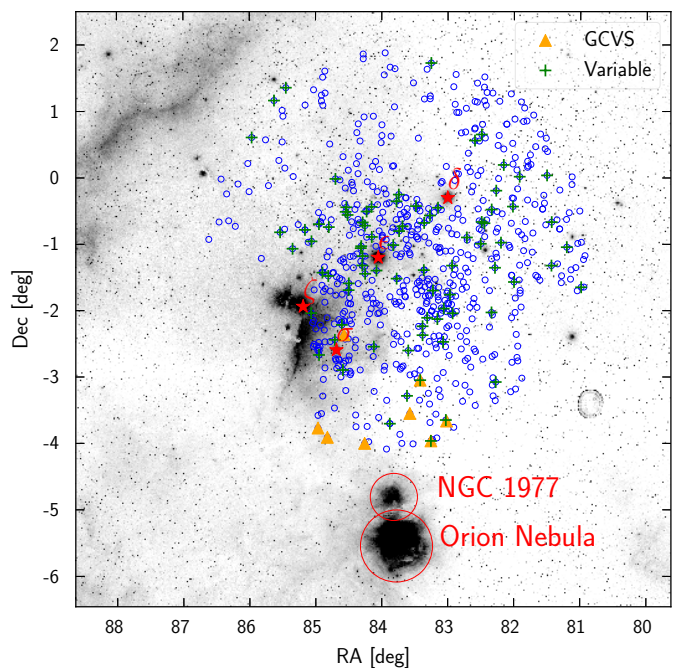
Fig. 1: Spatial distribution of the OBP members (blue dots). With the orange dots, we marked sources listed as a variable in GCVS. The green dots indicate the positions of stars selected as variable candidates based on Stetson index (see Section 3.1). Background is an inverse-colour DSS red-band image centered on ϵ Ori. North is up, and East is left.

has three such epochs available in AllWISE. That is why multi-epoch photometry from AllWISE makes a useful resource in cases where mid-infrared variability is expected to be present with large amplitudes, or for young stellar objects (YSO) where it can be connected to the presence of disks. We find that the average single-epoch photometry uncertainties for AllWISE are ∼0.03 mag for *W1* and 0.02 mag for *W2* which is not much larger than most of the variability measured in the literature.

The primary motivation for searching AllWISE photometry for variability was to inspect YSO variability at 3.4 and $4.6\,\mu$m amongst OBP members with a statistical approach. We employed the AllWISE Multiepoch Catalog (MEP), which is a compilation of 13 months of photometric observations from the mission, to compute the Stetson index for each object (Stetson 1996).

3.1. Stetson variability Index

The first way we identify variables is the Stetson index (Stetson 1996), which quantifies correlation of variability in two (or more) bands. A nice explanation of it being used to identify YSO variable stars can be found in Rebull et al. (2014). The Stetson variability index is computed for each object as:

$$I = \sqrt{\frac{1}{n(n-1)}} \sum_{i-1}^{n} \left(\frac{b_i - \bar{b}}{\sigma_{b,i}} \right) \left(\frac{v_i - \bar{v}}{\sigma_{v,i}} \right),$$

Table 1: OBP members listed as variable stars in GCVS.

OBP ID	GCVS ID	var. type	Ref	RA [deg]	Dec [deg]	g [mag]	d [pc]	I_{W1W2}	SET		Variability		
9622	V0708 Ori	UVN	1,2	83.255686	-3.974557	15.834 ± 0.004	347^{+11}_{-11}	0.66639	sp–smi	►◄	VIS		I
28111	V1244 Ori	UVN	5	84.259245	-4.011937	18.188 ± 0.007	312^{+10}_{-10}	-0.01963	sp-s-i	►◄			
34596	V0894 Ori	UVN	1,4	84.96592	-3.780531	17.906 ± 0.006	401^{+15}_{-15}	-0.30596	sp–h-i	►·◄	VIS		
69412	V1098 Ori	UVN	3	83.018879	-3.674376	16.808 ± 0.005		0.11151	sp–h-i	►·◄	VIS	NIR	
134205	V1217 Ori	UVN	5	83.574525	-3.559872	18.793 ± 0.009	347^{+11}_{-12}	0.32633	sp–h-i	►·◄			
252856	V1890 Ori	INB	8,9	83.418463	-3.056765	20.058 ± 0.018	377^{+13}_{-12}	2.13513	sp–hmi	►·◄	VIS		I
314963	V2723 Ori	INB	4,9	84.571605	-2.373802	20.088 ± 0.019	371^{+25}_{-20}	0.16934	sp–hmi	►·◄	VIS		
360225	V0513 Ori	IS	10,11	85.162108	-0.783966	16.401 ± 0.004	484^{+54}_{-44}				VIS		I
461826	V1253 Ori	UVN	5,6	84.824292	-3.920241	19.421 ± 0.013		0.1453	sp–hmi	►·◄	VIS		
606073	V2116 Ori	INB	7	83.757072	-0.77929	19.723 ± 0.016	344^{+23}_{-22}						

References. (1) Roslund (1969); (2) Lasker et al. (1990); (3) Natsvlishvili (1982); (4) Monet (1998); (5) Chavira & Parsamian (1991); (6) Chavira et al. (1992); (7) **?**; (8) Skrutskie et al. (2006); (9) Scholz & Eislöffel (2004) (10); Fedorovich (1960); (11) Haro & Moreno (1953)

Variability type (from GCVS description): **INB** *Orion variables of intermediate and late spectral types, F-M or Fe-Me (BH Cep, AH Ori). F-type stars may show Algol-like fadings similar to those of many INA stars; K-M stars may produce flares along with irregular light variations;* **UVN** *Flaring Orion variables of spectral types Ke-Me. These are phenomenologically almost identical to UV Cet variables observed in the solar neighborhood. In addition to being related to nebulae, they are normally characterized by being of earlier spectral type and greater luminosity, with slower development of flares (V389 Ori). They are possibly a specific subgroup of INB variables with irregular variations superimposed by flares;* **IS** *Rapid irregular variables having no apparent connection with diffuse nebulae and showing light changes of about 0.5 - 1.0 mag within several hours or days. There is no strict boundary between rapid irregular and Orion variables. If a rapid irregular star is observed in the region of a diffuse nebula, it is considered an Orion variable and designated by the symbol INS. To attribute a variable to the IS type, it is necessary to take much care to be certain that its light changes are really not periodic. Quite a number of the stars assigned to this type in the third edition of the GCVS turned out to be eclipsing binary systems, RR Lyrae variables, and even extragalactic BL Lac objects.*
VIS, NIR, I - refers to the adopted variability criterium in optical, near-infrared and mid-infrared, described in Section 3 and 4, respectively.

where b_i and v_i are the apparent magnitudes in two different filters obtained for each star in two observations closely spaced in time on some occasion i, $\sigma_{b,i}$ and $\sigma_{v,i}$ are the standard errors of those magnitudes, $\bar{b}$ and $\bar{v}$ are the weighted mean magnitudes in the two filters, and n is the number of measurements used to determine the mean magnitude. Objects with a large value of the Stetson index are typically taken to be variable. Since errors are included in the calculation, the change in measured brightness that is just an effect of bad photometry does not cause the star to be identified as a variable. Objects with variability in different bands that are not correlated will not be identified via the original method. We used the python implementation of the Stetson index (stetson.py[1]). The Stetson index allows us to investigate brightness changes in more than one band simultaneously, therefore, the more bands we use the more robust the selection will be. We decided to calculate the Stetson index for $W1$ and $W2$ bands, since there are on average twice as many observing points in $W1$ and $W2$ than in $W3$ and $W4$. The MEP database contains data for 638 OBP sources.

Figure 2 shows the Stetson statistic as a function of the H-band magnitude. For random noise, the Stetson variability index should be scattered around zero and have higher, positive values for stars with correlated variability. For this data set, the Stetson variability index has a positive value on average. The origin of this offset is unclear, but it suggests that a weak correlation exists between the $W1$ and $W2$ photometry, possibly from the fact that the two bands were observed almost simultaneously. Nonetheless, the Stetson variability index is skewed toward large positive values around the nominal value, indicating that a number of stars exhibit real variability that is correlated between the All-WISE bands. There is no trend in Stetson index value with brightness and no clear change as a function of spectral type.

The specific location of the cutoff between variable and nonvariable is unique to each data set, as it is affected by the sampling length and rate of the light curves. We now discuss how we chose this cutoff value for the Stetson index. Figure 3 shows a histogram of the Stetson indices I_{W1W2} for OBP objects. Each of the stars has at least 20 points in both $W1$ and $W2$. The bulk of the distribution around 0.1 are the non-variables, and that part of the distribution can be reasonably well-fit by a Gaussian. There are deviations from Gaussian toward higher values of the Stetson index, as expected for a population of identified variable stars. There is a change in the distribution of the Stetson index above and below 0.5; in Figure 3 the slope of the regression line for the $I < 0.5$ is ~ -107.8 (blue line and dots), and from a Stetson index of 0.5 to 1.0, the slope is ~ -11 (green line and dots). Based on this, we take 0.5 as the cutoff for variability in our data set. The Stetson index distribution for OBP members is not well described by a Gaussian. It is asymmetric with a substantial excess of objects with high positive Stetson values. This is expected since variable members are more likely to have a large amplitude, correlated variability. Since the Gaussian distribu-
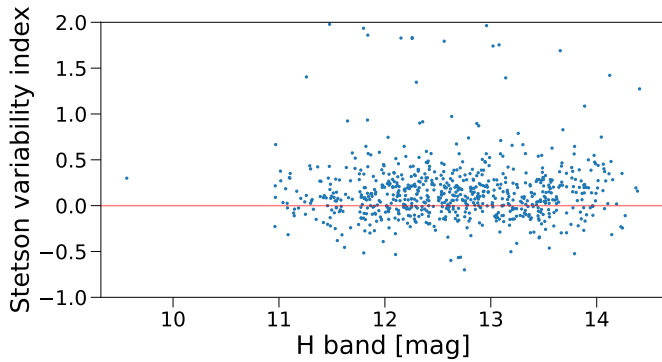
---

[1] https://github.com/tomr-stargazer/wuvars-proto

Fig. 2: Distribution of two-band Stetson index vs. mean *H* magnitude for the members of OBP. Only if both *W1* and *W2* are available they are used to compute the variability index. The solid line at $I = 0$ shows the expected value of the variability index for nonvariable stars. Note that 17 stars with $I \geq 2.0$ and one star with $I \leq -1.0$ are not shown, for clarity.
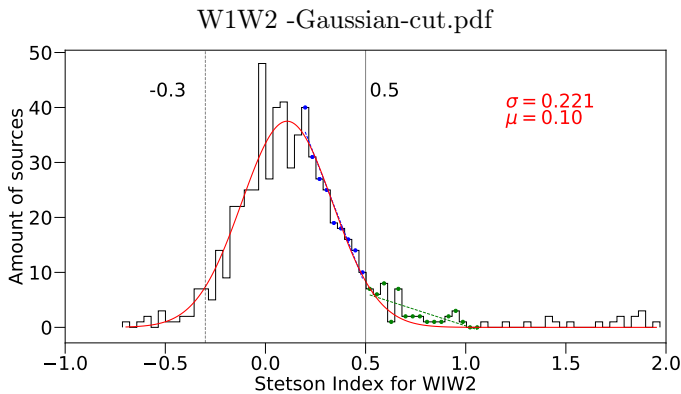

Fig. 3: Histogram between 0 and 2 of the Stetson indices calculated for the OBP. The red solid line indicates a Gaussian fit to the histogram, showing deviations from Gaussianity toward higher values of the Stetson index, as expected for a population of identified variable stars. The blue and green, dashed lines with two different slopes show that there is a break in the distribution defining our cutoff between variable (> 0.5) and non-variable (< 0.5), with the black vertical line at 0.5.

tion is not centered at 0 but at 0.1 we apply this shift to obtain a cutoff value for the negative Stetson index values as marked in Figure 3.

We conclude that a Stetson index cutoff of 0.5 (or -0.3 at the negative side of the distribution) is a sensible boundary for our data set. While the objects with Stetson indices of $\sim$0.1 have a very low chance of having legitimate correlated variability, and objects with Stetson indices > 0.5 have a high likelihood of correlated variability, there is a continuum between these values. Objects with Stetson indices between ~ 0.1 and 0.5 have low confidence for correlated variability.

With this method and adopted value of $I_{W1W1}=0.1$, we identify 83 stars as a variable in mid-IR (out of 638 for which we have data). Only two of those sources are listed

in the GCVS catalog, namely: source 6622 (V0708 Ori) and 252856 (V1890 Ori), see Table 1 for all Stetson index values for GCVS sources.

Both the positive and negative outliers in Fig. 3 are candidate variables that must be inspected to identify real variability. Large positive Stetson index values are derived from sinusoidal variations that are well sampled across the entire light curve. An example of this type of variability are the Cepheid variables for which the Stetson index was defined. With periods on the order of a few days to a couple months, two adjacent photometric measurements in the same night will have magnitude residuals with the same sign, and their product will be positive; this makes the Stetson index positive. For short period YSOs in AllWISE, two adjacent photometric measurements are separated by $\sim$0.5 hour and the light curve is only sampled a couple times for each rotation of the star. In this case, the Stetson index is determined to be negative. The impact of the sampling rate on the sign of Stetson index can hide variables with periods that beat with the WISE cadence of observation, but this can also be a tool for separating short and long-term variables.

4. Different surveys, similar bands

In order to search for variable stars in the optical or near-infrared range, we would ideally use observations of the OBP at (at least) two different epochs taken with the same telescope and with the same filters. We investigated the possible variability of members of OBP by taking advantage of the collected photometry spanning several years (even decades, see the years of the surveys in Figure 4). However, in this case, we have data from different surveys using similar but not identical spectral responses. Therefore, great care has to be taken when comparing the measurements. There are many ways discussed in the literature that help us to identify variable stars, most of them focus on identifying variables in time series photometry. Unfortunately, we do not have long-term multi-epoch photometric data from a dedicated single survey that could be used here for variability estimation in OBP (except the AllWISE database, see Section 3). Therefore, we decided to restrict ourselves only to identify the most probable variable candidates. This was done by comparing the observed brightnesses from different surveys in similar bands. The spectral response curves of the instruments used for the various datasets are shown in Figure 4. The filter response curves have been taken from VOSA (Bayo et al. 2008) and all appropriate references are provided there. In this paper, we make use of similarities between near-IR bands and the wavelength range covered by *griz* SDSS bands (Ahn et al. 2014). Selected filters are similar but not identical, one can easily notice that the *K*-band in UKIDSS (Lawrence 2013) is slightly shifted with respect to the *K*-band in DENIS (DENIS Consortium 2005) and 2MASS (Skrutskie et al. 2006). On the other hand, the UKIDSS survey *J*-band is much narrower than similar bands in 2MASS and DENIS. Therefore any comparison must be done carefully and any conclusions cannot be made without taking this issue into account.

In Figure 4 we present the transmission curves of filters from six surveys for which we have the best spatial coverage of OBP population in similar passbands. In this paper, we make use of similarities between the wavelength range covered by
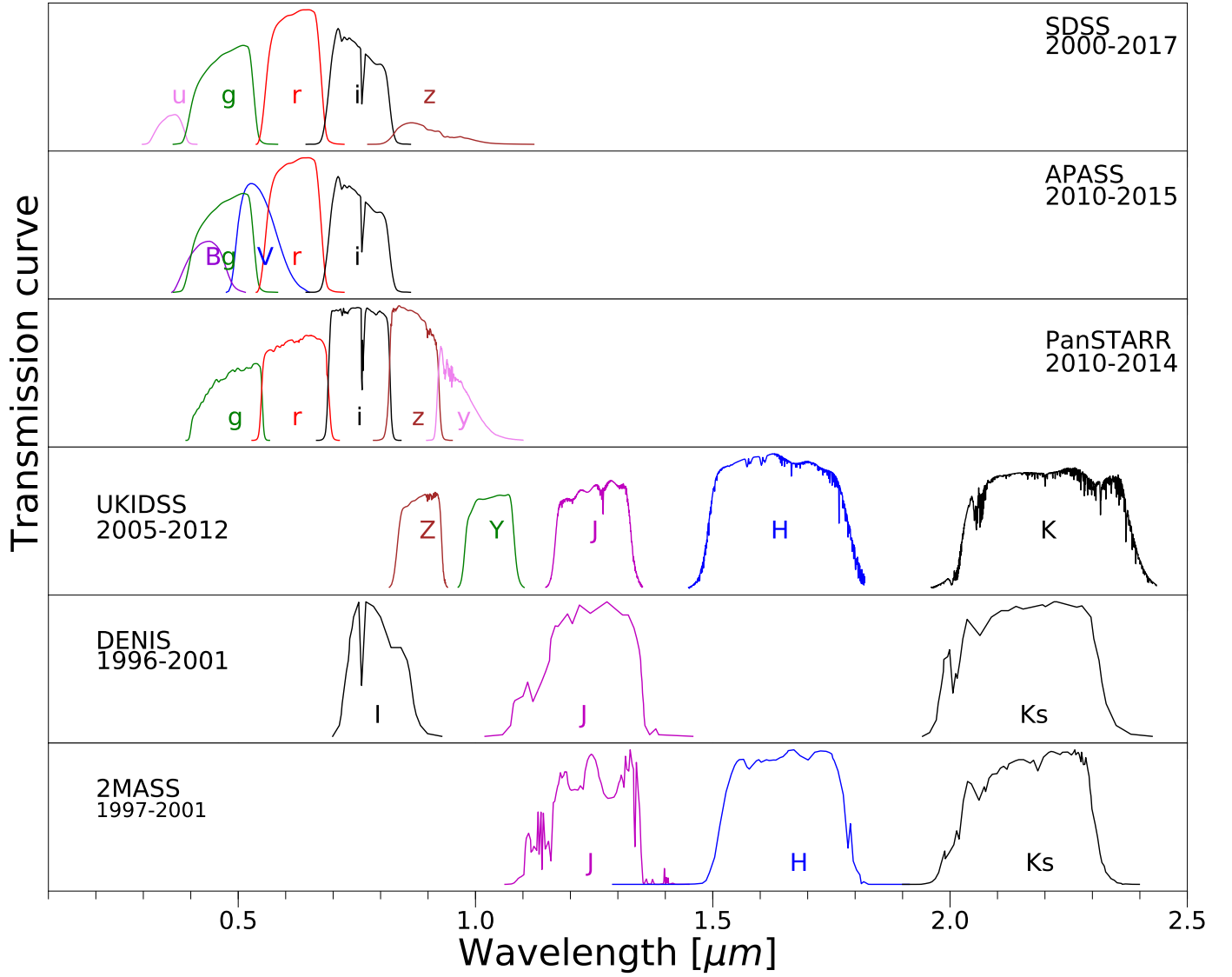
Fig. 4: Spectral response curves for SDSS $ugriz$, APASS $BgVri$, PanSTARRS $grizy$, UKIDSS $ZYJHK$, DENIS $IJKs$, and 2MASS $JHKs$, filters. Note that there is significant overlap between all J, H and K filters, and between the gri from SDSS and PanSTARRS surveys.

- gr bands in SDSS, APASS, and PanSTARRS,
- i band in SDSS, APASS, PanSTARRS and I in DENIS,
- z band in PanSTARRS and UKIDSS

as well as the similarity between NIR bands:

- JK in UKIDSS, DENIS, and 2MASS,
- H band in UKIDSS and 2MASS.

Our analysis is most sensitive to variability arising from photospheres and should be sensitive to sources with a wide range of variability timescales, extending up to a decade. Nevertheless, we are just sensitive to large changes in brightness, and we are not able to determine the timescale of variability.

4.1. Systematic offsets

Since we perform our analysis using different photometric systems, any systematic offset between them can affect our results, producing false positive detections in our search for

variables. Therefore we investigated a possible offset between brightnesses in each band. We analysed all pairwise combinations of surveys. Each time the difference of brightness between bands from two surveys for each star was plotted. Figure 5 presents as an example the magnitudes difference between brightness in the g-band for two surveys (SDSS and PanSTARRS) for each source for which the data were available. The horizontal line marks the 0 mag value that is expected if there is no systematic offset between the surveys. Random scattering around this line is natural and can be interpreted as e.g. variability, any pattern or clustering may indicate a form of systematic offset. We cannot see any kind of offset in H, K, r, and i-bands. In Table 2 we present the results of our search for systematic offsets between photometry from different surveys. Each offset has been measured as a median value of scatter for all available points, therefore sometimes we obtained very small values. Very small values (< 0.05mag) of offset are ignored and treated as negligible.
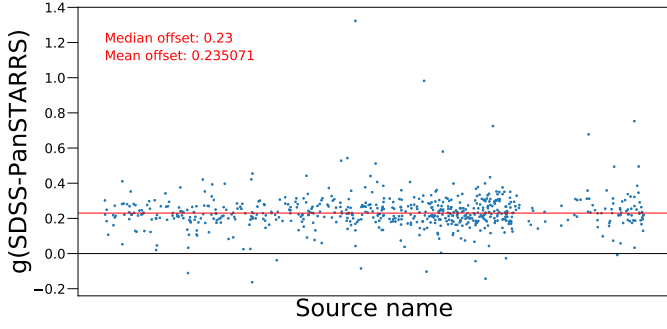
Fig. 5: The difference in g-band magnitudes for OBP members between PanSTARSS and SDSS. The horizontal black line indicates the 0 value, the red line is the offset median value of the sample. We applied the 0.230 offset correction for each point here.

Table 2: Systematic offsets in photometry adopted in this work.

Bang	Compared surveys	Measured offset
	SDSS-PanSTARRS	0.230
g	SDSS-APASS	0.079
	PanSTARRS-APASS	-0.290
	SDSS-PanSTARSS	0.012
r	SDSS-APASS	0.024
	PanSTARSS-APASS	0.027
	SDSS-PanSTARSS	-0.005
	SDSS-APASS	0.014
	PanSTARSS-APASS	0.032
i/I	SDSS-DENIS	0.725
	PanSTARRS-DENIS	0.733
	APASS-DENIS	0.605
z	PanSTARSS-UKIDSS	-0.679
	2MASS-DENIS	0.000
J	2MASS-UKIDSS	0.061
	UKIDSS-DENIS	0.060
	2MASS-DENIS	0.012
K	2MASS-UKIDSS	0.016
	UKIDSS-DENIS	-0.026
H	2MASS-UKIDSS	-0.030

We can find an offset in the g band between SDSS and PanSTARRS, and PanSTARRS and APASS surveys. We also find significant offset in z band. We investigated if the offsets are correlated in any way with the temperature of stars, in order to evaluate the correction. In Figure 5 we present the variation of the $\Delta g_{\mathrm{SDSS-PanSTARR}}$ with the $(r-i)_{\mathrm{SDSS}}$ color. We use $(r-i)_{\mathrm{SDSS}}$ color as a spectral index indicator following Davenport et al. (2014). There is no obvious correlation between them, therefore we assume that the offset is independent of stellar temperature and can be easily corrected by applying the constant correction value. We adopted the median of $\Delta g_{\mathrm{SDSS-PanSTARRS}}$ as a correction value, therefore the brightness of each source in $g_{\mathrm{PanSTARRS}}$ band should be increased by 0.23 mag. The maximum errors values are 0.04 mag and 0.086 mag for SDSS and PanSTARRS respectively.

4.2. Variability estimation

In Section 3.1 we described a very effective and commonly used method to find candidates for variable stars, namely the Stetson index method. Even though the formal lower limit in data required to calculate the Stetson index is two data points in a single filter, a large number of data points provides more reliable results. Therefore we decided to not use it for the photometry combined as measurements from different surveys presented in the section above. In order to identify sources that may present some variability, we compare the brightness measurement for each star from similar band pairwise (two bands at the time). The difference between two magnitudes ($\Delta_{\mathrm{band}} = \mathrm{mag}_{\mathrm{band1}} - \mathrm{mag}_{\mathrm{band2}}$) is compared against the estimated significance level ($\sigma_{\Delta\mathrm{band}} = \sqrt{\sigma_{\mathrm{band1}}^2 + \sigma_{\mathrm{band2}}^2}$) for each source separately.

4.3. g-band variability

We calculated differences in magnitudes between fluxes in g-bands from SDSS, PanSTARRS and APASS surveys for each source. In Table 3 we present a quick overview of g-band photometry from each survey. The first column shows the survey/band name. The second column contains a number of sources from OBP sample with measurements in a certain band (note that not all sources have the measurement with errors). Columns 3 to 5 give the mean, maximum and minimum brightness in g band for the sources in OBP (in mag). The coverage of all surveys is good enough to provide us a sample that is large enough to be considered as worth to investigate.

Figure 6 presents the distribution of differences in g-band magnitudes based on SDSS, PanSTARRs and APASS survey photometry measurements. Each panel shows a pair of compared surveys. In total 659 or 89, if we consider the APASS survey, sources have the measurements in both bandpasses with available error (blue filled histogram). With the red histogram, we present the amount of sources where the difference in brightness is larger than $|\Delta_g| > 3 \cdot \sigma_{\Delta g}$.

In Table 4 we present a sample of sources with significant changes in g-band brightness if compared between surveys. The first column gives the source number which is the ID of the source from OBP catalog. The next three columns contain the g-band magnitudes and associated errors, for SDSS, PanSTARRS and APASS, respectively. The final two columns give the absolute value of the calculated difference $|\Delta_g|$ and related level of significance $\sigma_{\Delta g}$ values.

The SDSS survey data has been dated to 2017, the PanSTARRS survey began in 2014 and the APASS between 2010 and 2015. However, it is almost impossible to investigate the time between two separate observations for each source. Our selection criterium, even though it takes measurement errors into account and is set to be at the level of 3σ, is more relaxed than the one used by Briceno et al. (2018) or Robitaille et al. (2007). Using our criterium we cannot identify all stars that are classified as variable in the GCVS catalog (only four sources fulfill our criterium).

The same kind of analysis has been done not only for the g-band differences but for all available pairs of bands. In

Table 3: g band photometry.

Band/ Survey	Number of sources	Brightness [mag] Mean	Min	Max
SDSS	664	18.7	15.4	21
PanSTARRS	658	18.5	15.4	21
APASS	89	16.8	15.4	18

Table 4: The sample of sources with variability in g-band.

Source	g SDSS	g PanSTARRS	g APASS	$|\Delta_g|$	σ_{Δ_g}
545748	19.109±0.014	18.661±0.034		0.448	0.037
437882	19.835±0.016	19.340±0.010		0.495	0.019
360225	16.401±0.004	15.649±0.025		0.752	0.025
434955		17.498±0.011	17.451±0.008	0.047	0.014
301705		17.393±0.012	17.263±0.026	0.123	0.029
58076		16.134±0.014	15.963±0.035	0.171	0.038
381356	17.467±0.005		17.117±0.115	0.350	0.115
102382	17.463±0.005		17.082±0.000	0.381	0.005
266683	17.914±0.006		17.439±0.065	0.475	0.065
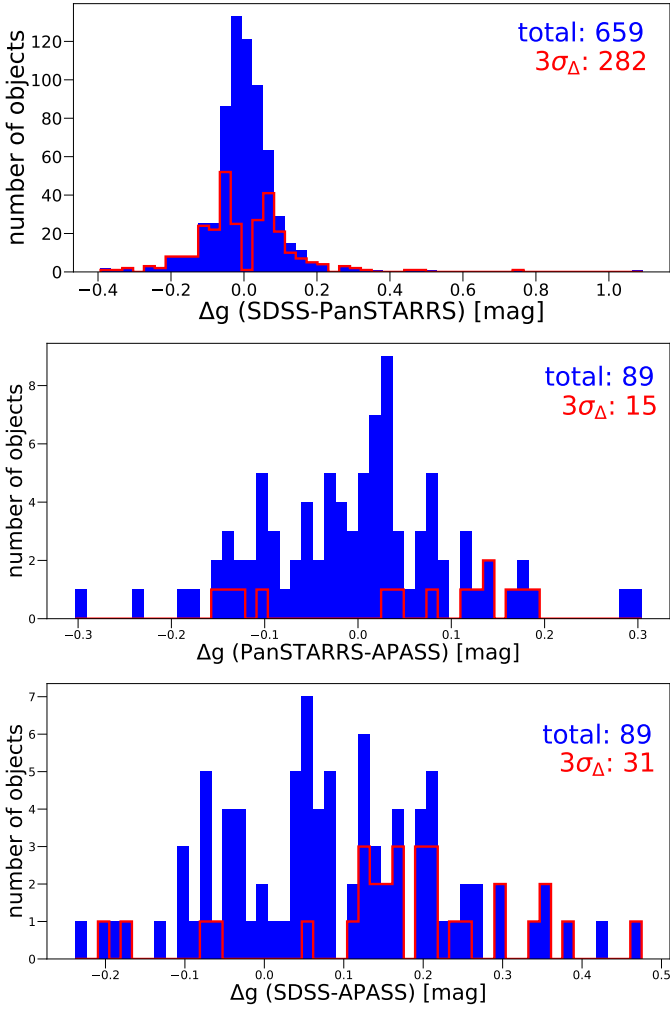
Fig. 6: The distribution of differences in g-band magnitudes compared pairwise (blue histograms). The red histograms shows differences larger than 3σ. The initial sample size and the number of stars selected as probable variable are listed with blue and red labels.

Table 5 we summarize the results from the variability check in each pair of filters. The first column gives the name of the band that was analyzed, the second provides the names of the surveys from which we took data to the analysis. Since this way of looking for the variable candidates works only if a star has certain band measurement in both considered surveys, this restricted the size of the sample we can work with substantially. The third column in Table 5 gives the number of stars in OBP sample that have measurements in both surveys. The next column gives the number of sources that have brightness changes at the level of 3σ or larger. The % values in the fifth column are calculated in relation to the total value from column 3, not to the total size of OBP (which is 664). This cannot be treated in any case as any indicator of an amount of variable stars in OBP, but shows us how robust the 3σ criterium is. The next two columns (labeled maximum and minimum) give the extreme of the results (maximum and minimum brightness changes that fulfilled appropriate criteria). By presenting this table we want to illustrate how complex and and important is variability of young stellar sources. The detailed analysis of variability in each band (each pair for every band) showed a few interesting aspects.

First of all we do not have data in any bands-pair for 1 star (Source 598625). For two stars where data are available the 3 σ is not fulfilled in any case. There are 30 stars that in each of available band pairs are always getting differences in brightness on the level above 3σ. We do not have sources with photometry measurements with errors in every possible band and the brightness changes larger than 3σ. There is no clear pattern that we were able to identify here. The critical discussion of the validity of a categorical syllogism presented here is hard to carry out. We cannot find any arguments that the variability in one certain band should be larger/smaller or should occur more/less often. Nevertheless this simple exercise shows how complex the variability estimation can be and that it may be impossible to create a complete census of variable candidates as a result. We decided to investigate the possible variability in OBP in optical ($ugriz$) and near-infrared (JHK) bands separately. For the source to be selected as variable we insist for the brightness changes at the level of 3σ or larger for at least two band-pairs.

We have 645 stars for which we have data in at least 2 band pairs, 271 in optical and 402 in IR. 81 stars show variability in at least two optical bands while 19 show variability in at least 2 infrared bands. 291 stars show variability in one optical and one IR band. In total, we find 391 variables in a sample of 645 stars for which we have enough data.

5. Variable star candidates selection

A star has been identified as variable under one of the following conditions:

- Stetson index calculated for *W1* and *W2* is larger than 0.5 or smaller than −0.3
- the brightness change in *griz*-bands analysis gives in at least two cases values greater than 3σ
- the brightness change in *JHK*-bands analysis gives in at least two cases values greater than 3σ
- the stars has already been marked as variable in the GCVS catalog

In Table 6 we present the list of variable candidates. The columns presents the source name, its position (RA, Dec coordinates), *g*-band brightness and *Gaia* DR2 distances with errors, in the first five columns. The last four columns presents the variability condition *flags*. SI means that the Stetson index I_{W1W2} condition is satisfied, VIS and NIR means that the source qualifies as variable by the brightness changes conditions in optical and near-infrared respectively, GCVS points out the sources identified before. The full version of the table is presented at the end of the paper. To summarise and for better understanding this results we decided to use a graphic representation, well known Venn diagrams (Quine 1982). In Fig 7 we present a modification of Venn diagram for our sample. Each variability criterium is presented with a different colour. We have a sample of 83 variable candidates identified by Stetson index and presented with the green ellipse. 405 visible and 18 NIR candidates represented by yellow and blue ellipses, respectively. The sizes of ellipses are not normalised to the size of the sample. This diagram allows us to easily quantify the mutual interplay between criteria. One can easily see that not a single star can be selected as variable candidates based on all four criteria. There are three stars that are consider as variable only because they are part of GCVS catalog. In total 10 members of OBP are part of the GCVS, 3 of them are also variable based on optical (VIS) criterium, 1 based on optical and NIR. The last 3 stars from the GCVS common sources are also selected as variable based on the Stetson index value.

6. Consequences of variability among YSO

As presented already in Section 3 we can identify 83 stars as variable candidates based on the mid-IR multi-epoch survey AllWISE. To the best of our knowledge this is the only multi-epoch survey with publicly available data, therefore it is the most reliable tool to investigate variability among stars in OBP. Variability is an important and complex issue among YSO. By making use of the AllWISE multiepoch photometry database we can investigate the influence of variability into our overall understanding of OBP.
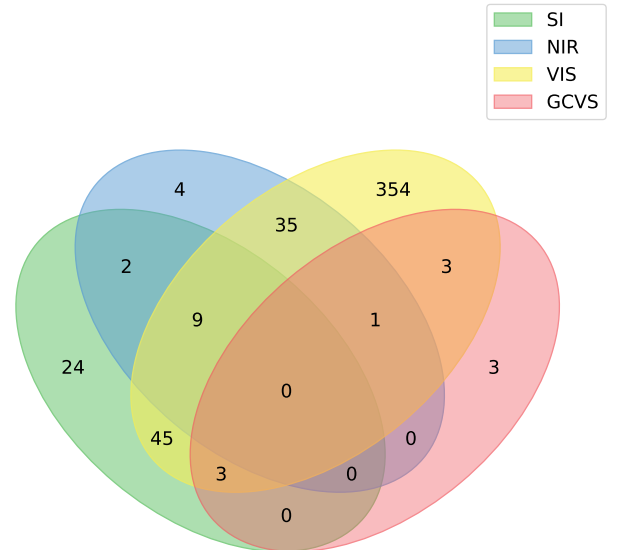
Fig. 7: Venn-diagram for variability selection criteria. Ellipses corresponds to the different variability criterium. Red ellipse illustrate the GCVS variable stars. Blue and yellow ellipses shows the results from the NIR and VIS selection criterium, respectively. With the green ellipse we present the Stetson index selection results.

6.1. Spectral index variations

The spectral index (α) has been defined in Lada & Wilking (1984) and Lada (1987) as:

$$\alpha = \frac{d\log(\lambda F_\lambda)}{d\log(\lambda)} \tag{1}$$

Lada & Wilking (1984) used the spectral index calculated between near- and mid-infrared bands to classify YSOs into three distinct classes (Class I – III). The original classification scheme has been widely used in the community and modified many times (in terms of used bandwidth, borders between, and/or number of distinctive classes). In Table 7 we present the classification scheme from Teixeira et al. (2012). We calculated the spectral index for stars selected as variable based on Stetson index criterium (see Section 3.1). Spectral indices were calculated in the same way as in Kubiak et al. (2018), using the Python polyfit routine based on flux measurements from $W1$, $W2$, $W3$, and $W4$. We deliberately calculate the spectral index from $W1$ to $W4$ without K since we do not have K band data taken simultaneously with AllWISE.

If the source is variable and if we are able to observe it with time steps we can derive the slope for each time point and analyze the evolution of the spectral index. The AllWISE Multiepoch photometry database provides us the possibility to investigate the evolution of the spectral index derived from $W1$-$W4$. We excluded the K_s band on purpose since we do not possess any data useful for our study as mentioned before.

Table 5: Results from the variability check in each pair of filters as described in Sec. 4.3.

band	Surveys	Total	3σ	%	maximum			minimum		
					source	value	sigma	source	value	sigma
g	SDSS-APASS	89	31	35	266683	0.475	0.065	58199	-0.059	0.005
	SDSS-PanSTARRS	659	282	43	360225	0.752	0.025	599841	0.020	0.006
	PanSTARRS-APASS	89	15	17	102382	0.304	0.003	331951	0.290	0.009
r	SDSS-APASS	87	25	29	2944577	0.362	0.097	196588	-0.017	0.005
	SDSS-PanSTARRS	661	365	55	360225	0.479	0.004	452025	0.014	0.004
	PanSTARRS-APASS	87	21	24	294457	0.326	0.098	164407	-0.027	0.004
i	SDSS-APASS	92	20	22	294457	0.387	0.124	83338	-0.027	0.004
	SDSS-PanSTARRS	664	428	64	360225	0.479	0.004	398071	0.014	0.004
	SDSS-DENIS	546	82	15	393168	1.001	0.240	58942	-0.085	0.0207
	PanSTARRS-APASS	92	14	15	363598	0.279	0.046	83338	0.016	0.002
	APASS-DENIS	78	4	0.5	139781	0.199	0.034	581778	-0.155	0.043
	PanSTARRS-DENIS	544	368	68	143277	1.227	0.140	375854	0.181	0.040
z	PanSTARR-UKIDSS	180	179	99	863598	0.906	0.021	289109	0.447	0.076
J	2MASS-UKIDSS	147	8	0.5	289109	-0.748	0.030	358646	0.091	0.023
	2MASS-DENIS	543	73	13	352190	-1.566	0.271	312490	0.156	0.048
	UKIDSS-DENIS	135	30	22	352190	-1.547	0.270	312490	0.148	0.040
K	2MASS-DENIS	474	32	7	117476	-0.93	0.023	358402	-0.353	0.113
	2MASS-UKIDSS	180	17	9	286438	-1.07	0.021	147195	0.067	0.021
	UKIDSS-DENIS	133	15	11	286438	0.986	0.110	358402	-0.369	0.110
H	2MASS-UKIDSS	174	26	15	312490	-0.856	0.023	308500	-0.071	0.023

Table 6: The members of OBP and their variability. Only part of the table is presented here.

source name	RA	Dec	g [mag]	d [pc]	flag VIS	flag NIR	flag SI	flag GCVS
9622	83.255686	-3.974557	15.834±0.004	347^{+11}_{-11}	VIS		SI	GCVS
27823	80.986564	-1.649833	17.474±0.005	329^{+63}_{-5}			SI	
30198	85.449493	1.361596	20.837±0.028	353^{+27}_{-}	VIS		SI	
33269	83.251648	1.734059	19.639±0.012	336^{+203}_{-183}			SI	
39200	85.628171	1.16814	19.813±0.015				SI	
71378	85.966127	0.610869	17.201±0.005	393^{+102}_{-10}	VIS	NIR	SI	
72659	83.029894	-3.658706	20.897±0.033	361^{+345}_{-294}		NIR	SI	
81889	81.503622	0.038833	19.888±0.014		VIS		SI	
607513	83.826168	-1.014437	18.465±0.008	463^{+45}_{-37}			SI	

Table 7: Source classification scheme using α_{WISE} adopted from Teixeira et al. (2012).

Source classification	α_{WISE} value
Class I (C I) sources	≥ 0.5
Flat spectrum (FS) sources	$-0.5 \ldots 0.5$
Sources with thick disks (TD)	$-1.8 \ldots -0.5$
Sources with anaemic disks (AD)	$-2.56 \ldots -1.8$
Sources with naked photospheres (NP)	≤ -2.56

In Fig. 8 we present the evolution of slopes calculated from W1 to W4 bands. Each vertical blue line corresponds to the change of slope value for one star. The black vertical lines indicates the approximate borders of spectral types for M2 – M5 stars. Horizontal red lines indicate the values used to distinguish between Classes (see Table 7). It is clearly visible that more than half of the sources exhibit slopes changes large enough to change the classification of the source, in some cases the change is large enough to cause the 'misclassification' of the source by two classes. In their study of YSOs in Cygnus OB7, Rice et al. (2012) showed that over 1.5 years, 36% of stars that show a K-band excess will drift in color-color space between 'having an excess' and 'not having an excess'. The misclassification of sources leads to false statistics of the basic star forma-tion observables for the region (e.g., ages, age spread, SFR, mass function, disk frequency, etc.).
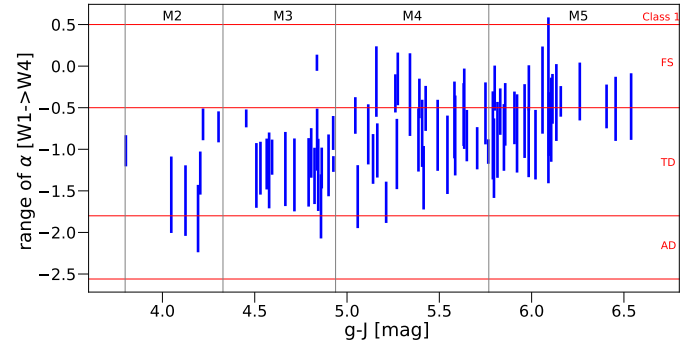
Fig. 8: The change of spectral index as a function of $g - J$ color.

6.2. Variability as a Function of Class

Young stars are known to be more variable than main-sequence stars. Using the evolutionary classes associated with the stars in our sample, we can refine this observed trend and investigate the variability associated with each

class. As discussed in Section 6.1, we obtain evolutionary classes for all of our variables selected based on the Stetson index; we also know classes for non-variable sources from Kubiak et al. (2018). A large fraction of these are identified as stars with disks: among 638 stars (for which we have enough data to calculate the Stetson index, both variable and nonvariable), 16 are flat spectrum sources (FS) and 472 and 141 have disks, thick (TD) or anaemic (AD) respectively, while only 13 have no disks. The Stetson index statistics presented below are from this sample.
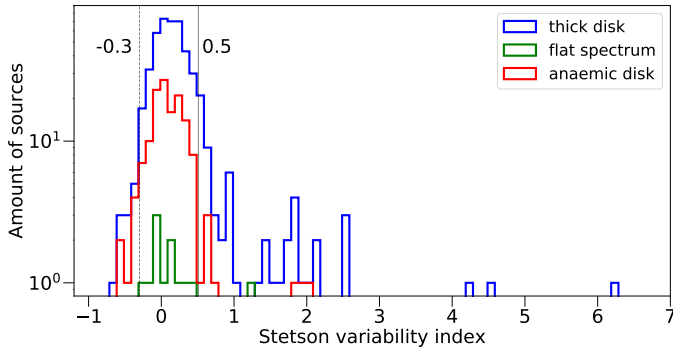
Fig. 9: Stetson index distribution within each YSO class.

In the following analysis we restrict ourselves to the 83 (13%) variables with classes, of which 71 (15%) are TD, 11 (7.8%) are AD and 1 (8.33%) is FS. The sources with disks have a mean Stetson index of 0.12 for anaemic disk sources, 0.17 for FS and 0.36 for TD (see Figure 9). Since the Stetson index is an aggregate of behavior across two bands, we analyze variability strength at different wavelengths among variable stars by inspecting amplitudes in each band. We find the TD are more variable: median $\Delta W1 = (W1_{max} - W1_{min}) = 0.241$ mag while the corresponding value for the other variables with disks is 0.212 ± 0.063 mag. Only one flat spectrum source is variable with the $\Delta W1 = 0.176$ mag. The distributions are presented on the left column of Fig. 10.

The color terms $\Delta(W1\text{-}W2)$ and $\Delta(W2\text{-}W3)$, measured as the difference between maximum and minimum color values show similar trends: color shifts are smaller for more evolved stars. As an example we show the results for changes of the $\Delta(W1\text{-}W2)$ color in Figure 10 (right panel). We primarily use the $\Delta(W1\text{-}W2)$ color term to probe changes in the disk excess. Indeed, we find the median $\Delta(W1 - W2) = 0.288 \pm 0.13$ for the anaemic disk variables, $\Delta(W1 - W2) = 0.264 \pm 0.116$ for the thick disk variables and $\Delta(W1 - W2) = 0.163$ for the flat spectrum source.

It is further interesting that thick disk sources are significantly more variable than more evolved anaemic disk systems. The AllWISE bands should only be measuring the disk, and the innermost edge of the dust disk. Thus, the inner disk edge and/or the star-disk interface can have a different structure between different disk source classes. The least evolved young stellar objects show stronger and likely more frequent instabilities and variability due to the distribution and stability of the hottest circumstellar dust grains, thought to be responsible for mid-infrared band excesses.

6.3. Light curves

For each variable star listed in Table 6 as SI, a figure has been generated showing the *W1* , *W2* , light curves for the time-series data. It is not feasible to present figures for all 83 variable stars here. Many of the stars display unique variability characteristics that can only be appreciated from inspection of these figures. Each figure is divided into 2 panels where the left presents the data collected in the first observing season (∼March 2010) and the right approximately six months later (∼September 2010). The time step between observations is not always the same but on average it is about 30 minutes.

Some of the larger amplitude variables also display significant color variations. Figures 12 – 19 present a sampling of the observed mid-infrared variability characteristics. Figure 12 shows a star with a Stetson index of 0.91 (the adopted threshold to identify variable stars is 0.51) that exhibits correlated, low-amplitude magnitude changes in two bands. The photometric fluctuations are $\Delta W1 = 0.139$ mag and $\Delta W2 = 0.225$ mag, and the stellar colors become bluer as the star gets fainter.

Carpenter et al. (2001) in their NIR study of Orion A measured the fraction of significant color variables that showed either a reddening behavior (associated with variable dust extinction) or blueing behavior (associated with accretion/disk activity); they found 6 times more reddening-type stars than blueing-type stars.

In this study we find 78 stars become bluer as their get fainter, thus finding substantially more blueing-type relative to their study. Whereas 5 stars do not present the signifant color changes. Part of this difference is likely to be from the fact that the region we study is older, focused on the off-cloud population in Orion, giving us less sensitivity to the types of stars likely to show large color changes. However, a large part of the difference might also come from the fact that our observed baseline covers only a few hours in two epochs separated by 6 months.

As opposed to the relatively rapid fluctuations illustrated thus far, Figure 17 shows a star that continuously brightened over the March 2010 time period. The brightness of the star has changed significantly between March and September 2010, suggesting these variations are a long term trend.

Not all stars with color changes vary continuously in time, as Figure 19 presents a star in which the photometry in *W1* was relatively constant for the first part of the observations prior to the star's becoming fainter by 0.1 mag in each band, with progressively bluer colors and variability in both bands.

7. Summary and conclusions

1. We present the first study of young stars variability for the off cloud region in the vicinity of ϵ Ori.
2. An advantage to our focus on a off cloud region of Orion, is that we have independent determination of the evolutionary classes of all of our variables (Kubiak et al. 2018), based on spectral index classification and SED modelling. Thus we can comment directly on the mid-infrared variability characteristics of young stars in different classes.
3. Four variability criteria results in 475 (72% of total number of sources) candidates in
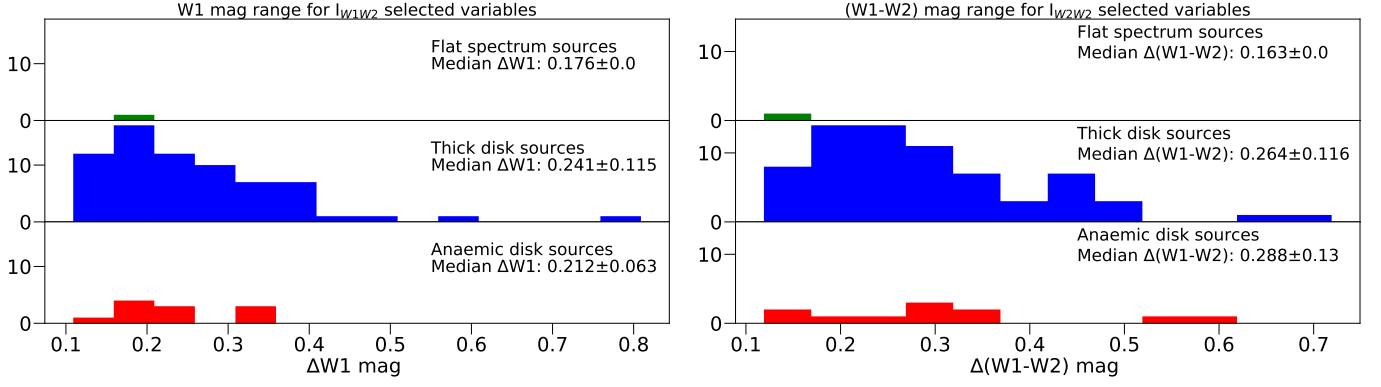
Fig. 10: The distribution of variability amplitude at W1 band and W1-W2 color, for flat spectrum, thick disk and amaemic disk sources.
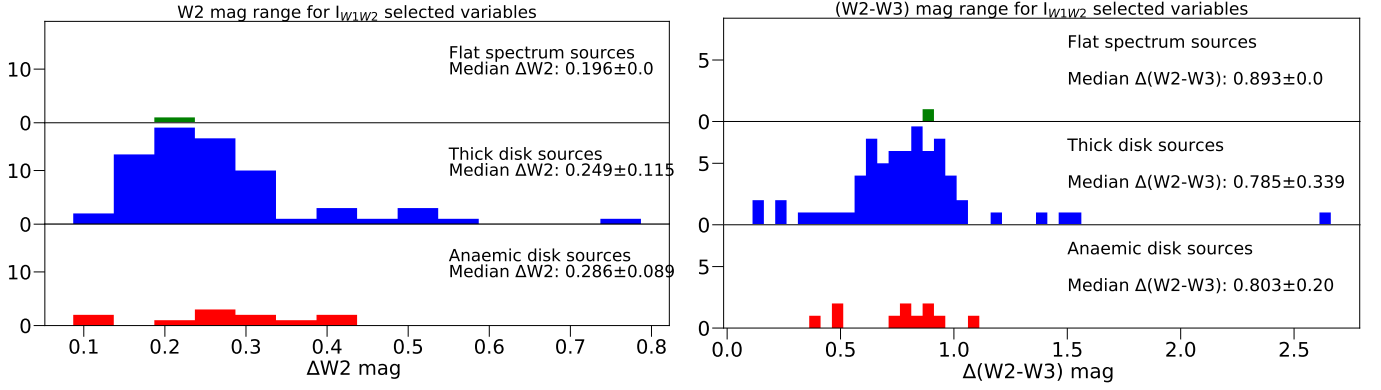
Fig. 11: The distribution of variability amplitude at *W1* band and *W1 -W2* color, for flat spectrum, thick disk and amaemic disk sources. Just to show it here i don't think we need two versions in the paper.
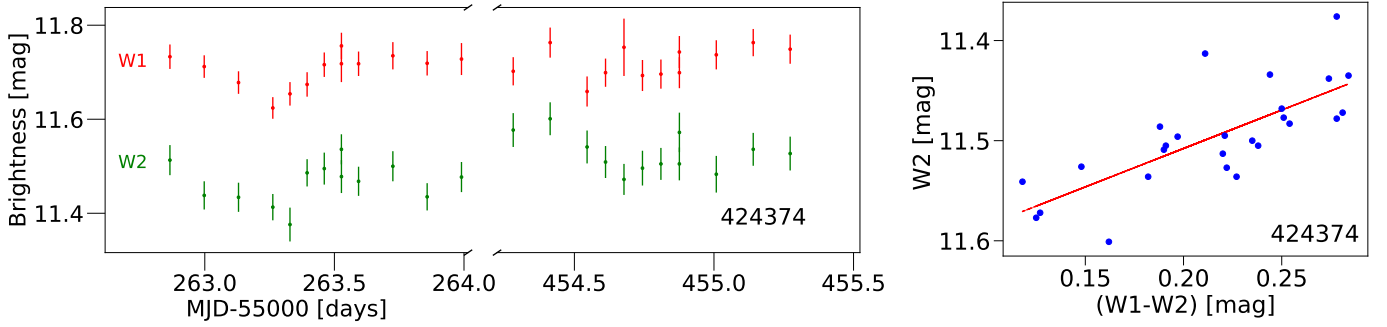
Fig. 12: Photometric data for star 424374, which has a Stetson variability index of 0.92. The left panels show the *W1* and *W2* light curves. The first data set in each light curve is from March 2010, the second data set from September 2010. The vertical bars through the data points represent the photometric uncertainties. The right panel shows the behaviour in color magnitude space. The star is getting bluer as it is getting fainter.

total selected as variable. Some stars are selected by more than one criterion.

- GCVS - 11 (0.2% of total number of sources)
- SI - 83 (12.5% of total number of sources)
- NIR - 51 (7.7% of total number of sources)
- VIS - 450 (67.8% of total number of sources)

Table 8 presents the summary of statistic among stars selected as variable by different variability criteria within each YSO class. The total amount of sources and the percentage values in brackets refer to the member-

ship of OBP, not taking the coverage in data into account. How the data coverage restrict our study for each variability criterion are described in respective paragraphs of the paper. Hence the statistics presented here should be interpreted as a lower limits for amount of variable stars.

4. The paper presents time series photometry of 83 variable stars in the OBP region identified by the Stetson index based on data available in the All-WISE Multiepoch Photometry database:
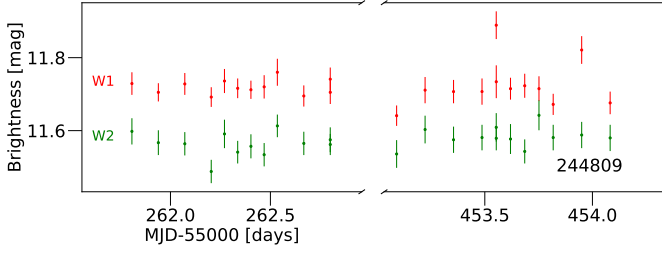
Fig. 13: Photometric data for star 244809 with the SI=0.52. Light curve for *W1* and *W2* exhibit the same 'single point' dropping pattern.
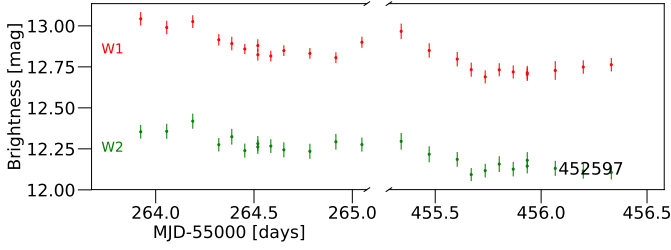
Fig. 14: Photometric data for star 452597. Stetson index is 4.28. Light curves for *W1* and *W2* exhibit very similar patterns.
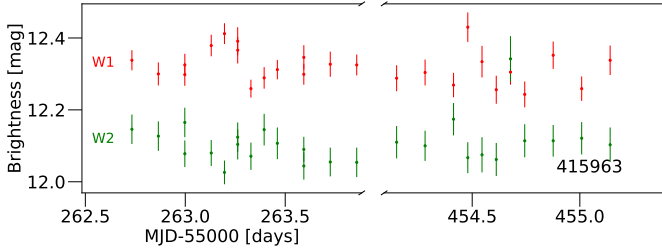
Fig. 15: Photometric data for star 415963 with a Stetson index of -0.58. Light curves for *W1* and *W2* presents opposite in phase brightness changes. The minimum brightnees of *W1* occures at the same time as maximum for the *W2*
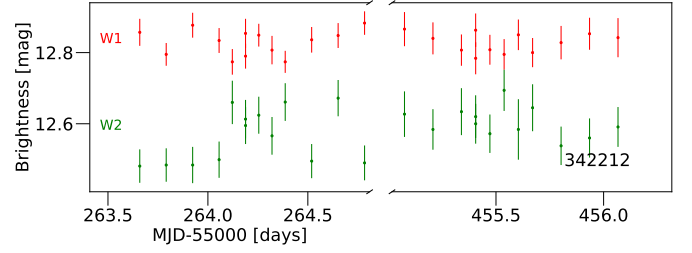
Fig. 16: Photometric data for star 342212. The light curves for *W1* and *W2* in March 2010 present brightness changes that are opposite in phase, i.e. the minimum brightness of *W1* occurs at the same time as the maximum for *W2*. for For the later observing period in September 2010, both light curves seem be in the same phase. The Stetson index is equal to -0.42.
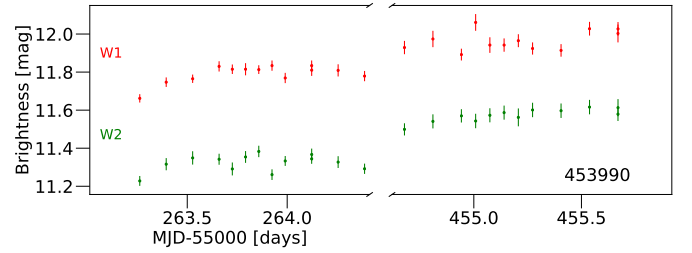
Fig. 17: Photometric data for star 453990 (SI=12.2), an example of a star that steadily increased in brightness in the March 2010 time period. The September 2010 photometry though indicates that this has been a long term trend.
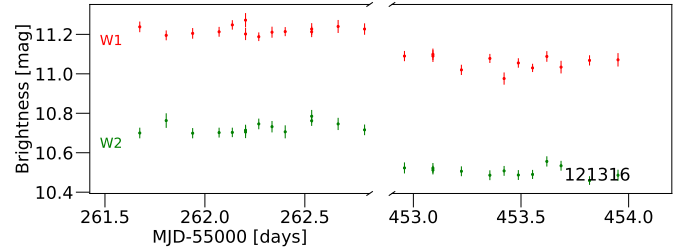
Fig. 18: Photometric data for star 121316 (SI=12.82), an example of a star that decreased in brightness in the March 2010 time period. The September 2010 photometry though dedicates that this has been a long term trend.

- The observed variability varies widely. Qualitatively different morphological types of light curves can be distinguished: 21 long-term variable light curves where the brightness decreased (7 stars) or increased (14 stars) from the first to the second observing epoch; light curves where variability is apparent to be in the opposite phase for W1 and W2 (4 stars), or light curves that have similar features simultaneously in both W1 and W2 (4 stars); there are two light curves that show similar features in one epoch and opposite features in another. In addition, there are light curves with short, nonrepeating bursts or dips seen only in one of the observing epochs.
- color behavior in *W2*-*W1* vs. *W1* color-magnitude space contains information about physical processes behind variability. The dominant processes causing color-variability involve dust extinction and accre-

tion/disk activity or geometry. In the MIR, most stars show color changes consistent with changes in the disk structure (Espaillat et al. 2010; Wolk et al. 2013; Günther et al. 2014).
- Among 638 stars analyzed in this study, we identify 472 thick disk stars of which 71 (15 %) are variable with amplitude $\Delta W1 > 0.1$ mag, 141 anaemic disk stars with 11 (7.8 %) variable with amplitude $\Delta W1 > 0.15$ mag. Out of 12 flat spectrum sources only one is variable $\Delta W1 = 0.176$ mag (6 %). None of the diskless sources has been identified here as variable in MIR.

Table 8: Sources selected as candidates variable stars in each YSO class.

	Total	SI	NIR	GCVS	VIS	non-variable
ClassI	0	0	0	0	0	0
FS	16	1 (6.25%)	1 (6.25%)	0	7 (43.75%)	7(43.75%)
TD	484	71 (14.7%)	37(7.64%)	6(1.24%)	316 (65.29%)	54(11.16%)
AD	147	11 (7.48%)	11 (7.48%)	3 (2.04%)	116(78.91%)	6(4.08%)
NP	17	0	2 (11.74%)	1 (5.88%)	11(64.7%)	3(17.65%)
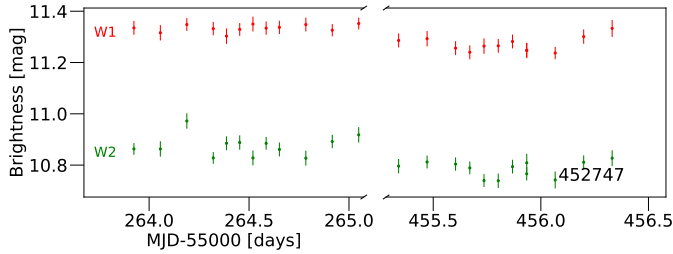
Fig. 19: Photometric data for star 452747, an example of a star that in *W1* appears to be non-variable in March 2010 and variable in September 2010. Moreover the Stetson index for this star is 1.16.

References

Ahn, C. P., Alexandroff, R., Allende Prieto, C., et al. 2014, ApJS, 211, 17
Bayo, A., Rodrigo, C., Barrado Y Navascues, D., et al. 2008, Astronomy & Astrophysics, 492, 277
Billot, N., Morales-Calderón, M., Stauffer, J. R., Megeath, S. T., & Whitney, B. 2012, ApJ, 753, L35
Briceno, C., Calvet, N., Hernandez, J., et al. 2018, ArXiv e-prints
Carpenter, J. M., Hillenbrand, L. A., & Skrutskie, M. F. 2001, AJ, 121, 3160
Chavira, E., Gonzalez, G., Escamilla, C., & Parsamian, E. 1992, Information Bulletin on Variable Stars, 3764
Chavira, E. & Parsamian, E. 1991, Rev. Mexicana Astron. Astrofis., 22, 15
Cutri, R. M., Wright, E. L., Conrow, T., et al. 2013, VizieR Online Data Catalog, 2328, 0
Davenport, J. R. A., Ivezić, Ž., Becker, A. C., et al. 2014, MNRAS, 440, 3430
DENIS Consortium. 2005, VizieR Online Data Catalog, 2263
Espaillat, C., D'Alessio, P., Hernández, J., et al. 2010, ApJ, 717, 441
Fedorovich, V. P. 1960, Peremennye Zvezdy, 13, 166
Gaia Collaboration, Brown, A. G. A., Vallenari, A., et al. 2018, ArXiv e-prints [arXiv:1804.09365]
Günther, H. M., Cody, A. M., Covey, K. R., et al. 2014, AJ, 148, 122
Haro, G. & Moreno, A. 1953, Boletin de los Observatorios Tonantzintla y Tacubaya, 1, 11
Herbst, W., Bailer-Jones, C. A. L., Mundt, R., Meisenheimer, K., & Wackermann, R. 2002, A&A, 396, 513
Herbst, W., Maley, J. A., & Williams, E. C. 2000, AJ, 120, 349
Joy, A. H. 1945, ApJ, 102, 168
Kubiak, K., Alves, J., Bouy, H., et al. 2017, A&A, 598, A124
Kubiak, K., Teixeira, P. S., Köhler, R., et al. 2018, A&A, submitted
Lada, C. J. 1987, in IAU Symposium, Vol. 115, Star Forming Regions, ed. M. Peimbert & J. Jugaku, 1–17
Lada, C. J. & Wilking, B. A. 1984, ApJ, 287, 610
Lasker, B. M., Sturch, C. R., McLean, B. J., et al. 1990, AJ, 99, 2019
Lawrence, A. 2013, in Astrophysics and Space Science Proceedings, Vol. 37, Thirty Years of Astronomical Discovery with UKIRT, ed. A. Adamson, J. Davies, & I. Robson, 271

Monet, D. G. 1998, in Bulletin of the American Astronomical Society, Vol. 30, American Astronomical Society Meeting Abstracts, 1427
Morales-Calderón, M., Stauffer, J. R., Hillenbrand, L. A., et al. 2011, ApJ, 733, 50
Natsvlishvili, R. S. 1982, Information Bulletin on Variable Stars, 2231
Parihar, P., Messina, S., Distefano, E., Shantikumar, N. S., & Medhi, B. J. 2009, MNRAS, 400, 603
Quine, W. 1982, Methods of Logic
Rebull, L. M., Cody, A. M., Covey, K. R., et al. 2014, AJ, 148, 92
Rice, T. S., Wolk, S. J., & Aspin, C. 2012, ApJ, 755, 65
Robitaille, T. P., Cohen, M., Whitney, B. A., et al. 2007, AJ, 134, 2099
Roslund, C. 1969, Arkiv for Astronomi, 5, 381
Samus', N. N., Kazarovets, E. V., Durlevich, O. V., Kireeva, N. N., & Pastukhova, E. N. 2017, Astronomy Reports, 61, 80
Scholz, A. & Eislöffel, J. 2004, A&A, 419, 249
Skrutskie, M. F., Cutri, R. M., Stiening, R., et al. 2006, AJ, 131, 1163
Stassun, K. G., Mathieu, R. D., Mazeh, T., & Vrba, F. J. 1999, AJ, 117, 2941
Stetson, P. B. 1996, PASP, 108, 851
Teixeira, P. S., Lada, C. J., Marengo, M., & Lada, E. A. 2012, A&A, 540, A83
Wolk, S. J., Rice, T. S., & Aspin, C. A. 2013, AJ, 145, 113
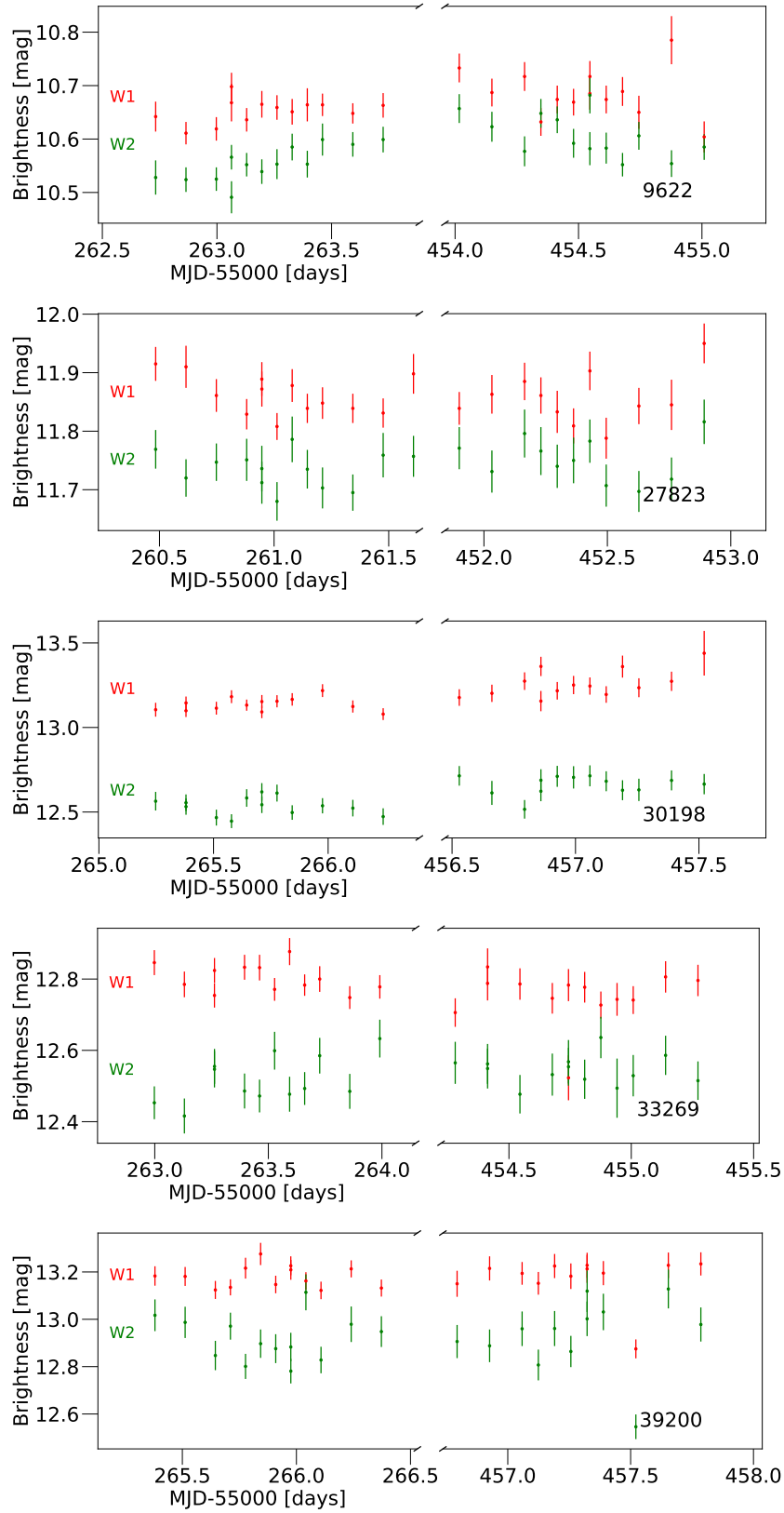
Figure 5.1: $W1$ in red and $W2$ in green light curve for the members of OBP identify as variable candidates based on Stetson index. The source ID numbers are presented in each of the figure in bottom right corner.
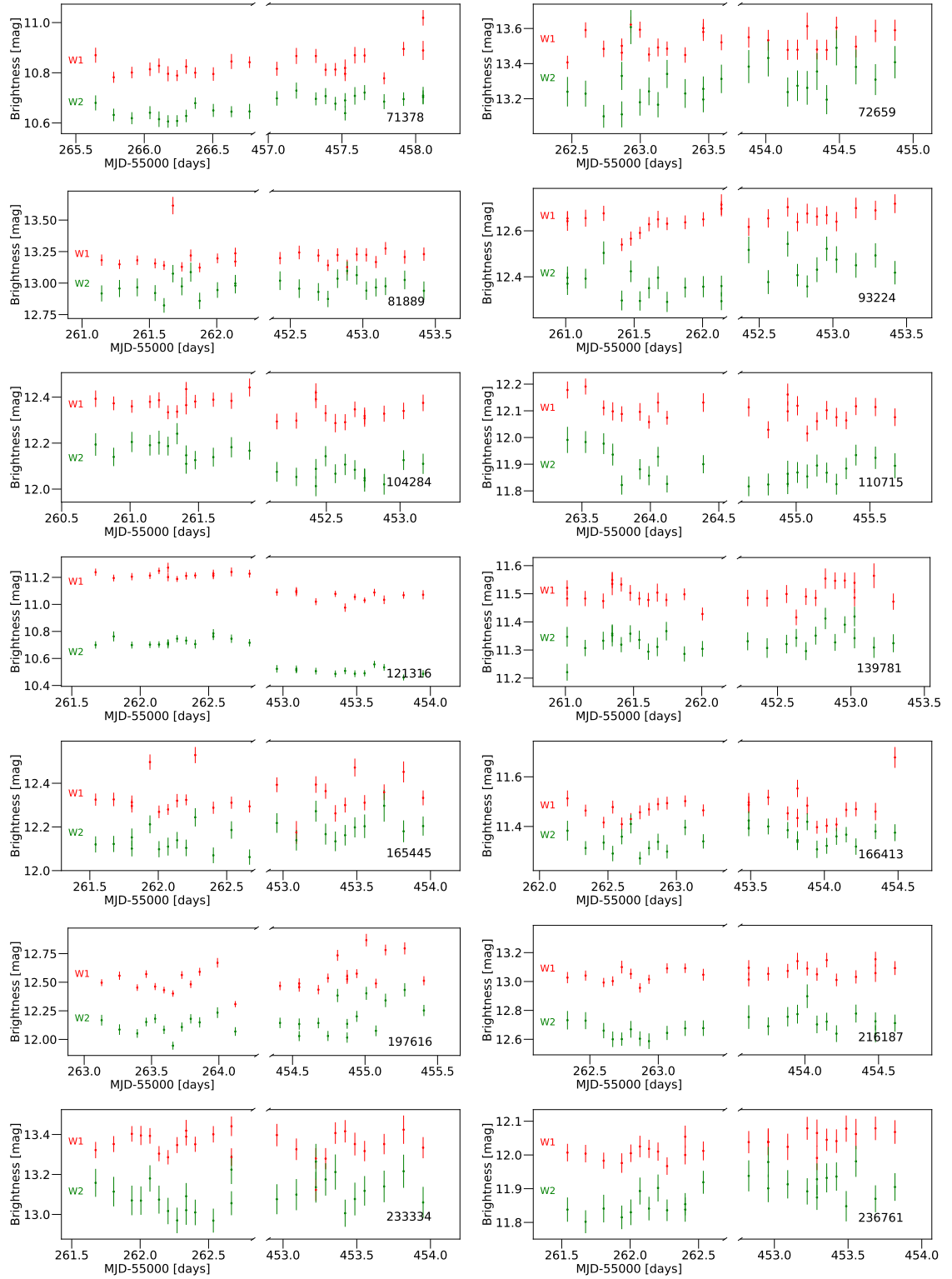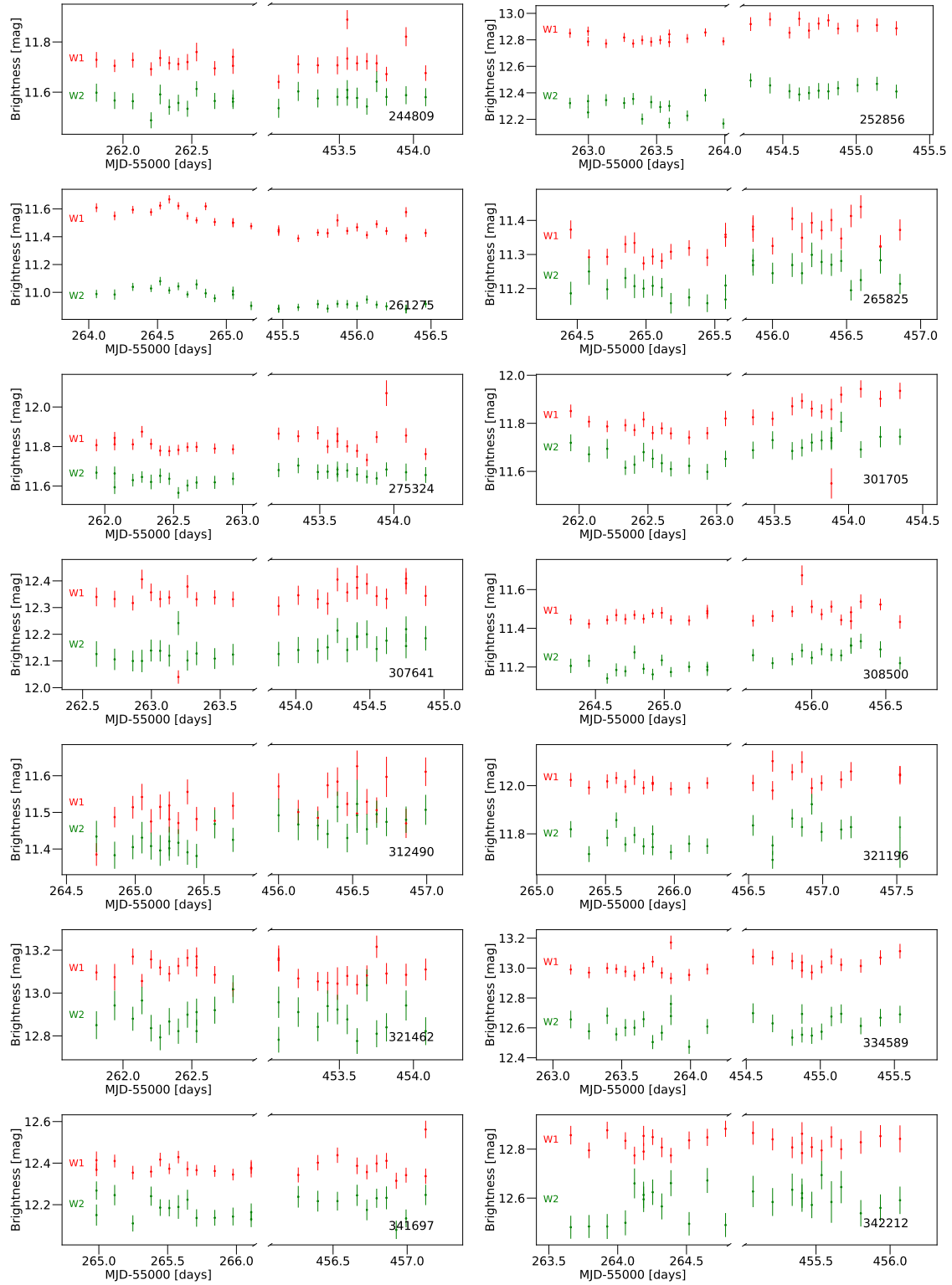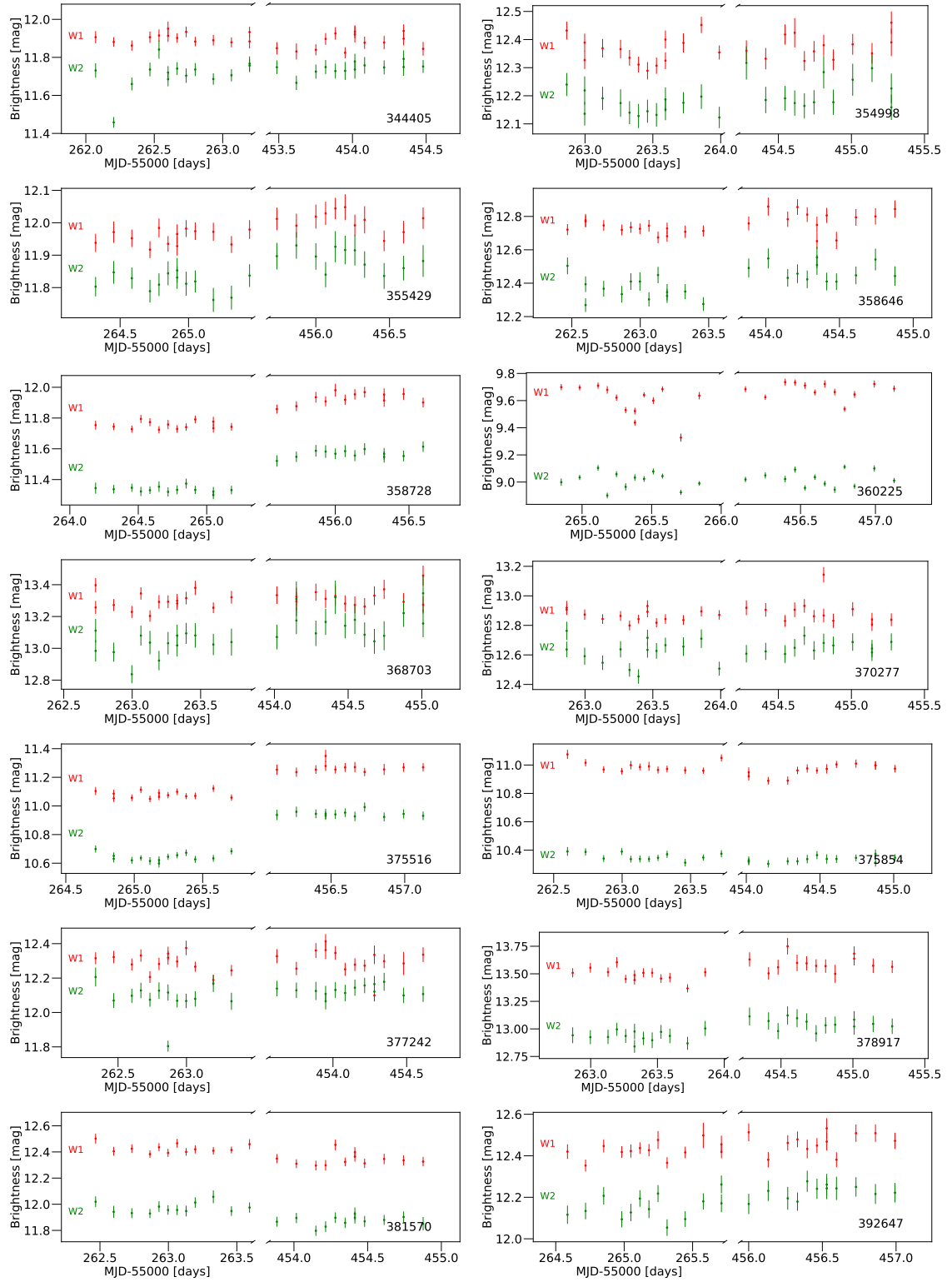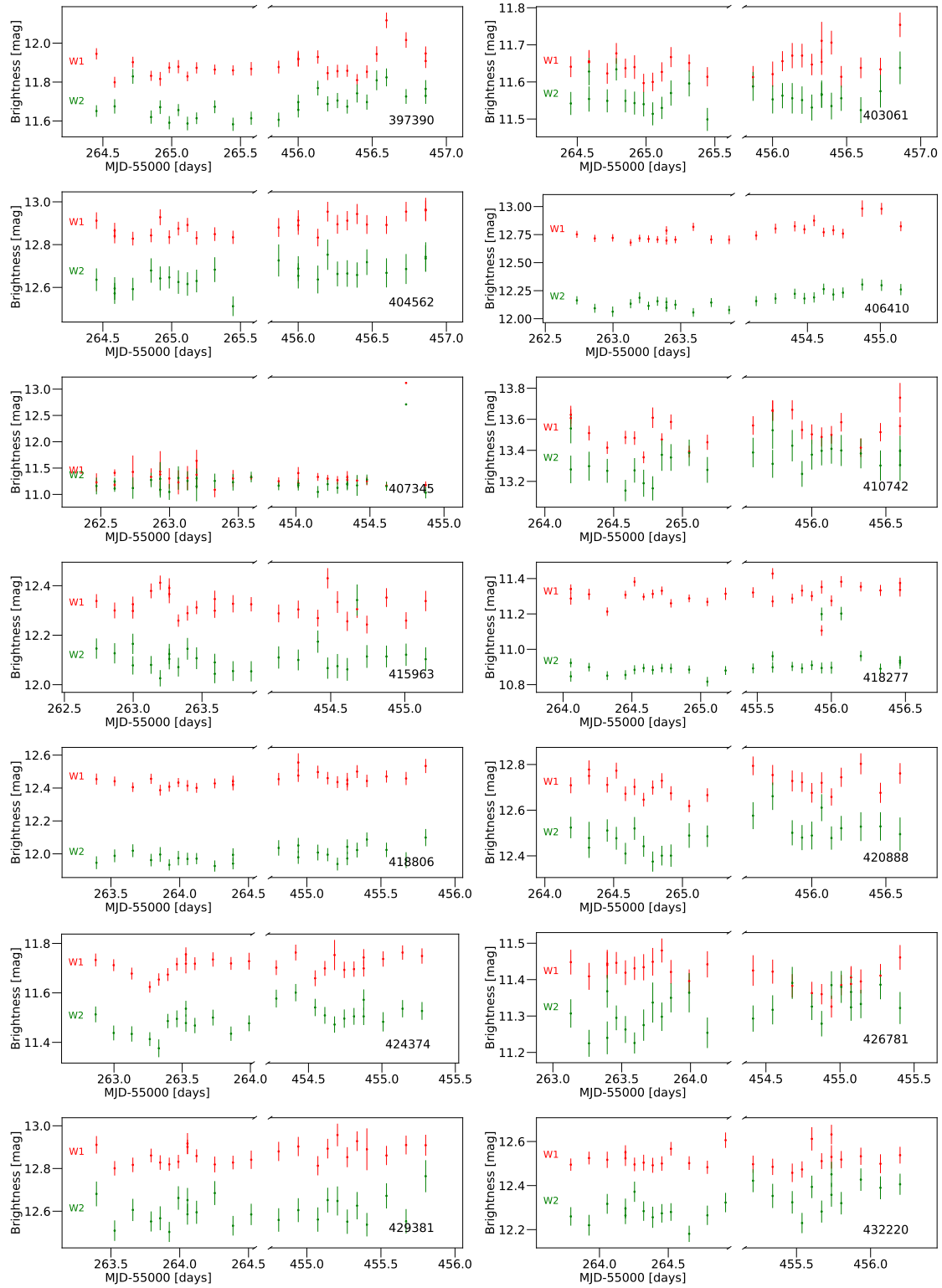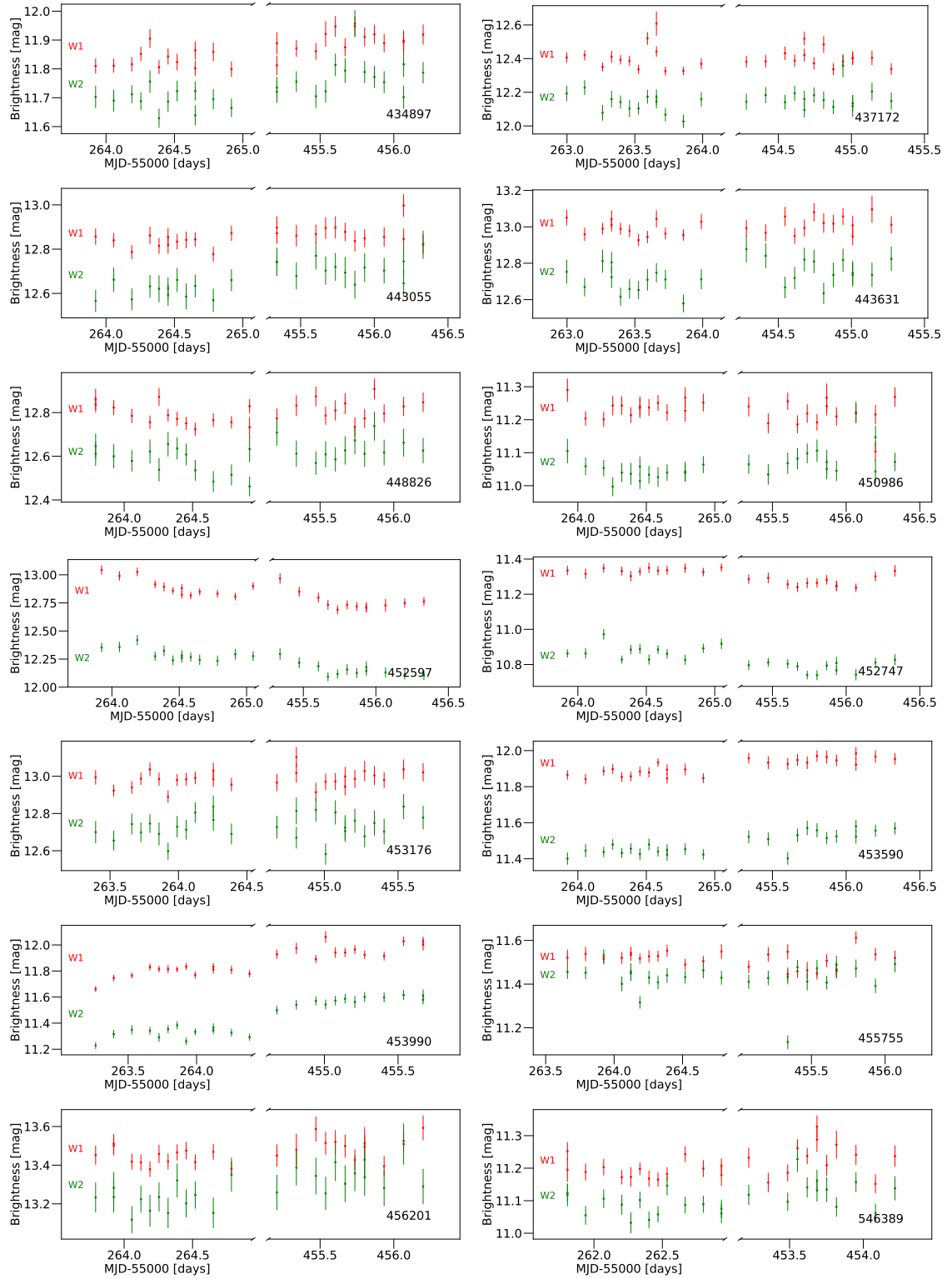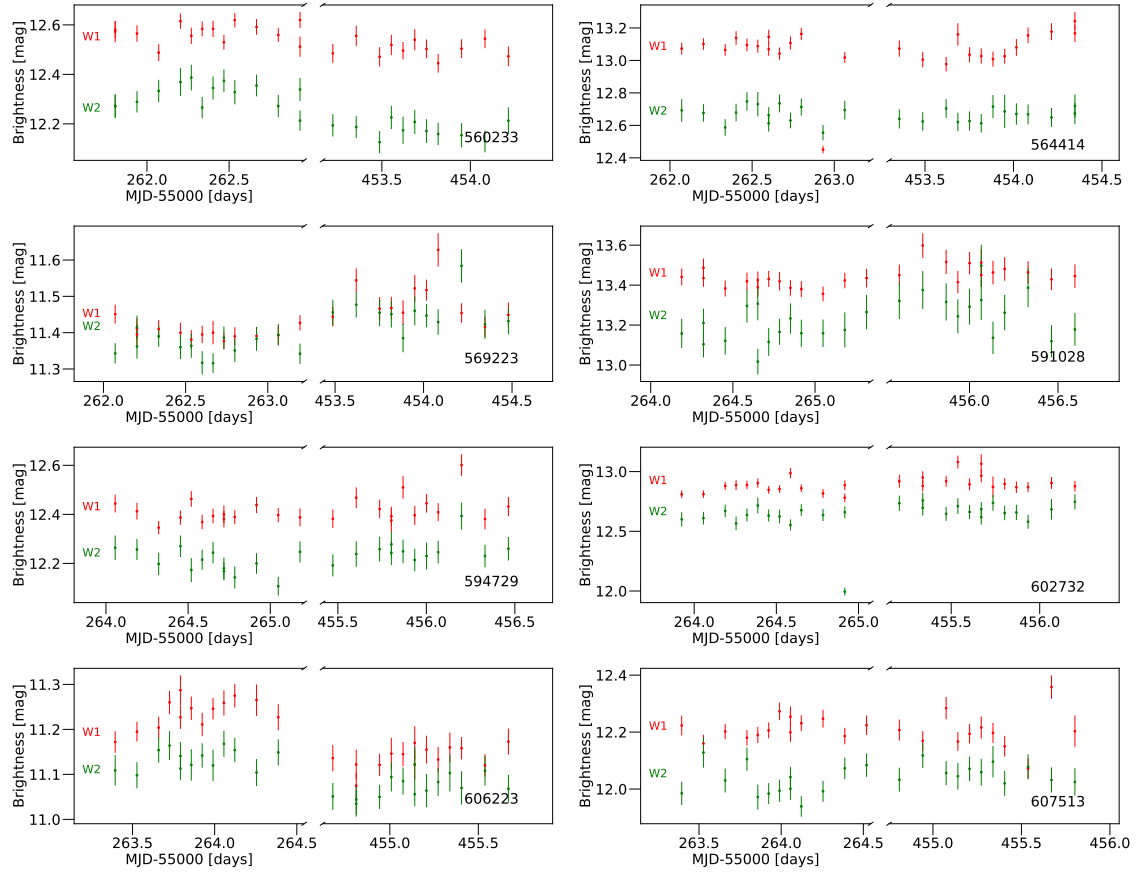
We shall not cease from exploration, and the end of
all our exploring will be to arrive where we started
and know the place for the first time.

— Thomas Sterns Eliot

6
Summary and Conclusions

The main result of this thesis is the discovery of a rich population of low-mass stars towards the Orion belt, a population we call the Orion Belt population. The discovery of this population was unexpected and raised several questions about the structure of the Orion star-forming region and OB associations in general. The thesis was then naturally built around the discovery and focused on the characterization and speculation about the origins of this population.

The extended overdensity of stars in the Orion Belt region, in particular around the ϵ Ori supergiant, has an unexpected complex structure. While the overdensity around the two nearby regions σ Orionis and NGC 2024 are uniform and compact, in line with what is expected of embedded or young clusters, the density enhancement around ϵ Ori is much more extended and shows clearly internal substructure as measured in the different density peaks. I made a first source selection for this new population based on probability estimation using a statistical multiband technique that selects objects associated with the remarkable color-magnitude sequence detected above the Galactic field. The optical and near-IR color-magnitude diagrams revealed that virtually all of the selected objects have the colors of M-stars.

The availability of the Gaia Data Release data, and in particular the availability of parallaxes for most of the Orion Belt population sources, brought an essential insight into not only correct size of the population (after interlopers were removed),

derive better physical properties, but more remarkably, to the 3D structure of this population: we found that the OBP extends for about 60 pc along the line-of-sight, comparable to its width, and is not homogeneously distributed in space. The Orion Belt population is not an expanded, dust free and older, 'Trapezium' cluster, as initially suspected.

To further characterize the OBP sources, I built Spectral Energy Distributions using the recently published models by Robitaille (2017). The SED fitting procedure to the observed data favors pre-main-sequence stars of low effective temperatures and most of them, with disks. This finding confirmed my pre-Gaia results based on optical and NIR photometry. An advantage of our focus on an off-cloud region of Orion is that we have extinction independent determination of the evolutionary classes of all of the sources, based on spectral index classification and SED modeling. The basic properties of the central source and the disk (if present) have been obtained from this modeling. Due to lack of FIR/submm observations for the region we interpret these values as upper limits to the true disk masses. We are currently exploring possibilities of obtaining long wavelength data for the OBP region to further constrain the disk masses of the population.

Finally, I pursued an investigation into the variability of the OBP sources. The mid-infrared variable candidates were selected based on AllWISE multi-epoch photometry, while optical and near-infrared surveys were searched to further complement this analysis. I find that the statistics among stars selected as a variable by different variability criteria, within each YSO class, is strongly affected by how the data coverage restrict the study, hence the statistics presented in this thesis should be interpreted as a lower limit for some of the newly found variable stars. I find different variability patterns in the mid-infrared time-series photometry of 83 variable stars identified in the OBP region by the Stetson index based on data available in All-WISE Multiepoch Photometry.

Altogether, the results presented in this thesis suggest that the OBP is likely to be the low-mass counterpart of the Orion OB Ib population, one of the groups in the Orion OB association Blaauw (1964). This group should not be considered a single

population, and this thesis makes clear that star formation in the region proceeded in a more complex fashion than suggested in the Blaauw's scenario. Although it cannot be fully confirmed with the current data, the results agree better with a scenario proposed recently, where the new population is part of a large foreground population to the Orion clouds (the Orion blue stream).

6.1   Work in progress and for the future

Perhaps the main impact the results from my thesis will have in the future is the realization that OB associations are inherently much more complex structures than "dispersed groups of OB stars" as compared to stellar clusters. Perhaps not surprisingly, my thesis leaves open more questions about the structure and origin of OB associations than the ones I had when I started my thesis. Although the Blue Stream scenario proposed by Bouy & Alves (2015) shows some promises regarding the structure of the region, we caution that independent work is needed to confirm the existence of the blue streams. Some of the work that could further enlighten this problem is described below.

Given that Gaia is "blind" to bright stars, at least for the near future, and that the radial velocity resolution will never be optimal for accurate kinematics, an obvious way forward would be to study the OB stars in the entire Orion star-forming region with high-resolution spectroscopy. These data will constitute an important test to the current description of the region (association or part of a stream). Throughout my Ph.D., I successfully submitted and executed a few observing proposals regarding the spectroscopic observation of massive blue stars (down to $M < 3\ M_{\odot}$) in the Orion constellation. The survey targets the entire complex and covers a contiguous area of about 300 deg sq, the largest spectroscopic survey ever carried out for this region. The data analysis is not trivial, a first goal of the study is to discover binary systems in our primary sample, which is crucial to disentangle the kinematics of the different young populations accurately. This survey will have immense legacy value, providing radial velocities an order of magnitude more accurate than Gaia for a genetically related population of massive stars. The preliminary results revealed a

large structure in radial velocity-position space, which is exciting. Further analysis is required since many unexpected problems during the reduction and analysis process have occurred. In order to obtain homogeneous results, we have to combine the observations from different instruments, with different properties and qualities. The obtained spectra contain not only the spectrum of the star but also of the interstellar medium in the line of sight. Both elements have different radial velocities components and have to be well identified and understood.

Another obvious follow-up, as already mentioned, is FIR observation of the disk candidates with, perhaps, the hopefully upcoming SPICA space mission. Much closer to home, and a prominent and exciting follow-up would be to combine the BRITE satellite results for the OB stars in Orion with the results from the high-resolution survey. In the meanwhile, Gaia DR3 should take place in 2020, and better parallaxes and proper motions (critical for this anti-apex region of the sky) will become available, hopefully allowing us to carry a kinematical study of the low-mass stars, and try to tie it with the results from the radial velocities for the high-mass, O and B stars. Much will be learned then about the dynamical state of a large population of young stars, and the role of gas-expulsion in the dispersion of young stars into the Galactic field.

The OBP population could become a benchmark region for future searches of brown dwarfs and planetary mass objects and the low-mass end of the IMF, as well as circumstellar disk evolution and planet formation, in particular with the next generation of telescopes, such as JWST and the ELT. The final ESA Gaia catalog, to be released around 2023, will be able to shed even more light on the origin of the OBP, the existence and role of the Orion blue stream, and the star formation process in the closest massive stellar factory, Orion.

7

Appendix

Grid of SEDs of the sources in the OBP sample. The source ID and icon representing the best model set is displayed for each SED, along with the best fit model name, χ^2 value of the best fit, The A_V fitted value. The figures present only the result from the model set selected by the relative score value (as described in the Sec 3. of the paper). The black line presents the best-fitted model; the grey lines show all the fits for $\chi^2 - \chi^2_{\min} < 9 \cdot n_{\text{data}}$ for this model set. The source names are from the Kubiak et al. (2017). The icon presentation of the model set is from Robitaille (2017).
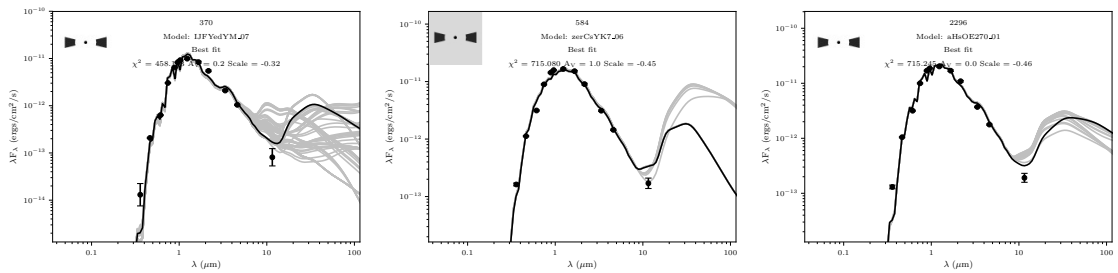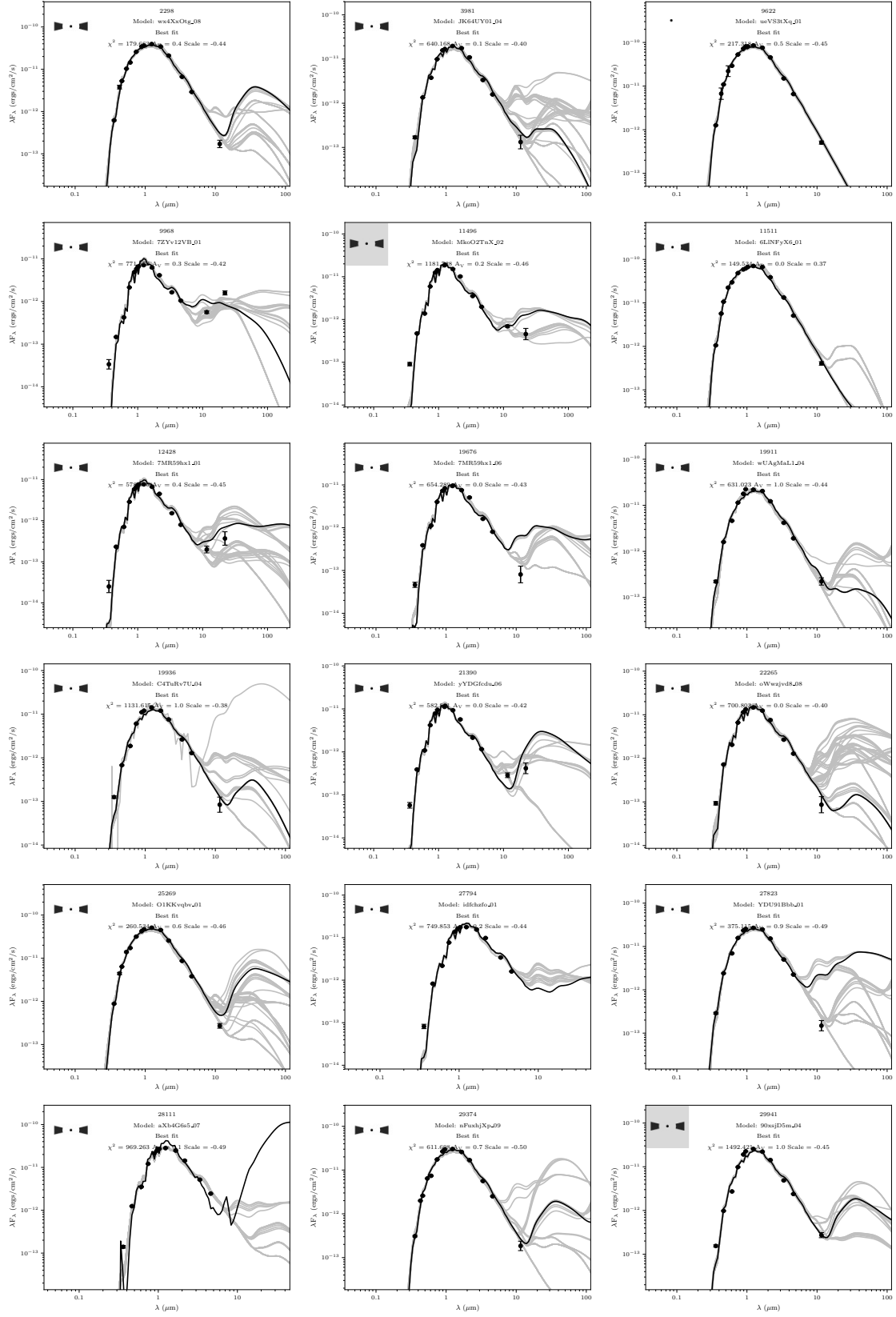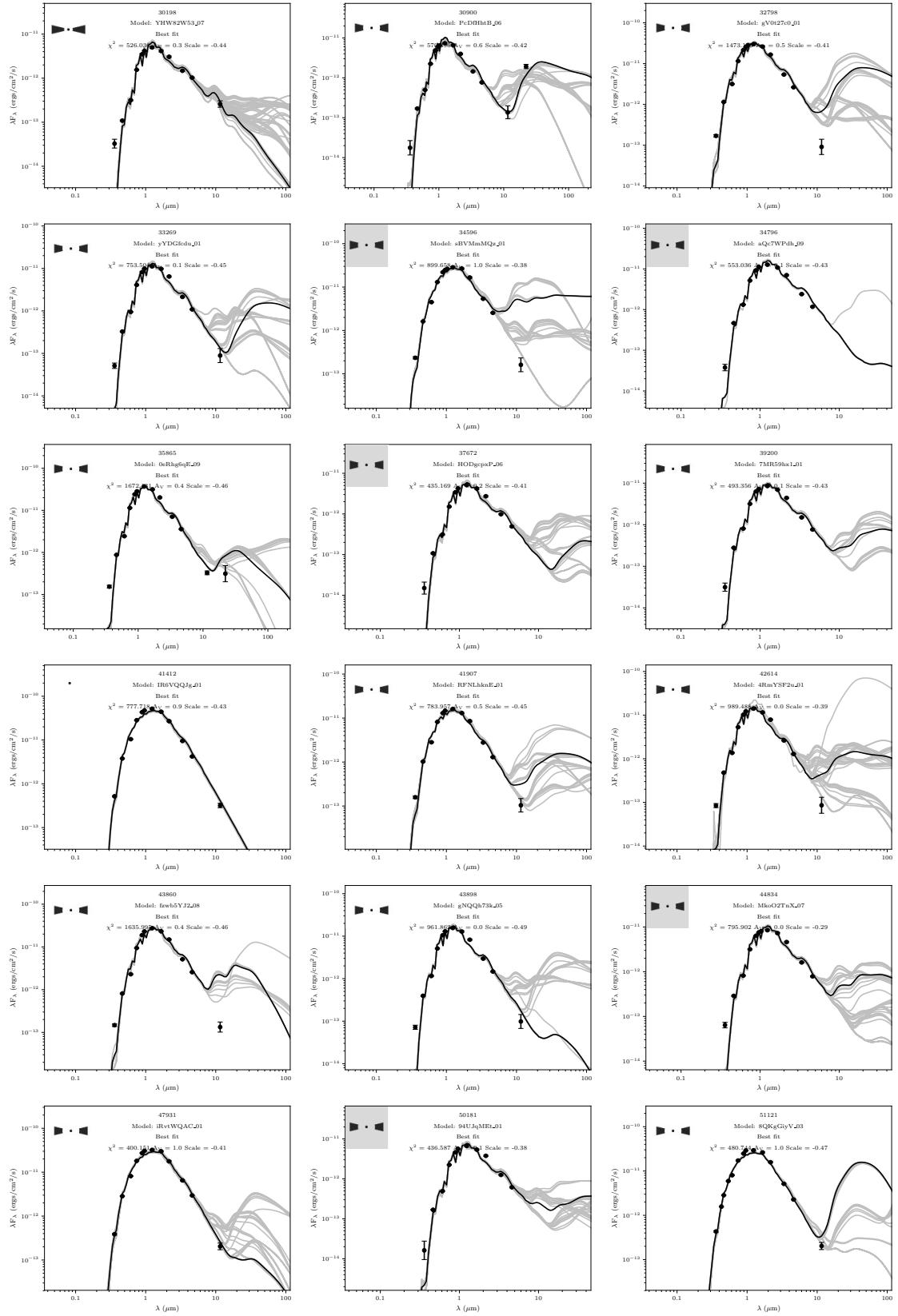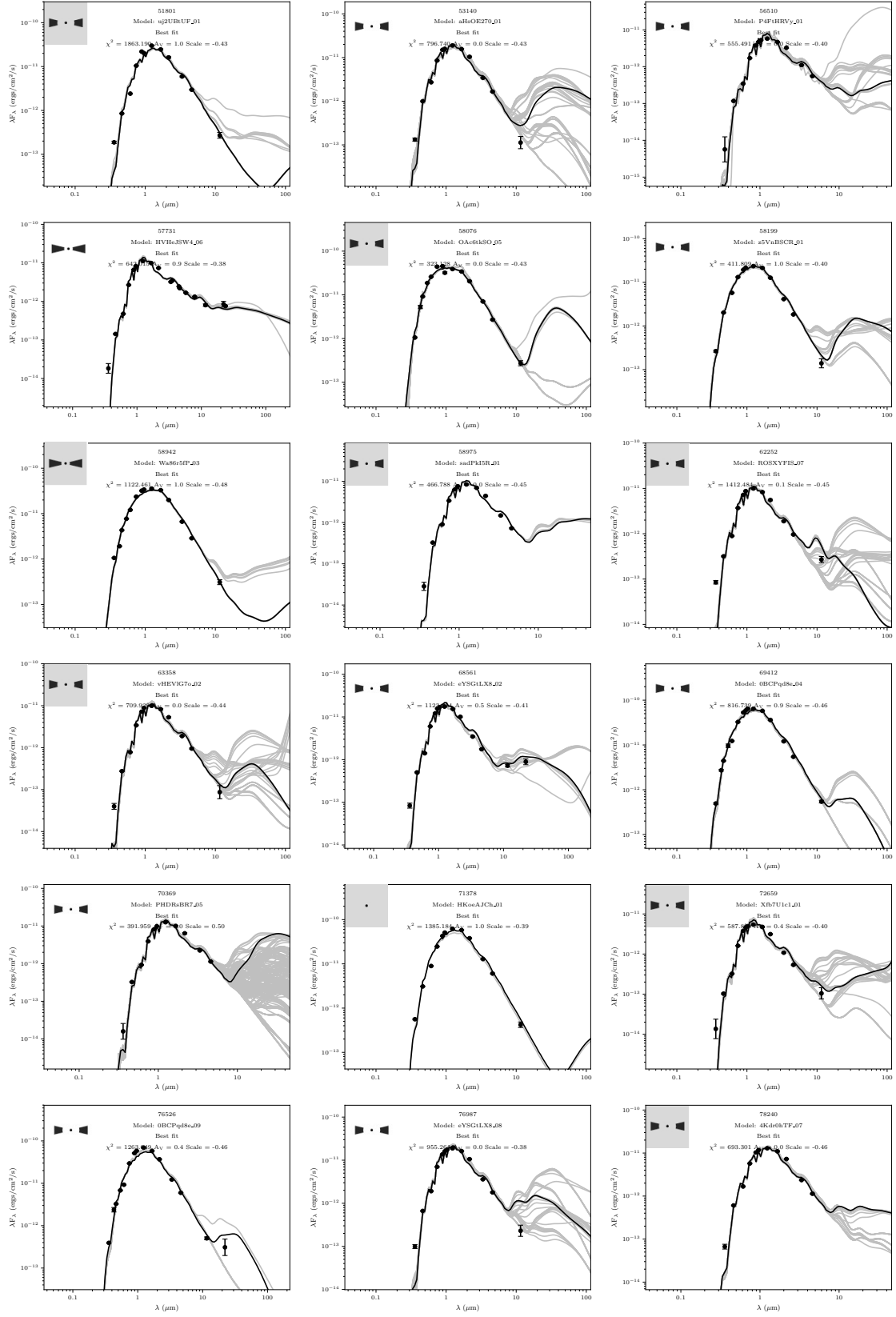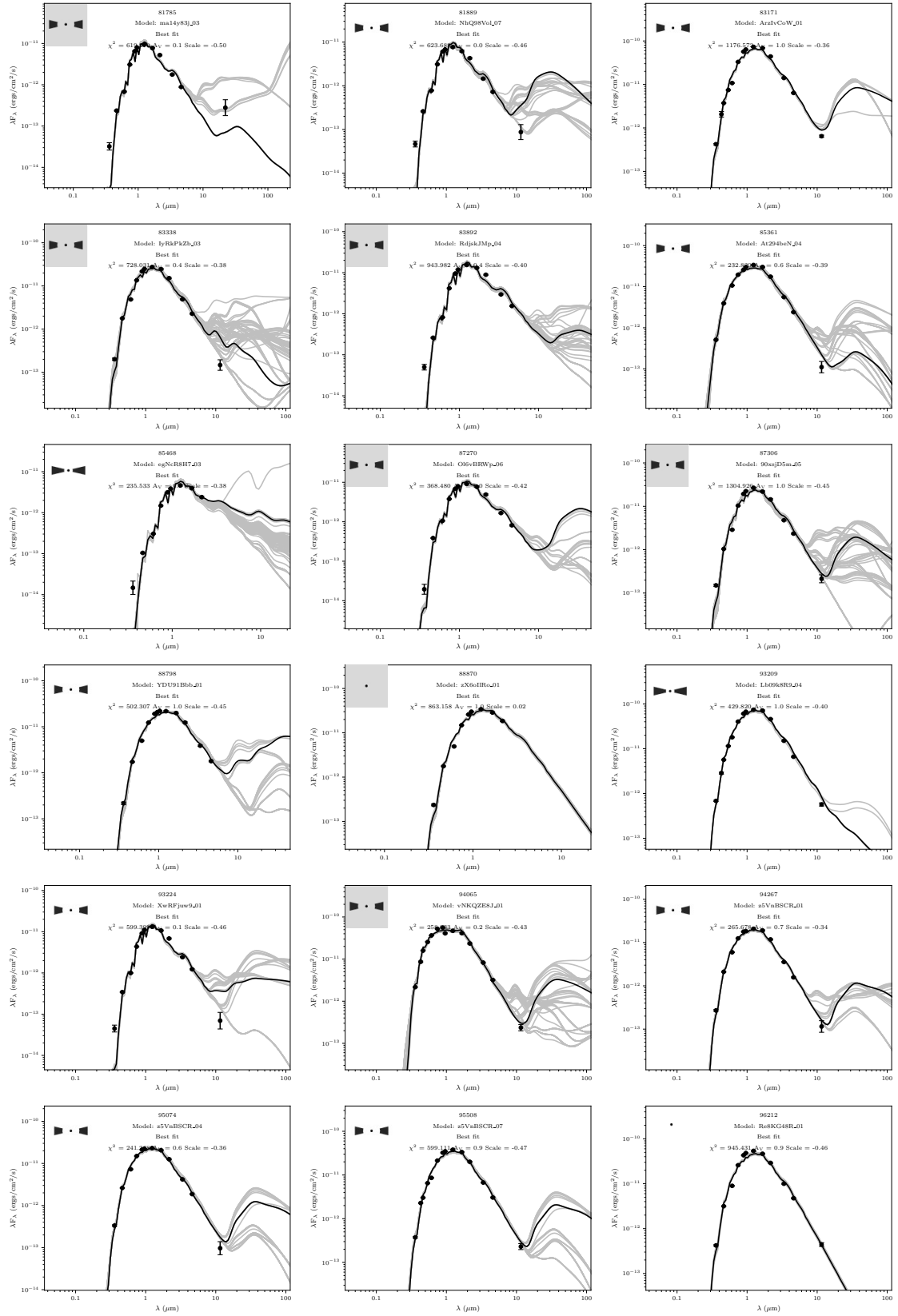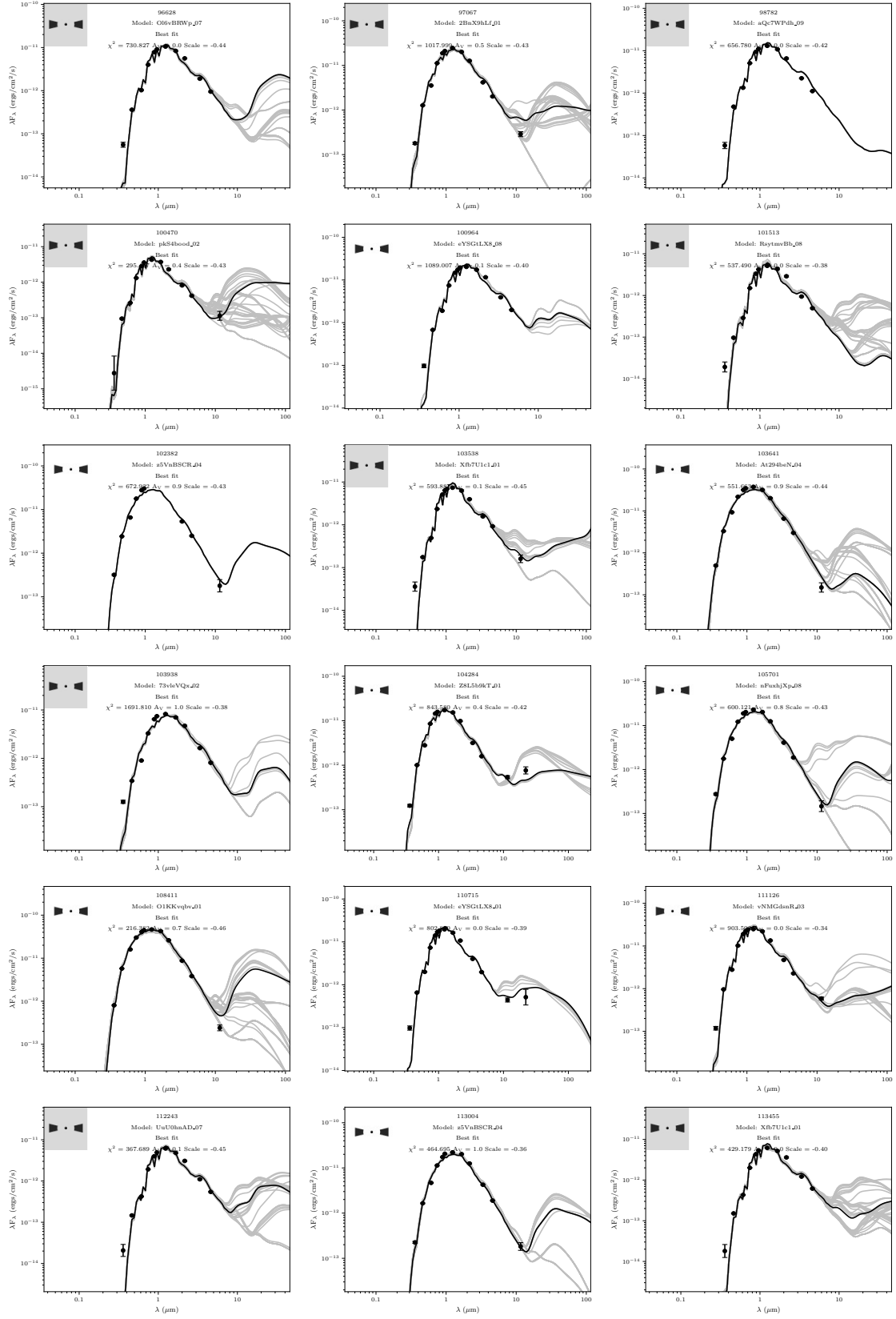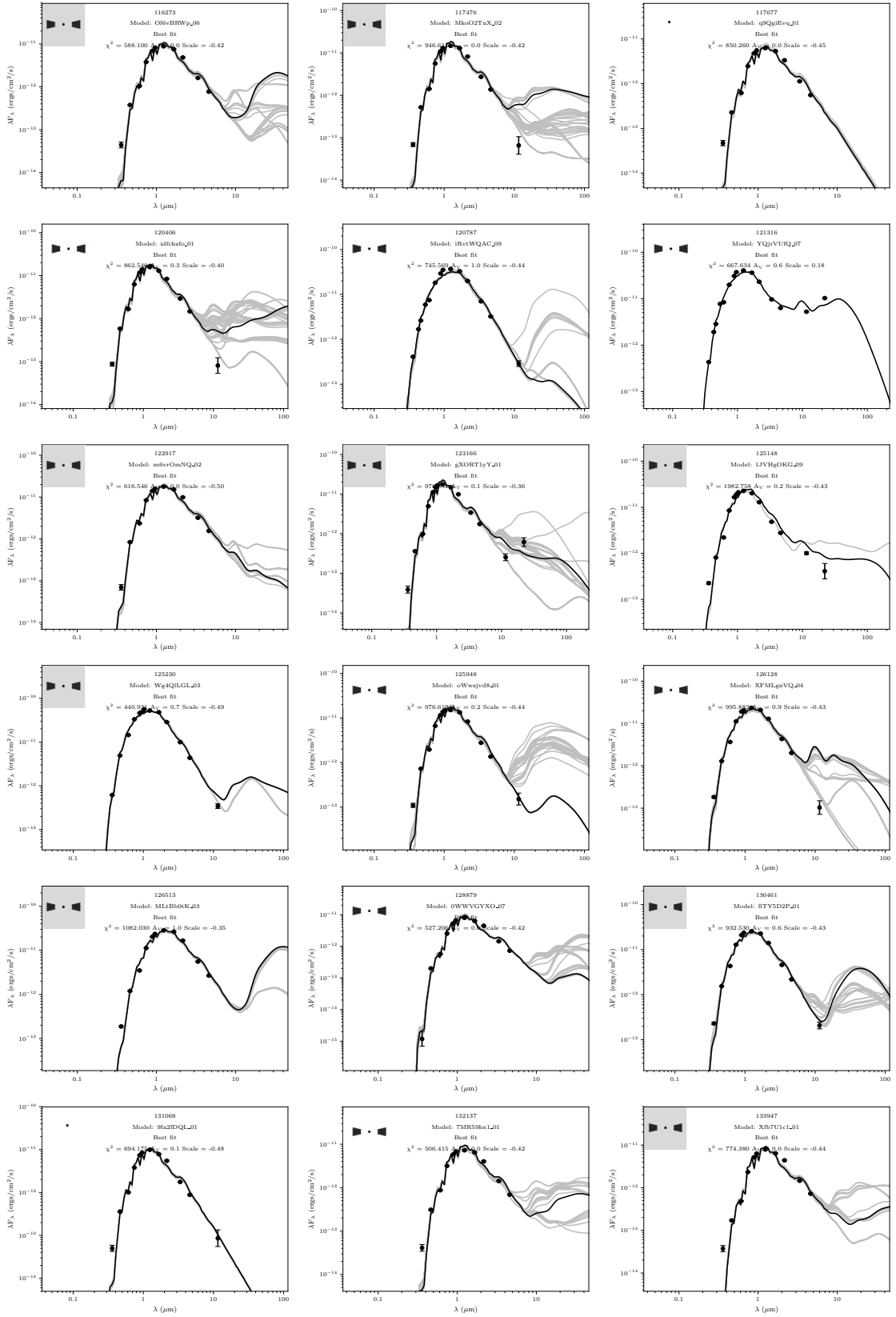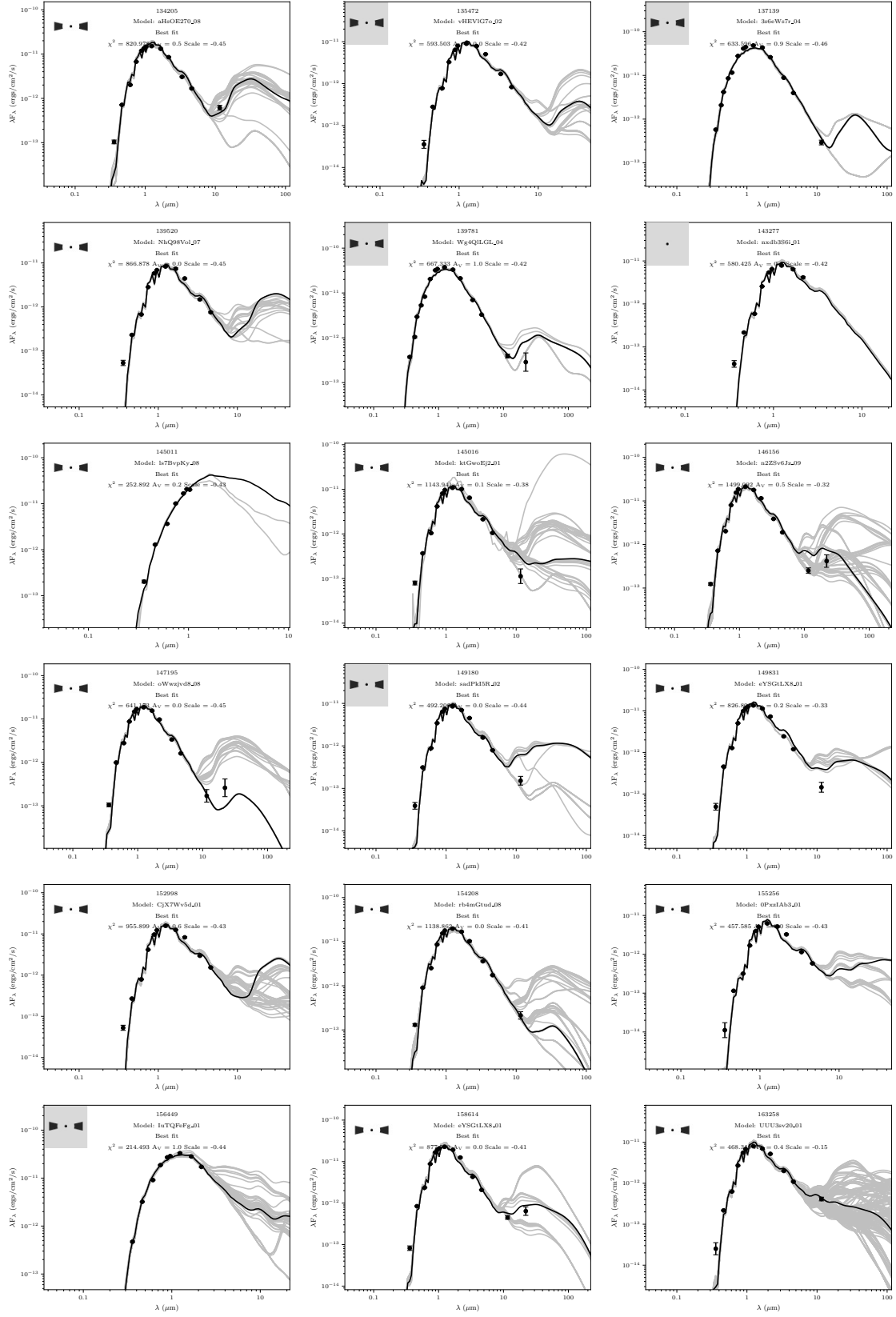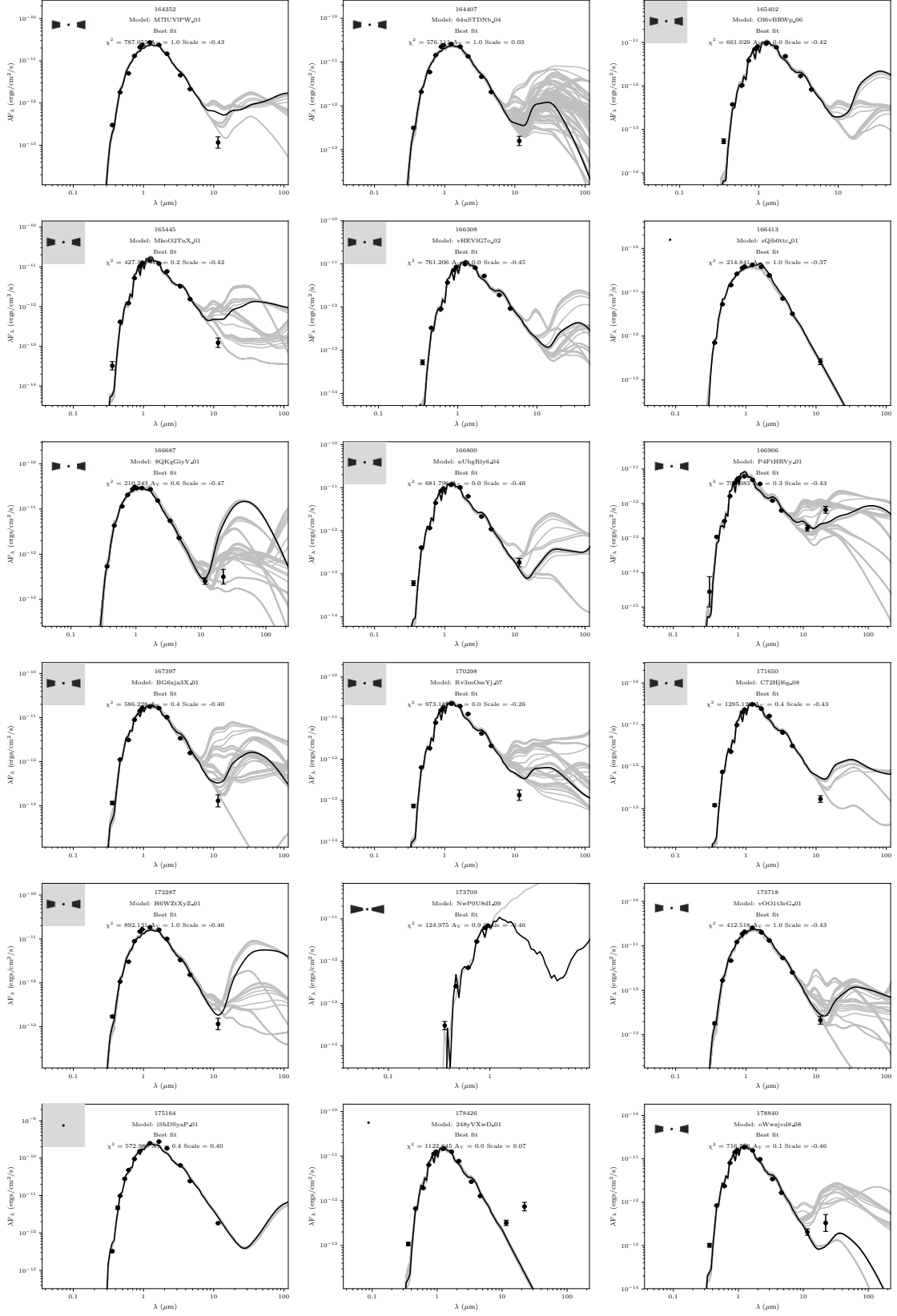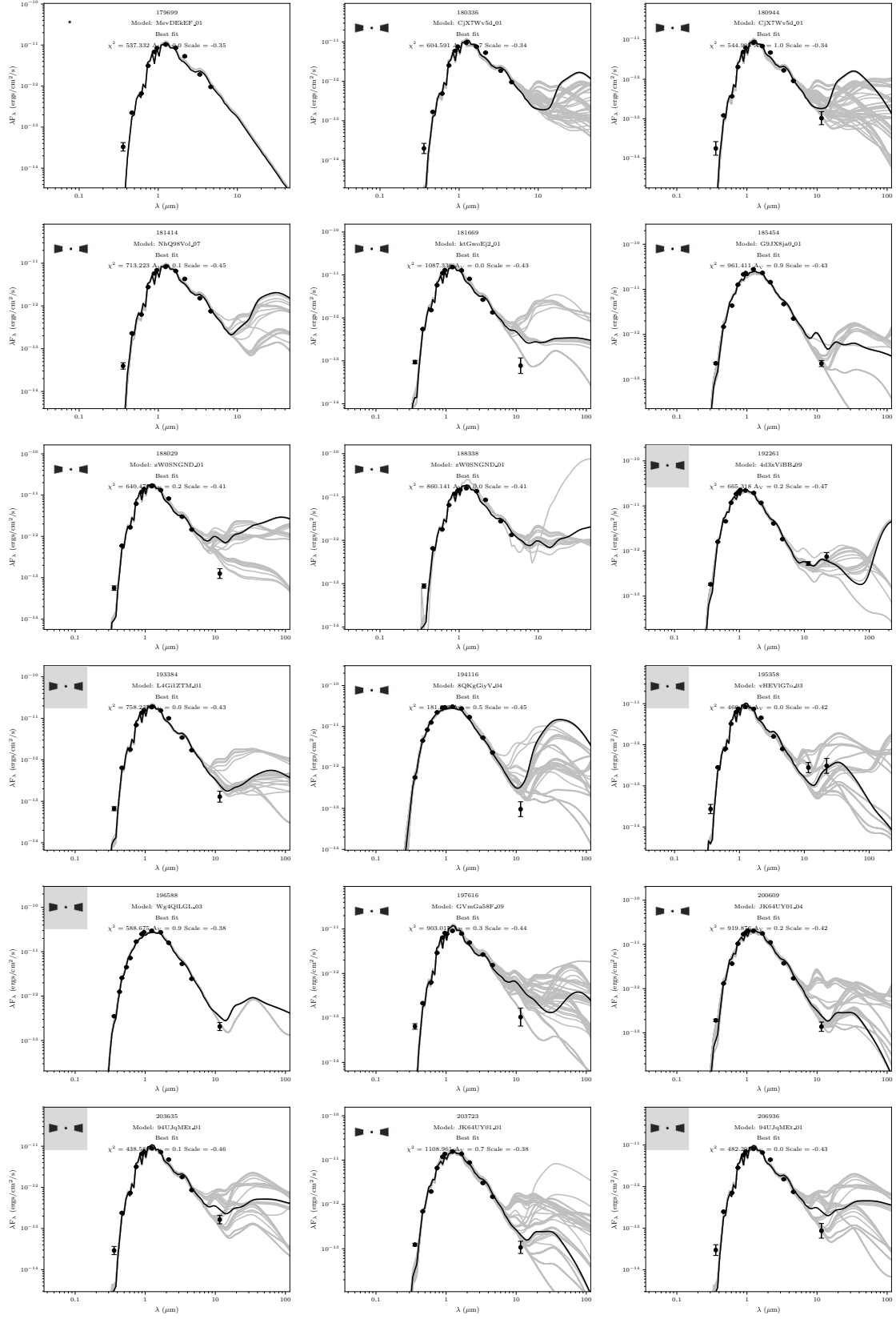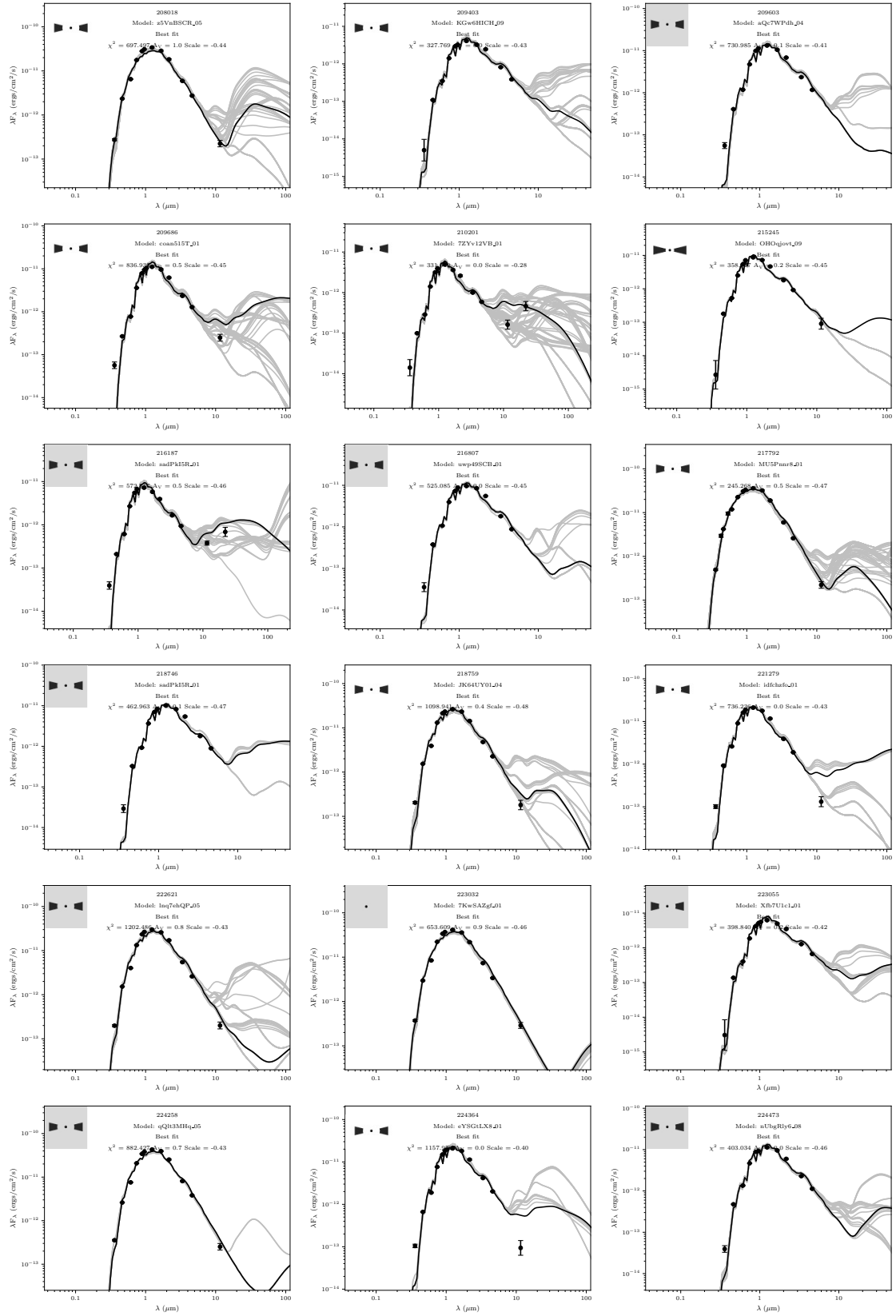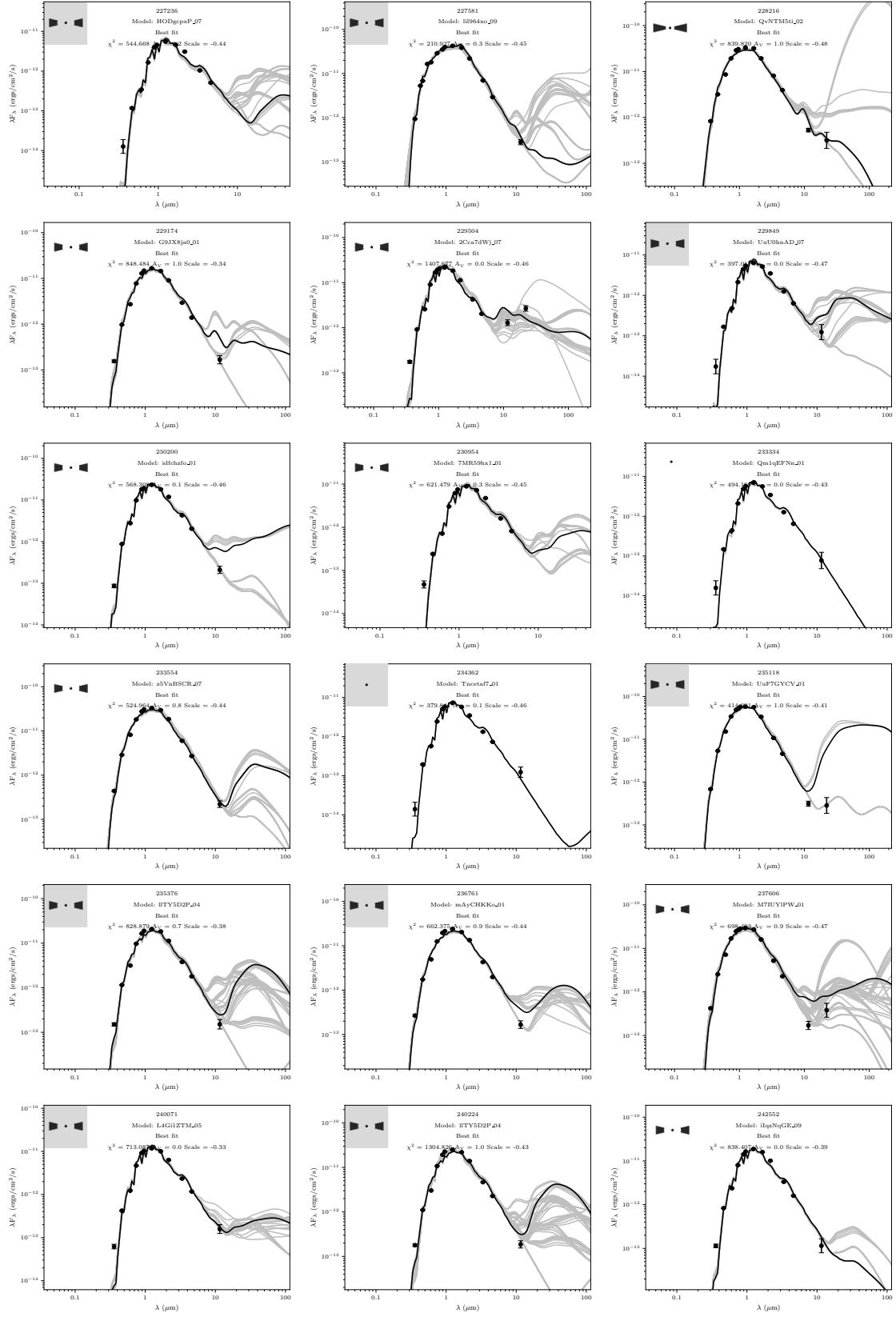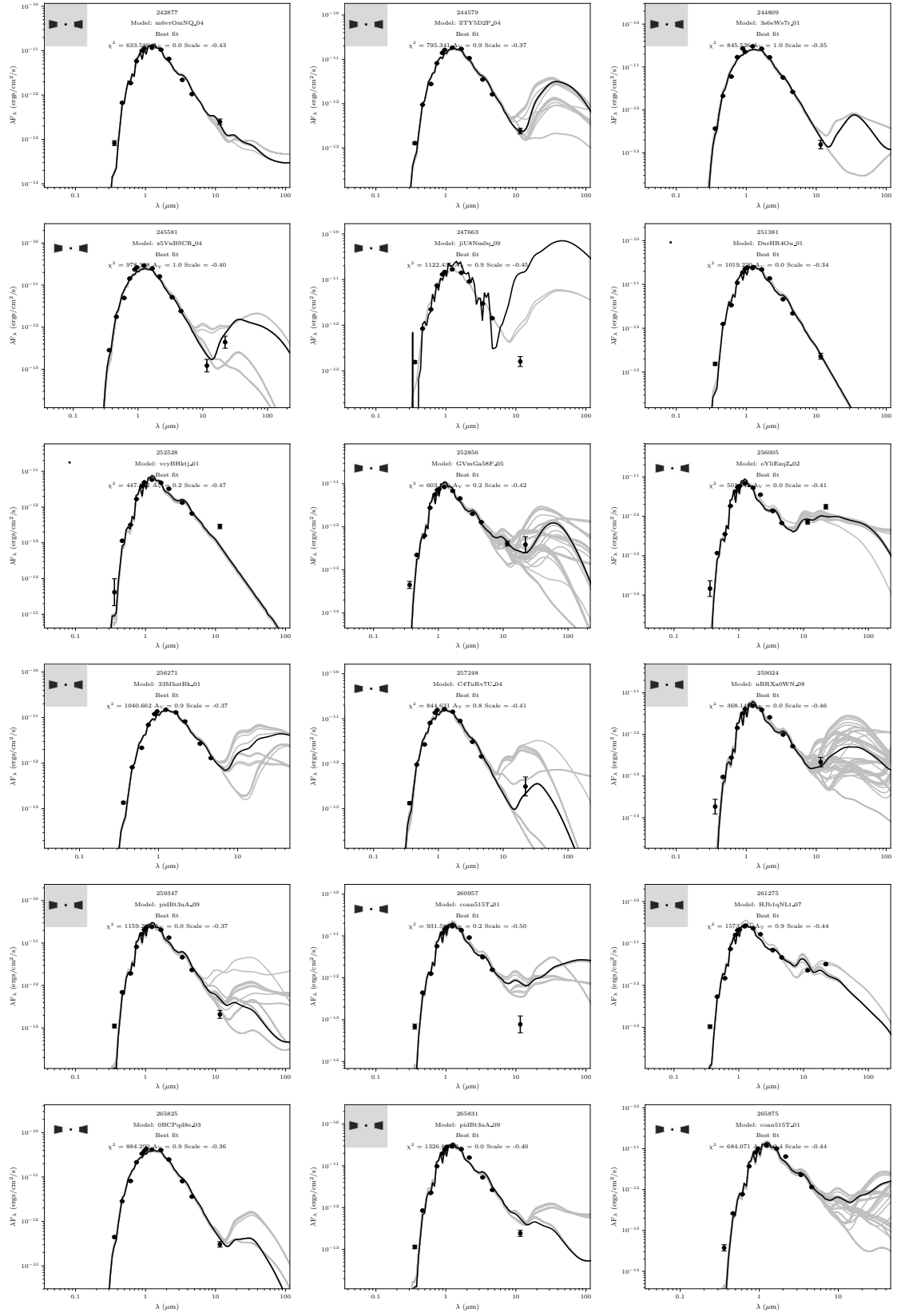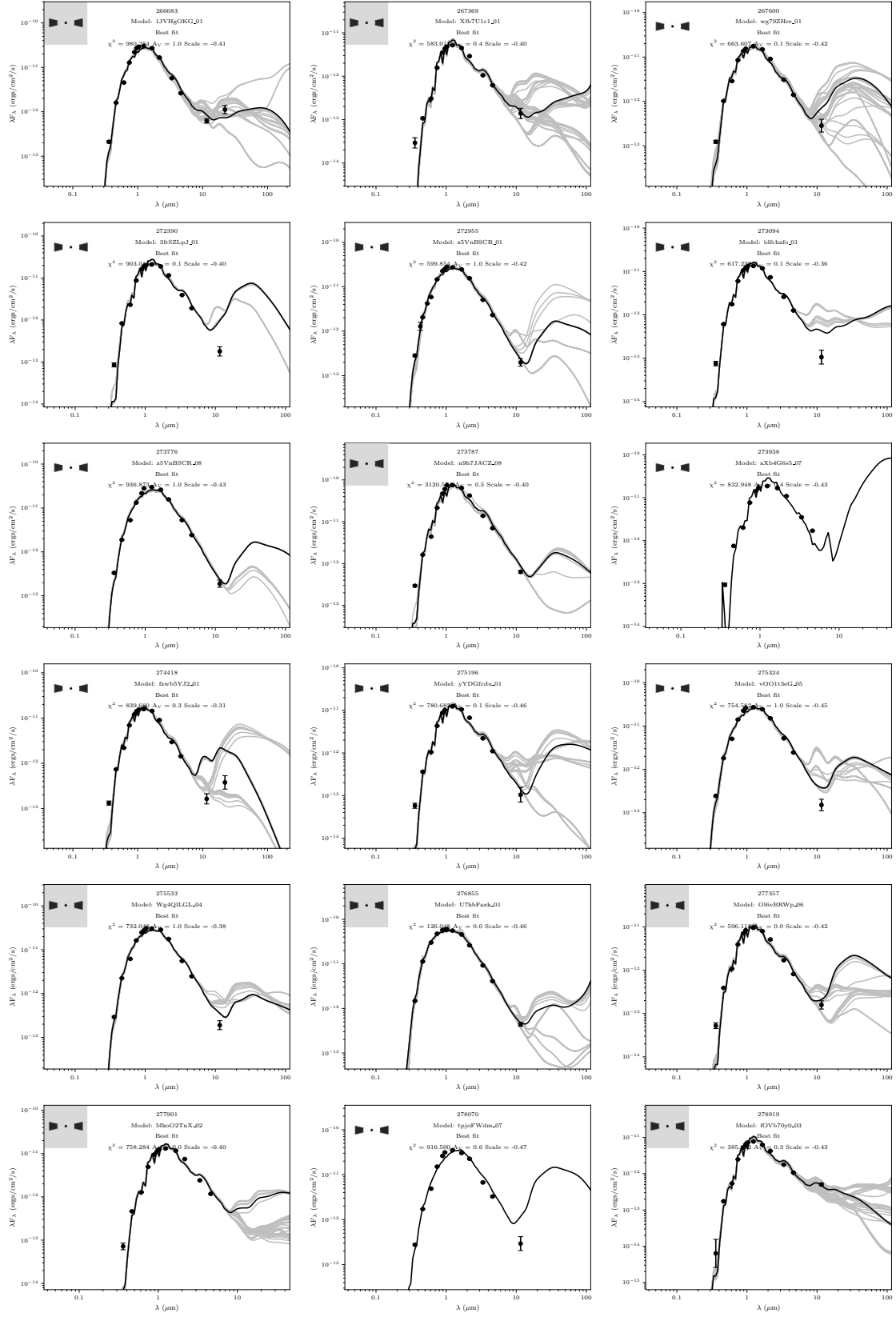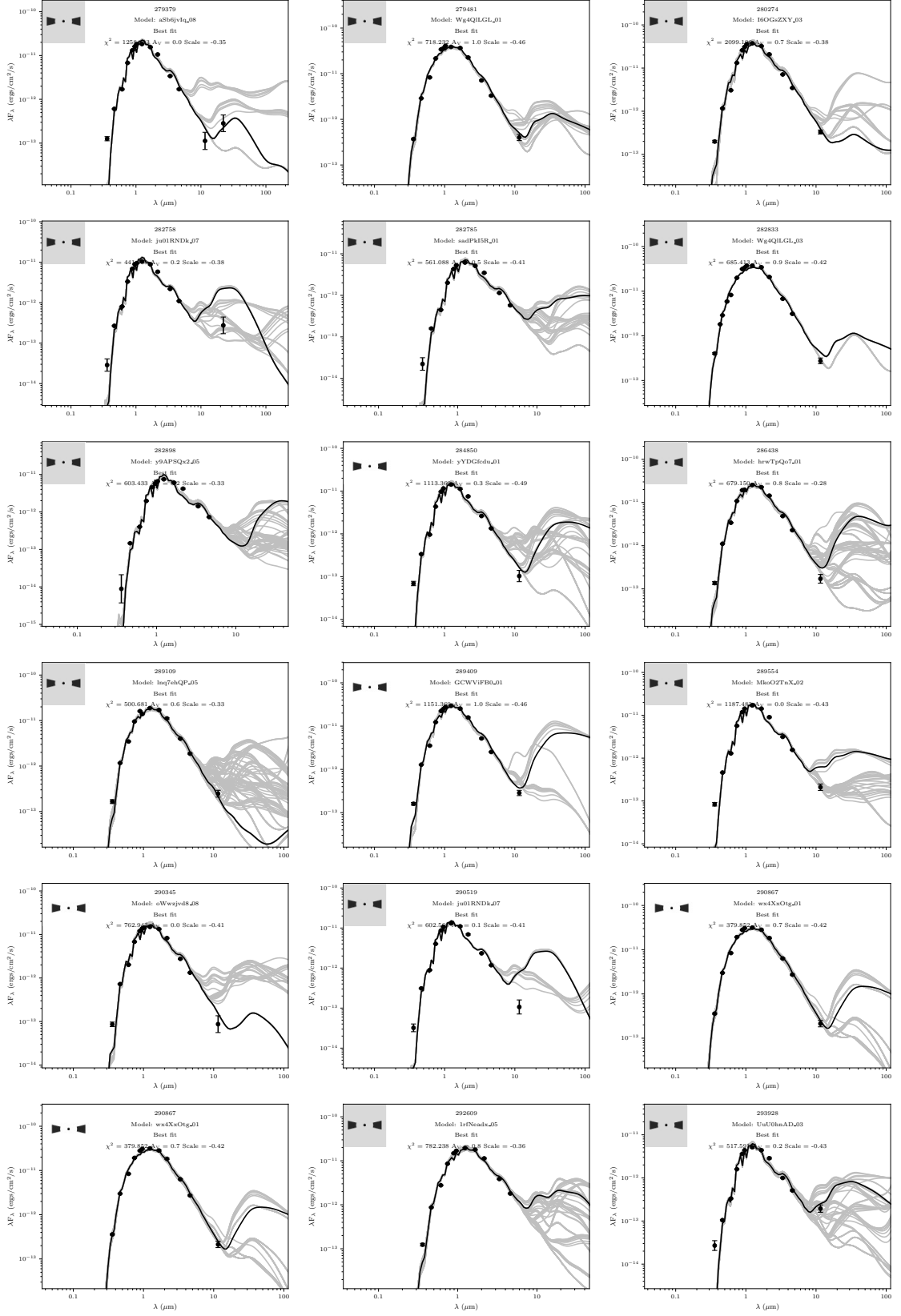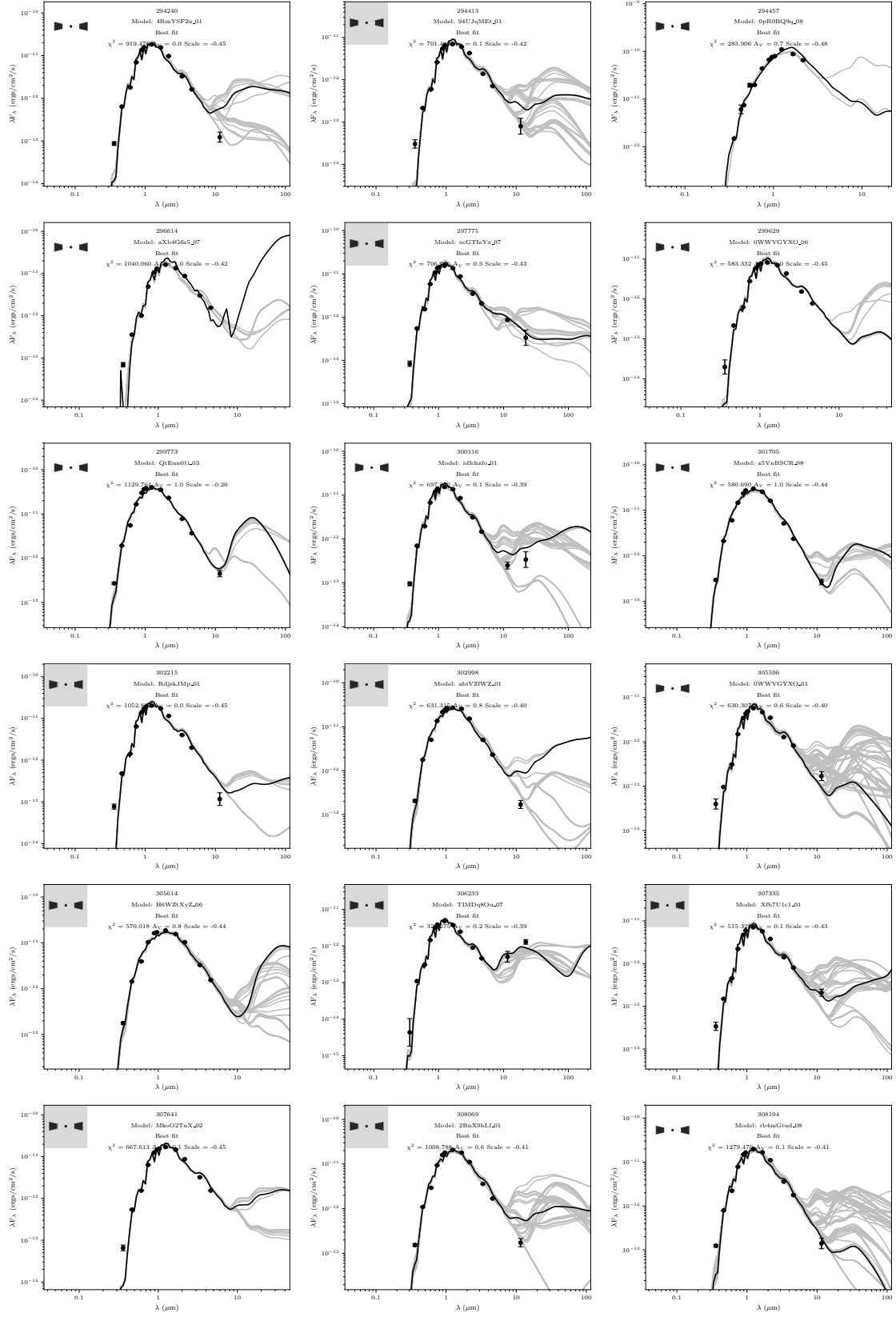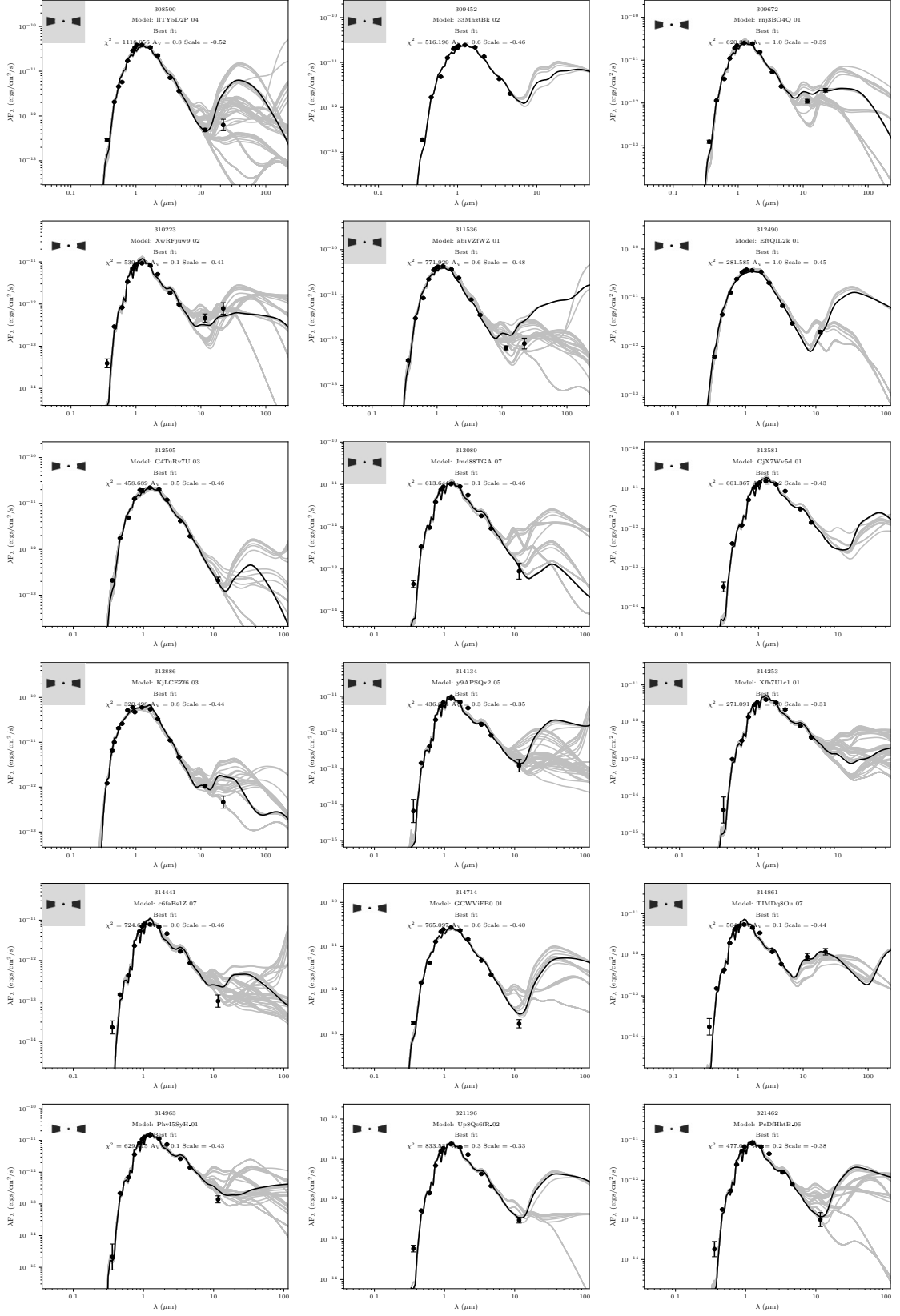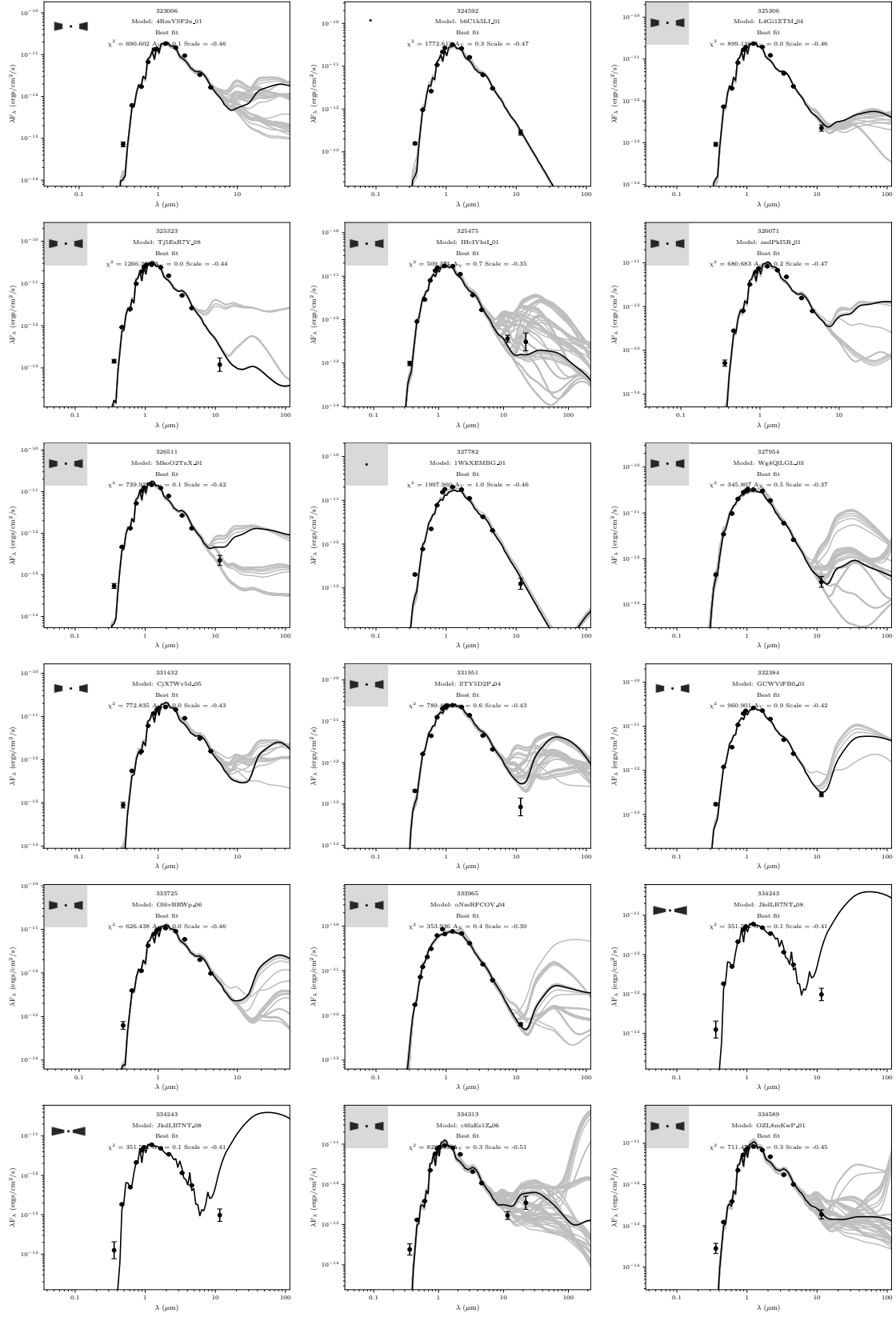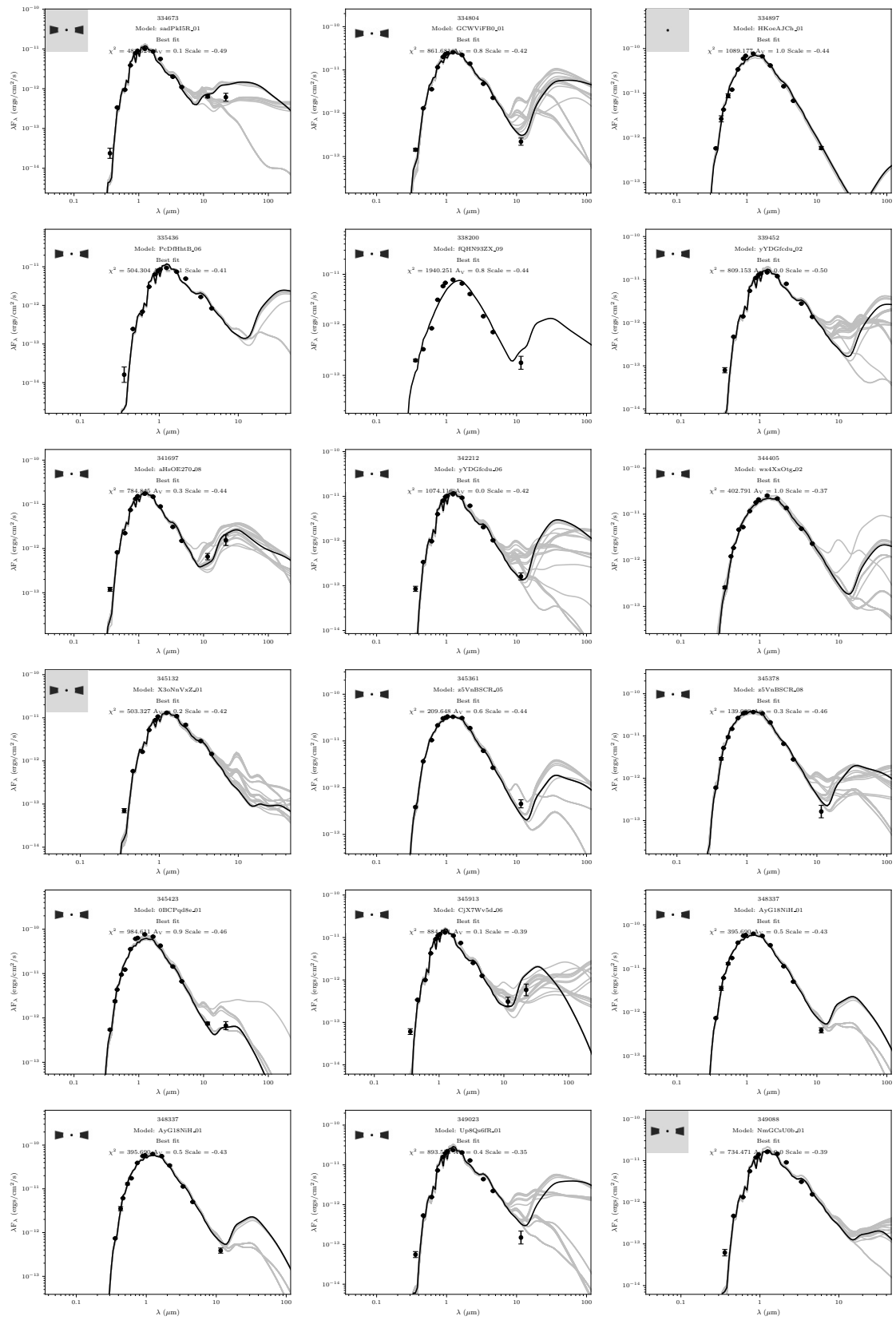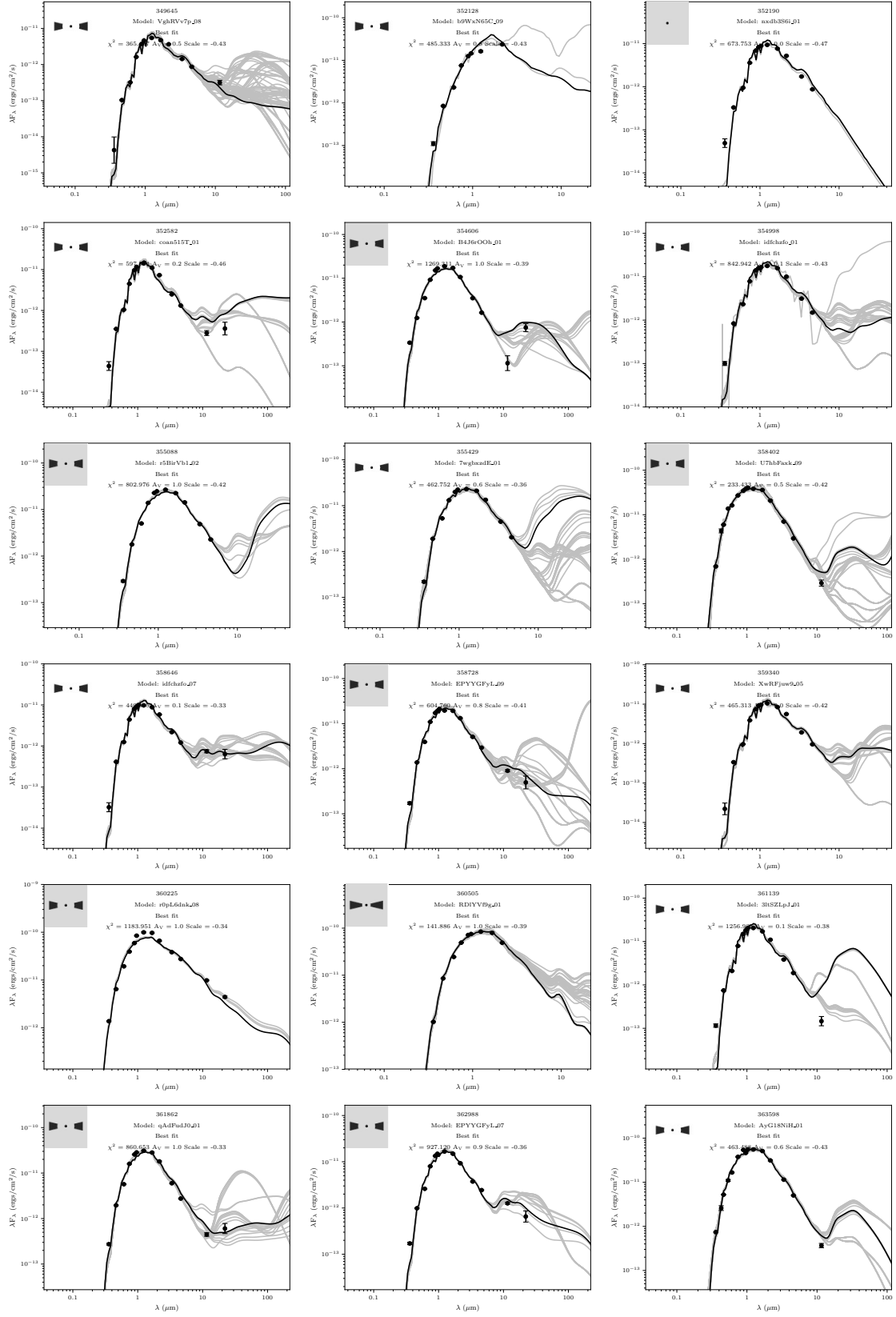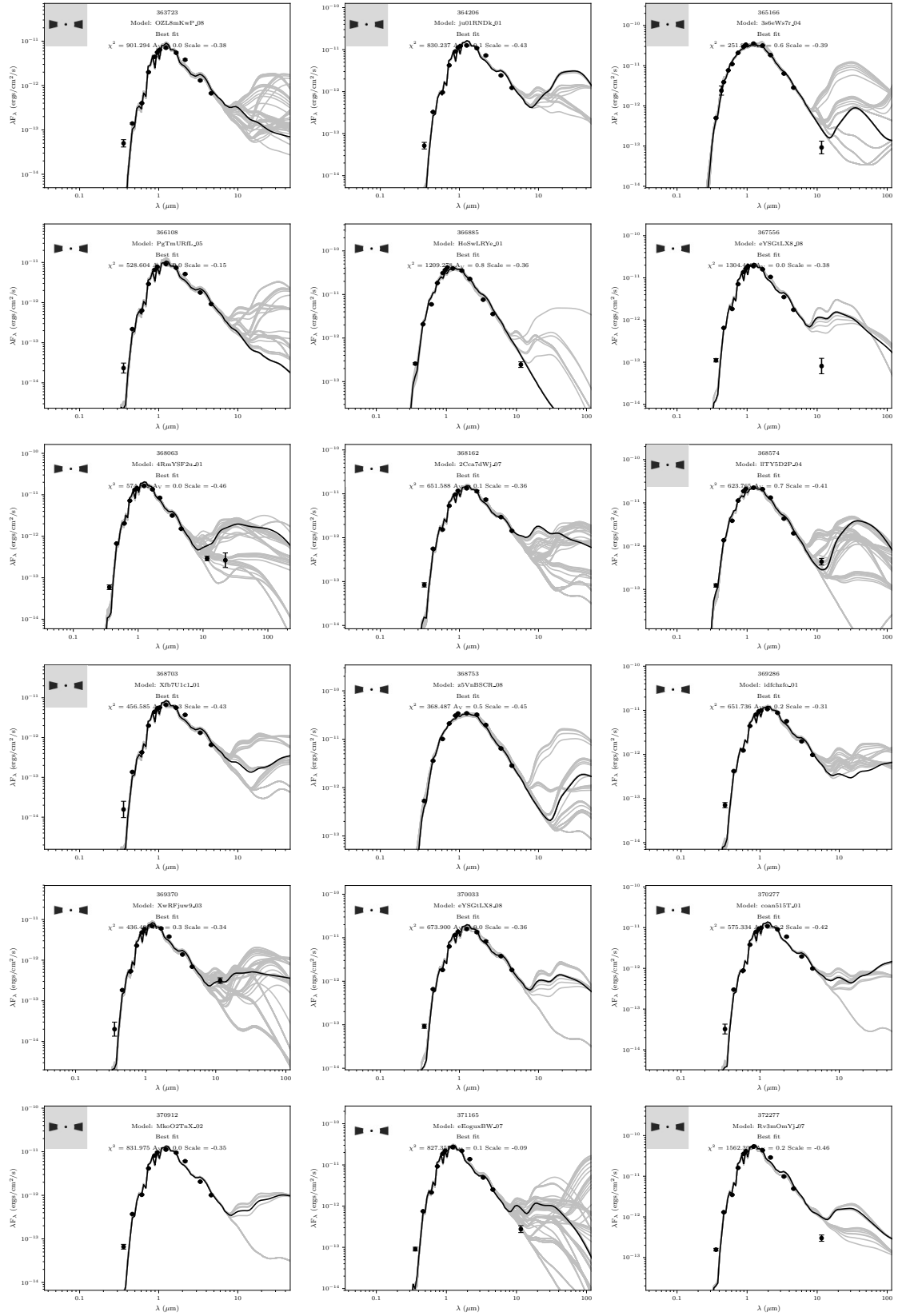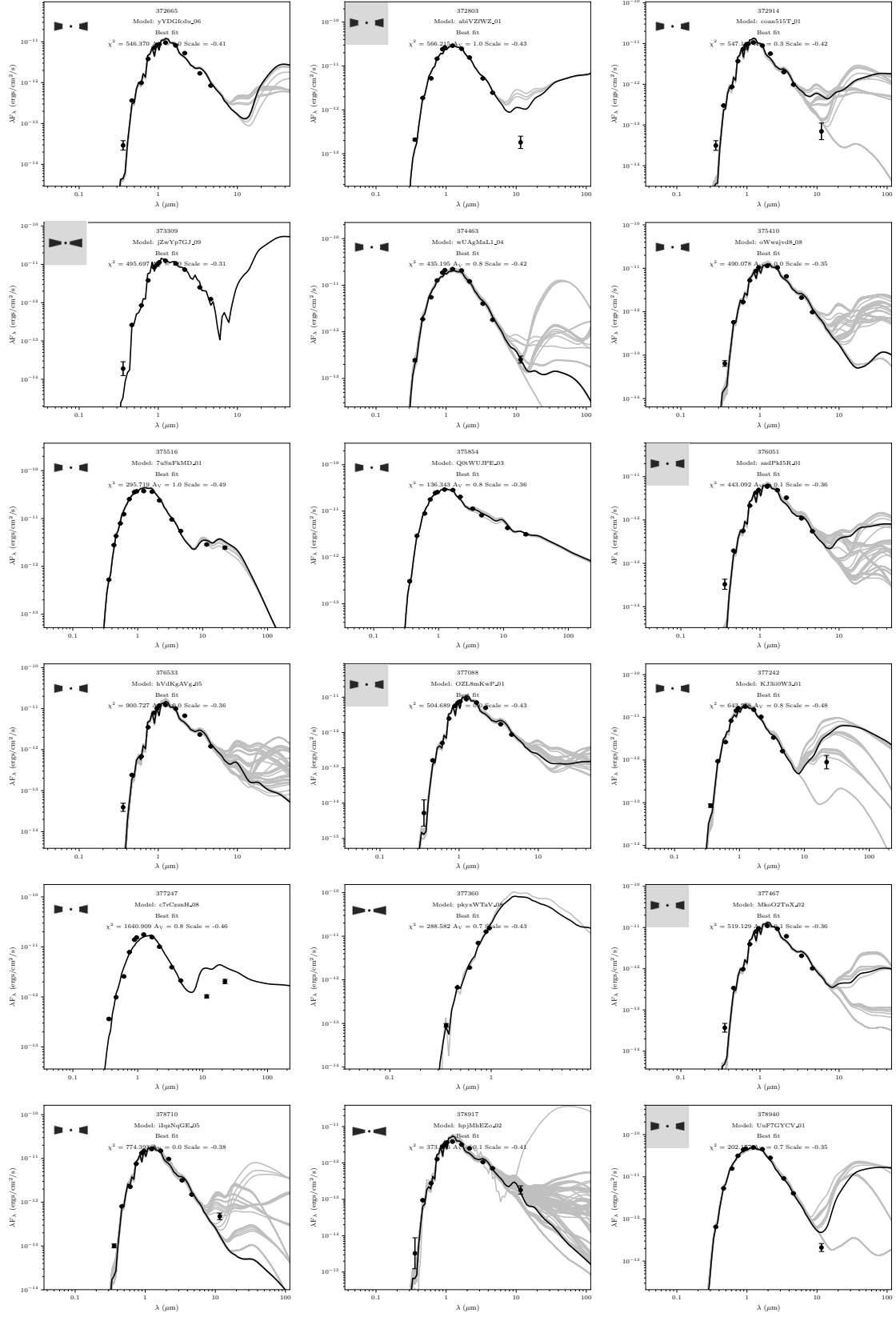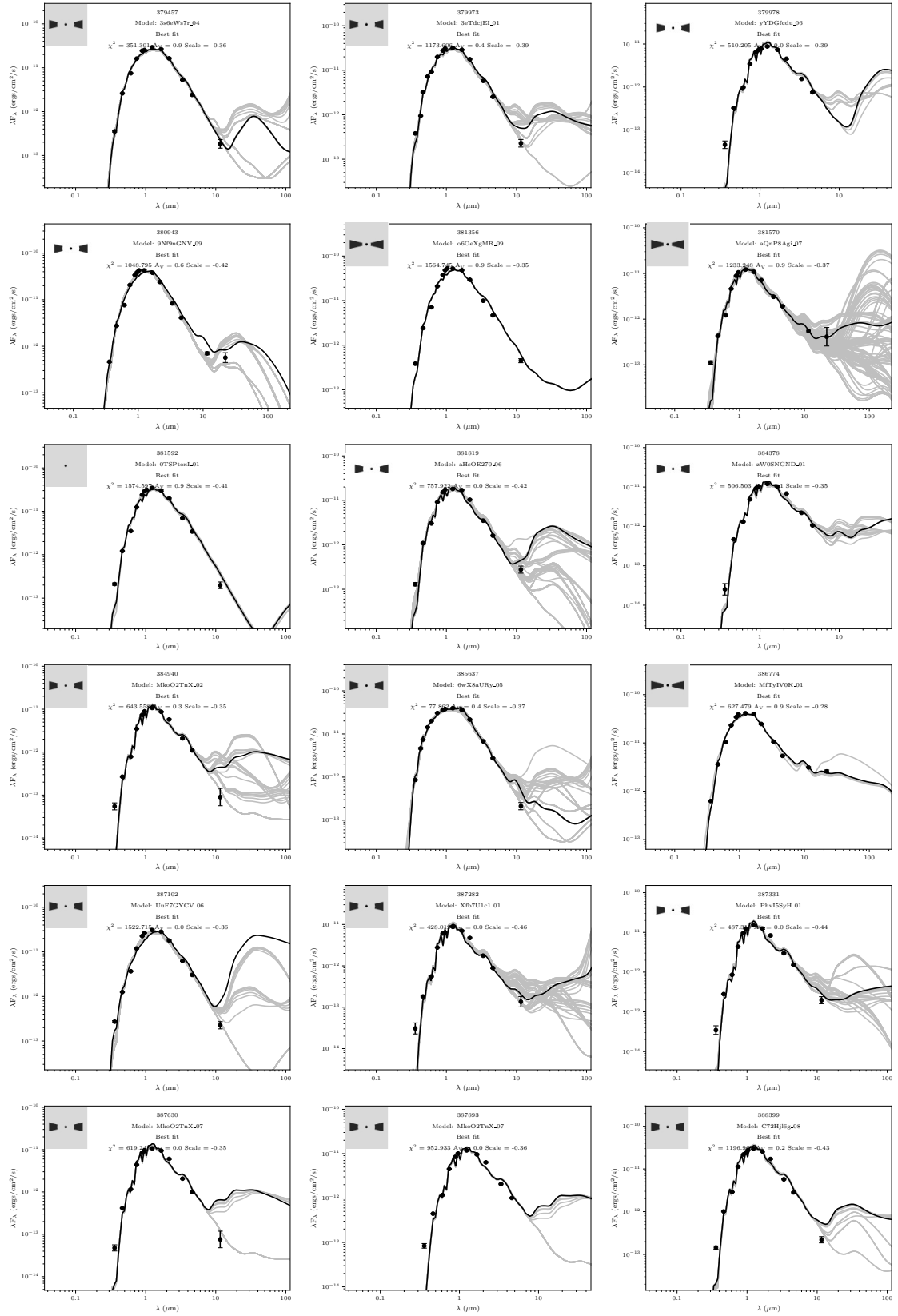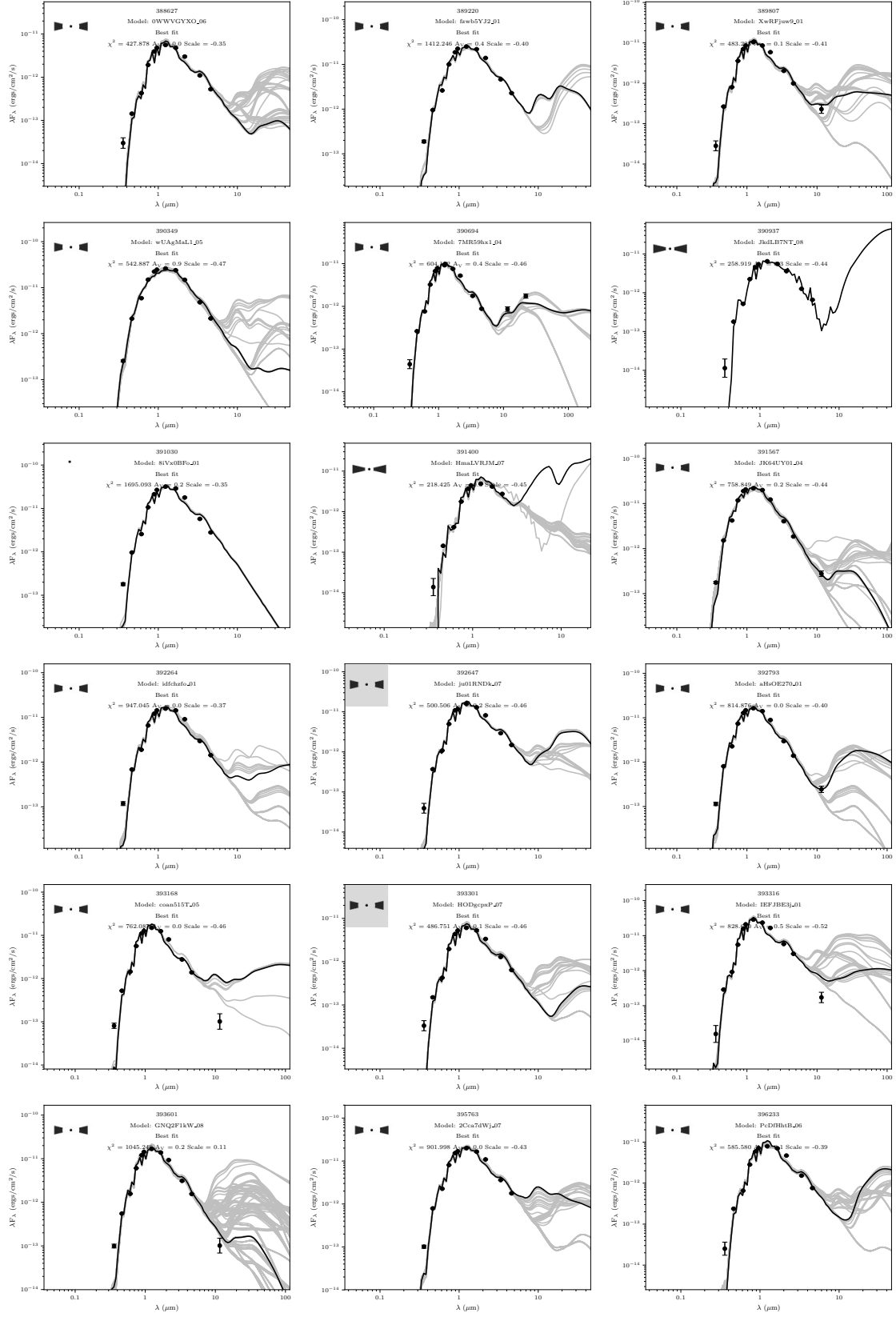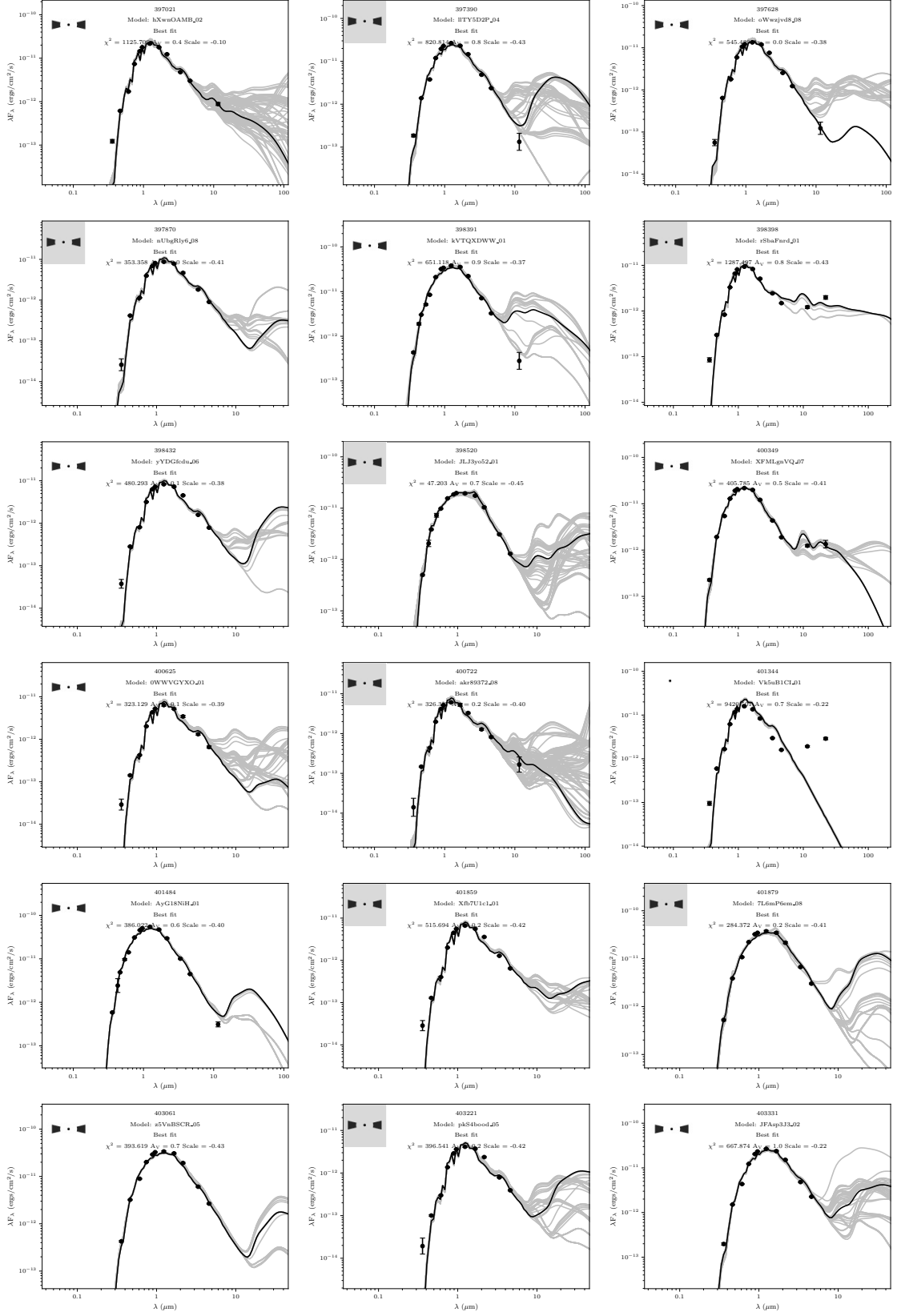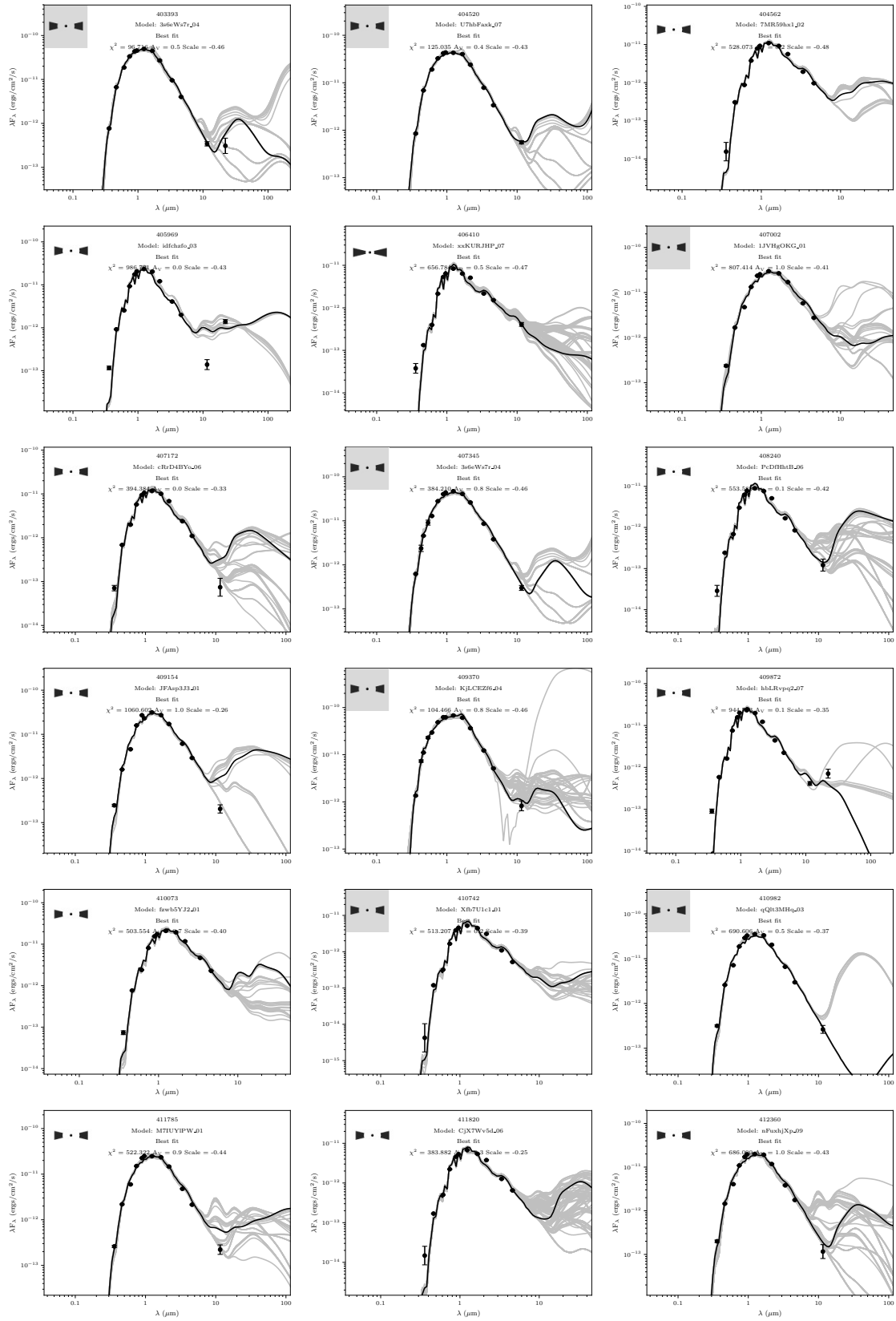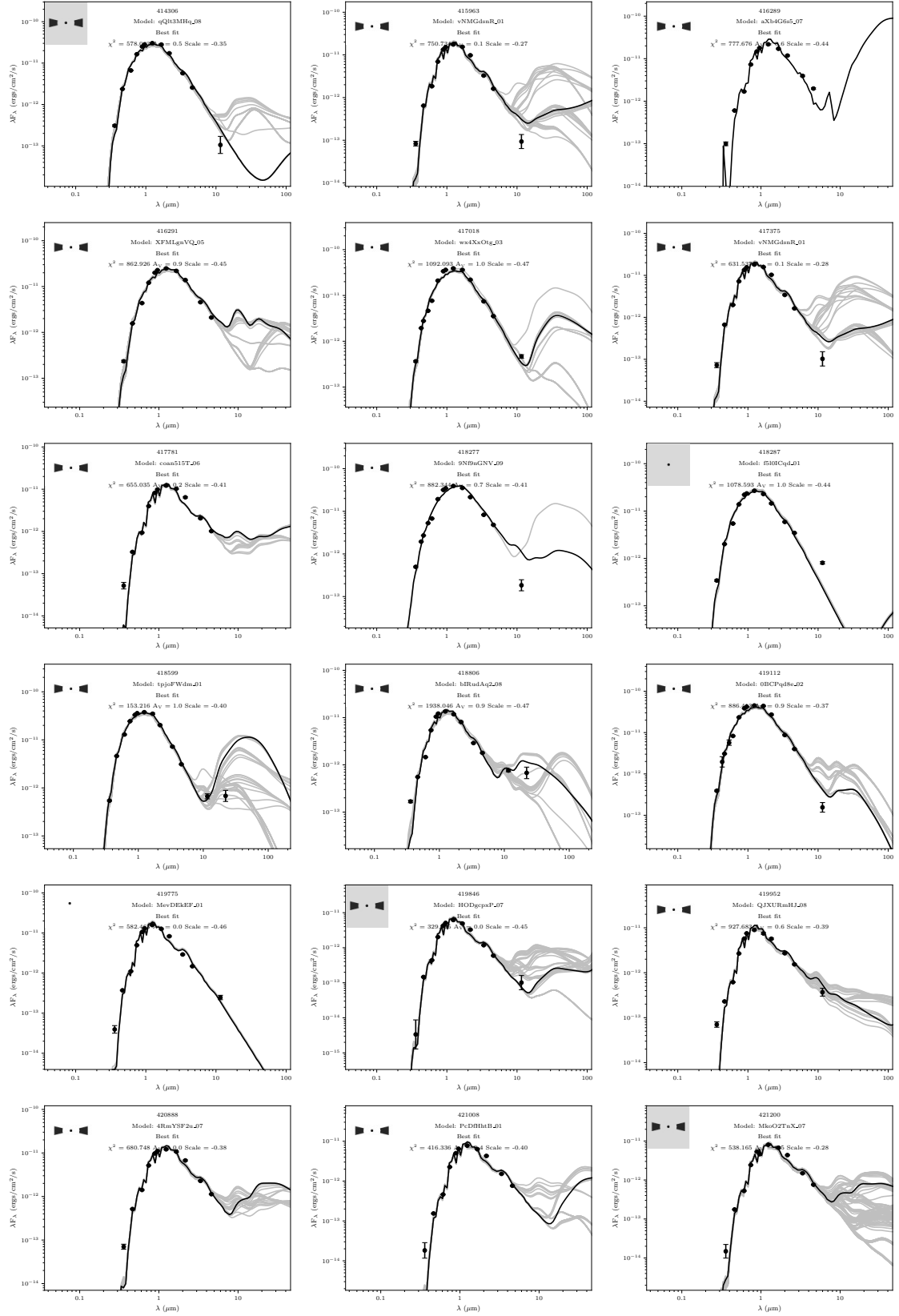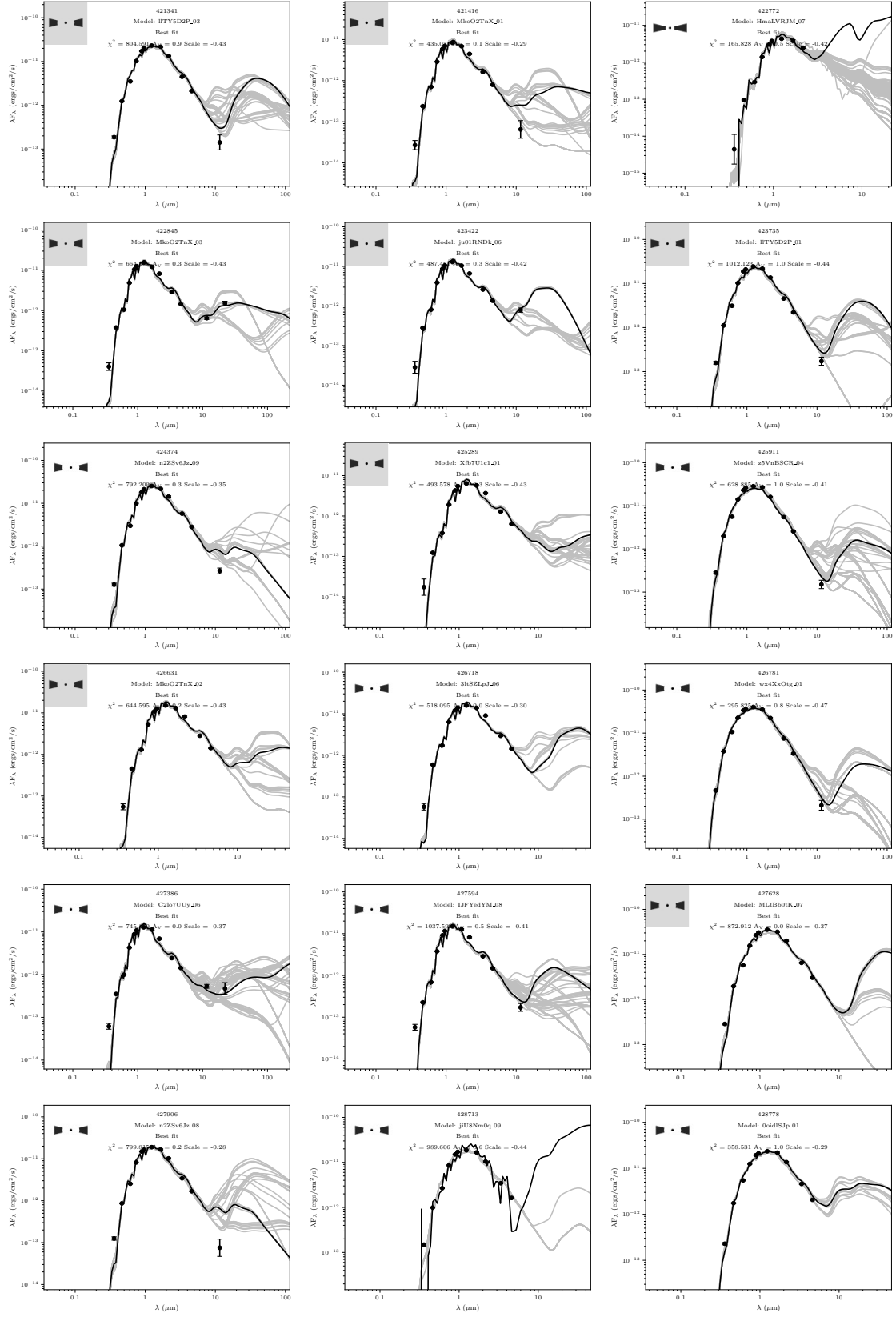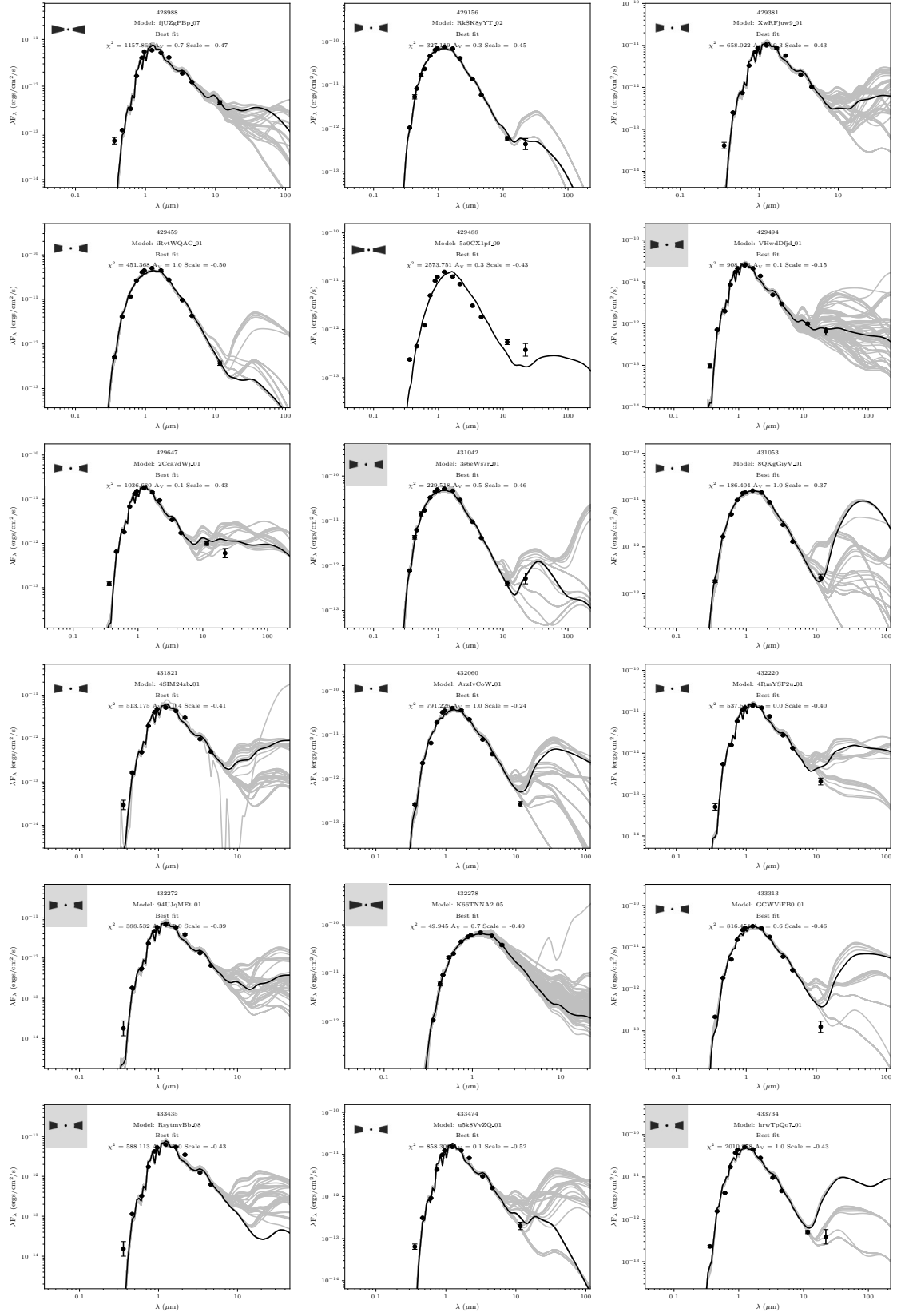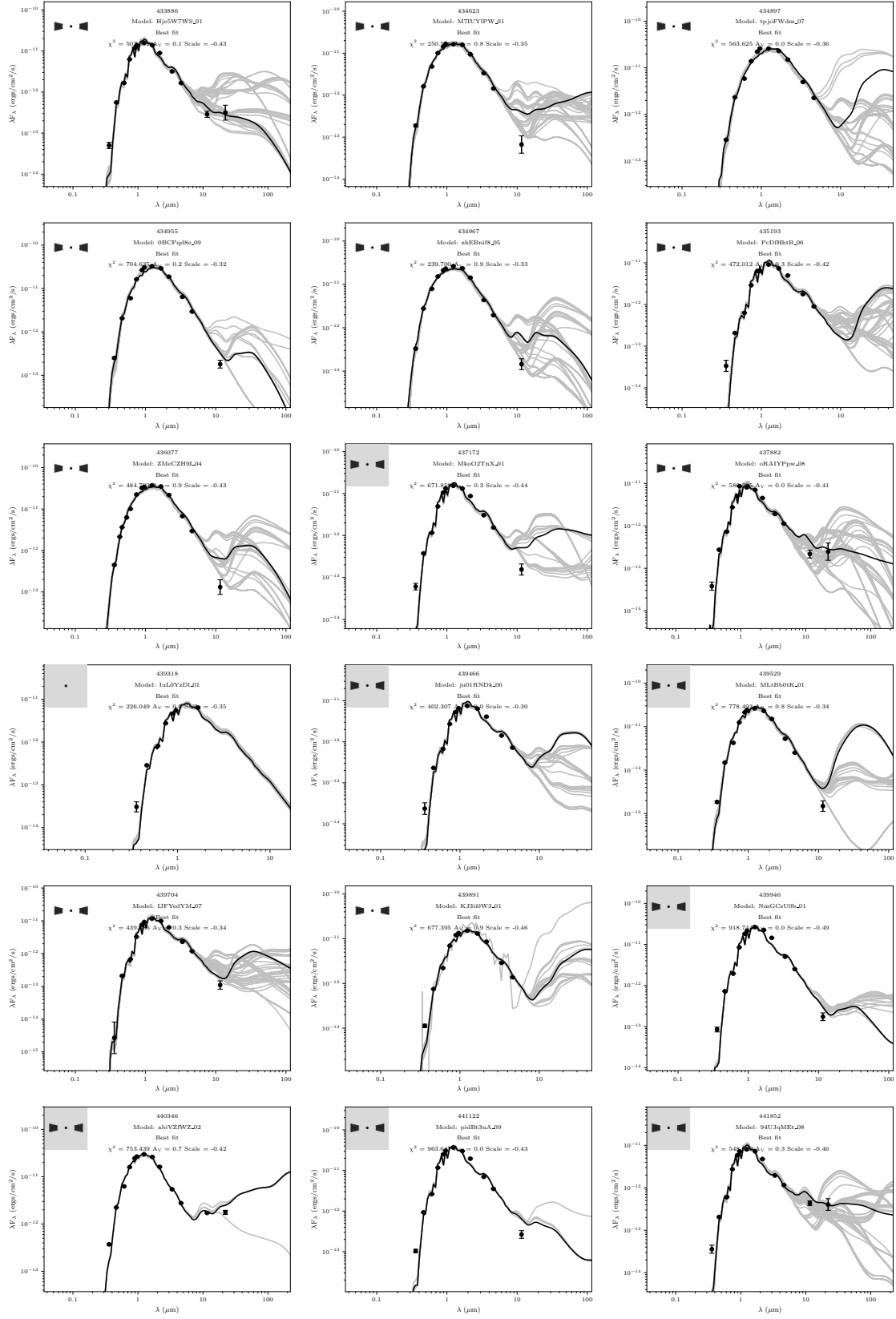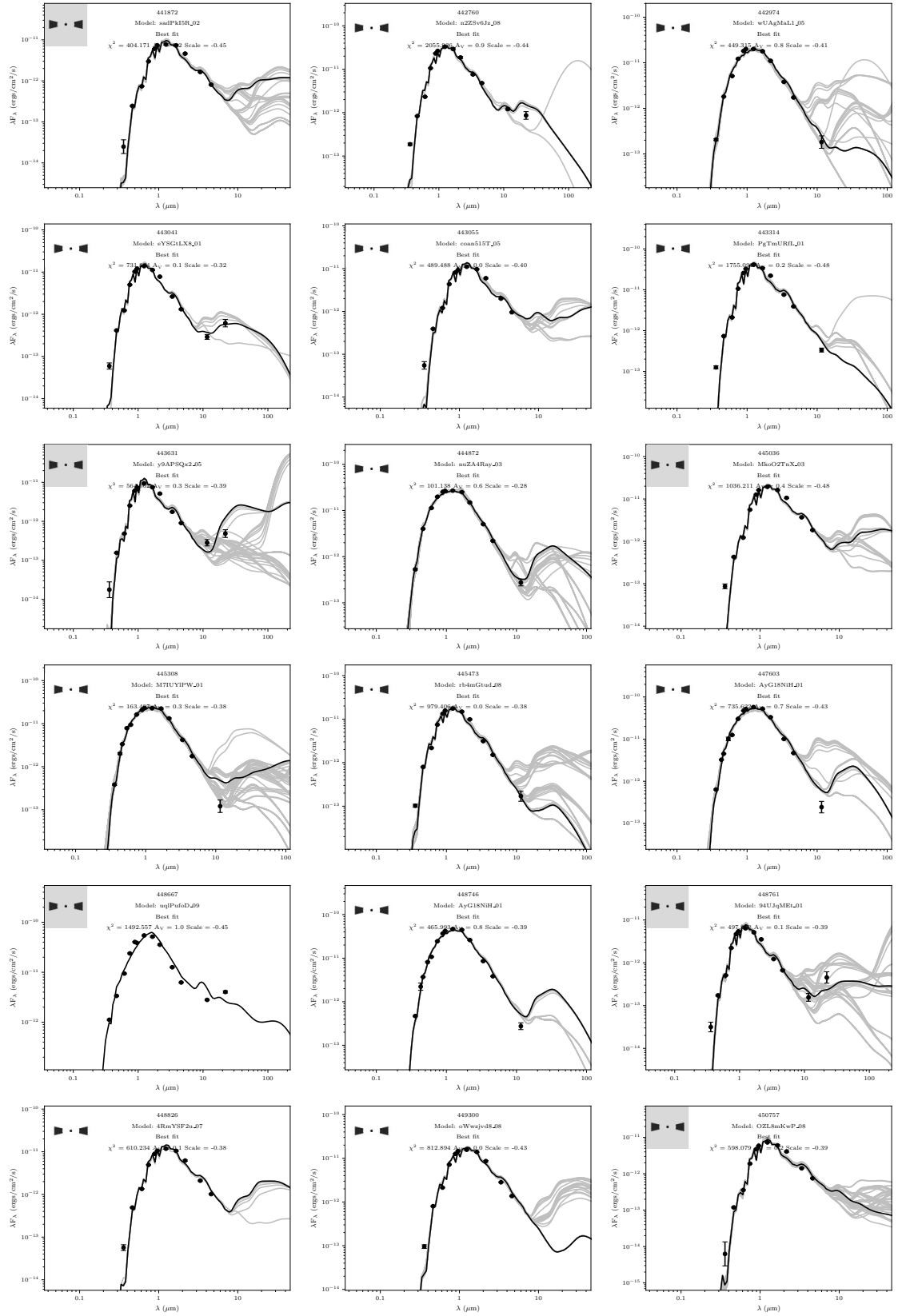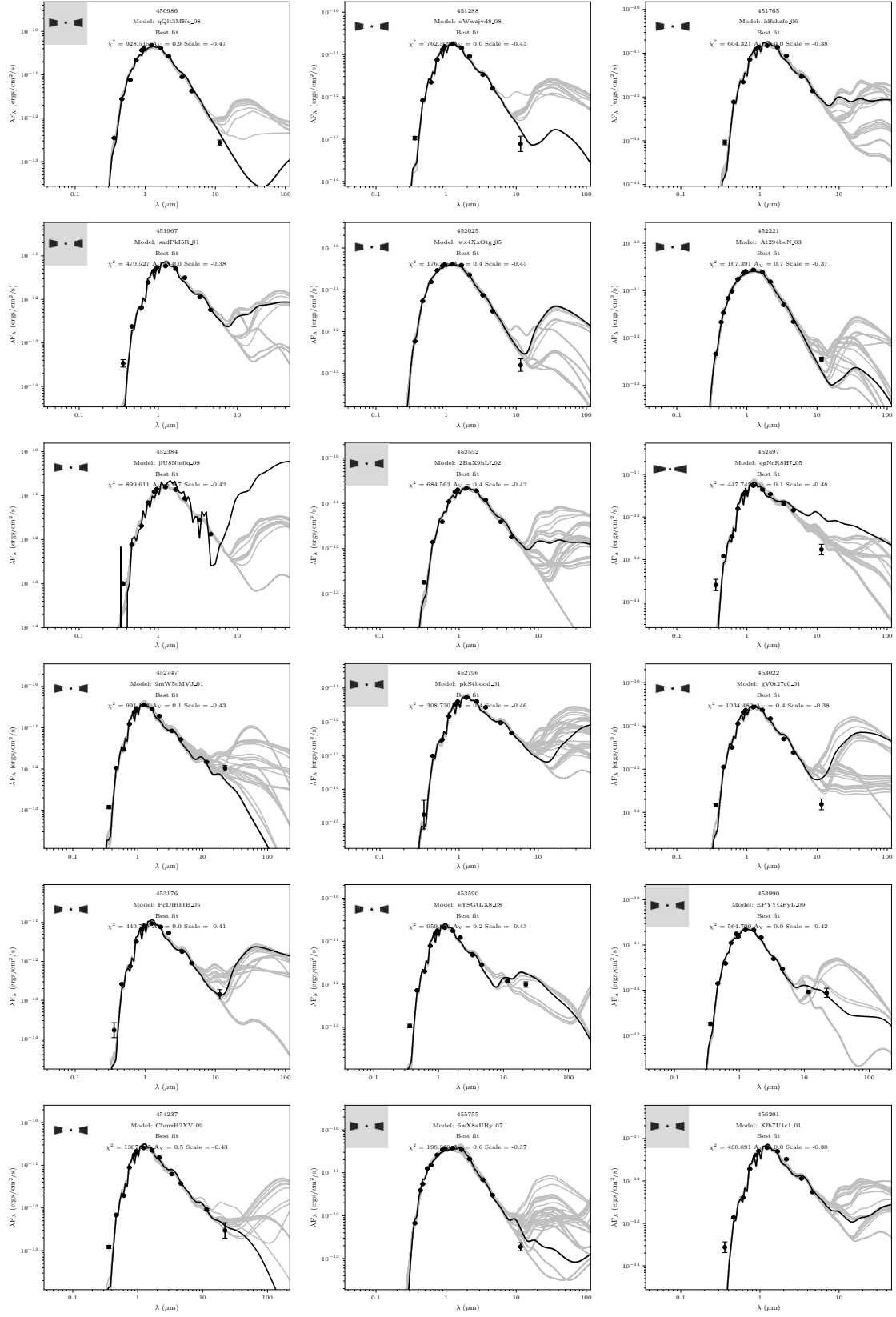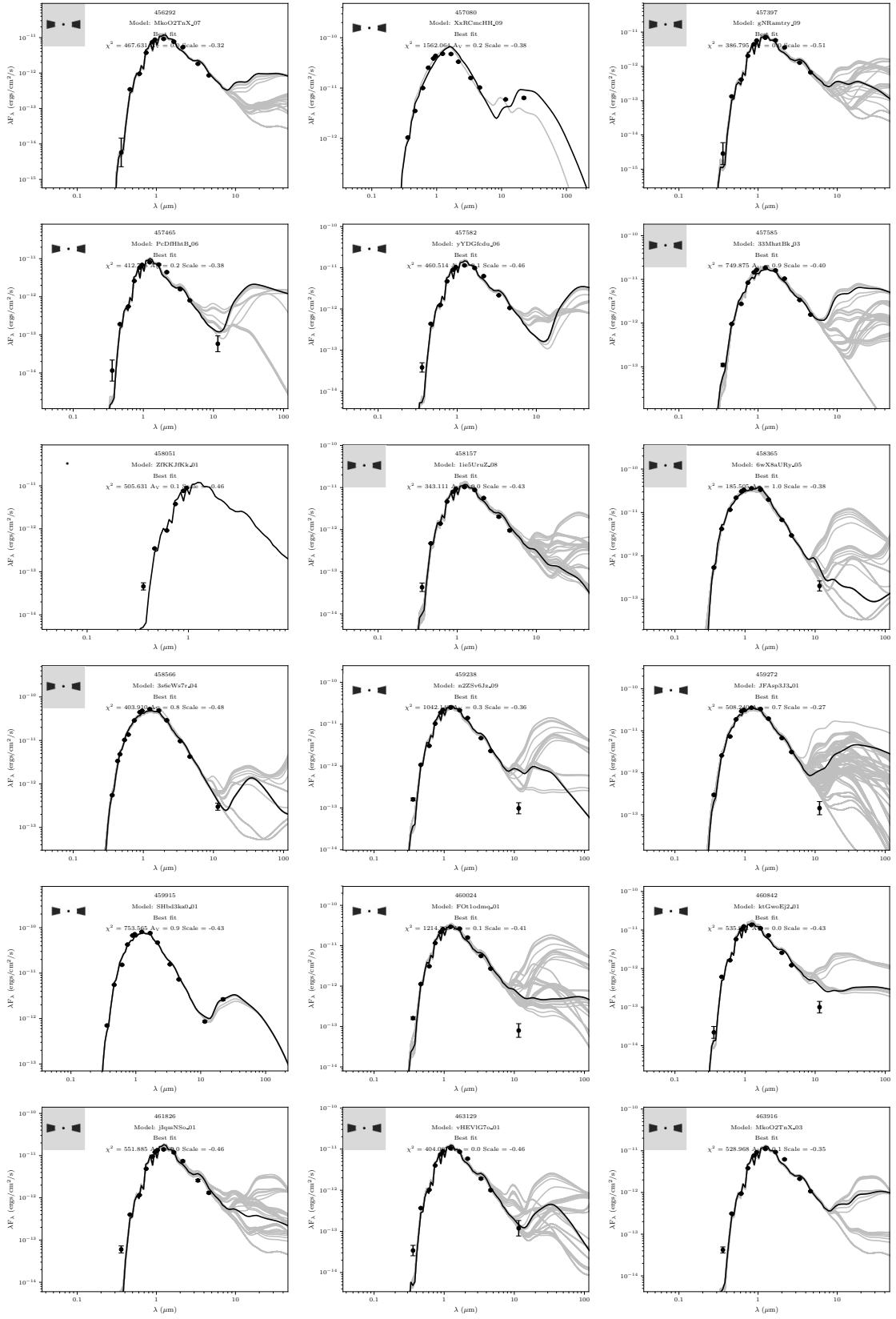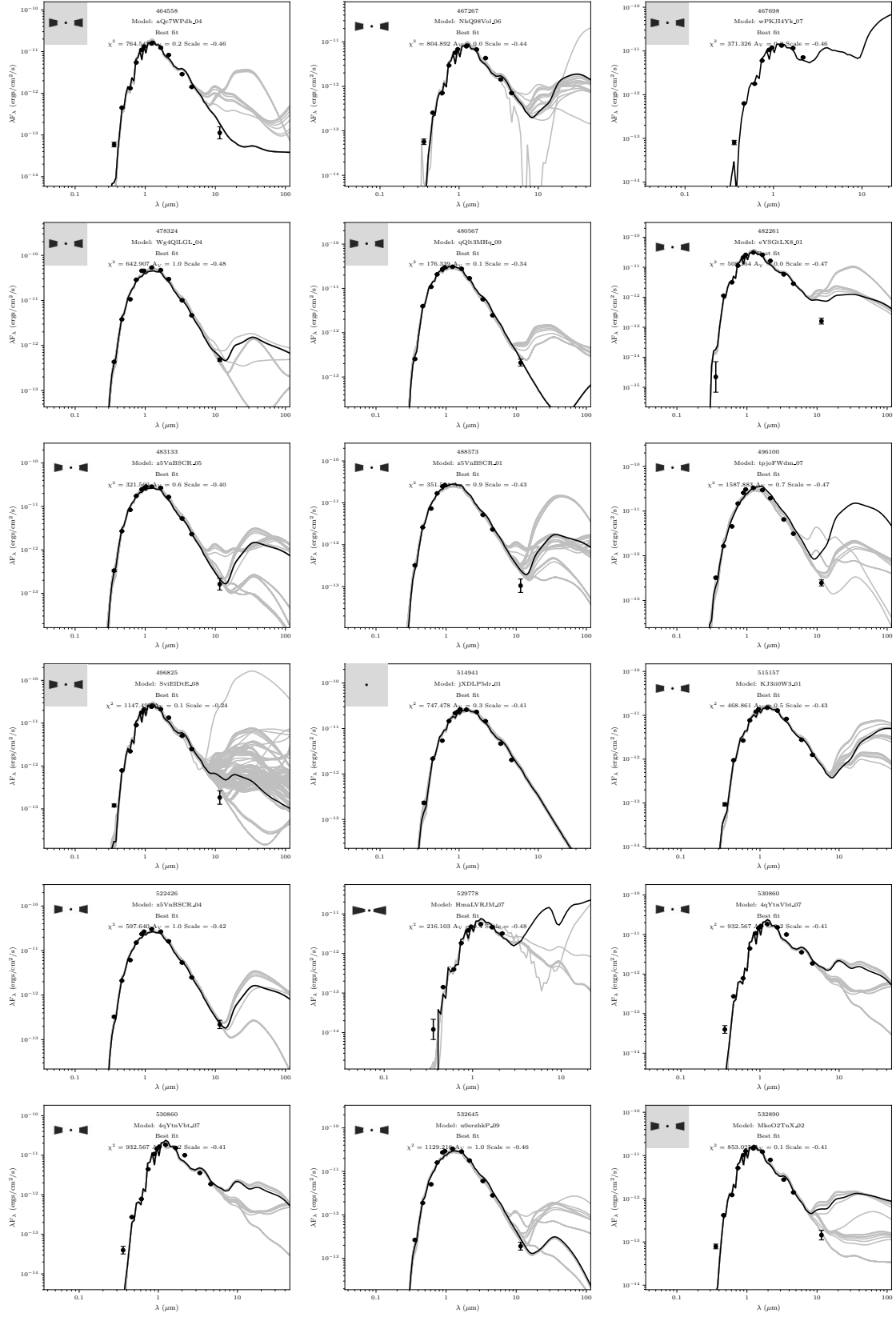
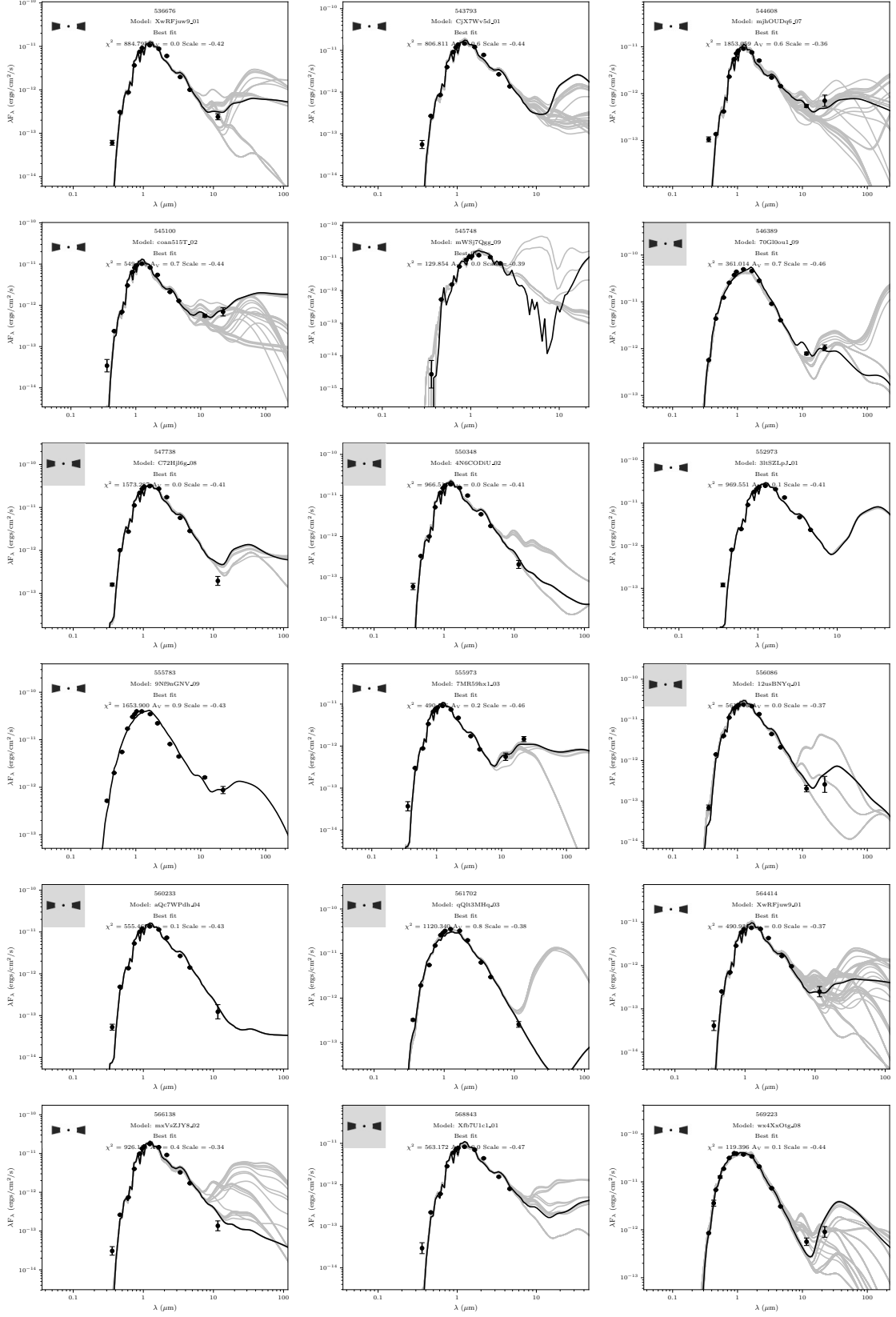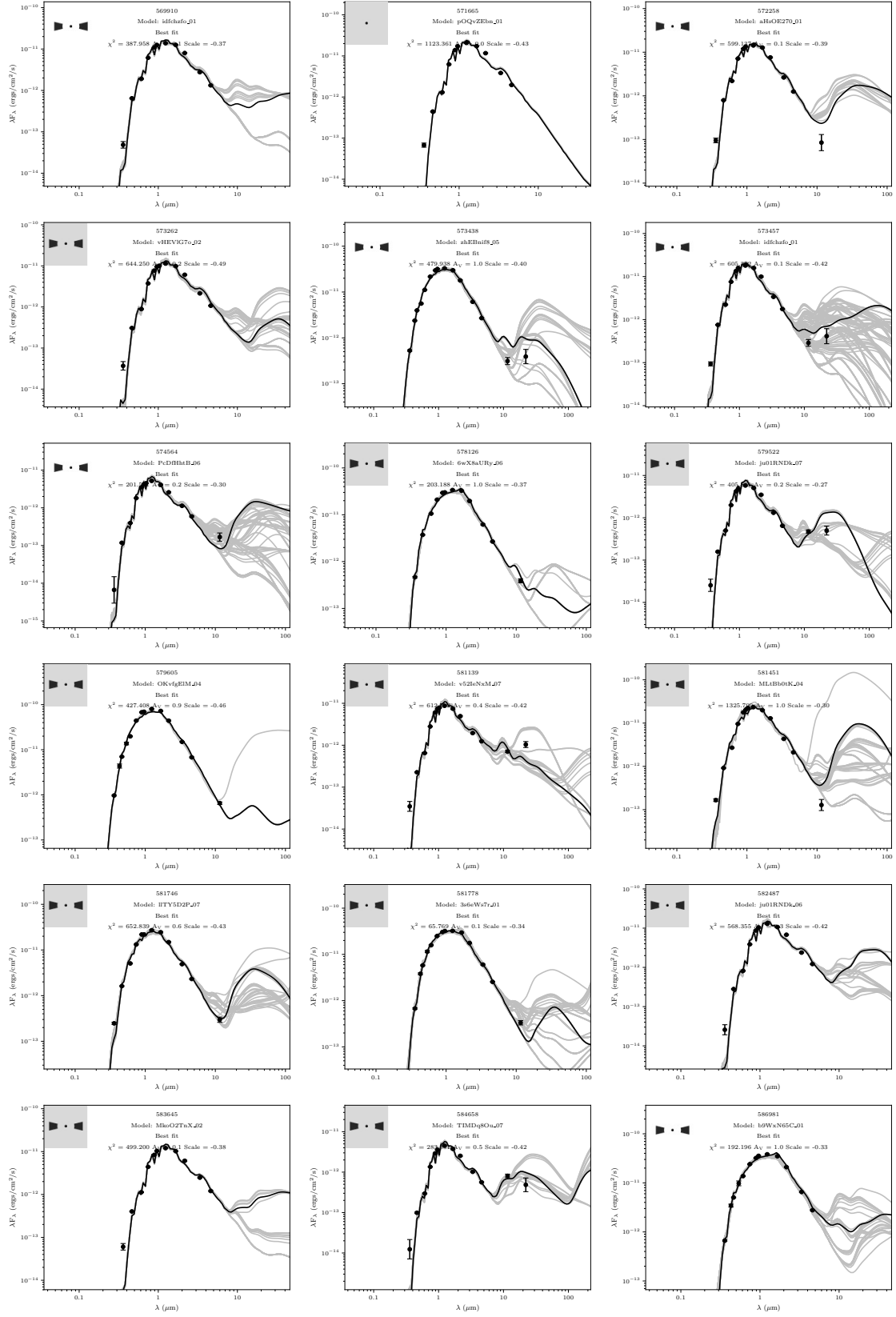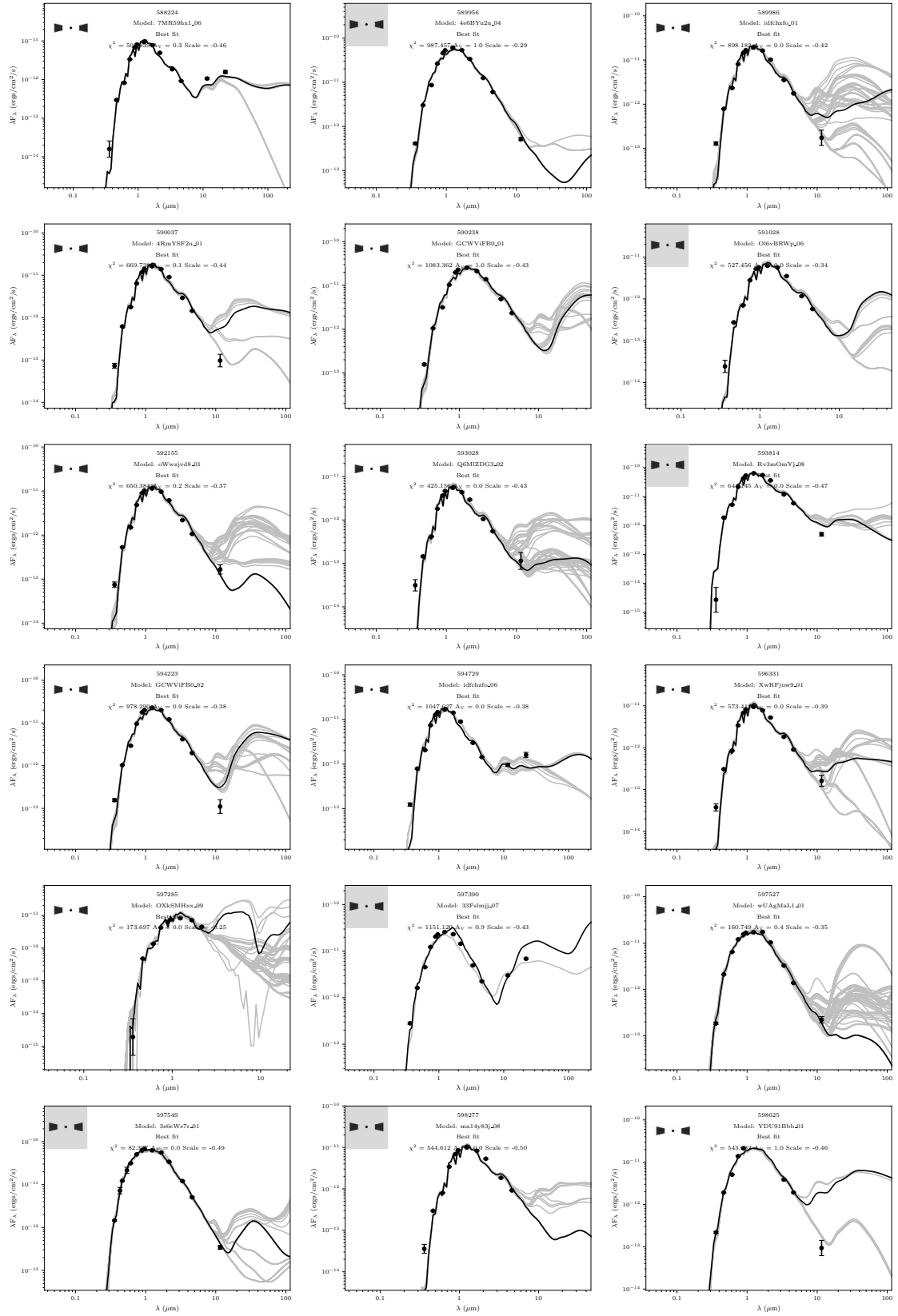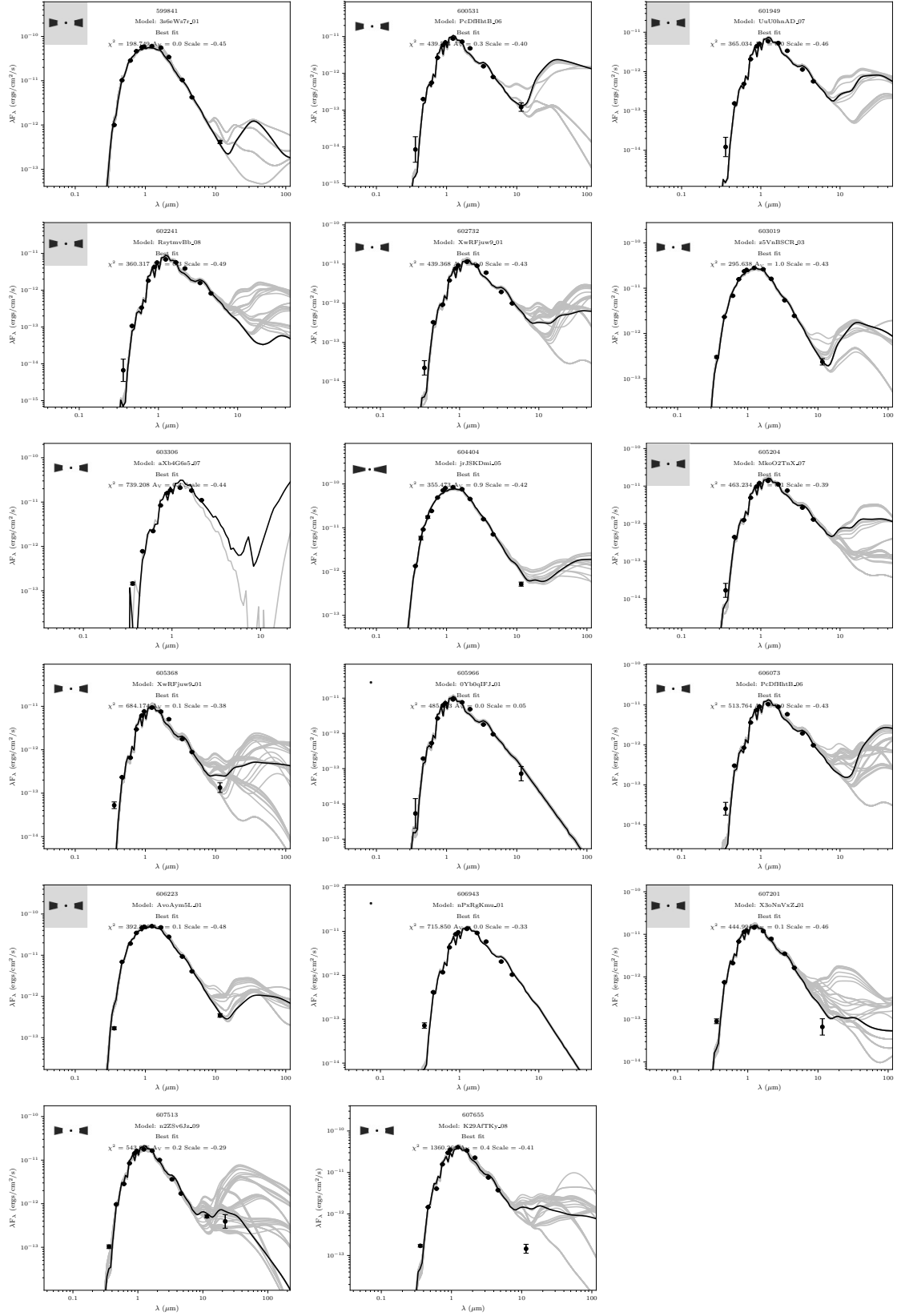# Bibliography

Adams, F. C., Shu, F. H., & Lada, C. J. 1987, in BAAS, Vol. 19, Bulletin of the American Astronomical Society, 1096

Alves, J. & Bouy, H. 2012, A&A, 547, A97

Ambartsumian, V. 1947a, Dokl. Adad. Nauk. SSR, 68, 22

Ambartsumian, V. 1947b, Stellar Evolution and Astrophysics

André, P. 2002, in EAS Publications Series, Vol. 3, EAS Publications Series, ed. J. Bouvier & J.-P. Zahn, 1–38

Andre, P., Ward-Thompson, D., & Barsony, M. 1993, ApJ, 406, 122

Bally, J. 2008, Handbook of Star Forming Regions, Volume I: The Northern Sky ASP Monograph Publications, Edited by Bo Reipurth, 4, 459

Bary, J. S., Weintraub, D. A., & Kastner, J. H. 2002, ApJL, 576, L73

Béjar, V. J. S., Martín, E. L., Zapatero Osorio, M. R., et al. 2001, ApJ, 556, 830

Belmonte, J. A. 2002, MmSAI, 73, 43

Blaauw, A. 1964, ARAA, 2, 213

Bok, B. J. 1934, Harvard College Observatory Circular, 384, 1

Bonnell, I. A., Larson, R. B., & Zinnecker, H. 2007, Protostars and Planets V, 149

Bouy, H. & Alves, J. 2015, A&A, 584, A26

Bouy, H., Alves, J., Bertin, E., Sarro, L. M., & Barrado, D. 2014, A&A, 564, A29

Briceño, C., Calvet, N., Hernández, J., et al. 2005, AJ, 129, 907

Briceno, C. 2008, Handbook of Star Forming Regions, Volume I: The Northern Sky, 4, 838

Briceno, C., Calvet, N., Hernandez, J., et al. 2018, ArXiv e-prints

Brown, A. G. A., Blaauw, A., Hoogerwerf, R., de Bruijne, J. H. J., & de Zeeuw, P. T. 1999, in NATO Advanced Science Institutes (ASI) Series C, Vol. 540, NATO Advanced Science Institutes (ASI) Series C, ed. C. J. Lada & N. D. Kylafis, 411

Brown, A. G. A., de Geus, E. J., & de Zeeuw, P. T. 1994, A&A, 289, 101

Caballero, J. A. 2008, MNRAS, 383, 750

Caballero, J. A. & Solano, E. 2008, A&A, 485, 931

Collinder, P. 1931, Annals of the Observatory of Lund, 2, B1

Corbelli, E., Palla, F., & Zinnecker, H., eds. 2005, Astrophysics and Space Science Library, Vol. 327, The Initial Mass Function 50 years later

Crawford, D. L. & Barnes, J. V. 1966, AJ, 71, 610

Dias, W. S., Alessi, B. S., Moitinho, A., & Lépine, J. R. D. 2002, A&A, 389, 871

Dias, W. S., Lépine, J. R. D., & Alessi, B. S. 2001, A&A, 376, 441

Eddington, A. S. 1924, MNRAS, 84, 308

Elmegreen, B. G. & Lada, C. J. 1977, ApJ, 214, 725

Gieseking, F. 1983, A&A, 118, 102

Gomez, M. & Lada, C. J. 1998, AJ, 115, 1524

Guetter, H. H. 1981, AJ, 86, 1057

Hardie, R. H., Heiser, A. M., & Tolbert, C. R. 1964, ApJ, 140, 1472

Herbig, G. H. & Bell, K. R. 1988, Third Catalog of Emission-Line Stars of the Orion Population : 3 : 1988

Hertzsprung, E. 1905, Zeitschrift Für Wissenschaftliche Photographie, Vol 3, p. 442-449, 3, 442

Jeffries, R. D., Maxted, P. F. L., Oliveira, J. M., & Naylor, T. 2006, MNRAS, 371, L6

Joy, A. H. 1945, ApJ, 102, 168

Kounkel, M., Covey, K., Suárez, G., et al. 2018, AJ, 156, 84

Kroupa, P. 2001, MNRAS, 322, 231

Krumholz, M. R. 2014, PhR, 539, 49

Kubiak, K., Alves, J., Bouy, H., et al. 2017, A&A, 598, A124

Lada, C. J. 1987, in IAU Symposium, Vol. 115, Star Forming Regions, ed. M. Peimbert & J. Jugaku, 1–17

Lada, C. J. & Wilking, B. A. 1984, ApJ, 287, 610

Leaman, T. M. & Hamacher, D. W. 2014, Journal of Astronomical History and Heritage, 17, 180

Lynga, G. 1987, Publications of the Astronomical Institute of the Czechoslovak Academy of Sciences, 69, 121

Markarian, B. E. 1951, Soobshcheniya Byurakanskoj Observatorii Akademiya Nauk Armyanskoj SSR Erevan, 9, 1

Massey, P., Johnson, K. E., & Degioia-Eastwood, K. 1995, ApJ, 454, 151

Massey, P., Parker, J. W., & Garmany, C. D. 1989, AJ, 98, 1305

Muench, A., Getman, K., Hillenbrand, L., & Preibisch, T. 2008, Handbook of Star Forming Regions, Volume I: The Northern Sky, 4, 483

Myers, P. C., Adams, F. C., Chen, H., & Schaff, E. 1998, ApJ, 492, 703

Needham, J. 1959, Science and Civilization in China: Volume 3, Mathematics and the Sciences of the Heavens and the Earth

Padgett, D. L., Brandner, W., Stapelfeldt, K. R., et al. 1999, AJ, 117, 1490

Pérez-Garrido, A., Díaz-Sánchez, A., & Villo, I. 2005, Astronomische Nachrichten, 326, 1028

Reiner, E. & Pingree, D. 1999, JHA, 30, 312

Robitaille, T. P. 2017, A&A, 600, A11

Rochberg, F. 2010, The mapping of the heavens.

Rogers, J. H. 1998, JoBAA, 108, 9

Russell, H. N. 1914, Popular Astronomy, 22, 331

Sadek, A. A. 1991, Memnonia I, 1350141

Salpeter, E. E. 1955, ApJ, 121, 161

Sarro, L. M., Bouy, H., Berihuete, A., et al. 2014, A&A, 563, A45

Scalo, J. M. 1986, FCPh, 11, 1

Scholz, A. & Eislöffel, J. 2005, A&A, 429, 1007

Sherry, W. H. 2003, PhD thesis, STATE UNIVERSITY OF NEW YORK AT STONY BROOK

Sherry, W. H., Walter, F. M., & Wolk, S. J. 2000, in Bulletin of the American Astronomical Society, Vol. 32, American Astronomical Society Meeting Abstracts, 1412

Shu, F. H. 1977, ApJ, 214, 488

Stahler, S. W. 1983, ApJ, 274, 822

Subramaniam, A., Gorti, U., Sagar, R., & Bhatt, H. C. 1995, A&A, 302, 86

Walter, F. M. 1986, PASP, 98, 1100

Walter, F. M. 1994, in Astronomical Society of the Pacific Conference Series, Vol. 64, Cool Stars, Stellar Systems, and the Sun, ed. J.-P. Caillault, 492

Walter, F. M., Alcala, J. M., Neuhauser, R., Sterzik, M., & Wolk, S. J. 2000, Protostars and Planets IV, 273

Walter, F. M., Wolk, S. J., Freyberg, M., & Schmitt, J. H. M. M. 1997, MmSAI, 68, 1081

Warren, Jr., W. H. & Hesser, J. E. 1977, ApJSS, 34, 115

Warren, Jr., W. H. & Hesser, J. E. 1978, ApJSS, 36, 497

Whitfield, P. 1995, The mapping of the heavens.

Wilking, B. A. 1989, PASP, 101, 229